ABSTRACT

Title of Dissertation OCEAN HEAT CONTENT CALCULATION IMPROVEMENTS FOR EARTH'S ENERGY IMBALANCE QUANTIFICATION

Timothy Paul Boyer, Doctor of Philosophy, 2024

Dissertation directed by Professor James Carton
Department of Atmospheric and Oceanic Science

Earth's Energy Imbalance, the difference between incoming and outgoing radiation at the top of the atmosphere, is stored in the atmosphere, land surface, cryosphere, and ocean, but is stored overwhelmingly (~90%) in the ocean on interannual and longer time scales. This imbalance, which is reflected in ocean heat uptake, is a primary indicator of the magnitude of change in energy the Earth's system as well as an essential variable for understanding short-term variations and their effects on long-term regional and global climate change. The primary methods for calculating ocean heat content all depend on situ measurements of ocean subsurface temperature. The ocean subsurface temperature observing system as it is currently configured, with a substantial but not exclusive contribution from autonomous Argo profiling floats, is shown here to allow estimation of annual global ocean heat uptake with an uncertainty well below that possible with earlier ocean observing systems. It is also shown that maintenance and improvement of a global best quality ocean temperature profile database will lower uncertainty,

both historically and for the current observing system and compensate to some extent for areas of sparse data in both direct calculation from observation and in data assimilation models. It is also shown that improvements to the methods used for mapping the inhomogeneous and anisotropic observations onto a regular grid spanning the global ocean will reduce uncertainty historically, currently, and into the future. On shorter monthly timescales regional changes in the Earth's Energy Imbalance requires tracking the storage within the atmosphere, land, and cryosphere, and the heat transport within the ocean especially to depths where the energy is stored on longer time scales, in addition to ocean heat uptake. Monthly heat uptake estimates discussed here can be utilized with additional terms from atmosphere/land and ocean/sea ice reanalyses to provide Earth's Energy Imbalance estimates on these shorter time-scales in the future.

OCEAN HEAT CONTENT CALCULATION IMPROVEMENTS FOR EARTH'S ENERGY IMBALANCE QUANTIFICATION

by

Timothy Paul Boyer

Dissertation submitted to the Faculty of the Graduate School of the
University of Maryland, College Park in partial fulfillment
of the requirements for the degree of
Doctor of Philosophy
2024

Advisory Committee

Professor James Carton, chair

Research Scientist Semyon Grodsky

Professor Daniel Lathrop

Professor Sumant Nigam

Professor Jacob Wenegrat

Professor Ning Zeng

Dedicated to

My mother, whose eyes always light up when she hears I am working toward my PhD.

That light keeps me going.

My wife Veronica, and daughters Winter, Isabel, and Maya who made so many

allowances for me day after day. How could I not succeed with all of you behind me?

My advisor, Professor James Carton for giving me this opportunity and encouraging me time and

again.

Syd Levitus who gave me a place to learn and generously taught me.

Doctor John Antonov who patiently shared his knowledge

Professor John Klinck who believed I had a future in oceanography

Tammy Hendershot who made sure everything was always in order on my path, even

when I had little clue.

My D League hockey team for all the encouragement, especially Mark Hosmer, Zach

Bonner, Chris Coates and Mike Sorrento who not only made sure I didn't stop, but also

taught me teamwork, perseverance, and getting through tough times on and off the ice.

Acknowledgements: My colleagues at the National Centers for Environmental

Information Ocean Climate Laboratory who I learn from every day. The Global Earth Water and Energy Exchange team, Doctor Benoit Meyssignac, Doctor Maria Hakuba, and Doctor Seiji Kato, who expanded my horizons well beyond *in situ* oceanography. The Atmospheric and Oceanographic Science Division of the University of Maryland for allowing me to learn from them, showing me what goes on above the ocean as well as in it, especially my dissertation committee who took me

on without much foreknowledge. All of the co-authors on papers with me – each one

teaching me something I did not understand before about subjects I thought I knew well

– especially Doctor Catia Domingues who had faith I could lead the uncertainties paper.

Contents

List of Tables

Table 5.1. Values of Ocean heat content anomaly ($OHCA_O$) in zetajoules (ZJ) calculated by the Institute of Atmospheric Physics (IAP) and the National Centers for Environmental Information (NCEI) from Cheng *et al.* (2019. 2020, 2021. 2022a. 2023, 2024) five highest OHCA anomaly years.

List of Figures

in orange at right for carbon dioxide, where the value is 280 ppmv (parts per million by volume). The latest values exceed 400 ppmv. For temperature, the 2015 value is more than 1 degree Celsius above preindustrial levels. Cited from Trenberth and Fasullo (2013).

Figure 2.2. Yearly ocean and atmosphere heat content anomaly. Yearly ocean (black) and atmosphere (blue) heat content anomaly (data from IPCC AR5 report, Rhein *et al.*, 2013). Ocean heat content combines upper and deep ocean heat content values for each year from that report. Microwave Sounding Unit (MSU) temperatures were used instead of GMST since GMST is a hybrid of 2 m land air temperatures and SSTs, while MSU temperatures cover the troposphere and stratosphere, giving an indication of change over a larger portion of the atmosphere.

Figure 2.3. Regime differences between 1999-2012 and 1976-1998. Mean surface temperature differences between 1999-2012 and 1979-1998 for NDJFM (a) and MJJAS (b) for surface temperature from Goddard Institute for Space Studies. For NDJFM, the global mean temperature for 1970 to 2013 and the linear trend for 1998-2013 (c) using NOAA data relative to the base period 1900-1999. Also shown in red are the temperature anomalies for 30-65°N relative to the mean for 1979-2013 from ERA-I data. In northern winter, when ENSO is strongest, the slight cooling trend in the 2000s exacerbates the hiatus and the coldest values are in La Niña years, however the coldest years for 30-65°N are years of negative NAO. Cited from Trenberth *et al.* (2014).

Figure 2.4. Latitudinal profiles of surface temperature trends. Zonal mean trends and statistical uncertainty of the trend estimates for global, ocean, and land surface temperature, averaged in

30-degree latitudinal belts, for the second half of the 20th century (dashed) compared to the past 15 years (solid). Trends are cosine-weighted within latitude belts, and the vertical axis is on a sine scale to reflect the proportional surface area of the latitude bands. Note that only the uncertainty related to the trend estimates is provided because zonal standard errors of estimate are not available in contrast to the global averages. Cited from Karl *et al.* (2015).

Figure 2.5. The linear SST trends along the world's coastlines in the warming and "hiatus" periods. The linear SST trends (unit: °C/decade) along the world's coastlines in the warming (1982–1997, a) and hiatus periods (1998–2013, b). Black points/lines in the shading color indicate the trends in those locations are significant in statistics ($P < 0.05$). Cited from Liao *et al.* (2015).

Figure 3.1. Geographic distribution of marine meteorological and ocean surface observations from ships (blue), moored buoys (red) and drifting buoys (green) for April through June a) 2019, b) 2020, and c) 2021. Subsurface observations (at any depth) from Argo floats (turquoise), Expendable Bathythermographs (purple), ship-based Conductivity-Temperature-Depth (orange), gliders (light blue), tropical moored buoys (red), pinniped mounted sensors (yellow), and ice-tethered profilers (dark green) for April through June: d) in 2019, e) in 2020, and f) in 2021. Note that surface observations from other platforms overlay drifting buoys (green) in a), b), c) while subsurface observations overlay observations from Argo floats (turquoise) in d), e), f). Drifting buoys and Argo floats are well represented, but not visible in all areas outside of marginal seas and high latitudes.

https://www.aoml.noaa.gov/phod/gdp/; Lumpkin *et al.*, 2016) based on GOOS criteria for SST and ocean surface current monitoring.

Figure 3.8. a) Argo float first cycles, 2000-2021 (orange). A first cycle is the first transmitted pressure-temperature-salinity profile set, signifying a newly deployed and actively reporting float. Total reporting Argo floats 2000-2021 (gray). The time period January 1, 2020 – December 31, 2021 shaded yellow. The black line denotes the 4000 reporting floats level. b) Newly deployed minus stopped reporting floats by quarter. Green denotes quarters with more deployments than cessation, red denotes more float cessation than floats deployed.

Figure 3.9. Average age of the Argo fleet (red line) and percent of floats in each age distribution (bars) 2000-2021.

Figure 3.10. Number of moored buoys in the ICOADS R3.0.2 (Liu *et al.* 2021) near real-time collection: solid line and left y-axis are for the coastal buoys, and dashed and right y-axis are for the tropical buoys.

Figure 3.11. Individual instrumented pinnipeds by quarter 2004-2021 in the northern hemisphere (blue) and the southern hemisphere (orange). Total number of actively reporting instrumented pinnipeds by quarter (red). Yellow shading for January 1, 2020 – December 31, 2021.

Figure 3.12. Glider missions 2000-2021 by season as reflected in the three main glider data assembly centers (Everyone's Gliding Observatories, EGO - blue; Australia's Integrated Marine Observing System, IMOS - red; NOAA Integrated Ocean Observing System Glider Data Assembly Center, IOOS, purple) and posted to the Global Telecommunications System (GTS) found in the Global Temperature and Salinity Profile Program (GTSPP, orange). Total number of glider missions in green, total glider cycles in gray shading.

List of Abbreviations

Abbreviation	Definition
ACC	Antarctic Circumpolar Current
ACECRC	Antarctic Climate and Ecosystems Cooperative Research Centre
AMO	Atlantic Multidecadal Oscillation
AMOC	Atlantic Meridional Overturning Circulation
AMSU	Advanced Microwave Sounding Units
AniBOS	Animal born ocean sensors
APB	Autonomous Pinniped Bathythermograph (data set in World Ocean Database)
AR5	Fifth Assessment Report
AR6	Sixth Assessment Report
AVISO	Archiving, Validation and Interpretation of Satellite Oceanographic Data
AT	Air Temperature
AU	Astronomical Unit
AXBT	Air Drop Expendable Bathythermograph
BGC Argo	Biogeochemical Argo
BSRN	Baseline Surface Radiation Network
CERES	Clouds and Earth's Radiant Energy System
C1_H	Alory *et al.* (2007) baseline climatology without XBT data
C13	Cowley *et al.* (2013) XBT correction
C2_H	Alory *et al.* (2007) baseline climatology with XBT data
C3_M	Locarnini *et al.* (2013) 2005-2012 baseline climatology
CIGAR	Cnr Ismar Global historicAl Reanalysis
CMEMS	Copernicus Marine Environmental Monitoring Service
CMIP	Coupled Model Intercomparison Project
CO_2	Carbon Dioxide
CORA	Coriolis Ocean Dataset for ReAnalysis

COVID-19	Corona Virus Disease 2019
Abbreviation	Definition
CSIRO	Commonwealth Scientific and Industrial Research Organisation
CTD	Conductivity-Temperature-Depth
DBT	Digital Bathythermograph
DOM	Domingues *et al.* (2008) mapping method
DRB	Drifting Buoy (data set in World Ocean Database)
EBAF	Energy Balanced and Filled
ECMWF	European Centre for Medium-Range Weather Forecasts
ECS	Equilibrium Climate Sensitivity
ECV	Essential Climate Variable
EDOF	Effective Degrees of Freedom
EEI	Earth's energy imbalance
EGO	Everybody's Glider Observations
eGOOS	executed Global Ocean Observing System
EOF	Eigenvalue Orthogonal Function
EOS80	Equation of State 1980
EN4	not an abbreviation, related to ENACT
ENACT	Enhanced Ocean Data Assimilation and Climate Prediction
ENSO	El Niño – Southern Oscillation
EOV	Essential Ocean Variable
ERA-I	ECMWF Reanalysis-Interim
ERA-20C	ECMWF 20th Century atmospheric model
ERSST	Extended Reconstruction of Sea Surface Temperature
ETOPO	Earth TOPOgraphy
FOO	Framework for Ocean Observing
G11	Good (2011) XBT correction
GCOS	Global Climate Observing System
GDP	Global Drifter Program

GMST	Global Mean Surface Temperature
Abbreviation	Definition
GEBA	Global Energy Balance Archive
GHCN	Global Historical Climatology Network
GLD	Glider (data set in World Ocean Database)
GO12	Gouretski *et al.* (2012) XBT correction
GLODAP	Global Ocean Data Assimilation Project
GODAR	Global Oceanographic Data Archaeology and Rescue
GOOS	Global Ocean Observing System
GO-SHIP	Global Ocean Ship-based Hydrographic Investigations Program
GOU	Gouretski *et al.* (2012) mapping method
GPCP	Global Precipitation Climatology Project
GPS	Global Positioning System
GR10	Gouretski and Reseghetti (2010) XBT correction
GRACE	Gravity Recovery and Climate Experiment
GRACE-FO	Gravity Recovery and Climate Experiment Follow-On
GSTH	Ground Surface Temperature Histories
GTS	Global Telecommunications System
GTSPP	Global Temperature and Salinity Profile Program
H95	Hanawa *et al.*, 1995
I09	Ishii and Kimoto (2009) XBT correction
IAP	Institute of Atmospheric Physics
IAPSO	International Association for the Physical Sciences of the Ocean
IAPWS	International Association for the Properties of Water and Steam
ICOADS	International Comprehensive Ocean Atmosphere Data Set
IMAS	Institute for Marine and Antarctic Studies
IMOS	Integrated Marine Observing System
INSIT	*in situ*
ISAS	in-situ Analysis System

Abbreviation	Definition
IOC	Intergovernmental Oceanographic Commission
IODE	International Oceanographic Data Exchange
IOOS	Integrated Ocean Observing System
IPCC	Intergovernmental Panel on Climate Change
IPO	Interdecadal Pacific Oscillation
ITF	Indonesian Through Flow
IQuOD	International Quality Controlled Oceanographic Database
ISH	Ishii and Kimoto (2009) mapping method
ITP	Ice-Tethered Profiler
J	Joule
JAMSTEC	Japanese Agency for Marine-Earth Science and Technology
JASON	Joint Altimetry Satellite Oceanography Network
JPOTS	Joint Panel on Oceanographic Tables and Standards
JRA-55	Japanese 55-year Reanalysis
L09	Levitus *et al.* (2009) XBT correction
LEV	Levitus *et al.* (2012) mapping method
LMS	Lockheed-Martin Sippican
MBT	Mechanical Bathythermograph
MJJAS	May, June, July, August, September
MJO	Madden-Julian Oscillation
MRB	Moored Buoy (data set in World Ocean Database)
MSU	Microwave Sounding Units
NAO	North Atlantic Oscillation
NCEI	National Centers for Environmental Information
NDJFM	November, December, January, February, March
NGDAC	National Glider Data Assembly Center
NGDC	National Geophysical Data Center
NOAA	National Oceanographic and Atmospheric Administration

NODC	National Oceanographic Data Center
NRT	Near Real-Time
Abbreviation	Definition
OceanOPS	Ocean Observing Platform Support
OceanSITES	Ocean Sustained Interdisciplinary Timeseries Environment observation System
OCG	Observation Coordination Group
OHC	Ocean Heat Content
OHC_N	Ocean Heat Content calculated with NCEI method
OHC_O	Ocean Heat Content from observations
OHCA	Ocean Heat Content Anomaly
$OHCA_N$	Ocean Heat Content Anomaly calculated with NCEI method
$OHCA_O$	Ocean Heat Content Anomaly from observations
OHU	Ocean Heat Uptake
OHU_N	Ocean Heat Uptake calculated with NCEI method
OHU_O	Ocean Heat Uptake from observations
ORA-20C	Ocean ReAnalyses for the 20^{th} Century
P-ALACE	Profiling Autonomous Lagrangian Circulation Explorer
PFL	Profiling float (data set in World Ocean Database)
PCHIPS	Piecewise Cubic Hermite Interpolating Polynomials
pCO_2	partial pressure of Carbon Dioxide
PDO	Pacific Decadal Oscillation
pH	potential of Hydrogen
PIRATA	Pilot Research Moored Array in the Atlantic
PMEL	Pacific Marine Environmental Laboratory
PMEL_M	PMEL mean of the maps
PMEL_R	PMEL representative mean
PSS-78	Practical Salinity Scale 1978
PV	Passenger Vessel

RAMA	Research Moored Array for the Asian-African-Australian Monsoon Analysis and Prediction
Abbreviation	Definition
RA	Reanalysis
RO	Radio Occultation
RT	Real-Time
RV	Research Vessel
SI	Simple Area Integral
SLP	Sea Level Pressure
SORCE/TIM	Solar Radiation and Climate Experiment/Total Irradiance Monitor
SOAR	Second-Order Auto-Regression
SOCAT	Surface Ocean CO_2 Atlas
SOOP	Ship of Opportunity Program
SST	Sea Surface Temperature
SSS	Sea Surface Salinity
SUMD	Surface Underway Marine Database
SY24	Storto and Yang, 2024
TAO	Tropical Atmosphere Ocean
TEOS-10	Thermodynamic Equation of State 2010
TSI	Total Solar Irradiance
TOA	Top of the Atmosphere
TSK	Tsurumi Seiki
UNESCO	United Nations Educational, Scientific and Cultural Organization
USGCRP	United Stated Global Change Research Program
UTLS	Upper Troposphere/Lower Stratosphere
UOR	Undulating Oceanographic Recorder (data set in World Ocean Database)
USV	Uncrewed Surface Vehicles
UxS	Uncrewed Systems
VOS	Volunteer Observing Ship

Abbreviation	Definition
XBT	Expendable Bathythermograph
XCTD	Expendable Conductivity-Temperature-Depth
W08	Wijffels *et al.* (2008) XBT correction
WIL	Willis *et al.* (2004) mapping method
WMO	World Meteorological Organizations
WOA	World Ocean Atlas
WOCE	World Ocean Circulation Experiment
WOD	World Ocean Database
ZJ	Zetajoule (10^{21} Joules)

Chapter 1. Introduction

1.1 Purpose of dissertation

Earth's energy imbalance (EEI) is the difference between incoming and outgoing radiation at the top of the atmosphere (TOA). The increased residence time of longwave radiation in the Earth's system due to absorption and reemission by greenhouse gases in the atmosphere is a major factor in EEI. Quantifying EEI and energy storage in the Earth's system is critical to understanding past, present and future effects of increasing greenhouse gases in the atmosphere. The ocean with its coverage of approximately 71% of the Earth's surface (using ocean area of 360,663,099 km2 from Costello *et al.* 2010), its high specific heat capacity (3,953 $Jkg^{-1}K^{-1}$ for temperature of 0°C, salinity of 35, surface pressure (0 decibars; db); 4,217 $Jkg^{-1}K^{-1}$ for temperature of 0°C, salinity 35, pressure of 1000 db, as per algorithm of Millero, 1973) is the main storage component in the Earth's system for EEI. The ocean stores approximately 90% of EEI by recent estimates (von Schuckmann *et al.* (2023). The transport of heat absorbed at the ocean's surface to deeper depths sequesters the energy for long time scales, from interannual to decadal to millennial, mitigating the effects of EEI. Since ocean heat content is the predominant storage component for EEI in the Earth's system, it can, and is, used to estimate changes over time to EEI (ΔEEI), to detect any acceleration of ΔEEI over time. Minière *et al.* (2023) calculate ocean warming has increased 0.91 ± 0.80 Wm^{-2} between 1960-1970 and 2010-2020. While the calculated increase in the rate of ocean warming is significant, the uncertainty is large compared to the increase. The warming increase and the uncertainty are taken from an ensemble of ocean heat content change time series which are calculated from *in situ* ocean temperature profiles, the Global Climate Observing System (GCOS) ensemble (von Schuckmann *et al.*, 2023). A component of the uncertainty is the difference of the yearly values between the ensemble

members. The uncertainty in the GCOS ensemble is much smaller in the 2010-2020 period than the earlier 1960-1970 period used in Minière *et al.* (2023) to calculate changing rates of ocean warming. This is due to the Argo profiling float ocean observing system (Roemmich *et al.*, 2019) in the later time period with its high-quality observations geographically and temporally homogeneously distributed globally. The ocean is the main sink of EEI, a main driver of environmental change. Calculations of ocean heat content change from temperature observations are indispensable for providing a baseline understanding of historic and recent EEI and a means to calibrate and check climate models for future prediction. Improving ocean heat content change calculations from a single member of an ensemble can lower the overall uncertainty of the ensemble and be used singly as a comparison for other (non-*in situ* observation) methods for EEI calculation and for climate models. The use of ocean heat content change results with optimized process, from treatment of observations to optimized calculation method, can increase certainty in a single member and an ensemble, enabling use with high confidence as a baseline indicator for environmental change in the Earth's system. Even though the ocean stores 90% of EEI in the long-term, it is the interaction with the other storage components which affect short (sub-annual) to decadal storage patterns in the Earth's system as a whole. An understanding of the mechanisms by which transport of ocean heat to deeper depths, or conversely leaves ocean heat at shallower depths from where it can be reintroduced into the other components of the Earth's system requires an understanding of all components of the Earth's energy budget and their interactions.

The dissertation will be structured first with the rest of the introduction, beginning with a definition of the ocean heat content variables to be examined, placing definitions of ocean heat

content and related variables in a thermodynamic conceptualization. An examination of the Earth's energy budget, storage of EEI in Earth system components, and the interaction of the different components as it relates to changes in ocean heat storage follows. A brief survey of methods for calculating ocean heat content, their relative uncertainties and relation to methods for calculation from *in situ* temperature observations will provide context for why *in situ* calculation methods and uncertainty quantification are necessary despite methods which utilize more complete data representations as input. A brief description of methods for calculating ocean heat content from irregular *in situ* observations will complete the introduction, with a detailed appendix for the method which is the main method (Levitus *et al.*, 2012) employed in this dissertation. The body of the paper consists of an examination of energy in the Earth's system and the relation between GMST and ocean heat content during a multi-year event, termed the global warming hiatus, an examination of the resiliency of the observing system with which ocean heat content change is measured during the covid-19 pandemic, an essential key to continuing high certainty calculations, and an examination of differences between an ensemble of observation-based calculations of ocean heat content change to help quantify uncertainty and identify components of analysis methods which can be examined and improved. Conclusions and future work will discuss points for further examination of GMST and ocean heat content as climate indicators, the requirements for ocean heat content calculations for an understanding of the atmosphere-ocean interactions which govern monthly to long-term sequestration of heat in the deep ocean, a plan for optimizing the flow of data globally to allow for more homogeneous observation choices, quality assurance, and a more complete uncertainty quantification, with a final section on necessary improvements in calculation method to reduce uncertainty. Some final remarks will end the dissertation.

1.2 Definition of ocean heat content, ocean heat content anomaly, ocean heat uptake

In order to calculate ocean heat content from *in situ* observations of temperature, the relation of energy and the temperature observations must be established. This is not as straightforward as it appears. A great deal of effort has been devoted to the question of defining heat in the ocean in terms of conservation of energy - the first law of thermodynamics. Enthalpy (H) is defined as

$$H = E + PV \qquad (1.1)$$

where E is internal energy of the system, P is pressure, and V is volume. Heat Content per unit mass is equivalent to enthalpy with heat content based on the formulation of Bohren and Albrecht (1998). Potential temperature, the temperature of a parcel of seawater raised from ambient depth to the surface adiabatically has long been used in ocean models to calculate heat fluxes. But potential temperature is not conserved during mixing (at constant pressure), it is potential enthalpy (enthalpy of a parcel of water raised adiabatically, and without salt loss/gain) which is conserved (McDougall, 2003). Calculations of heat content or heat fluxes using potential temperature and constant specific heat capacity values have an inherent error (0.6 mWm^{-2} for heat content represented at approximately 25 m as per McDougall *et al.*, 2021). The Thermodynamic Equation of State 2010 (TEOS-10; IAPWS, 2008) addresses this by using potential enthalpy as the basis for the calculation of conservative temperature. Conservative temperature is defined on the basis of conservation of energy using Gibbs free energy function which encompass both enthalpy and entropy. The equation for seawater account for energy changes due to dissolved molecules through absolute salinity, where absolute salinity includes all dissolved molecules in seawater including silicates which are not measured by conductivity sensors. When there is no exchange of heat or salt, such as assumed at the time of an

instantaneous measurement, entropy and absolute salinity are constant, so conservative temperature is a function of enthalpy. So, an ideal representation of ocean heat content utilizing conservative temperature (Θ) (OHC(TEOS10); IOC *et al.*, 2010) would be

$$OHC(TEOS10) = \iiint_{h2}^{h1} \rho C_p \Theta dx dy dz \qquad (1.2)$$

at a density ρ and a constant specific heat C_p, integrated over all depths (h), and all global ocean area. The necessity of salinity observations with each temperature observation in order to calculate conservative temperature precludes the use of conservative temperature (or indeed potential temperature) in calculations of ocean heat content directly from *in situ* observations, especially historically, where temperature-only oceanographic observations are prevalent, but even in the modern era where a significant subset of observations are temperature-only. Instead, *in situ* temperature is used and a pressure variable specific heat capacity, $C_{pM,}$ calculated as per Millero (1973). C_{pM} calculation is based on the Equation of State 1980 (EOS80, UNESCO, 1981) which was derived to fit standard seawater and tested using highly accurate *in situ* density measurements (Millero, 2010, Pawlowicz *et al.*, 2013). EOS80 uses the Practical Salinity Scale 1978 (PSS-78) salinity from conductivity measurements. So, EOS80 is an operational definition, rather than one constructed from thermodynamics. Algorithms for calculating oceanographic variables in EOS80 are not always consistent (Pawlowicz *et al.*, 2012). Moreover, C_{pM} is dependent on salinity as well as pressure and temperature. To minimize any uncertainty in the use of PSS-78 instead of absolute salinity, C_{pM} is applied not to individual observations, but to objectively analyzed means of temperature, where a long-term climatology of monthly salinity is used for C_{pM}. for each latitude (i), longitude (j), and depth (z). *in situ* density, ρ, variable in latitude (i), longitude (j) and depth (z) is also applied to the objectively

analyzed means, from long-term monthly climatological mean fields of *in situ* density. So, the quantity calculated here, OHC_N (where the N is for NCEI (NOAA National Centers for Environmental Information), the calculation of OHC from temperature observations first introduced in Levitus *et al.*, 2000 is

$$OHC_N = \iiint_{z_2}^{z_1} \rho_c C_{pc} T \, didj \, dz \qquad (1.3)$$

where ρ_c is climatological density at the given point, C_{pC} is specific heat capacity at the given climatological mean temperature and salinity, T is *in situ* temperature in Kelvin. OHC_N equation uses EOS80 and has small uncertainties due to the use of climatological density and specific heat capacity. It does not account for the effects of salinity on differentials of enthalpy, an expected small contribution (see above, McDougall *et al.*, 2021). OHC_N from monthly long-term climatological means of temperature 1955-2006 (World Ocean Atlas 2009; WOA09; Locarnini *et al.*, 2010) using equation (1.3) (adding 273.15K to the temperature values) for the surface to 2000 m is $735.576 \pm 0.046 \times 10^{24}$ J, where 0.046×10^{24}, 46 ZJ, is the annual cycle standard deviation). The calculated amplitude of the annual cycle is 64 ZJ, similar to the annual cycle calculated by Johnson *et al.* (2023) for the mixed-layer + 50 m and by Pan *et al.* (2023) for the upper 1500 m from an ensemble, larger than for Antonov *et al.* (2004) in the upper 250 m (37 ZJ).

To monitor interannual changes in OHC, which is four orders of magnitude smaller than OHC itself, the actual quantity of interest is OHC anomaly (OHCA) the cumulative change of OHC relative to a baseline mean. EEI over a given time period is (90%) quantified by Ocean Heat Uptake (OHU), which is change in OHCA over the same given time period, reflecting that OHCA is due mainly to surface flux from the atmosphere which is stored for an extended period

in the ocean. OHCA itself can be thought of as OHU for the time period between the center point in time of the baseline mean to the center point in time represented by the value of OHCA. So yearly OHCA for 2023 from a baseline mean 1955-2006, approximates an estimate of OHU between years 1980.5 and 2023.5. To distinguish between the concept of OHCA (OHU) in general and methods for calculating OHCA (OHU) from *in situ* ocean temperature observations, $OHCA_O$ (OHU_O) will be used for the latter. To further distinguish the NCEI *in situ* temperature observation-based method for calculation of OHCA (OHU), the method which is the specific calculation under examination for improvement in this work, $OHCA_N$ (OHU_N) will be used. Other $OHCA_O$ have many similarities to $OHCA_N$, but also have differences which lead to uncertainties in an ensemble.

$OHCA_N$ is calculated from ocean temperature anomalies (ΔT), the change in observed mean temperature from a baseline temperature mean over a given time span over discrete defined area (A) multiplied by ρ_c and C_{pc} integrated over depth. So, for each discrete area denoted by grid indices i,j,

$$OHCA_N\,(i,j) = A \int_{z_1}^{z_2} \rho_c C_{pC} \Delta T \, dz \qquad (1.4)$$

where A, ρ_c, C_{pc}, and ΔT are all dependent on i,j. Z_1 is always the surface, Z_2 is dependent on either the bottom depth of grid (i,j) or the depth of integration, whichever is deeper. Depth of integration in $OHCA_N$ is based on observation availability (see below), in Levitus *et al.* (2012) 2000 m. for yearly $OHCA_N$. The depth integration is actually a summation of $OHCA_N$(i,j) over standard depth levels, where ΔT at the standard depth level represents the depth interval half the distance to the next shallower standard depth +half the distance to the next deeper standard depth, with the shallowest standard depth only representing half the distance to the next deeper

standard depth and the deepest standard depth only representing half the distance to the next shallower depth.

To obtain a global integral (summation), all $OHCA_N(i,j)$ values for each discrete area are summed:

$$OHCA_N = \sum_{I_1}^{I_2} \sum_{J_1}^{J_2} OHCA_N(i,j) \qquad (1.5)$$

where units of OHCA are units of heat energy – joules (J), often Zetajoules (ZJ). For comparison with EEI over a time period (mainly yearly in this work), units of power per unit area are used – Wm^{-2}. A watt is a joule per second, so the conversion from OHCA in J to EEI in Wm^{-2} is OHCA divided by the number of seconds in the time period over which OHCA was calculated and divided by the area of the Earth system at TOA.

It is difficult to conceptualize just how much heat the ocean sequesters and thus the magnitude of 90% of EEI. One way to look at it is to estimate the change in an 'idealized atmosphere', ignoring volume change and internal dynamics if the annual amount of heat entering the ocean were instead instantaneously added as per equation (1.6),

$$\Delta T_a = \frac{OHCA_O}{M_a C_{Pa}} \qquad (1.6)$$

where ΔT_a is the instantaneous change in temperature in the atmosphere, M_a is the mass of the atmosphere, 5.1480 x 10^{18} kg as per Trenberth and Smith (2005), and C_{pa}, the specific heat capacity of the atmosphere, 700 $Jkg^{-1}K^{-1}$. Using OHU_N from Cheng *et al.* (2024) for 2023, 9 ±5 ZJ, ΔT_a is 2.5 ± 1.4 K (°C). Using Institute of Atmospheric Physics (IAP; Cheng *et al.*, 2022a) OHU_O for 2023, shown in Cheng *et al.* (2024) as 15 ± 10 ZJ, ΔT_a is 4.1 ± 2.8 K. This is not

realistic, rather a thought experiment to show the magnitude of the heat energy absorbed by the ocean (and the importance of constraining the uncertainties).

Limitations of $OHCA_N$, and most $OHCA_O$ calculation, are mainly the limitations of the observing system. Choices of time resolution, geographic resolution, and vertical resolution are limited by available observations. The length of the time series for $OHCA_N$ is governed by the historic ability, instrumentational and logistically, to observe the ocean. The heterogeneity of the temperature observations, with a changing observing system over time with varying quality of observations, increases uncertainty in longer time series and makes bias correction and quality assurance an important part of the process for calculating $OHCA_N$ time series. Techniques to construct a global integral from discrete, often sparse, observations, need to be optimized in every aspect in order to minimize uncertainty in the $OHCA_N$ integral. The measurement and data flow of the input observations to the $OHCA_N$ calculations, the quality control of the observations, and the calculation of observed means from the observations are also necessary points to consider in optimization of $OHCA_N$ (and $OHCA_O$) as well as in calculating, and minimizing uncertainty.

1.3 Earth's Energy Budget

Now that the relation between the OHU_O and EEI is established in terms of energy storage, an understanding of the components of the Earth's energy budget and storage of EEI is necessary to explore the interaction of components of the Earth's system with the ocean and on OHU. The vast majority of energy in the Earth's system comes from the Sun, 3,000 times more energy than from all other sources (heat flux from Earth's interior, magnetic storm dissipation, fossil fuel combustion, etc.) combined (Kren *et al.*, 2017). Total solar irradiance (TSI; also known as the

solar constant) is 1,361 Wm^{-2}, based on 17 years of measurements from the Solar Radiation and Climate Experiment/Total Irradiance Monitor (SORCE/TIM) between 2003 and 2020 (Kopp, 2021). TSI varies on different time scales, including variations of 0.3% on 27-day solar rotational time scale, and variations of 0.1% over 11-year solar cycles (Kopp, 2014). TSI is calculated as Sun's radiation incident on a disk with the radius of the Earth at TOA at a distance of one Astronomical Unit (AU; the distance from the center of the Sun to the center of the Earth). Given that the Earth is a rotating sphere with four times the surface area of a disk the radius of the Earth, the actual radiation which enters the Earth's system at the TOA, is one quarter TSI, or 340 Wm^{-2} with an uncertainty range of 1 Wm^{-2} (Wild *et al.*, 2015). A portion (80 Wm^{-2}) of incoming radiation is absorbed by water vapor and particles in the atmosphere, while a similar portion (100 Wm^{-2}) is reflected by clouds back to space, leaving the remainder (185 Wm^{-2}) to reach the Earth's surface. Surface refection of 25 Wm^{-2}, leaves absorption at the Earth's surface of 160 Wm^{-2}. Values in the radiation budget given here are updates of Wild *et al.* (2015, land plus sea values) in Forster *et al.* (2021, all-sky values; Figure 1.1, their figure 7.2a). There has been considerable effort to constrain the values for each component of the Earth's energy budget (Wild *et al.*, 2015; L'Ecuyer *et al.*, 2015; Kato *et al.*, 2018) based on satellite observations and model analysis, using the values from Forster *et al.* (2021) here is to give a general understanding of the magnitude of the components, rather than the latest values and uncertainties of each component. Thermal energy radiated from the Earth's surface is calculated using black-body radiation equation with Stefan-Boltzmann constant and a surface temperature data set as 398 Wm^{-2}. Downward longwave radiation, from absorption and remission by greenhouse gases is calculated from the Coupled Model Intercomparison Project 5 (CMIP5) model ensemble and observations as 342 Wm^{-2}. Observations are from the Global Energy

Balance Archive (GEBA; Gilgen *et al.*, 1998) and the Baseline Surface Radiation Network (BSRN; Ohmura *et al.*, 1998), the same observational data set used for surface solar radiation measurements. Outgoing longwave radiation at the TOA, 239 Wm^{-2}, is measured by satellite, and is a combination of upward minus downward longwave radiation plus longwave cooling (emission of longwave radiation from atmospheric particles which is larger than the absorption of shortwave radiation by the same particles). The final major component of the Earth's energy budget is latent and sensible heat, mainly evaporation from the surface. Given that evaporated water flux to the atmosphere is returned to the surface as precipitation, estimates of latent and sensible heat are obtained from precipitation estimates (Trenberth *et al.*, 2009) from the Global Precipitation Climatology Project (GPCP; Huffman *et al.*, 2023), estimated at 82 Wm^{-2} and 21 Wm^{-2} for latent and sensible heat respectively. There are few long-term combined surface flux observations for latent and sensible heat calculations, especially over the ocean (Bentamy *et al.*, 2017), so uncertainty in this component is large, 11 Wm^{-2}. It is important to understand and quantify with certainty all of the components of the Earth's energy budget to understand the regional and global transport of heat in the atmosphere and ocean and the concurrent changes and consequences in shifts in the respective components. The unaccounted energy in the Earth's energy budget in Figure 1.1 is EEI (0.7 Wm^{-2}) which is small and not easily calculated as the residual of the components of the Earth's energy budget given the large values and relatively large uncertainties in each component.

1.4 Earth's Energy Imbalance and global scale storage in the Earth's system

While EEI is small in comparison to the components of the Earth's energy budget and their uncertainties, it is critical to quantify EEI on a global scale in order to monitor and understand expected changes in the Earth's system due to increasing greenhouse gases, which are mainly responsible for downward longwave radiation which increases energy residence time in the Earth's system. A quantification of EEI leads to estimates of the magnitude of reduction in anthropogenic greenhouse gas emissions needed to ameliorate further increases in EEI. Fortunately, we do not need to resolve the uncertainties in the components of the Earth's energy budget to quantify EEI. Satellite measurements at the TOA measure cumulative incoming and outgoing radiation (see section 1.4 for details) and quantification of change in energy storage in the different components of the Earth's system, provides an independent estimate of EEI (Figure 1.2, from von Schuckmann *et al.*, 2023; their Figure 8). The ocean plays the largest role in the Earth's energy storage in absorbing approximately 90% of the excess energy in the Earth's system since the 1970s (Minière *et al.* 2023). Only a small portion of EEI remains in the atmosphere (1%), a small portion is absorbed by land surface (5%) and a small portion is utilized in state change of water, mainly in ice melt/freeze – the cryosphere (3%), but also in state changes associated with evaporation and precipitation (percentages as in Minière *et al.* 2023 from von Schuckmann *et al.* 2020; von Schuckmann *et al.* 2023; Forster *et al.*, 2021).

1.5 Quantifying energy storage components of the Earth's system

1.5.1 Relation of GMST and OHU through Equilibrium Climate Sensitivity

EEI and ocean heat content change are also essential variables for climate models and calculations of climate sensitivity. Forster (2016; after Forster and Gregory, 2006; Gregory *et*

*al.*2002) relate change in GMST (ΔT_S) to time dependent change in EEI (ΔN in their formulation), as

$$\Delta N = \Delta F - \alpha \Delta T_S + \gamma \qquad (1.7)$$

where ΔF is the change in radiative forcing calculated for a given level of atmospheric carbon dioxide (CO_2), α is the climate feedback parameter, and γ is a term for variability not related to ΔT_S. From this equation an equilibrium climate sensitivity (ECS) can be calculated in terms of ΔT_S due to ΔF with the new equilibrium state where Earth is in energy balance (and γ is considered negligible), based on α. The case most often reported is for a doubling of atmospheric CO_2, F_{2xCO2}. The ocean would take centuries to reach a new equilibrium given the long-time scales of transfer of heat from the upper to deep ocean. Effective ECS, in which EEI in equation (1.7) is non-zero, can be calculated, from which ECS can be inferred with care (Forster *et al.* 2021). An increase in annual ocean heat gain of 5 ZJ would push the lower bound of effective ECS from 1.5K (Kelvin) to 2.0K expected warming from given emissions, significantly lowering the allowable CO_2 emissions to meet projected thresholds (Resplandy *et al.* 2018 – paper retracted, but not for the above calculation.). Note that recent calculations of ECS do have a lower bound of 2.0K (Forster *et al.* 2021). For perspective two of the time series in the GCOS ensemble calculate ocean heat uptake in 2023 of 9 ± 5 ZJ (NOAA National Centers for Environmental Information; NCEI) and 15 ± 10 ZJ (Institute of Atmospheric Physics; IAP) (Cheng *et al.*, 2024). Indeed Forster (2016) notes that ocean heat content change calculated from observations does not have sufficient certainty to use in the calculation of effective ECS. Another aspect of the effective ECS calculation is shown if α is split into two components,

$$\alpha = (\lambda + \kappa) \qquad (1.8)$$

as in Raper *et al.* (2002), with climate sensitivity (λ), based on mechanisms which radiate energy out to space, and ocean heat uptake efficiency (κ). κ can be estimated from observations, with a recent estimate of 0.58 ± 0.08 $Wm^{-2}K^{-1}$ on average 1970-2019 with an increase since 1970 of 0.19 ± 0.08 $Wm^{-2}K^{-1}$ (Cael, 2022). So, in this formulation, ocean heat content change from observations and its uncertainty are factors in both EEI and α. In the long-term, it may be that there is a linear relation between κ and ΔT_S, but on the short-term, on interannual to decadal scales, ocean circulation, such as leading up to and during an El Niño events can change the heat uptake of the ocean and redistribute energy between ocean and atmosphere. With 90% of EEI absorbed by the ocean, and 1% by the atmosphere, it only takes a small change in ocean heat uptake to change the short-term atmospheric heat accumulation by a relatively large amount. Even in the equilibrium situation, where the ocean is no longer storing additional heat in the long-term, the ocean will be either taking in/releasing heat on seasonal time scales or simply become a source of heat release of the potentially large quantities of heat absorbed in earlier, non-equilibrium phases. With the variability of climate sensitivity with ocean heat gain and the small portion of EEI which is retained long-term by the atmosphere, and the possibility of the ocean as a short or long-term source of heat for the atmosphere in an EEI equilibrium situation, it is worth considering the use of ocean heat content directly as the benchmark environmental variable rather than GMST.

1.5.2 The need for regional and short-time scale storage estimates

Quantifying global energy storage/use in the components of the Earth's system gives a full accounting of EEI and is dominated by ocean sequestration of heat energy on annual and longer time scales. On shorter time scales (monthly to seasonal) the other components can store

significant amounts of energy. During El Niño years 1998 and 2010, the average annual atmospheric heat storage spiked by ~2 Zetajoules (10^{21} J; ZJ) over prior and following years (von Schuckmann *et al.*, 2023; their Figure 4). Further, it is the interaction between storage components which creates the conditions for poleward transport of heat and sequestration of heat to deeper layers in the ocean, thereby removing it from further short-term availability to the atmosphere and cryosphere. For example, one of the main regions for movement of heat energy from the mixed-layer, the upper ocean in direct interaction with the atmosphere, to deeper depths, is the southern hemisphere at latitudes south of 40°S (Rintoul, 2018). Ekman transport of warm near-surface ocean waters north induces upwelling, damping warming south of the Antarctic Circumpolar Current (ACC), while the northward transported heat enhances warming north of the ACC, where subduction carries intermediate and mode waters to the deep ocean (Armour *et al.*, 2016). Changes to atmospheric forcing, both wind stress and air-sea flux affect eddy formation and strength, where eddies are the main mechanism of heat transport poleward across the ACC (Rintoul *et al.*, 2018). Overturning circulation in the area of the ACC is a function of surface buoyancy forcing (Marshall and Radko, 2003) and is affected by changes in wind stress (Gao *et al.*, 2018). So, to track energy storage on a regional basis is key to understanding variations in energy storage in the Earth's system, and is dependent on ocean heat content monitoring on short time scales in relation to atmospheric forcing. Similarly, decadal variations in ocean heat content to depths away from atmospheric interaction can only be understood through examination of surface conditions and their effect on heat storage at deeper depths. The Pacific Decadal Oscillation (PDO) is a climate cycle defined by sea surface temperature (SST) and sea level pressure (SLP), with a positive phase where the first Eigenvalue Orthogonal Function (EOF) of SST is below the long-term mean in the North Pacific open

ocean, above long-term mean along the coast of North America, and SLP anomaly low compared to the long-term mean in the North Pacific (Mantua *et al.*, 1997; Zhang *et al.*, 1997). The PDO has been shown to be a combination of short-term and long-term forcing with atmospheric and oceanic components on different time scales (Newmann *et al.*, 2016). Marine heat waves have been found to be stronger, more frequent, and of longer duration during positive phases of the PDO, such as the recent 2013-2022 positive phase. Utilizing the Simple Ocean Data Assimilation (SODA) reanalysis, Carton et al. (2005) calculate a PDO index using the 20℃ isotherm in the north Pacific, which closely tracks the PDO index using SST. At deeper depths, a monthly upper ocean heat content index 0-300 m depth has been shown to reduce the noise and better represent interannual to decadal PDO conditions than an SST index (Kumar and Wen, 2016), which is subject to more short-term fluctuation due to short time scales of atmospheric factors. The negative phase of the PDO has been associated with the global warming hiatus, a period (1998-2012) in which GMST was increases at a lower rate (0.05 ℃ per decade) than the long-term (1951-2021) rate (0.15℃ per decade) (Hartmann *et al.*2013). Chapter 2 will explore the atmospheric-ocean interaction in the global warming hiatus on regional and sub-annual to decadal time scales, including the PDO and other phenomena which affect GMST and OHU. Given the importance of the energy storage components of the Earth's system on regional and short-time scales, a brief survey of estimates for atmosphere, land, and cryosphere energy storage/use will be given.

1.5.3 Atmospheric energy storage

Atmospheric heat content can be estimated or reconstructed using radiosonde observations of the tropospheric and stratospheric temperature structure. However, radiosonde observations are mainly over land and often burst before reaching higher altitudes (Ladstädter *et al.*, 2023). From

1978, satellite measurements from microwave sounding units (MSU) and later Advanced MSU (AMSU) provided temperature profiles of layers of the atmosphere based on passive measurements of upwelling radiance of atmospheric oxygen in a particular absorption band (as described in Zou *et al.* 2021). Heat energy was then calculated from the temperature profiles. As detailed in Santer *et al.* (2021), MSU/AMSU calculations of atmospheric warming are too small to support water vapor trends in CMIP models and low compared to radiosonde and radio occultation (RO, see below) observations. A new processing of AMSU data (Zou *et al.*, 2021) yields temperature profiles 14% higher than previous processing. RO measurements are made using Global Positioning System (GPS) satellites as they set behind or rise above the Earth's horizon, with the phase difference between receipt of a signal by low Earth orbiting satellite and a receiver on the ground due to atmospheric density, from which temperature can be calculated (Steiner *et al.*, 2020). RO temperature profiles have the advantage of better vertical resolution in the upper troposphere/lower stratosphere (UTLS) than MSU/AMSU measurements. RO UTLS atmospheric temperature trends 2002-2021 are a factor of two larger than the trend calculated from MSU/AMSU (Ladstädter *et al.*, 2023). Changes in temperature calculated from observations difference from a baseline mean are not sufficient to measure the heat content of the atmosphere because they do not include change in enthalpy due to precipitation and evaporation (Mayer *et al.* 2017). A full calculation of atmospheric heat content, as in von Schuckmann *et al.* (2023), includes the enthalpy factor from models. These modifications to atmospheric heat content calculations can be important over short-time scales, but globally, long-term atmospheric heat content still accounts for ~1% of EEI.

1.5.4 Land heat storage

Land covers 29% of the Earth's surface so is the recipient of a similar proportion of incident shortwave radiation and downward longwave radiation. Land heat content changes are calculated from ground surface temperature histories (GSHTs) calculated from deep borehole profiles. GSHTs have been used to calculate the flux due to geothermal activity, flux out of the solid Earth, but less attention was paid to flux into solid earth due to surface forcing (Beltrami, 2001a, 2001b). Global calculations of land heat content from GSHT were presented by Beltrami *et al.* (2002) based on an inversion algorithm dependent on a series of temperature ramps (temperature change rate) for solid earth, the heat conductivity and diffusivity of the solid earth, and the measured temperature change over the borehole samples. An improved inversion technique (Cuesto-Valero *et al.*, 2022) using the same observational dataset has resulted in lower uncertainties in the global value of 24 ±2 ZJ over the years 1960-2020 (von Schuckmann *et al.*, 2023). This global value also includes terms for permafrost melt and heating of inland water bodies. 90% of continental heat content change is in solid earth, with 2 ZJ due to permafrost melt and 0.2 ZJ in inland water heat content (Cuesto-Valero *et al.*, 2023). Land surface temperatures are measured from satellite, but problems with lack of observations under cloud cover, and time of day and angle of incidence uncertainties preclude these data for use for climate monitoring pending improvements (Li *et al.*, 2022).

1.5.5 Cryosphere energy storage

Energy storage in the cryosphere is estimated as the energy necessary to melt continental glaciers (Greenland and Antarctica), alpine glaciers, and sea ice as per von Schuckmann *et al.* (2023). This does not include permafrost melt (included in land energy storage) or changes in non-glacier snow cover. Multiplying mass change by the latent heat of fusion and the specific heat capacity of ice times the change in temperature needed to bring the ice to the melting point

estimates the total energy storage. A constant value of latent heat of fusion, 3.34×10^5 J kg^{-1} and a constant value of specific heat capacity of 2.01×10^3 J kg^{-1} °C^{-1} are used. For sea-ice where volumes are known rather than mass, first year ice density of 917 kgm^{-3}, and multi-year ice density of 882 kgm^{-3} are used as per Slater *et al.* (2021). The greatest uncertainty in the calculation is estimating changes in the mass/volume of continental glaciers, alpine glaciers, and sea-ice. As per table 3 in von Schuckmann *et al.* (2023) estimates of mass or volume for Antarctic and Greenland continental glaciers, alpine glaciers, Arctic sea-ice, and Southern Ocean sea-ice are based on *in situ* observations, satellite observations, and models. The estimate from von Schuckmann *et al.* (2023) for cryosphere heat storage/utilization is 14 ± 4 ZJ, 1970-2020 with the largest proportions associated with Antarctic ice (continental and sea ice; 33%) followed by Arctic sea-ice (26%).

1.6 Ocean Temperature Observations in the World Ocean Database

As noted in section 1.2, the main limitation on the calculation of $OHCA_O$ is the quality and irregular distribution of the underlying subsurface ocean temperature observations. This is especially true for historical data, but even so for more recent observations. Chapter 3 explores the effects of COVID-19 pandemic on ocean observing in the context of sustained observations for $OHCA_O$ calculation. The implications for both the current and historic ocean observing system related to the uncertainty of $OHCA_O$ calculation can be best understood with a description of the evolving ocean observing system over time. The World Ocean Database (WOD; Conkright *et al.*, 1999; Conkright *et al.*, 2002; Boyer *et al.*, 2006; Boyer *et al.*, 2009; Boyer *et al.*, 2013; Levitus *et al.*, 2013; Boyer *et al.* 2018; Mishonov *et al.*, 2024) is the mechanism to utilize temperature profile data for calculation of baseline mean temperature

climatologies and observed mean ΔT for $OHCA_N$, and at least in part for all $OHCA_O$ calculation. The WOD consists (currently) of 22,190 archived data sets at NCEI of oceanographic cast data, where a cast is a set of co-located (in time and space) profiles of oceanographic variables – almost always including temperature, actually many times including only temperature. A profile is a set of observations of a single oceanographic variable at multiple depths (pressures) in the ocean at the same geographic location (or as close to the same as possible in a fluid in motion) and time (allowing for transit time of instrument to different depths). The utility of the WOD is in presenting all the archived data sets in a uniform format with uniform quality control. The archived data are in a wide variety of formatting with a wide variety of metadata presentation even within the same formats, often with vital metadata outside the data files completely, as in cruise reports. Uniform quality control is necessary as the observations sent to the archive were made for numerous different purposes (e.g. fisheries research and monitoring, specific physical/chemical oceanographic research objectives, meridional flux calculations, as complimentary data to bathymetric soundings, hurricane tracking and research, ships of opportunity for weather forecasting, etc.). Some observations were indeed made for climate monitoring for which it is necessary to measure small changes over time. Others, were made for purposes such as locating the thermocline depth, a relatively large signal compared to long-term change signals. Only with rigorous quality control, often in addition to the quality control (in the form of flagging or withholding of low-quality observations) performed by the data provider, can these observations be made 'climate quality' – useful for the tracking of long-term change in the ocean. There are 18.5 million oceanographic casts in the WOD. Figure 1.3 shows the yearly distribution of casts by observation type in the WOD. Figure 1.4 shows the global vertical percent coverage based on the number of 3° x 3° latitude/longitude grid boxes over the global

ocean in which there are at least one observation at standard depths (greyed boxes in Table 1.2 below). Coverage and quality assessment based on data type are key factors in the uncertainty of $OHCA_O$ calculations so a brief review of the changing observing system over time is important for understanding the changing uncertainty of $OHCA_O$ over time. The information below is an expansion on the summary in Abraham *et al.* (2013).

1.6.1 Ocean observing pre-systematic (1772-1899)

There are ocean casts in the WOD from as far back as 1772 when participants in British explorer, Captain James Cook's Second Voyage measured surface waters and water at 100 fathoms (183 m) in the Southern Ocean (Cook and Forster, 1821). Indeed, the temperature at 100 fathoms was found to be 34°F (1.1°C) while it was 30°F (-1.1°C) at the surface. The temperature at depth was measured by a mercury thermometer immersed for 15-20 minutes. The recorded measurements were in whole degrees Fahrenheit and there is an expectation that the thermometer mercury level would change when the instrument was pulled back to the surface for reading. Still the observations were and are valuable for the simple knowledge that the temperature at 183 m depths was warmer than at the surface. 100 years later, the Challenger expedition (1872-1875) observed temperature profiles across the global ocean with sufficient accuracy that it could be used by Roemmich et al (2012) to compare global ocean temperatures from the Challenger expedition to modern observations to estimate a 0.33°C± 0.14 average temperature difference 0-700m depth over 135 years since the expedition.

1.6.2 The bottle cast era (1900-1939)

Around the same time, the reversing thermometer was developed as detailed in Negretti and Zambra (1873). This thermometer, when tripped at depth would rotate, sending the portion of

mercury measuring the temperature into a smaller compartment. A set of thermometers, one protected (from pressure effects) one unprotected measured pressure and temperature to a high degree of accuracy. The Nansen water sampling bottle to which the paired reversing thermometers were attached (Mill, 1900; Hellend-Hansen and Nansen, 1909) formed the main means of observing the subsurface ocean 1900-1939. It was not an ocean observing system in that there was no attempt to coordinate and share observations or to systematically sample the ocean. Subsurface oceanographic observations were mainly to increase basic understanding of the ocean rather than monitor ocean conditions and variability. On the other hand, given the logistical difficulties for research cruises to many (if not most) parts of the ocean, and the basic research nature of most cruises, with the reversing thermometers and Nansen (replaced in the 1960s by Niskin) bottles, temperature data from this era are often of high quality. Gouretski *et al.* (2012) uses much more prevalent SST observations compared with near-surface ocean profile data to show consistent near-surface warming from 1900 into the 2000s. However, observational coverage from bottle casts is not sufficient by itself to have a reasonable degree of certainty in $OHCA_N$ calculations 1900-1939. Figure 1.5 shows all observations from reversing thermometer/bottle casts for 1934, a year of typical to above average global coverage for the pre-systematic observing era of research oceanography. Further, given the discrete nature of bottle casts – usually with a maximum of 36 Nansen (Niskin) bottles on a rosette frame (but more often 24 or 12 bottles) lowered by winch, the vertical resolution of temperature profiles can make it difficult to accurately define features, such as the thermocline, in the water column

1.6.3 The Mechanical Bathythermograph era (1940-1966)

In 1938, Athelstan Spilhaus developed and deployed an instrument based on the ‘oceanograph’ idea of Rossby and Montgomery (1935) with a recording device which scratched a continuous

pressure/temperature trace on a smoked brass (later glass) plate (Spilhaus, 1938). These instruments, named Mechanical Bathythermographs (MBTs) could be deployed from ships without stopping and staying on station as was necessary with bottle casts. The ships did have to slow, to around 5 knots, so the mechanical recording device would have time to register the pressure and temperature accurately, but the ships could keep moving. The continuous nature of the recorded observations allowed for more certain identification of features such as the base of the mixed layer. Most MBT devices operated in the upper 125 m of the water column, with some later models to 250 m. For most of the water column the only observations were still from bottle casts, but for the upper 125 to 250 m there was potential for organization of an observing system utilizing merchant and naval vessels as well as research ships. And since OHCA is a function of surface fluxes (at the global scale) the MBT observations in an ocean observing system could begin to estimate $OHCA_O$. The U. S. Navy, along with Scripps Institute of Oceanography in La Jolla, California, and the Woods Hole Oceanographic Institute in Woods Hole Massachusetts developed the first global subsurface ocean observing system, beginning in World War II and reaching maturity in the 1950s. Figure 1.6 shows MBT and reversing thermometer/bottle casts in 1955 at the height of the MBT observing system. The observation system included not only identifying and outfitting ships for taking observations, but collecting the observations and processing them to ensure quality. The U. S. Navy also funded research to improve the quality of the instrumentation and the recording system. However, the MBT had a high uncertainty in temperature and pressure (0.3°C; 5 db; Cowley *et al.*, 2021). Gouretski and Koltermann (2007) found a time varying warm bias in MBT observations (as compared to bottle casts and Conductivity-Temperature-Depth – CTD casts) which was higher in the earlier days of MBT, lower in the 1980s. The higher bias in earlier MBT observations, gradually becoming

lower may be due to the instrument improvements and quality control processing implemented in the organized observing system. A systematic reason for the bias is unknown. Gouretski and Cheng (2020) developed a new correction for MBTs through a new comparison with bottle and CTD casts. The results are compared with the three extant bias correction sets available (from Ishii and Kimoto, 2009; Levitus *et al.*, 2009, hereafter L09; and Gouretski and Reseghetti, 2010) and found Gouretski and Cheng (2020) results to better correct for the bias. Observed mean ΔT in the OHCA calculations described here are calculated using the L09 bias correction. This bias correction was calculated in a similar manner to Gouretski and Cheng (2020).

A percent coverage metric for $OHCA_N$ calculations directly related to the objective analysis technique described below gives a better understanding of how observational coverage affects the uncertainty of the $OHCA_N$ calculation better than a simple 3°coverage metric as in Figure 1.4. A 1° area is defined as covered for the objectively analyzed ΔT if there are at least 3 observed means within the smallest radius of influence for the objective analysis. Less than 3 observed means do not have sufficient information for a robust correction factor to the first-guess field based on empirical examination (Boyer et al., 2005). The current earliest year for the $OHCA_N$ calculation described here is 1955, based on the percent coverage in the upper ocean for this and subsequent years, due in the early years to the MBT observing system. Some other $OHCA_O$ time series start at similar years based on differing definitions of percent coverage and also measurement uncertainty considerations for the MBT and other instruments. Ishii *et al.* (2017) time series starts at 1955, Cheng *et al.* (2022b;2022c) starts in the 1940s, but with lowered uncertainty in 1957. Lyman and Johnson (2008) estimate a later sufficient start, 1967 or slightly later based on altimeter data as a proxy.

1.6.4 Expendable Bathythermograph era (1967-2000)

The main reason for the start date for OHCA$_O$ time series in Lyman and Johnson (2008) is the deployment of a new instrument in the late 1960s, the expendable bathythermograph (XBT). A torpedo shaped body with thermal resistor (thermistor), connected to shipboard recorder by a thin wire which unwound from the body as it dropped through the water column, the XBT could be deployed at higher ship speeds (initially 15 knots) than an MBT (5 knots) and did not have to be winched back up. When the wire reached its limit, it broke and the XBT continued to the bottom of the ocean. The measurement and recording system resulted in lower uncertainty in the temperature measurement. XBTs were (and are) relatively cheap instruments and their high speed and easy deployment allowed for many more merchant ships enlisting in the ocean observing system as ships of opportunity. The development of the XBT, summarized in Snodgrass (1968), led to a contract between the U. S. Navy and Sippican (now Lockheed-Martin Sippican; LMS) which led to LMS becoming the main supplier of XBTs. Tsurumi Seiki (TSK) manufactures XBTs under license with LMS and there have been some other smaller suppliers of independently manufactured XBTs over the years, notably the Canadian Sparton XBT manufacturer. LMS remains the main supplier of XBTs, though the number of XBTs deployed per year has dropped below 10,000 in recent years from a high of nearly 90,000 in 1989. The majority of XBTs between the 1960s and the 1980s were T-4s with a rated depth limit of 400 m, but with wire stretch as deep as 460 m. T-7s and the later Deep-Blue have similar design with rated depth of the T-7 700 m, 840 with wire stretch and for Deep-Blues 700 m rated depth with wire stretch to around 920 m. Most XBTs in the 1990s and beyond are T-7 or Deep-Blue. There have been other types of XBTs for specific uses – among them the T-5 for deep (> 1800 m) temperature profiles, T-6 and Fast Deep to be deployed at higher ship speeds, and air drop

(AXBT) for deployment from aircraft rather than ship. The XBT was the main component of the ocean observing system from its inception until about 2000. Figure 1.7 shows XBTs, Ocean Station Data (OSD; bottle rosette) and CTD casts, and moored buoy observations in 1990, the year with the maximum number of XBT drops. Coverage along repeat lines on merchant ship regular routes, scientific ship riders, international best practices in quality assessment, posting to the World Meteorological Organizations (WMO) Global Telecommunications System (GTS) for incorporation into weather and climate models are all aspects of the highly developed XBT ocean observing system (Goni *et al.*, 2010; 2019).

1.6.4a XBT bias correction

There is no depth or pressure sensor on an XBT. Depth is calculated from time since the instrument enters the water. Problems with the depth equation were documented in the literature almost from the start of the XBT observing system (Flierl and Robinson, 1977, Seaver and Kuleshov, 1982; Heinmiller, 1983; Green, 1984). An international effort to recalculate the depth equation and to correct depths in the existing data resulted in a new depth equation, the 'Hanawa' equation (Hanawa *et al.*, 1995; hereafter H95) which was applicable to all T-4, T-6, and T-7 XBT types. The first calculations of $OHCA_N$ by Levitus *et al.* (2000) corrected all XBT data to H95. $OHCA_N$ for the 1970s-2000 can only be calculated from *in situ* temperature profiles if XBT observations are utilized based on percent coverage with and without. It was soon apparent that models could not replicate a large increase and decrease found in $OHCA_N$ in the late 1970s, early 1980s (Gregory *et al.*, 2004; AchutaRao *et al.*, 2006). Gouretski and Koltermann (2007) calculated an XBT bias through comparison with CTD data within a given temporal and spatial proximity which varied with time, so rather than the H95 static correction, corrections for each year were calculated. A number of studies within a few years of Gouretski

and Kolterman (2007) pointed out XBT uncertainty due to height of drop (Bringas and Goni, 2015), recorder type (Kizu and Hanawa, 2002a), start-up transients (Kizu and Hanawa, 2002b), and probe manufacturer (Kizu *et al.*, 2005, 2011). Further study (Wijjfels *et al.*, 2008; Ishii and Kimoto (2009); L09; Gourestki and Reseghetti, 2010; Good, 2011; Hamon *et al.*, 2012; Cowley *et al.*, 2013; Cheng *et al.*, 2014, hereafter C14) refined the necessary correction, with some corrections by XBT type and thermal corrections, and startup transient corrections in addition to depth corrections. Cheng *et al.* (2016) ran each XBT correction noted above through a series of metrics finding that C14 corrections performed the best in reducing XBT bias for $OHCA_O$ calculations with L09 giving similar results despite employing only a statistical temperature correction based on comparison with CTD and bottle casts nearby in space and time. The XBT bias correction used for the current $OHCA_N$ calculation is L09, which is updated annually to incorporate new XBT casts and to allow for improvements to earlier year corrections based on increased historical data for comparison.

1.6.4b Other observations in the XBT era

Niskin bottle casts were still the main research grade means to observe subsurface temperature profiles well into the mid-1980s. MBTs were also still commonly deployed into the 1980s. The development of the CTD in the 1950s and1960s brought a highly accurate pressure sensor, platinum thermistor, and conductivity sensor into use for high vertical resolution temperature and salinity profiles, often attached to rosettes carrying Niskin bottles, lowered and raised by shipboard winch. Hamon (1955) and Hamon and Brown (1958) detail the early development of the instrument which went into commercial production in 1964 with analog shipboard recording. Brown (1974) details improvements to the CTD which allowed for higher accuracy, with modern CTDs reaching 0.001°C and 0.15% uncertainties in temperature and pressure respectively.

Calibrated ship-based CTDs are considered the highest quality oceanographic temperature measurement system, used for calculating bias in other instrumentation, even reversing thermometers/bottle casts (Gouretski *et al.*, 2020). Even though CTDs recorded at high resolution, many historical CTD data, into the 1990s, are found in the WOD only at low resolution (> 5 m intervals) due to limitations of recording and exchanging data. As higher resolution digital data records became more prevalent, higher vertical resolution analyses became possible with higher certainty. Because CTDs were often lowered along with Niskin bottles, and temperatures were reported only at the levels where bottles were tripped, there is often no indication in the WOD of whether the temperature was from a reversing thermometer or a CTD. Gouretski *et al.* (2020) presents information on when particular countries and research institutes switched their fleets from primarily reversing thermometers to CTDs for temperature (and salinity) observations, allowing sorting of data into low-resolution CTD, which has no known bias, and reversing thermometers which have small biases in pressure and temperature (Gouretski *et al.*, 2020). CTD and bottle casts were prevalent in the XBT era (Figure 1.7), often in areas of interest for national fisheries. While these data were not specifically for the global observing system, they are of high value for $OHCA_O$ calculations given their low uncertainty and observations area coverage.

Tropical moored buoy arrays with subsurface thermistors, later full CTDs, have been set up in the Pacific (Tropical Atmosphere Ocean; TAO; Chen *et al.* 2018) beginning in 1984, the Atlantic (Pilot Research Moored Array in the Atlantic; PIRATA; Bourles et al, 2019) beginning in the mid-1990s, and Indian (Research Moored Array for the Asian-African-Australian Monsoon Analysis and Prediction; RAMA; McPhadden *et al.*, 2009) beginning in the early 2000s. The moored buoys initially recorded temperatures as daily means, but later in higher time resolution,

as high as every 12 minutes. The sets of thermistors/CTDs on each moored buoy are treated as profiles in the WOD, with data stored as daily means, even the modern data which are recorded and archived at higher resolution. Non-tropical array research buoy observations (again as daily means) are also found in the WOD, mainly through the OceanSITES program (http://www.oceansites.org/).

1.6.5 The Argo profiling float era (2001-present)

Profiling Autonomous Lagrangian Circulation Explorer (P-ALACE) floats were developed and deployed in the 1990s during the World Ocean Circulation Experiment (WOCE) (Davis *et al.*, 1992; Davis *et al.*, 2001). A pressure resistant tube with a bladder which fills with fluid external to the tube to lower density to allow the tube to rise or return fluid to the interior of the tube, increasing density to allow it to descend through the water column is the basic design of the float. The addition of a CTD allows for recording of temperature and salinity profiles which are transmitted to satellites. About 1,200 floats were deployed by 2000 in total, though battery life had ended the observations from most floats well before. In 1998, plans for a global array of profiling floats were drafted (Argo Science team, 1998) and floats were deployed as part of the Argo program beginning in 2001. (A side note, Argo is not an acronym, the program is named after the ship used by Jason in Greek mythology. In modern oceanography, JASON is the Joint Altimetry Satellite Oceanography Network. Argo supports JASON in its ability to monitor the steric components of sea level.) An in-depth description of the Argo program and the Argo profiling float observations themselves is found in Wong *et al.* (2020). As of December, 2023, there are 2.8 million profiles of temperature and salinity from 18,458 deployed floats between 2001-2023. In 2023, there were 160,835 temperature profiles from 4,527 individual floats. Figure 1.8 shows the observing system with slightly more profiling float temperature profiles in

2019 (164,503), pre-pandemic, as well as other contributing systems. By contrast, the peak year of XBT observations, 1990, saw 82,926 temperature profiles from 2,398 cruises. XBT observations are mainly in the upper 700 m. Argo profiling float observations go to 2000 m, with a small but growing subset which reach to the ocean bottom. There were 8,596 temperature profiles from 232 Deep Argo profiling floats in 2023 which reached depths deeper than 2,100 m. XBT observations are predominantly along merchant shipping lanes in the northern hemisphere. Even merchant ships need to make allowances for weather so XBT observations are at a minimum in the northern winter. Argo profiling float temperature observations are global, excepting seasonal ice-covered regions, enclosed seas, and shelf regions, have equal coverage in the northern and southern hemisphere, and no seasonal minimum in observations. The target Argo coverage of at least one cycle (in which the oceanographic cast is usually recorded on the ascent) per 3°x 3° latitude/longitude grid box over the open ocean (deeper than 2000 m, ice-free, outside of enclosed seas) was roughly achieved at some point in 2005-2008. Argo profiling floats drift with the ocean currents at a parking depth, usually 1,000 m., ascending to the surface while recording an oceanographic cast using a CTD (for core Argo measurements of pressure, temperature, salinity) and broadcasting the observations to a satellite. Time at the surface has been minimized using Iridium satellite communications to minimize surface drift and biofouling. However, even parked at 1,000 m depth, the floats will move out of their immediate deployment location, requiring ship time to replenish areas of the ocean with new floats. Profiling floats have a battery life which now exceeds 4 years on average. Still a major cost of maintain the Argo float array is ship time to replenish the floats globally. A major logistical hurdle is arranging ship time for some of the remoter areas of the ocean.

The comparison above with the XBT ocean observing system is not to show that system inadequate, it was a major achievement and advance in oceanographic observing. The comparison is to show the advances in ocean observing made possible by the Argo profiling float program, most especially in this case, the calculation of $OHCA_O$. The utility for calculating $OHCA_O$ is more than the technological and logistical hurdles overcome in the development and deployment of the Argo array, it is the international cooperation in the careful scientific management of the observations from cooperation with and feedback to the instrument and float manufacturers, to the near-real time posting of the data to the GTS, to the quality control, bias detection and correction done in the post-observation phase, to the formatting and metadata in the final data files. All of these aspects are coordinated by the Argo Data Management Team and have been since the inception of the program. This allows for the maintenance of a reliably high-quality temperature profile observation set for the calculation of $OHCA_O$. This was and is the purpose of the Argo program, to monitor the oceans heat and freshwater budgets. However, it is important to note that even the highly coordinated quality assurance and data flow from the Argo program is not sufficient to detect every problem in observations. A cooling of the global ocean detailed by Lyman *et al.* (2006) was found to be an artifact of a subset of Argo profiling floats with a pressure sensor problem (Willis *et al.*, 2007). This pressure sensor problem was detected through a comparison of Argo observations with other ocean temperature profile observations in the North Atlantic Ocean. Nor can Argo floats alone observe the entire ocean (yet). The Indonesian Throughflow area is highly variable in steric sea level and OHCA. von Schuckmann *et al.* (2013) estimates that global steric sea level change could be underestimated by as much as 7% between 1993-2011 if the Indonesian Throughflow area was not accounted

for. There are no Argo profiling floats in the Indonesian Throughflow region, most temperature observations in recent years are still from XBTs (Figure 1.8).

1.6.5a Other observations in the Argo era

XBT observations have diminished greatly in the Argo era (9,830 temperature profiles in 2023), but still have an impact on $OHCA_O$ calculations as in the Indonesian Throughflow region noted above. Gliders equipped with CTDs are another major source of temperature observations since the mid-2000s. Gliders are, like Argo floats, buoyancy driven. Gliders are different in that they are programmed to move through the water column at an angle set through the programmed tilt of 'wings' on either side of the pressure resistant tube. Gliders undulate to a predetermined depth in the water column moving horizontally at the same time based on the tilt, providing a high spatial density of temperatures profiles from attached CTD. The prominence of glider observations in Figure 1.8 are due to the high density of the observations, many profiles in a short time period in a limited geographic area. The first gliders were tested with a battery-powered buoyancy engine at Wakulla Springs, Florida in 1991 and in Seneca Lake, New York in 1991 (Webb *et al.*, 2001). There are three prevalent glider types: Seaglider (Eriksen *et al.*, 2001), Slocum (Webb *et al.*, 2001) and Spray (Rudnick *et al.*, 2004; Rudnick et al, 2016). An overview of the three gliders initial designs is provided in Davis *et al.* (2002). Gliders provide temperature profiles for $OHCA_O$ calculation in some areas, especially continental shelves and near-shore, where Argo floats are not often observing. The data flow for gliders is handled through three main glider data assembly centers, in the United States (the Integrated Ocean Observing System National Glider Data Assembly Center, IOOS NGDAC), the European Union (Everybody's Glider Observations; EGO) and Australia (Integrated Marine Observing System, IMOS). The quality assurance and calibration of glider data are dependent on the primary

investigator utilizing the vehicle. Animal born ocean sensors (AniBOS) provide temperature profiles mainly from temperature sensors and later CTDs attached to pinnipeds (Boehme *et al.*, 2009; McMahon *et al.*, 2021). AniBOS provide temperature observations, mainly in high latitudes, where Argo floats are often sparsely distributed or not distributed at all. Depth of dives can vary widely based on animal feeding habits, but routinely go deeper than 400m and as deep as 1,500 m. Sensors last for approximately one year due to battery life and sensor replacement is carried out usually by research cruises during the hemispheric summer. AniBOS temperature profiles are in the WOD, but are not currently used in $OHCA_N$ (though they are used in some other $OHCA_O$). In the almost always data sparse ice-covered Arctic, subsurface temperature observations from instruments deployed through openings in sea ice is a solution which has been implemented sporadically historically due to the difficult logistics. Buoys with subsurface thermistors or profiling floats are a more recent development. In 2000 10 Japanese Agency for Marine-Earth Science and Technology (JAMSTEC) Compact Arctic Buoys (J-CAD) were deployed in Arctic sea ice (Kikuchi *et al.* 2007). In 2005 the Polar Ice Profiling System (POPS; Kikuchi *et al.*, 2007) was designed as an ice anchored Argo-like float and deployed near the North Pole. In 2007, the ice-tethered profiler (ITP) program began deploying. The ITP program continues to this day, providing high-quality temperature observations under-ice through Woods Hole Oceanographic Institute (Krishfield *et al.*, 2008), a vital source of quality assured temperature observations from the high Arctic. There are also temperature observations from Expendable CTDs (XCTD), undulating oceanographic recorders (vehicles towed behind a ship undulating in the water column to record temperature profiles from CTDs), digital bathythermographs (DBT; winched bathythermographs with digital recording) which are

incorporated into the WOD with their own characteristics and quality assurance issued, which are used in $OHCA_N$ calculations but comprise a small fraction of total temperature observations.

1.7 *in situ* based and other methods of calculating EEI and OHCA

Despite the limitations of the observing system for subsurface ocean temperatures, uncertainty in calculation of $OHCA_O$ has a lower uncertainty than other methods for calculation of OHCA. From table 3 of Meyssignac *et al.* (2019), $OHCA_O$ uncertainty surface to ocean bottom, in terms of EEI, is 0.11 Wm^{-2}, for the Argo period 2006-2015, compared to 0.38 Wm^{-2} for altimeter minus GRACE (section 1.7.2), 0.14 Wm^{-2} for RA (section 1.7.3), and 0.21 Wm^{-2} 2000-2010 for CMIP5 models (section 1.7.3). The first thing to note about $OHCA_O$, is that the uncertainty from Meyssignac *et al.* (2019) is not a complete uncertainty, not accounting for measurement uncertainty, or irregular and sparse data, nor the representativeness of point source observations in time and space. The second thing to note is that there are multiple methods for calculation of OHCAO statistically from sparse observations, with some of the methods utilizing more complete coverage data sets, such as altimeter sea level change. Examining the uncertainty due to different methods is the subject of Chapter 4. Better quantifying uncertainty for $OHCA_O$ is an important outcome, but so is examining improvements to calculation of $OHCA_O$, and specifically $OHCA_N$, as $OHCA_N$ is a statistical method which does not use any information other than *in situ* temperature observations and therefore is an independent check for other methods of $OHCA_O$ calculation. Appendix A details all the steps in the procedure for utilizing the *in situ* oceanographic temperature observations in the WOD to calculate $OHCA_N$. $OHCA_N$ has many similarities to other $OHCA_O$ calculations. It also has differences which the exploration of uncertainty in Chapter 4 can highlight as areas for method improvement to lower uncertainty.

Other methods for calculation of EEI and OHCA have some dependency on $OHCA_O$ estimates. A brief view of these methods and their relation to *in situ* temperature profile methods will clarify why $OHCA_O$ is still the primary method for calculation of OHCA despite the relative lack of data.

1.7.1 Satellite measurements of incoming and outgoing radiation

Combining satellite measurements of TOA incoming solar radiation using the Total Irradiance Monitor (TIM) of the Solar Radiation and Climate Experiment (SORCE; Rottman, 2005) and reflected solar and outgoing thermal radiation from the Clouds and Earth's Radiant Energy System (CERES; Wielicki *et al.*, 1996) has provided monthly time series of EEI as the difference between incoming and outgoing radiation at TOA since March 2000. The CERES single scanner Terra EEI 12 month running mean (Hakuba *et al.*, 2024; mean value 4.44 Wm^{-2}) is higher than any realistic estimate of EEI due to uncertainties in calibration and retrieval of the relatively small signal of EEI in relation to the global magnitude of incoming and outgoing radiation (Loeb *et al.*, 2009). Hakuba (*et al.* 2024) contrast the Terra time series with the time series from the Energy Balanced and Filled (EBAF) multi-platform (Aqua; Terra; Suomi National Polar-Orbiting Partnership, SNPP; NOAA20) product with a mean value of 0.76 Wm^{-2}. The EEI trends for Terra and EBAF are virtually indistinguishable, 0.46 $Wm^{-2}dec^{-1}$ and 0.48 $Wm^{-2}dec^{-1}$, respectively. The difference is that EBAF 'anchors' their calculations to an absolute value using a July, 2005 to June, 2015 yearly mean *in situ* OHU_O (method of Lyman and Johnson, 2008 to 1800 m depth; Purkey and Johnson, 2010 for the deep ocean, plus small values for energy stored in the atmosphere, land, and energy used for state change of water) (Loeb *et al.*, 2012; Johnson *et*

al., 2016; Loeb *et al.* 2018b). The uncertainty of the EBAF EEI is ±0.17 Wm^{-2} (Loeb *et al.* 2018a) at the monthly time scale.

1.7.2 Derived from altimeter and gravimeter

The main components of sea level variations as measured from satellite altimetry are steric and barystatic. Steric sea level variation consists of ocean volume change due to thermal expansion (thermosteric) and saline contraction (halosteric). Barystatic change to the mass, but not the volume of the ocean, mainly additions or subtractions of fresh water to the ocean. (The term eustatic has been deprecated in favor of barystatic; Gregory *et al.*, 2019). Freshwater additions or subtractions come by way of the inverse change in land water storage, mainly through continental glacier mass changes and groundwater storage changes from evaporation over the ocean deposited as precipitation over land or vice-versa. Mass change over the ocean is calculated from gravity anomalies measured by the Gravity Recovery and Climate Experiment (GRACE; Chambers *et al.*, 2010; Wouters *et al.*, 2014). Currently, it is estimated that two-thirds of sea level change as measured by altimeter is due to barystatic change, 2.1 ± 0.4 mm/yr of a total 3.4 ± 0.4 mm/yr in 2022 (Thompson *et al.*, 2023). Most often in recent years this change has been mainly due to melt in continental glaciers. However, in 2022 precipitated mass gain in Antarctica exceeded mass loss due to glacial melt due to the intrusion of atmospheric rivers (Clem and Raphael, 2023). Given that the mass of salts in the ocean is relatively static, with deposition on the ocean bottom and particulates carried over land after entering the atmosphere in sea spray balanced by atmospheric deposition from land to ocean, riverine input, coastal erosion, and entrainment from ocean bottom to water column, any change in the salinity of the ocean is due to addition or subtraction of freshwater. It has been noted that globally, halosteric

change is essentially zero as the freshwater additions from continental glacial melt are negligible relative to the oceans volume (Gregory *et al.*, 2019). While there is some evidence that Arctic sea ice melt may have some effect on global halosteric sea level (Schmidt *et al.*, 2023) steric sea level change on a global mean scale is often assumed to be due wholly to the thermosteric component. Thus, OHU can be estimated from the difference between global change in sea surface height measured by altimeter and change in sea surface mass converted to units of equivalent sea surface height under the assumption that changes to sea surface height due to steric factors or mass addition/subtraction is generally equilibrated across the global ocean on short time scales. The resultant mean height difference is then converted to units of energy (joules) and units of power (Wm^{-2}) as an estimate of OHU and EEI. Altimeter observations from TOPEX and JASON cover the global ocean from about 66°N to 66°S. At about the same time as a change in observation system for ocean mass from GRACE to GRACE Follow On (GRACE-FO), the sea level budget as represented by GRACE/GRACE-FO mass + steric components from *in situ* profiles of temperature and salinity have been less than the sea level change measured by altimeter. Barnoud *et al.* (2023) attributes the difference to the hydrographic models used for terrestrial water storage and to thermosteric component calculated from *in situ* observations, finding that CERES-EBAF or ocean reanalysis model calculated OHU provide improved closure.

1.7.3 Models

Climate and ocean data assimilations models are an ideal means to reanalyze historical (and recent) ocean observations. These reanalyses (RAs) use the ocean and atmosphere dynamics algorithms and parameterization of a model modified by the actual observations to quantify

OHCA. A recent paper (Storto and Yang, 2024, hereafter SY24) examines OHCA from the Cnr Ismar Global historicAl Reanalysis (CIGAR) large ensemble RA system for the period 1961-2022, coming to a very similar $OHCA_N$ estimate (mean EEI 0.43 ± 0.08 Wm^{-2}, with 0.15 ± 0.04 $Wm^{-2}dec^{-1}$ acceleration) as Minière *et al.* (2023), with smaller uncertainty. In addition to uncertainties associated with the observational input data, SY24 notes CIGAR may be affected by vertical parameterization of ocean physics uncertainty and systematic model errors as per Semmler *et al.* (2021), assumptions made for data assimilation and uncertainty in other input datasets (than the ocean temperature profiles, including atmospheric forcing and sea surface data) as per Storto *et al.* (2016), Storto and Yang *et al.* (2019). SY24 found that OHCA uncertainty constituted 40% of the signal from 1961 to the mid-2000s, 15% afterwards to 2022, with the decrease mainly due to improvements in spatial coverage due to the Argo profiling float array. This compares to the GCOS ensemble of $OHCA_O$ (von Schuckmann *et al.*, 2023; used in Minière *et al.*, 2023) uncertainty range of 10% to 50% for 1961-early 2000s, 15% mid-2000s to 2022. Other studies of RA OHCA and OHCA uncertainty, include the Ocean ReAnalyses for the 20th Century (ORA-20C; de Boisséson, *et al.*, 2018) a 10 member ensemble forced by the ECMWF 20th Century atmospheric model (ERA-20C) for years 1900-2010 shows altering of the mean state by observations causes a deceleration in the warming trend, altering the long-term signal as well as memory of initial conditions and a convergence toward surface fluxes, observations, and model constraints in the ensemble spread. Palmer *et al.* (2017) show large regions of the Indian and Pacific Ocean where an RA ensemble mean interannual variability exceeds ensemble spread in the upper 300 m for 1997-2009 due to the ocean R models being well-constrained by observations. However, at deeper depths, the study found less agreement in the RA ensemble on patterns of change linked to difference in model dynamics related to water

mass formation. The study concludes that ocean RAs should be used with caution for historic reconstructions of ocean heat content in observation sparse depths below 300m. Xue *et al.* (2012) notes a minimum in uncertainty as measured by signal to noise ratio spread across 10 ocean RAs in OHCA for the upper 300 m in the early 2000s after the introduction of Argo profiling floats. An interesting note from this paper, in focusing on the Equatorial Pacific (2°S to 2°N latitude), comparing RA results with $OHCA_N$ results, a removal of all subsurface temperature observations from the Tropical Atmospheric Ocean (TAO) moored buoy from the calculation of $OHCA_N$ during quality control was shown to have damped the OHCA signal of the 1998 El Niño event in $OHCA_N$. While this did not significantly affect the global $OHCA_N$ integral, it was noticeable in the regional geographic distribution of $OHCA_N$. Durack *et al.* (2014) uses OHCA from the CMIP5 ensemble to calculate the underestimate of *in situ* method OHC due to data sparsity in the Southern Hemisphere, finding a 22 to 71 ZJ underestimate over the period 1970-2004. Lyu *et al.* (2021) use *in situ* observations from Argo profiling floats in the period 2005-2019 to constrain CMIP5 model projections of OHCA. They find that the high-end projections from climate models with high climate sensitivities are unrealistically large and that under high emission scenarios, there is a 66% probability that OHCA increase 2081-2100 over 2005-2019 will be 1,546–2,170 ZJ. Cheng *et al.* (2022c) estimate, using CMIP5 and CMIP6 models an increase of OHCA by 2100 ranging from 1,030 [839–1,228] ZJ for a low-emission scenario to 1,874 [1,637–2,109] ZJ for high emission scenario. Analysis ocean heat content in CMIP6 models has been the subject of a number of recent studies. Investigating the increased warming of the Atlantic Ocean relative to the Pacific Ocean, Ren *et al.* (2024) find CMIP6 models due capture this inter-basin difference and attribute the increased warming in the Atlantic to fewer aerosols in the atmosphere from 1980 to present, as well as the shape of the Atlantic

basin better facilitating OHU and transport. Oh *et al.* score 17 CMIP6 models on their ability to reproduce OHU in the north and northwest Pacific, finding high scores for most models in the physical quantities related to OHU, but these scores do not translate to a comparable trend in OHU found in observation-based references. Kuhlbrodt *et al.* (2023) find, for two sets of CMIP6 models, OHCA below 700 m is underestimated relative to observational estimates, similar to the Palmer *et al.* (2017) results for earlier models. Above 700 m, the model studies closely follow $OHCA_O$ estimates with some variations. Illustrating understanding which can only come from model analysis, and the importance of observational based estimates of OHU as a check, Shi *et al.* (2023) demonstrate anthropogenic aerosols as the driver behind a hemispheric asymmetry in OHC caused by shifts in atmospheric and oceanic circulation. Sohail *et al.* (2021) show, based on CMIP6 models and observations, that 50% of OHU occurs in the coldest 90% of the ocean, which interfaces with the surface in 23% of the ocean area, mainly in subpolar regions. Huguenin *et al.* (2022) details improvements in models based on the Japanese 55-year reanalysis (JRA-55), showing that 50% of recent global OHU change is due to wind and thermodynamic changes, and Southern Ocean forcing accounts for almost all recent OHU trend. The relevance here of this mini-review of OHCA in ocean RA and climate models is that results vary dependent on initial conditions, model physics, atmospheric data assimilation, and other factors but the major constraint on RA OHCA uncertainty is the subsurface ocean temperature observations available for assimilation both in geographic and depth coverage. Not as explicit here is the quality of the ocean observations and hence the quality control choices made on the observations. The observations are also important for forecast models in that they act as a check on the model reproduction of recent OHCA and hence the underlying model physics and ability to calculate future OHCA. Models can also, when used with care, act as a check on calculations

of $OHCA_O$, especially in data sparse regions. Overall, it is imperative to produce $OHCA_O$ estimates using only *in situ* ocean temperature profiles with well-considered and realistic uncertainty estimates as independent comparison with ocean RA and forecast models. Secondarily, the calculation of $OHCA_O$ estimates solely from observations provides a purpose specific quality control of the observations which are assimilated into the models.

1.74 Other techniques in development

There are also other techniques for calculating OHCA, in different stages of research and implementation. These include calculating OHCA using magnetometers (Trossman and Tyler, 2019; Trossman and Tyler, 2022), using acoustic thermometry (Munk and Worcester, 1976; Munk *et al.*, 1995; Dushaw, 2018; Howe *et al.*, 2019), using electromagnetic signal from ocean tides (Irrgang *et al.*, 2019), and using atmospheric oxygen and CO_2 (Resplandy *et al.*, 2019) among others. There are also $OHCA_O$ which incorporate machine learning methods, such as the Random Forest Regression Ocean Map (RFROM; Lyman and Johnson, 2023) which can increase the spatial and temporal resolution of $OHCA_O$. For all of these methods, it is important to have an independent baseline comparison from $OHCA_O$ calculated solely from *in situ* ocean temperature profiles.

1.8 Figures

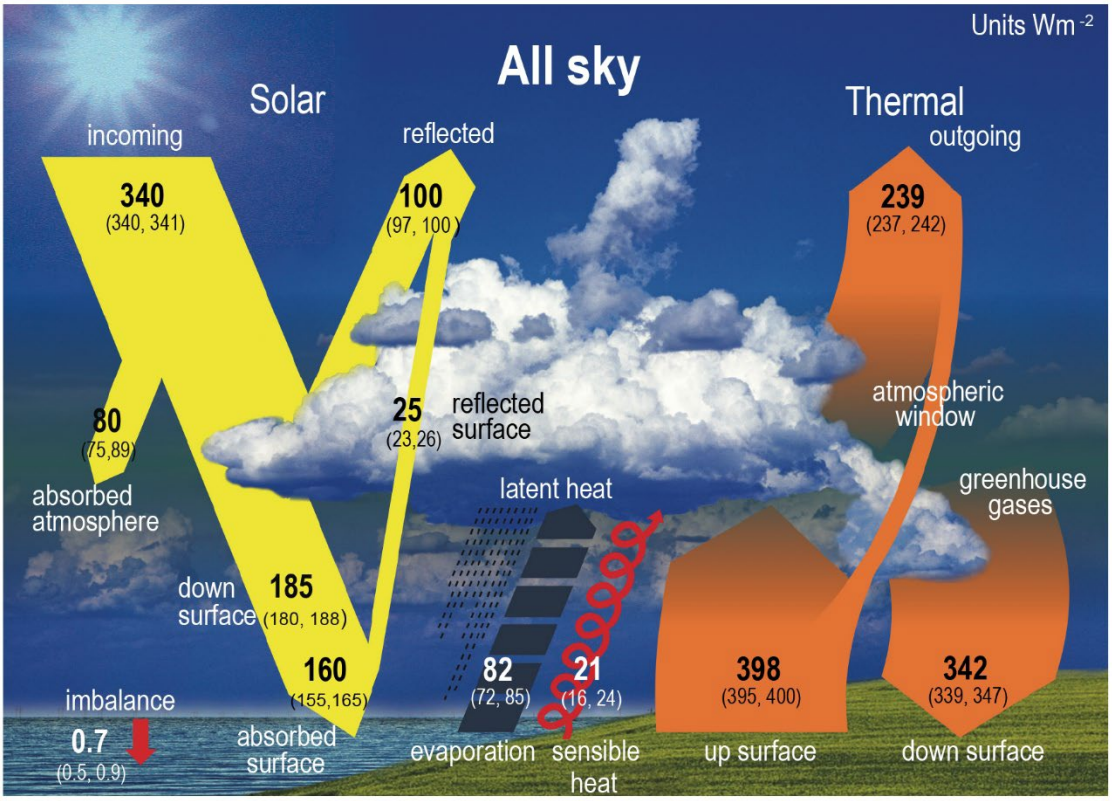

Figure 1.1 a) Earth's global mean energy budget All-Sky case (from Forster *et al.*, 2021; Their figure 7.2a).

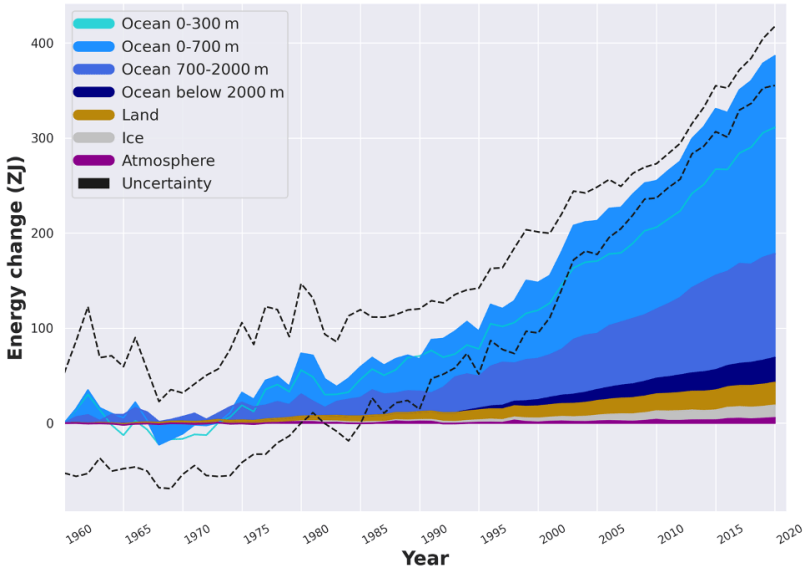

Figure 1.2. Total Earth system energy gain 1961-2020 from von Schuckmann *et al.* (2023)

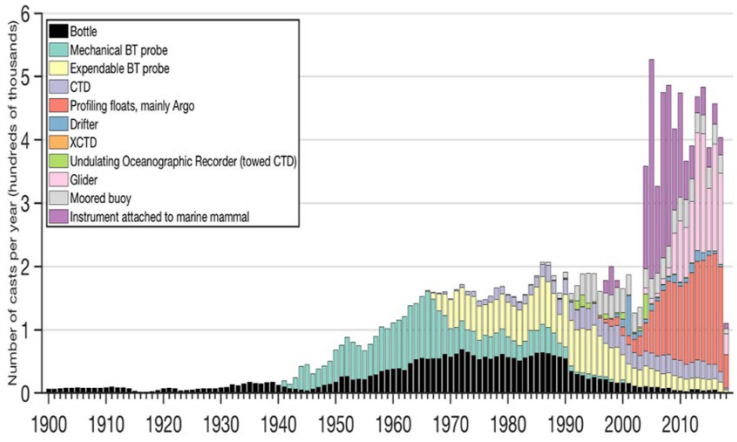

Figure 1.3 Yearly distribution 1900-2018 of oceanographic casts in the WOD by data type from Meyssignac *et al.* (2019).

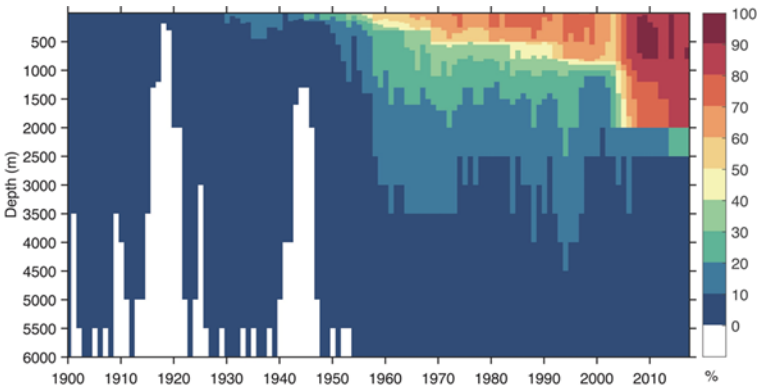

Figure 1.4. Percentage (%) of data coverage for 3° × 3° latitude longitude grid boxes over the global ocean area from 5 to 6000 m. from Meyssignac *et al.* (2019).

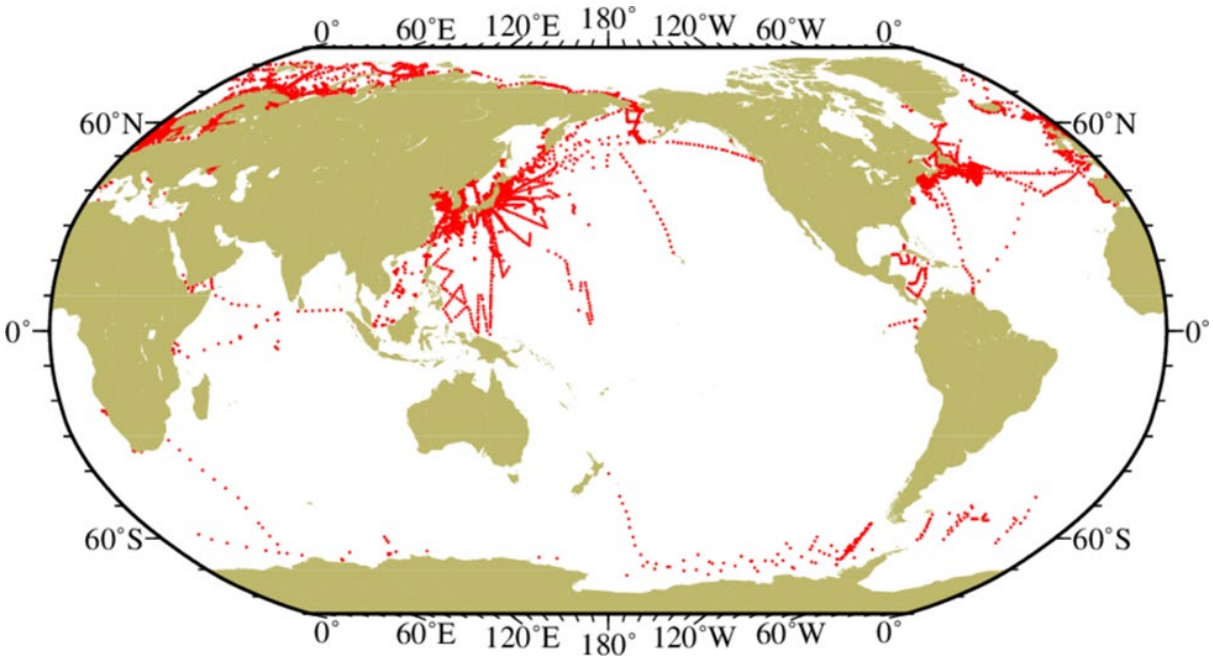

Figure 1.5. Ocean Station Data (OSD) Nansen bottle casts with reversing thermometer) in 1934.

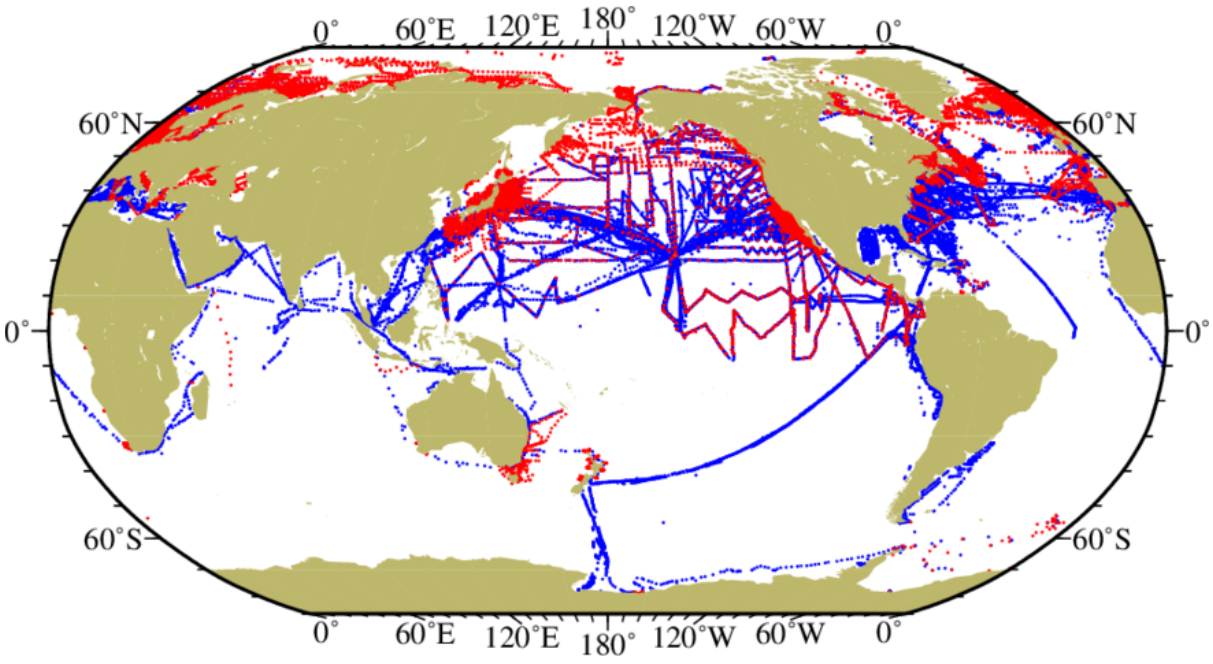

Figure 1.6 Mechanical Bathythermograph casts (MBT; blue) and OSD casts (red) in 1955.

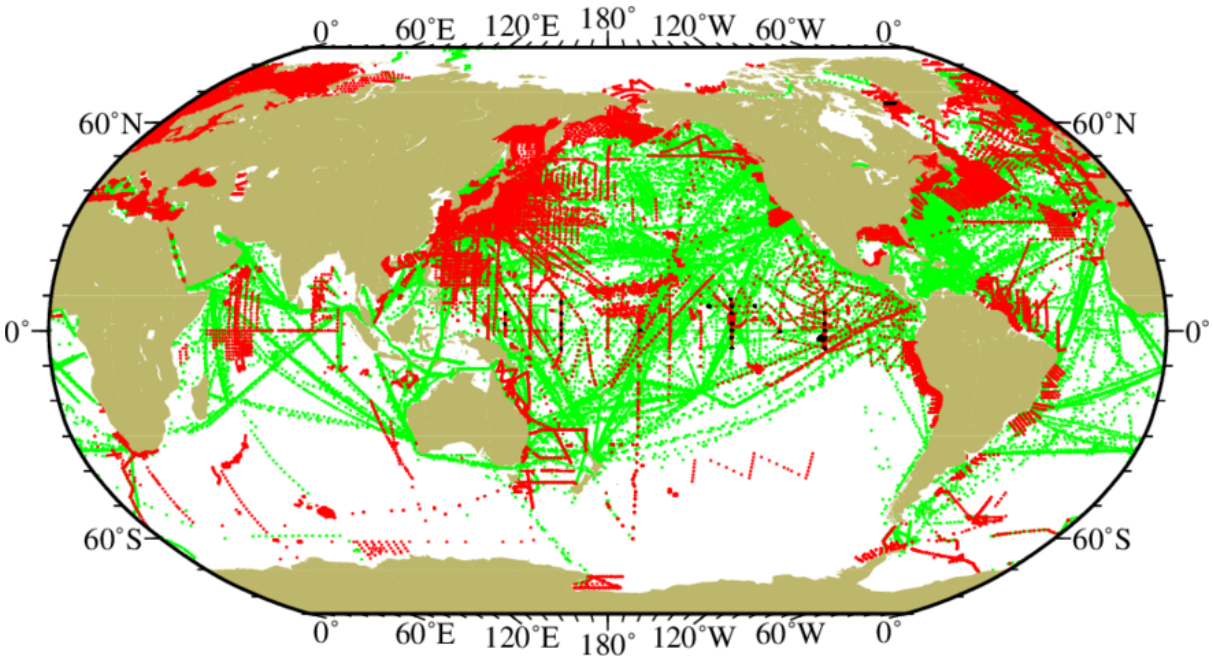

Figure 1.7. Expendable Bathythermograph casts (green), OSD and Conductivity-Temperature-Depth (CTD; red) casts and moored buoy (MRB) observations (black) in 1990.

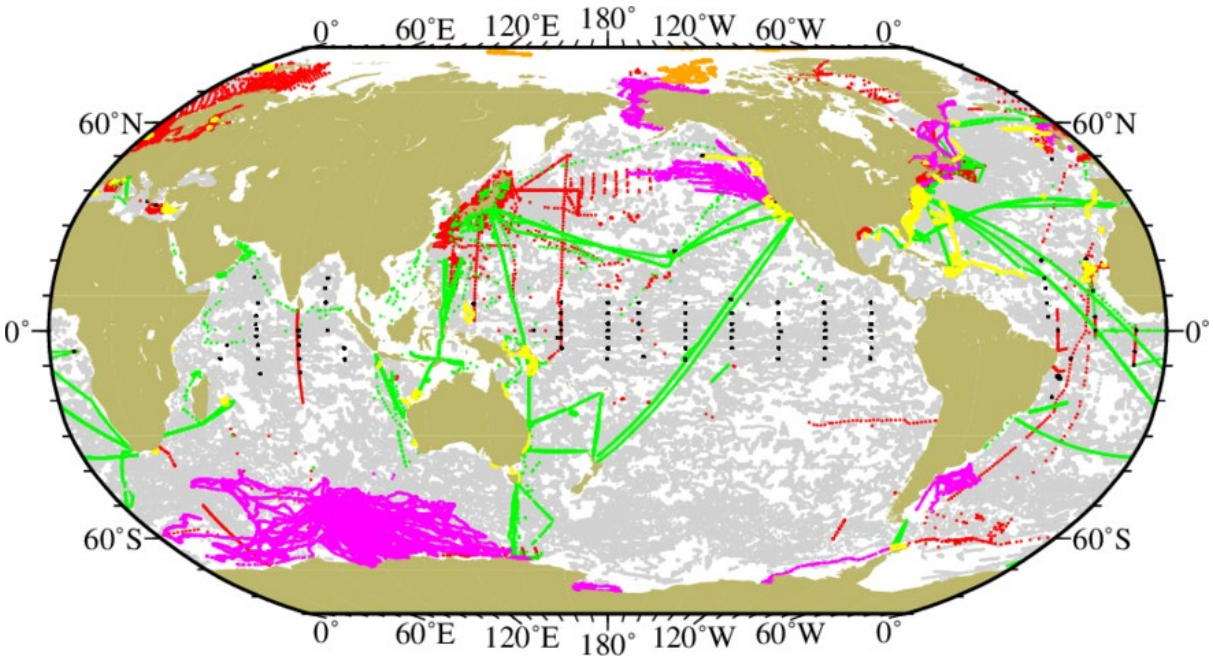

Figure 1.8. Casts from profiling floats, mainly from the Argo program (PFL; grey), XBTs (green), OSD and CTD (red), moored buoys (black), gliders (GLD; yellow), instrumented pinnipeds (APB; purple), and ice-tethered profiles (DRB; orange) in 2019, height of the ocean observing system prior to the pandemic.

Chapter 2. The global warming hiatus: Slowdown or redistribution?

This material appeared in: Yan, X.-H., Boyer, T., Trenberth, K., Karl, T.R., Xie, S.-P., Nieves, V., Tung, K.-K. and Roemmich, D. (2016), The global warming hiatus: Slowdown or redistribution?. Earth's Future, 4: 472-482. https://doi.org/10.1002/2016EF000417 (Yan and Boyer co-first authors)

2.1 The Hiatus: A Redistribution of Energy

Global Mean Surface Temperature (GMST) is a key indicator of climate change. It was noted by the Intergovernmental Panel on Climate Change (IPCC) Fifth Assessment Report (AR5), that "...the rate of warming over the past 15 years (1998-2012; 0.05^0C (-0.05^0C to$+0.15^0$C) per decade), which begins with a strong El Niño, is smaller than the rate calculated since 1951 (1951-2012; 0.12^0C (0.08^0C to 0.14^0C) per decade)" (Hartmann *et al.*, 2013), despite the continued increase in atmospheric greenhouse gas concentrations (Figure 2.1) (Trenberth, 2015). Although, neither shown to be a statistically significant change in the rate of warming nor a "true" hiatus in the strict definition of the word, this difference has been referred to as the "global warming hiatus" in the IPCC Assessment Report (2013). Note that the IPCC AR5 came out before the "hiatus" was over in 2013, and more recently GMST shows substantial increases when viewed over the past 10 or 15 years ending in 2016 (0.34°C/decade and 0.17°C/decade respectively).

Before going further, a particular question relevant to the understanding of the hiatus is the time period over which it occurred, more specifically the starting point of the hiatus. The IPCC AR5, uses the time period 1998-2012 in comparison to the period 1951-2012. The 1951-2012 period coincides with previous detection and attribution work cited by IPCC with respect to human contributions to global surface and tropospheric spatial and vertical patterns of change, i.e., anthropogenic fingerprints. The IPCC report goes on to note that changing the starting point of the hiatus period significantly changes the GMST rate of change and similarly its statistical significance in comparison to the longer baseline trend (see also (Karl *et al.*, 2015)). Moving

back the start point just one or two years means a rate of change close to the long-term trend. There was a large El Niño event ending in 1998 which led to an increased GMST, and which flattens out the GMST curve when using 1998 as a starting point. It is found (Fyfe *et al.*, 2016) that the time period chosen for the hiatus is important, and a more apt description of the so-called "hiatus" is a decadal climate fluctuation or variation (Lewandowsky *et al.*, 2015b). In fact, the GMST increase was only around 0.02 ºC/decade from 1951 to 1970. There was a much stronger increase in GMST from the mid-1970s (e.g., 1974-1998) of 0.19ºC/decade, possibly in association with a positive phase of the Pacific Decadal Oscillation (PDO) (Trenberth, 2015), or the Atlantic Multidecadal Oscillation (Tung and Zhou, 2013). These trends are based on NOAA data ERSSTv4 and GHCNv3, and are robust with other datasets, including satellite derived ocean surface temperatures, as shown by IPCC (Hartmann *et al.*, 2013) and Huang *et al.* (2016). Hence studies on the hiatus cited here do not necessarily follow the IPCC definition, and although it makes it harder to compare results, many studies refer to a slowdown in rate of change of GMST in the early 21st century as the hiatus, as compared to the decades after mid-1970s.

There are a number of differing views, uncertainties, and knowledge gaps regarding the hiatus, starting with the very name (Fyfe *et al.*, 2016; Lewandowsky *et al.*, 2015a, b). As a hiatus is a pause in a process, a global warming hiatus might imply a pause in the rate of increase of heat energy in the Earth's system, but the definition above really defines a slowdown in the rate of increase of GMST over a decade or more, not a hiatus of the rate of energy increase. Why the observed GMST was much less (by a factor of two) than many model projections needs to be understood.

GMST represents only a surface manifestation of the Earth's heat energy accumulation. Rather than a change in accumulation of heat in the Earth's system, the lower than predicted GMST rise can be traced to a redistribution of heat within the Earth's system (Balmaseda *et al.*, 2013; Chen and Tung, 2014; Trenberth *et al.*, 2014a; Trenberth *et al.*, 2014b; von Schuckmann *et al.*, 2016). The Earth's system includes not only the atmosphere, but also the land (including ice cover) and ocean. Most of the excess heat in the Earth's system does not accumulate in the atmosphere. Heat energy is absorbed by land surface as well as used in state changes in the Earth's water cycle (melting/forming ice, evaporation/precipitation). But it is the liquid ocean which absorbs the vast majority (> 90%) of excess heat in the Earth's system. Not only does the ocean have a much higher heat capacity than the atmosphere, allowing it to hold more heat energy within the same volume, but the motion of the ocean, the constant horizontal and vertical advection and mixing, removes water from direct contact with the atmosphere, sequestering heat at depths far from surface interaction and direct influence on GMST. Arguably, the most appropriate single variable in the Earth's system that can be used to monitor global warming is ocean heat content (OHC) integrated from the surface to the bottom of the ocean (von Schuckmann *et al.*, 2016). This is a difficult task, requiring instrumentation to be deployed to the remotest regions of the ocean, under ice, and to the deepest depths. Placing the present and future ocean measurements in historical context requires investigation using a relatively short and incomplete historic record of *in situ* measurements (Abraham *et al.*, 2013) and/or the use of models, which introduce their own uncertainties (Meehl *et al.*, 2013). Unfortunately, the OHC record is not nearly as long as for GMST. The recent "hiatus" period presents an excellent opportunity to understand the short- to long-term variability in the ocean/atmosphere climate system and how it resulted in a noticeable change in the rate of GMST increase. It also offers a chance to explore the

uncertainties in measurements of our climate system and a chance to potentially fill the gaps in observing system (Roemmich *et al.*, 2015).

2.2. Uncertainties

A recent paper (Karl *et al.*, 2015) describes corrections to ocean surface temperatures, also known as sea-surface temperatures (SSTs). Corrections for systematic differences between co-located ship and drifting buoys measuring SSTs and systematic differences between merchant-ship measured SSTs and simultaneous ship-deck nighttime marine air temperatures were primarily responsible for revealing previously undetected warming in recent decades in IPCC and other work. It is also noteworthy that by using nighttime marine air temperatures to correct SSTs, the index of global surface mean temperature is not a direct measure of SSTs as these trends are modified by marine air temperatures. Also, studies found that by including the polar regions in the global mean temperature trend estimation, the trend increases (Cowtan and Way, 2014; Karl *et al.*, 2015). Karl *et al.* (2015) showed that global surface temperature, even with recent corrections, still underestimate the global mean temperature increase by more than 0.02°C/decade from 2000 to 2014 in their regularly updated global mean temperature data set. Nonetheless, the global mean temperature trend 2000-2014 is still not as fast and steep as in the 1980s and 1990s. As different methods of trend estimation on the land surface temperature only (e.g., nonlinear estimation by Ji *et al.* (2014)) did not reveal a hiatus feature, the ocean plays the main role. Moreover, the continents occupy only 30% of the surface area. Accurate SST and GMST are important since they measure that part of the Earth's system with which we are in direct contact, and were used by IPCC and climate community to define climate change and "global surface warming hiatus" (IPCC, 2013)." If there are difficulties in estimating changes at the surface of the earth, it is not hard to fathom that there can be even more difficulties in estimating subsurface ocean changes. The Argo Program (Roemmich, 2009) of autonomous

ocean profiling floats has revolutionized a process which previously required specially equipped ships to travel the global ocean, including the most remote and hostile environments. Since 2006, the Argo floats provide spatially and temporally consistent temperature and salinity data from the surface to nearly 2000 m over the ice-free ocean, excepting continental shelves/coastal regions and marginal seas. There has never been such a good view of the oceans physical structure. However, as the 2000m depth is little more than half of the ocean's mean depth, we do not yet have regular measurements for the lower half of the Earth's heat reservoir. Fortunately the ocean deeper than 2000 m does not sequester nearly the amount of heat that is stored in the 0-2000 m layer, but it still makes a significant contribution to OHC change (Purkey and Johnson, 2010). The capacity to regularly monitor the ocean below 2000 m is changing dramatically with the introduction of Deep Argo (Johnson *et al.*, 2015b; Riser *et al.*, 2016). This program has started introducing floats that can dive as deep as 6000 m, providing ocean profiles of temperature from the surface to the bottom (or near bottom), usually delivered within 48 hours of measurement. Argo and Deep Argo will give us a more complete three-dimensional picture of the ocean's temperature structure and hence will allow us to track OHC changes over most of the ocean, as long as these programs are fully supported.

Historical subsurface oceanographic data are sparse and there are not sufficient data even near surface (20 m) before 1950 (Gouretski *et al.*, 2012). Similar to SST data, certain instrumentation used to measure temperature has biases. The most notable is the depth and temperature biases in historical expendable bathythermograph (XBT) data. These instruments revolutionized subsurface ocean temperature measurements and dominated the observing system from 1967 until the advent of Argo because they could be released from a ship moving at normal speed. This allowed deployment from a network of merchant ships without an appreciable time cost.

The XBT was and is still a very useful instrument, but it was not manufactured for climate change accuracy. The XBT community has worked very hard in recent years to quantify and correct biases in the instruments depth calculation algorithm and in the temperature measurement/recording system to great success (Cheng *et al.*, 2016) although work still needs to be done in this area. Further, the poor spatial and temporal coverage of early data necessitates techniques for estimating temperature and OHC change in historically data sparse ocean regions. While this does cause uncertainty in the estimation of OHC change it does not obviate the use of global OHC integrals as a measure of global warming (Boyer *et al.*, 2016; Lyman *et al.*, 2010; Cheng *et al.*, 2016). Note that, even though it has been shown that most observational decadal-scale upper-ocean (above 700 m) temperature trends since the 1990s are robust signals using different types of error analysis (Nieves *et al.*, 2015), the variable quality of the subsurface ocean measurements through the entire water column is a factor in the uncertainty of OHC estimation. While many projects such as the World Ocean Circulation Experiment (WOCE) from 1990-1998 were geared to high quality climate standard measurements, other applications such as fisheries research or sound speed investigation do not require such precise measurements and painstaking procedures and calibration. As all measurements are important in a data sparse environment, this results in a polyglot data set of varying quality. The International Quality Controlled Oceanographic Database (IQuOD) project (http://www.iquod.org/index.php/about) aims to examine the data and metadata for all historic subsurface oceanographic temperature observations to determine the quality of the individual ocean profiles and assign quality flags and uncertainties based on instrumentation and procedures used on each observation project. This will help to standardize the historic database for climate studies and reduce, or at least identify, uncertainties in the observations.

Beyond their direct investigative value, observations are an indispensable check on climate models. One possible reason that the CMIP5 model ensemble did not show the hiatus is that 'forced and internal variations might combine differently in observations and models' (Fyfe *et al.*, 2013). As Fyfe *et al.* (2013) went on to note, the simulated ENSO cycle is not expected to match the observed cycle. But there are solutions to this problem. Meehl *et al.* (2014) noted that some members of the CMIP5 ensemble had individual runs which did exhibit the global warming hiatus in GMST. These runs had a phase of the Interdecadal Pacific Oscillation (IPO) which, by coincidence, matched the negative phase of the IPO in observations that occurred during the warming hiatus. If hindcasting methodology of initialized decadal climate prediction were used in the mid-1990s, the CMIP5 ensemble could have exhibited the global warming hiatus over the multi-model average (Meehl *et al.*, 2014).

Another tool for monitoring the ocean's energy uptake is satellite altimetry. Sea level rise as measured from altimeters represents, in part, the expansion of ocean volume due to increase in thermal energy and coverage is near-global since 1992. Changes in sea level are also due to the addition of freshwater from melting continental glaciers and other changes to water storage on land. Also, thermal expansion, although usually the dominant steric component of sea level, can be compensated in some regions by haline contraction (Antonov *et al.*, 2002). The contributions of these different factors have been widely reported (Levitus *et al.*, 2012; Llovel *et al.*, 2014; Rietbroek *et al.*, 2016; Willis *et al.*, 2008). However, there are significant differences in the inferred Earth's net energy imbalance across studies (subject to data, methodology, error estimates, and time periods) that range from 0.5 Wm^{-2} to 1 Wm^{-2} since the early 2000s (Trenberth *et al.*, 2016). Some other challenges in monitoring the Earth's energy imbalance were described in (von Schuckmann *et al.*, 2016).

2.3. Advances: What We Know About the Hiatus

The phenomena of the "hiatus" has spurred much research into the repository for the heat which would have otherwise increased GMST more rapidly over the recent period. Most research has been looking at increased heat sequestration over regions of the ocean or to depths far removed from atmospheric forcing at the surface. The problem in detecting changes in the OHC which can account for a decrease in atmospheric heat uptake is that the rate of change in atmospheric temperature, though robust, when converted to units of heat energy is so small relative to the ocean change as to be lost in the noise. Figure 2.2 gives the heat content change in zeta joules (ZJ, 10^{21} joules) for the atmosphere and the ocean for 1980-2011 from the IPCC AR5 report (Rhein *et al.*, 2013). Rates of change 1980-2011 in the atmosphere are 0.06 ± 0.1 ZJyr^{-1} compared to 6.98 ± 1.5 ZJyr^{-1} in the ocean. However, it should be pointed out that the SST change does not simply reflect changes in atmospheric heat content. SST change reflects the change in the mixed layer of the ocean. The latter's heat capacity is not negligible. Further, full depth (or even surface to 700m) OHC change and GMST are not well correlated for unforced natural variability (Palmer *et al.*, 2011; von Schuckmann *et al.*, 2016; Xie *et al.*, 2016). Hence ocean heat uptake must be inferred from changes in ocean state and ocean/atmosphere interaction due to other physically observed and/or theoretically postulated phenomena.

It is generally understood that on top of the long-term ocean warming signal, there are shorter-time period fluctuations, from seasonal to interannual, to decadal. The El Niño/Southern Oscillation (ENSO) phenomenon, for instance, at interannual time scales, can transfer large quantities of heat energy from the atmosphere to the shallow central Pacific Ocean. This energy is released back to the atmosphere or shifted vertically and horizontally in the ocean during the transition from El Niño to mean conditions and to cooler La Niña conditions (Mayer *et al.*,

2016). The buildup to the 2009 El Niño transferred approximately 66 ZJ of heat energy to the upper 100 m of the Equatorial Pacific, with a similar heat loss between 100 m and 300 m (Roemmich and Gilson, 2011). Other variability such as the PDO and Atlantic Meridional Overturning Circulation (AMOC) rearrange heat around the ocean and in the vertical on decadal time scales, damping or enhancing the GMST depending on the stage of the oscillation (Meehl *et al.*, 2011; Meehl *et al.*, 2013; Trenberth and Fasullo, 2013; Chen and Tung, 2014; Trenberth, 2015) and with greatest effects in northern winter (Trenberth *et al.*, 2014b). Intermittent events such as the eruptions of major volcanoes like El Chichón (began erupting in1982) and Pinatubo (began erupting in 1991) can temporarily counteract long-term warming (Church *et al.*, 2011; Santer *et al.*, 2014). Man-made signals, other than greenhouse gas accumulation can have an effect on heat energy in the Earth's system – before the Clean Air Act of the 1970s, accumulated tropospheric and stratospheric aerosols likely slowed global warming by reflecting incoming solar radiation back to space (Trenberth, 2015). There is uncertainty in the future extent and variability of aerosols, both man-made and natural which will enter the atmosphere (Solomon *et al.*, 2011).

So, which of the many possible short-term to decadal-scale climate system phenomena was responsible for the "hiatus?" With our current understanding of the Earth's climate system, especially regarding the ocean, and the relatively minute signal of atmospheric heating relative to the ocean it is not easy to come to a definitive answer, especially in identifying the specific oceanic heat sink. Cooling in the central and eastern equatorial Pacific surface waters (Kosaka and Xie, 2013), indicative of increased wind-driven subduction and attendant heat sequestration (England *et al.*, 2014; Trenberth and Fasullo, 2013) is one possible means by which heat has been removed from the atmosphere during the hiatus. Some recent studies show that the cooling

shallow equatorial Pacific not only sequesters heat to upper ocean (100-300m) depths in the Pacific (Nieves *et al.*, 2015), but also shifts heat to the upper layer of the Indian Ocean (Lee *et al.*, 2015; Liu *et al.*, 2016; Nieves *et al.*, 2015). Going one step further, other studies posit that the concurrent effects of changing amplitudes of the PDO and the Atlantic Multidecadal Oscillation (AMO) are responsible for the hiatus (Steinman *et al.*, 2015). It has also been suggested that the main cause of the hiatus is movement of heat to deeper layers of the Atlantic and Southern Ocean due in part to the multidecadal variability of the AMOC (Chen and Tung, 2014). Finally, a recent study shows a global water column pattern of cooling (0-100m), warming (100-300m), cooling (300-700m), and warming (700-1500m) which the study hypothesizes is indicative of the mechanisms leading to the hiatus (Cheng *et al.*, 2015c).

None of these findings are necessarily contradictory. Many go beyond the global aspects of GMST to emphasize the regional and seasonal patterns (such as with the PDO, AMO, ENSO) where regime-like behavior is more clearly evident. However, they show the difficulty and complexities in pinpointing the oceanic sink of the missing heat which defines the "hiatus" (Trenberth *et al.*, 2016). They also point to the immense amounts of heat being advected vertically and horizontally in the ocean and our still limited ability to piece together a complete picture of ocean heat advection and uptake from our present observing system. In light of these findings above, we note that surface temperature difference (Figure 2.3) clearly shows that the central and eastern Pacific failed to warm in the "hiatus" years, in a pattern associated with the PDO. To show the seasonality, two extended seasons November-March (NDJFM), northern winter (Figure 2.3a), and May-September (MJJAS), northern summer (Figure 2.3b), were examined (Trenberth *et al.*, 2014b). The Pacific cooling is stronger in northern winter (Figure 2.3a& c), noting that Figure 2.3c uses a 1900-1999 baseline, different from IPCC. The surface

temperature warming in the 21st Century over the land centered around 45°N ±15° was net zero and similarly around Antarctica and significantly less 0-30°S (Figure 2.4). Everywhere else it was warmer generally. However, cold patterns occur also in a few areas, e.g., Southern Ocean, Siberia, Australia. In general, surface warming deviates considerably from the PDO pattern outside of the Pacific basin, perhaps signaling a substantial role for external forcing of the climate system and other factors such as internal variability beyond that associated with the PDO (Trenberth and Fasullo, 2013; Trenberth *et al.*, 2014b; Trenberth *et al.*, 2016).

In spite of the aforementioned challenges in examining the hiatus, there is more confidence now that warming of the ocean as a whole has continued (Boyer *et al.*, 2016; Cheng *et al.*, 2016; Levitus *et al.*, 2012; Nieves *et al.*, 2015; Wijffels *et al.*, 2016). The physical drivers of such increase in ocean heat content vary depending on regions, which limits full understanding of this global phenomenon. However, it is still important to understand the potential mechanisms driving decadal variability in all basins. First there is a westward heat pathway connecting the Pacific and the Indian Ocean. A previous study has identified the subsurface warming in the Pacific due to more La Niña events and the formation of a La Niña-like cooling pattern at the surface of tropical Pacific (Kosaka and Xie, 2013), though this cooling pattern is reversed by the strong 2016 El Niño(Wijffels *et al.*, 2016) (Figure 2.1e). Some recent studies found that the accumulated subsurface heat anomaly in the Western tropical Pacific can propagate into the Indian Ocean by the Indonesian Through Flow (ITF) on decadal scale (Lee *et al.*, 2015), where heat was mostly stored in the 100-300 m layer of the Indo-Pacific warm pool during the most recent hiatus (Nieves *et al.*, 2015). The Southern Hemisphere Ocean played a strong role in the warming of subsurface layers in the past decade, with 75 – 99% of global ocean heat gain occurring south of the Equator (Roemmich *et al.*, 2015; Wijffels *et al.*, 2016). There are other

studies suggesting a different pathway for the warming signal (also westward) from the Atlantic to the Pacific through teleconnection that directly links enhanced warming in the Atlantic region since the early 1990s with strengthening of the Walker circulation and La Niña-like Pacific anomalies (McGregor *et al.*, 2014). The precise mechanisms that control variability in the Atlantic Ocean are also still a topic of debate, but one possible explanation for increased heat storage in the Atlantic is a salinity-driven mechanism (Chen and Tung, 2014). Further assessment of basin-wide and regional distributions of heat, and of atmospheric versus ocean bridges, will be needed to predict future decadal variability. Besides explaining the periodical upper-ocean heat migration that mainly regulates the global temperatures, it will be critical to know how much of the trapped heat will be absorbed into the deeper layers of the ocean in the coming decades.

4. Outlook and Recommendations

To truly understand the flow of heat into and through the ocean, oceanography/climate community must first maintain and increase support for Argo, the main system monitoring OHC (von Schuckmann *et al.*, 2016). We must also ensure the continued development of Deep Argo in order to monitor the lower half of the ocean (Roemmich *et al.*, 2015). But even this is not sufficient. Argo's basic mission is to monitor the global ocean, subject to technical limitations of profiling floats. Earlier problems in observing the seasonal ice zones and marginal seas have been overcome, and coverage is expanding in those regions. Continental shelves and permanent ice zones remain problematic for Argo floats. It is imperative to support and enhance ship-based subsurface ocean temperature monitoring through programs such as the Ship of Opportunity Program (SOOP) and GO-SHIP (Hood *et al.*, 2009; Sloyan *et al.*, 2019). Increased and more concerted use of gliders (Rudnick *et al.*, 2004; Rudnick, 2016) to monitor marginal seas and

shelf and coastal regions is imperative for improved coverage in these areas. Although these areas are only a fraction of the ocean volume, their changing rate of ocean heat content is much faster than the global ocean (e.g., for East/Japan Sea, the changing rate of ocean heat content is 4 times faster than that of the global ocean mean) and their contribution to overall ocean heat content is not trivial when compared with atmospheric heat content (Liao *et al.*, 2015; Trenberth *et al.*, 2014a; Yoon *et al.*, 2016).

In addition, there is considerable scope to further improve the past record (Boyer *et al.*, 2016; Cheng *et al.*, 2016) both in terms of improved quality information about observations as well as much improved mapping and gap-filling – in both space and time – techniques.

Efforts to improve climate models need to be implemented to enhance hindcast and predictive skill in order to ensure prediction and mechanisms of future warming "hiatus". The ability of models to learn from observations and exhibit indicators of slowdown in GMST is present (Meehl *et al.*, 2014) and can be applied to the existing climate models.

For several decades satellite sensors have been providing sea surface observations at various spatial and temporal scales. Satellite remote sensors cannot see far beneath the surface layers of the ocean. However, recently new algorithms are being developed to estimate ocean interior thermal and thermohaline structures and subsurface flow fields using multi satellite sensors and *in situ* measurements and to improve the spatial and temporal coverage of these physical properties (Klemas and Yan, 2014; Su *et al.*, 2015; Wu *et al.*, 2012; Yan *et al.*, 2006). Further improvements are needed in the accuracy of large-scale subsurface thermal structure in near-real time for the heat content estimations for deeper layers. Finally innovative Arctic monitoring programs, such as the Ice Tethered Profilers (Toole *et al.*, 2011) are necessary to contribute measurements from ice covered regions.

While many studies have focused on the mechanisms that caused the purported hiatus, few have paid attention to the coastal response to the hiatus. It was found by a recent study (Liao *et al.*, 2015) that there have been large-scale changes in the rates of coastal SST change. The cooling and warming rates in some coastal area (e.g., China coast, U.S. eastern coast) are three times larger than in the open ocean (Figure 2.5). A significant cooling trend occurred in the low and mid-latitudes (31.4% of the global coastlines) after 1998, while 17.9% of the global coastlines changed from a cooling trend to a warming trend concurrently (Figure 2.5). Is it significant to the energy budget for the hiatus? Is that a signature of hiatus or just a coincidence? This area of study is needed not only for the need to answer above questions, but also because approximately 50 percent of the world's population lives within 200 km of coastal waters, with many more relying on the world's coasts for commerce and natural resources (Liao *et al.*, 2015; Trenberth *et al.*, 2014a). Once we have a full monitoring system for OHC, we can begin to answer with more precision questions of atmospheric changes in heat content related to OHC variations. Moreover, to understand the redistribution of OHC by the ocean circulation requires observations of ocean boundary current transports and inter-basin exchanges, and these key elements of the circulation are not yet systematically measured in the Global Ocean Observing System. Hopefully, before the next decadal fluctuation in the rate of GMST or so-called "hiatus", we will be able to discern the oceanic sink with more certainty and thus be able to inform our climate models and our understanding of future climate change.

The community would be well served to more vigorously assess observing uncertainties, help to prioritize observing system gaps in the oceans, and analyze rates of change in context with multiple data sets that represent different components of the climate system. Also, and important part of the difficulty in understanding the recent "hiatus" is in poor definitions, incomplete

assessments, and confusion about what might have been expected to occur in the climate system using appropriate modeling experiments. In the future, comprehensive problem-focused assessments, e.g., perhaps like the Synthesis and Assessment Reports of the USGCRP, or National Academy Reports, would do well to focus on the above-mentioned aspects of climate change.

Finally, the term “global warming hiatus” is a misnomer, though we will continue to use the widely used phrase to describe the slowdown or pause in the increase of GMST in the late 20th century – early 21st century, with quotation marks. Alternatively, we would like to suggest to the climate community to use "global surface warming slowdown" instead in the future, to avoid confusion. There is no absolute consensus on the specific oceanic sink for the excess heat which led to the slowdown in rising GMST (the Southern Ocean may be worth further attention though), but there is a general agreement in this group and in the literature that rather than a “global warming hiatus”, the slowdown of GMST increase 1998-2013 was a result of increase uptake of heat energy by the global ocean during those years.

2.4 Figures

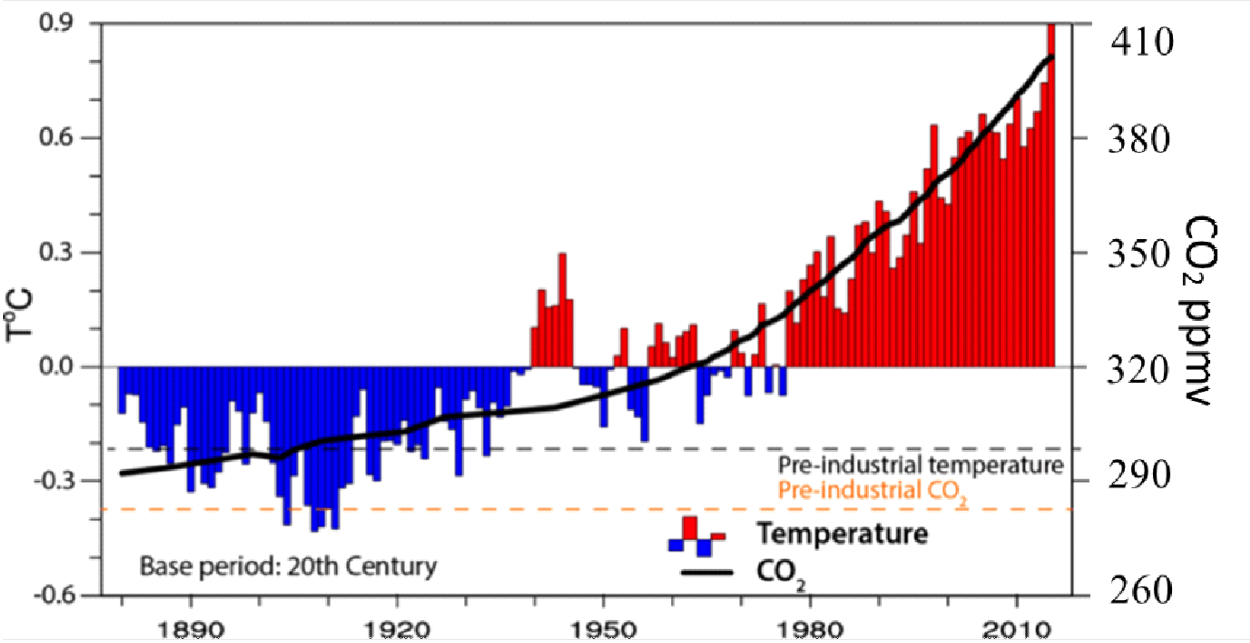

Figure 2.1. Time series of annual values of global mean temperature anomalies and carbon dioxide concentrations at Mauna Loa and from the ice core record. Time series of annual values of global mean temperature anomalies (red and blue bars) in degrees Celsius, and carbon dioxide concentrations at Mauna Loa, both from NOAA. Data are relative to a baseline of the 20th-century values. Also given as dashed values are the preindustrial estimated values, with the scale in orange at right for carbon dioxide, where the preindustrial value is 280 ppmv (parts per million by volume). The latest values exceed 400 ppmv. For temperature, the 2015 value is more than 1 degree Celsius above preindustrial levels. Updated from Trenberth and Fasullo (2013).

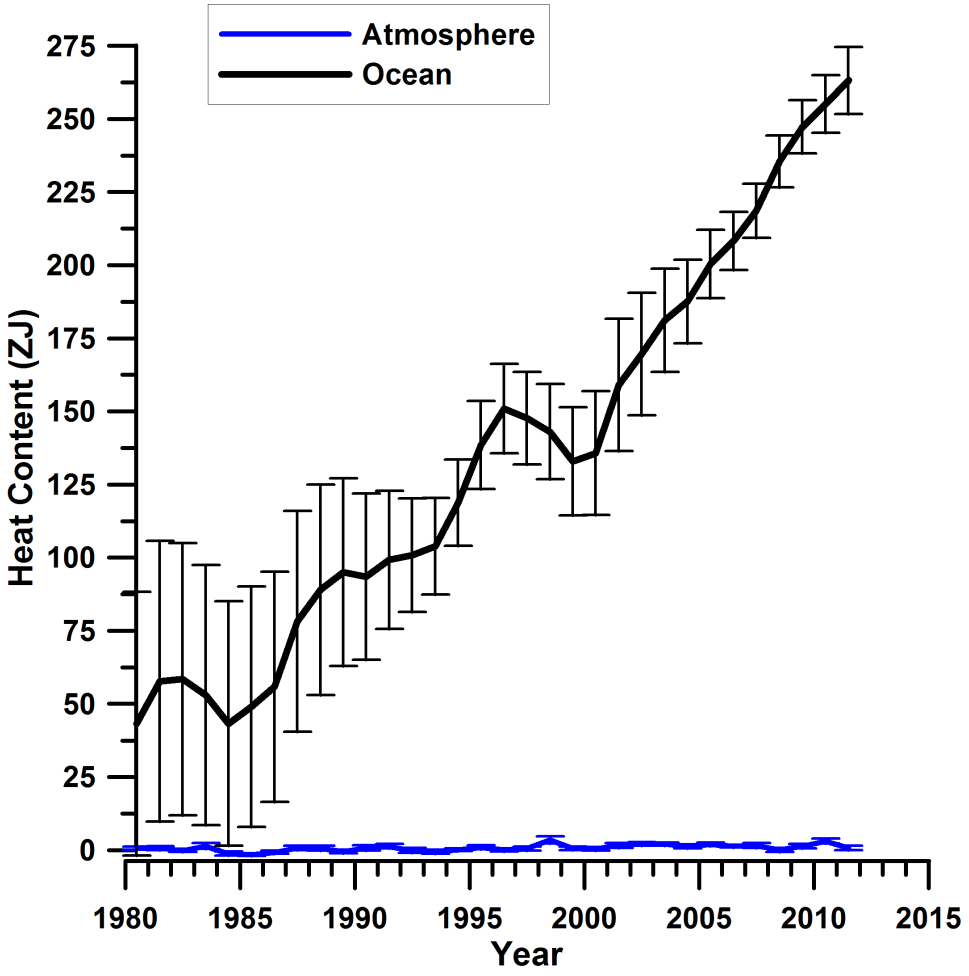

Figure 2.2. Yearly ocean and atmosphere heat content anomaly. Yearly ocean (black) and atmosphere (blue) heat content anomaly (data from IPCC AR5 report, Rhein *et al.* 2013). Ocean heat content combines upper and deep ocean heat content values for each year from that report. Microwave Sounding Unit (MSU) temperatures were used instead of GMST since GMST is a hybrid of 2 m land air temperatures and SSTs, while MSU temperatures cover the troposphere and stratosphere, giving an indication of change over a larger portion of the atmosphere.

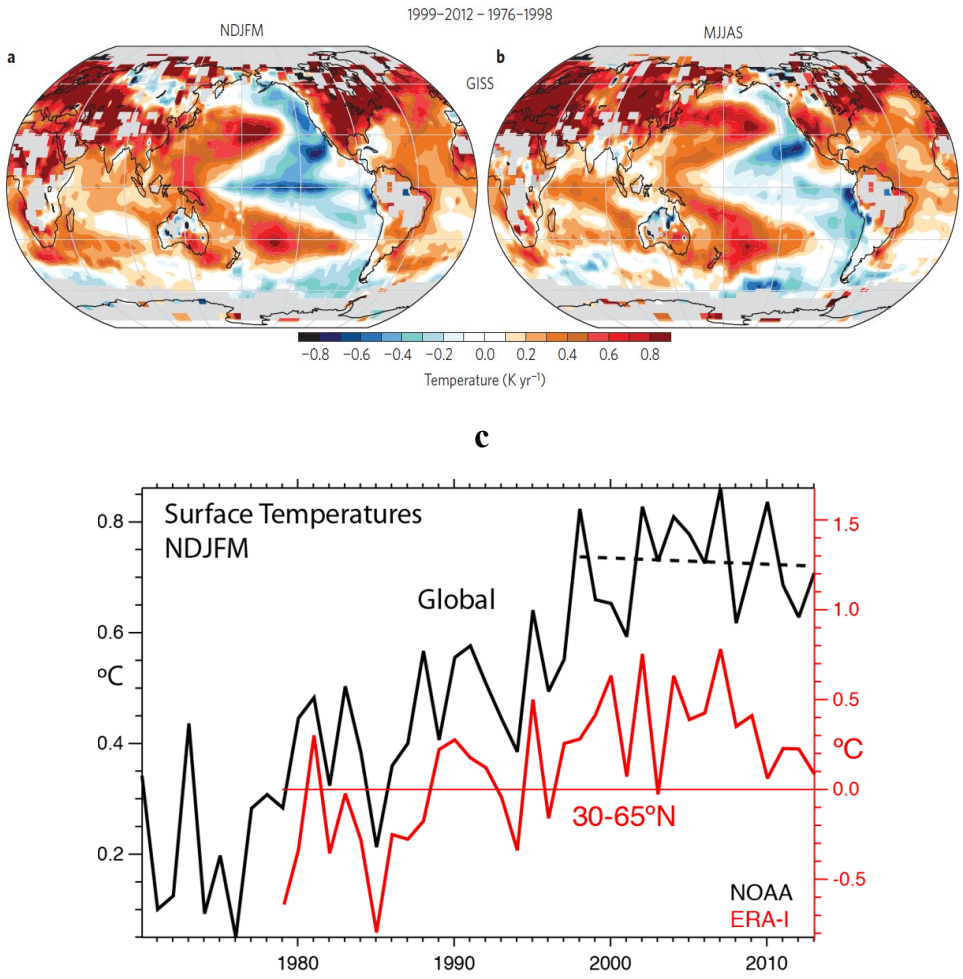

Figure 2.3. Regime differences between 1999-2012 and 1976-1998. Mean surface temperature differences between 1999-2012 and 1979-1998 for NDJFM (a) and MJJAS (b) for surface temperature from Goddard Institute for Space Studies. For NDJFM, the global mean temperature for 1970 to 2013 and the linear trend for 1998-2013 (c) using NOAA data relative to the base period 1900-1999. Also shown in red are the temperature anomalies for 30-65°N relative to the mean for 1979-2013 from ERA-I data. In northern winter, when ENSO is strongest, the slight cooling trend in the 2000s exacerbates the hiatus and the coldest values are in La Niña years, however the coldest years for 30-65°N are years of negative NAO. Cited from Trenberth *et al.* (2014).

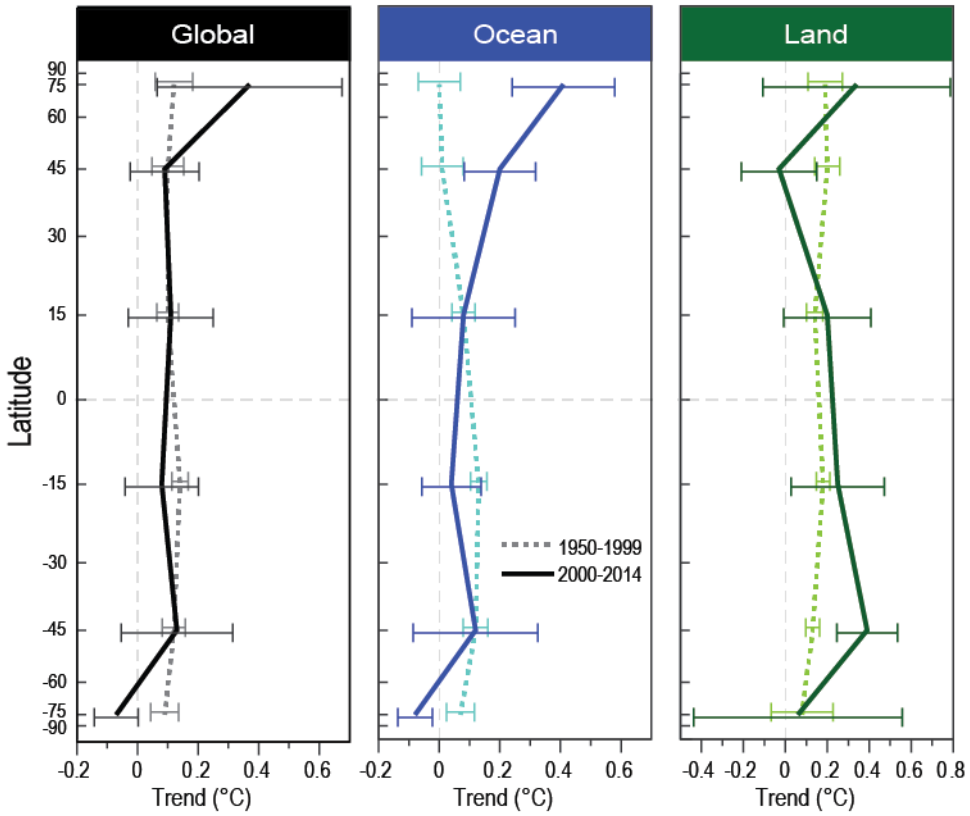

Figure 2.4. Latitudinal profiles of surface temperature trends. Zonal mean trends and statistical uncertainty of the trend estimates for global, ocean, and land surface temperature, averaged in 30-degree latitudinal belts, for the second half of the 20th century (dashed) compared to the past 15 years (solid). Trends are cosine-weighted within latitude belts, and the vertical axis is on a sine scale to reflect the proportional surface area of the latitude bands. Note that only the uncertainty related to the trend estimates is provided because zonal standard errors of estimate are not available in contrast to the global averages. Cited from Karl *et al.* (2015).

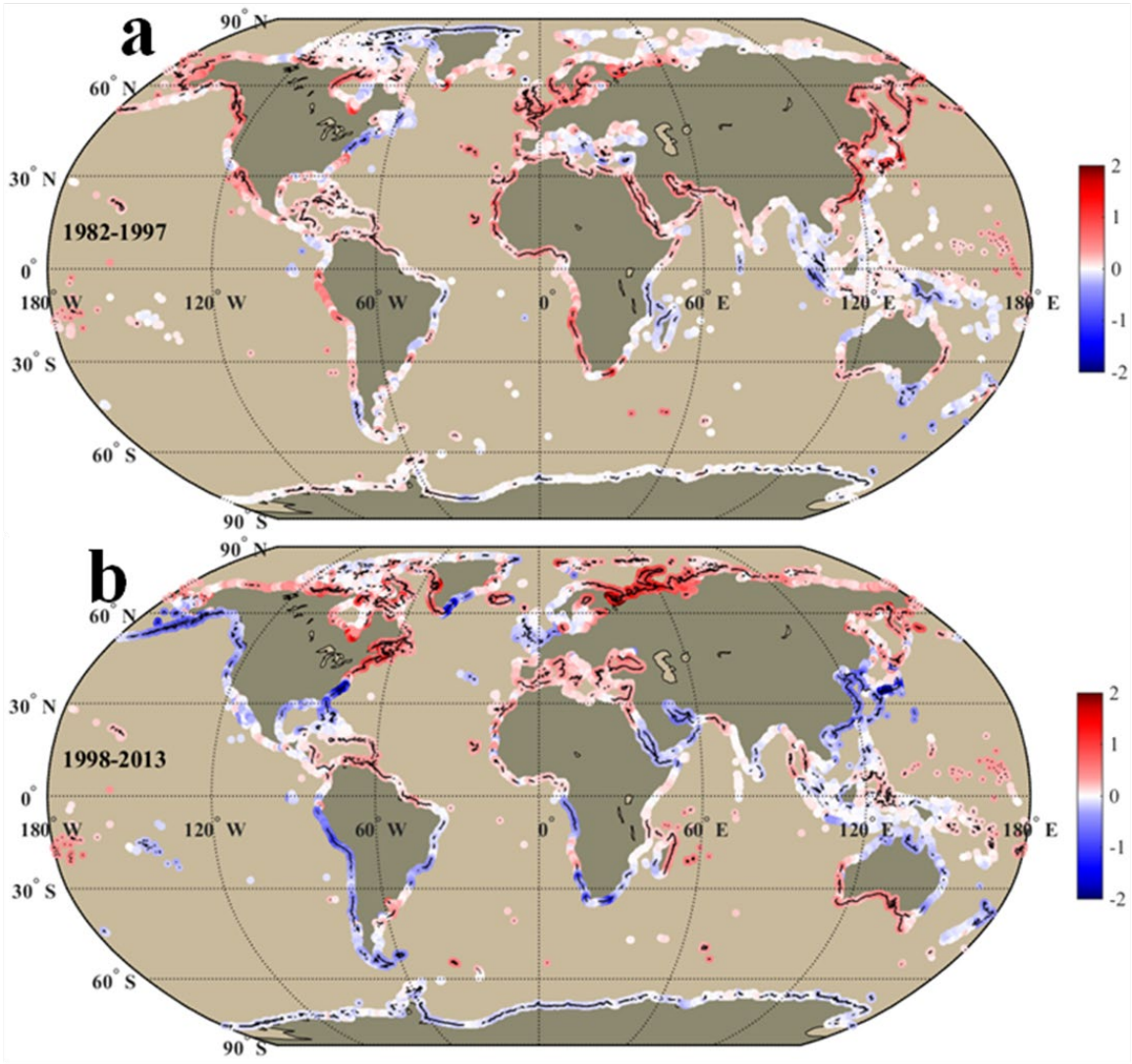

Figure 2.5. The linear SST trends along the world's coastlines in the warming and "hiatus" periods. The linear SST trends (unit: °C/decade) along the world's coastlines in the warming (1982–1997,a) and hiatus periods (1998–2013, b). Black points/lines in the shading color indicate the trends in those locations are significant in statistics ($P < 0.05$). Cited from Liao *et al.* (2015).

Chapter 3. Effects of the Pandemic on Observing the Global Ocean

This material appeared in: **Boyer, T., H.-M. Zhang, K. O'Brien, J. Reagan, S. Diggs, E. Freeman, H. Garcia, E. Heslop, P. Hogan, B. Huang, L. Jiang, A. Kozyr, C. Liu, R. Locarnini, A. V. Mishonov, C. Paver, Z. Wang, M. Zweng, S. Alin, L. Barbero, J. A. Barth, M. Belbeoch, J. Cebrian, K. J. Connell, R. Cowley, D. Dukhovskoy, N. R. Galbraith, G. Goni, F. Katz, M. Kramp, A. Kumar, D. M. Legler, R. Lumpkin, C. R. McMahon, D. Pierrot, A. J. Plueddemann, E. A. Smith, A. Sutton, V. Turpin, L. Jiang, V. Suneel, R. Wanninkhof, R. A. Weller, and A. P. S. Wong , 2023: Effects of the Pandemic on Observing the Global Ocean. Bull. Amer. Meteor. Soc., 104, E389–E410, https://doi.org/10.1175/BAMS-D-21-0210.1**.

3.1 Introduction

The Global Ocean Observing System (GOOS; Lindstrom *et al.* 2012; Moltmann *et al.*, 2019), structured under the Framework for Ocean Observing (FOO; Lindstrom *et al.* 2012), consists of the requirements, assessment, design, execution, and utilization/dissemination of networks of measurements of relevant essential ocean variables (EOVs). These are a subset of essential climate variables (ECVs; Bojinski *et al.*, 2014) used to monitor the environmental conditions immediately above the surface of the ocean, at the surface of the ocean, and throughout the water column down to the ocean/bottom interface. The focus of this work is on the execution of the network as realized in the short and long-term monitoring of ECVs. To clearly delineate this focus from the full system defined under the FOO, we will use the term eGOOS (executed GOOS). Further, the focus here will be on ocean measurements of ECVs rather than EOVs to include marine meteorology measurements and to exclude ocean biological measuring systems, which for the most part, have not achieved FOO mature readiness levels.

The eGOOS is an evolving (and growing) system of complementary observing networks coordinated through the Observation Coordination Group (OCG) of the Intergovernmental Oceanographic Commission (IOC) of the United Nations Educational, Scientific and Cultural Organization (UNESCO), with monitoring support from joint World Meteorological Organization (WMO) - IOC OceanOPS center (Revelard *et al.* 2021). Shipboard measurements allow versatile sampling and high-quality measurements, but come at higher cost and with more human and environmental limitations. Independent platforms allow measurement without immediate ship or proximate human assistance, but require regular maintenance and replenishment. There has been a steady increase in measurements in the global ocean since the end of World War II thanks to dedicated resourcing from countries around the globe. This is due

to increased awareness of the importance of ocean observation for weather forecasting, increased interest in protecting marine ecosystem, understanding the ocean's role in the climate system, and exploiting the ocean's economic potential.Technological advances in observing platforms and their sensors have also contributed to this increase in ocean measurements. Today there is an unprecedented availability of data for the global, regional, and coastal oceans, as well as improved data analysis techniques, which gives us the capability to make increasingly reliable weather and climate predictions and to better understand the ocean environment and its changes. Given the increasing importance of ocean observations, it is well worth assessing the impact of the COVID-19 pandemic (hereafter simply pandemic) on the eGOOS. Such an assessment will help to plan and prescribe steps needed to restore the eGOOS, to identify weaknesses in the deployment and maintenance of the system, and to mitigate future unforeseen disruptions. It should be noted that satellites are a vital element of the eGOOS, which are not directly affected by the pandemic (except in the context of resourcing, planning, and launching), but satellites depend on *in situ* data for validation and calibration. The focus of this paper is to determine the repercussions of the pandemic on the *in situ* eGOOS. Specifically, we endeavor to follow up and assess further the risks to the eGOOS identified a few months into the pandemic (Heslop *et al.*, 2020) and the remediation efforts which have unfolded through two years of the pandemic (January 2020-December, 2021).

3.1.1 Marine Meteorology and ocean surface ECVs

Marine Meteorological (surface atmosphere) ECVs (air temperature, water vapor, surface pressure, wind speed and direction) and ocean surface observations (e.g. sea surface temperature - SST, salinity - SSS, surface currents, sea state) in real-time (RT, public availability within one hour of measurement) and near real-time (NRT; public availability mostly within hours to a

couple of days of measurement) are essential for accurate global weather and ocean forecasts, and for satellite data calibration/validation, as well as provision of some climate services, e.g. seasonal forecasting and rapid turnaround event attribution. ECV observations are collected from ships, both dedicated research cruises and Voluntary Observing Ships (VOS) commercial vessels (Smith *et al.*, 2019), and independent platforms such as surface drifters and moored ocean buoys, and recently uncrewed surface vehicles (USVs, e.g. Saildrones). [Note that the remaining surface atmosphere ECVs – precipitation and surface radiation budget, and ocean surface ECVs - surface stress, sea ice, ocean surface flux, sea level, which are not routinely observed from moving platforms, are not addressed here.] The WMO Global Telecommunication System (GTS) is the main mechanism by which these measurements are made available in NRT. For long-term use, data are assembled in databases such as the International Comprehensive Ocean Atmosphere Data Set (ICOADS, Freeman *et al.* 2017, Liu *et al.* 2022) and Surface Underway Marine Database (SUMD, Mesick *et al.*, 2020). During the 2020-2021 period of the pandemic the GTS functioned as normal with no major negative consequences. As the major distribution mechanism for weather and climate forecast data, the GTS contains redundancies and safeguards to ensure that the data continue to flow despite short or long-term stressors. Marine meteorological and ocean surface data delivery over the GTS in 2019 (Figure 3.1a), 2020 (Figure 3.1b), and 2021 (Figure 3.1c) show, superficially, the changes in the overall eGOOS.

3.1.2 Ocean Subsurface ECVs

The subsurface eGOOS is vital for understanding our global climate system both in the physical (temperature, salinity) and the chemical (carbon, oxygen, nutrients, transient tracers, nitrous

oxide, ocean colour) domains. Subsurface ECVs temperature and salinity are important inputs for weather and climate models in near-real time. The subsurface eGOOS shares some of the same challenges in building and maintenance as the surface eGOOS, with added difficulties unique to measuring ocean variables up to 6000 m depth. The subsurface eGOOS ECV observations available in the World Ocean Database (WOD; Boyer *et al.*, 2018), mainly from NRT sources, anchored by Argo floats (Wong *et al.* 2020), exhibited changes through the April - June period in 2019 (Figure 3.1d), 2020 (Figure 3.1e) and 2021 (Figure 3.1f). Most subsurface ECV observations other than temperature and salinity, except those from Argo floats, are not available in NRT due to necessary post-measurement processing and quality assurance. Long-term assembly of data for most ECVs is executed by databases such as the WOD for reuse of the data for climate study. While changes to some elements of the eGOOS are discernable from Figure 3.1, an exploration of the details of both ship-based and independent platform measurement performance is necessary to understand the effects of the pandemic on the eGOOS.

3.2 Ship-based observations

Historically, ship-based observations have formed the backbone of the eGOOS. Even as technological advances have allowed for the utilization of independent observation platforms, ships are still major contributors to the eGOOS. Cargo and passenger vessels (PVs) contribute NRT marine meteorological, ocean surface, and subsurface measurements of ECVs through the VOS network (Smith *et al.*, 2019). NRT data are utilized in the short-term for weather and climate forecasting. For some marine meteorological measurements (e.g. air temperature, relative humidity) the VOS provides the main source of NRT measurements. The related Ship of Opportunity Programme (SOOP; Goni *et al.*, 2010) focuses on subsurface NRT and ocean (non-

weather) focused surface ECVs from volunteer ships. Research vessels (RVs) contribute high quality measurements of all ECVs, indispensable for detection of long-term climate signals both regionally and globally. High quality measurements from RVs are also necessary for maintaining baseline quality standards for NRT measurements and independent platform measurements. RVs extend measurements to geographic regions and ocean depths not readily accessible to other platforms. RVs are the main platform for maintaining long-term climate monitoring for non-NRT subsurface ocean ECVs.

3.2.1 The VOS network

The number of reporting VOS ships increased steadily from 2016 to the end of 2021 for container/cargo and PVs as per reports in ICOADS (Figure 3.2). The pandemic's impact is shown in the number of ships from the RV and PV fleet (Figure 3.2) - both decreased significantly in the Spring of 2020. Reporting RVs reached a short-lived minimum (about half of their 2019 numbers) in May 2020, but have rebounded since then due to implementation of safety measure mitigations and the dedication of the research community. Even with that, the RV reports are still about 10% lower than for 2016 - 2019. The number of reporting PVs remained low during the pandemic years (roughly about 60% of its peak in 2019), until rebounding in mid-2021. The pandemic has led to a steady drop in participating container/cargo ships that were in operation pre-pandemic, but these losses have been offset by newly participating VOS ships (Figure 3.2a, solid vs. dashed lines). Of the marine meteorological measurements, almost all ships are reporting air temperature (AT). SST is reported by roughly 30-70 fewer ships than AT, depending on the year. Water vapor (in the form of relative humidity; RH, not shown) is measured by 30-50 fewer ships than SST, again depending on the

year. The curve for the number of ships reporting relative humidity follows the same pattern as SST and AT.

3.2. 2 SOOP network

The SOOP, closely related to the VOS, also leverages volunteer vessels that routinely transit in strategic shipping routes globally to monitor vital ocean variables, including upper ocean water temperature, using Expendable Bathythermographs (XBT). XBTs were the main component of the subsurface temperature observing system from the 1960s to the advent of the Argo program. They continue to augment Argo by maintaining long time series along particular shipping lines that are chosen because they cross key currents and ocean basins. These XBT surveys are repeated several times a year and at high spatial density, thus providing valuable data to monitor meridional heat transports. The XBT deployment process is largely manual, but increasingly using programmed auto launchers capable of deploying up to 12 XBTs at designated times, and are conducted by the ship crew or by ship riders during a transit. There has been a drop-off in XBT temperature profiles from 2016 to present (Figure 3.3) due to budget constraints and changes in ship traffic patterns. This trend was accelerated in 2020 due to the pandemic, although not yet approaching pre-pandemic levels by the end of 2021. A continuing problem is the lack of ship-riders due to the logistics of getting to the ship as well as the shipboard infection risk (both for crew and rider). In some cruises, the crew has been taking on ship-rider duties, but usually at a reduced deployment frequency. So, while the number of XBT cruises during the pandemic dropped in 2020 at a steeper rate than the long-term trend, it recovered by the end of 2021 to 2019 levels. However, the number of XBTs deployed fell at a much steeper rate in 2020, given fewer deployments per cruise, and has not yet recovered. Some long-term lines,

notably in the Arabian Sea and the Bay of Bengal, ceased during the pandemic and will be restarted in the near future. SOOP thermosalinograph (TSG) reporting vessels supply high resolution underway SST and SSS measurements, augmenting the VOS NRT SST (included in Figure 3.2). The SOOP is integral to surface ocean carbon underway measurements. This is a complex measurement, requiring more processing and quality assurance than temperature or salinity, is available on a limited number of ships, and is consequently more vulnerable to the pandemic.

The Pacific equatorial underway time-series, which has operated via container ships since 1982, has experienced a hiatus of a few years, with travel and access restrictions due to the pandemic prolonging the hiatus**.** Three of the 15 NOAA funded SOOP ships that carry automated surface water CO_2 measurement equipment are cruise ships that have not returned to service as of July 2022, leaving a 1.5-year hiatus. Two other SOOP are cargo vessels that ceased SOOP-CO_2 operations because of restricted boarding for routine maintenance. Some of the 30 % loss of capacity is made up by increased use of RVs and PVs but with changes in geographic coverage.

3.2.3 Research Ships

The Global Ocean Ship-Based Hydrographic Investigations Program (GO-SHIP; Sloyan *et al.* 2019) is responsible for coordinating climate quality observations along repeat transects with varying temporal resolution (annual, biennial, decadal, etc.) in the global ocean. During these repeat hydrographic cruises, high (climate) quality referenced measurements of physical, biological, and chemical ocean properties are made from the surface to the ocean's bottom. Additionally, many of these cruises deploy Argo profiling floats, drifting buoys, and are a testbed for new technologies and measurements to probe the ocean. While most measurements

are not available in NRT, GO-SHIP cruises are critically important for observing many ocean variables, including carbon, oxygen and nutrient ECVs. Additionally, GO-SHIP cruises help monitor the deep ocean and provide critical information for detecting long-term changes. During 2020, 11 GO-SHIP cruises were scheduled, in which an estimated 1400–1500 oceanographic casts (simultaneous profiles of multiple ECVs) were planned; however, only three of these cruises were completed as planned and contributed roughly 320 casts. Additionally, one US cruise, GO-SHIP line A13.5 was cut short due to the pandemic and made only eight of the planned 128 stations (Figure 3.4). It was rescheduled for January 2022, but was canceled at the last moment. This resulted in a loss of over three thousand discrete samples in the Eastern South Atlantic, a data-poor region where no high-quality carbon and tracer measurements have been taken since 2010. The rest of the planned GO-SHIP cruises were either postponed by 6-12+ months or canceled. In addition, only 15 of ~80 planned Argo deployments were completed. While some of these cruises may be made up in the future, the state of the ocean as would have been determined by GO-SHIP for 2020 is irretrievably lost.

While 2020 saw many GO-SHIP cruises outright canceled or delayed due to the pandemic, 2021 cruises experienced their own set of pandemic-related restrictions. While more GO-SHIP cruises were able to set sail in 2021, many of them were restricted in the number of people allowed to partake in the cruise. The reduced number of embarked personnel, coupled with instrument supply chain issues, led to less stations being occupied on a given cruise with less information being retrieved from the sea. For example, in some cases physical state variables such as temperature and salinity were observed, but ocean chemistry observations, which are historically much less abundant than physical ocean observations, were unable to be retrieved. In other

cases, limited personnel did not allow for full 24-hour rotating shifts, limiting the number of casts able to be taken during a cruise.

In addition to GO-SHIP cruises, research fleets from countries around the world contribute important observations, research, and deployments outside the GO-SHIP repeat transect framework. For example, the U. S. National Oceanographic and Atmospheric Administration (NOAA) currently has 16 active research, survey, and fisheries vessels, which occupy both Atlantic and Pacific waters. The fleet has a wide variety of uses, and many contribute to the global observation system in some manner. Ship days for the fleet went to zero in the April-June quarter of 2020 (Figure 3.5); however, most vessels returned to at least 66% of their pre-pandemic levels by the end of 2021 and a few have surpassed pre-pandemic levels, bringing the overall NOAA fleet ship days close to 2019 levels. Some national fleets, notably Japan's, continued to go to sea and report temperature and salinity observations in NRT (Figure 3.1). Illustrative of the dependence of specific ECVs on RV; among the pandemic canceled RV operations were coastal US cruises supported by NOAA's Ocean Acidification Program, which would have obtained approximately 3000 water samples to study ocean acidification status along the North American Pacific coast. One of the two cruises was successfully completed in summer 2021, but the other has not yet been rescheduled. Coastal ocean acidification cruises along the West Coast of the US, and Gulf of Mexico that occurred in 2021 were also hampered by reduced availability of certified reference materials, travel limitations, and more complicated logistics and quarantine times for participating scientists due to the pandemic. Pandemic-related supply chain issues have made replacing obsolete and mal-functioning equipment or expanding analytical capacity difficult to impossible. Collectively, these challenges make it difficult to

provide partners and stakeholders timely information about ocean carbon and acidification conditions in open ocean, coastal, and estuarine habitats.

3.3 Independent platforms

3.3.1 Surface drifting buoys

Surface drifting buoys make essential observations of SST, atmospheric (surface) pressure and near-surface ocean currents (calculated from trajectories). All surface drifters measure SST. Drogued buoys, about 50% of all drifters, measure near-surface currents. 50% of surface drifters measure atmospheric pressure. Drifting buoys are deployed globally from RVs, commercial vessels and air drops. Drogued buoys move with the nominal 15 m depth ocean currents. Surface drifters send measurements to communication satellites at approximately hourly time intervals, which are then transmitted to global data collection centers on shore. Drifting buoys have become the main source of spatial and temporal coverage for the *in-situ* surface eGOOS, but have a more limited range of measurands than ships. Surface drifting buoys have an expected lifetime of about 18 months. Figure 3.6 shows when the surface drifting buoys in ICOADS (Liu *et al.*, 2021) reported data for the first time after deployment into the ocean. There are seasonal and interannual variations normally. At the pandemic onset in March 2020, the number of new drifter deployments significantly decreased, until early June when special actions were taken to address the decline (Figure 3.6). Over the course of the pandemic, the Global Drifter Program (GDP; Lumpkin *et al.*, 2016) shifted many deployments from research cruises, which were being delayed or canceled in 2020, to merchant vessels. The difficulty with merchant ship deployments is that these are mainly along major shipping routes, with many important ocean areas left unvisited and consequently in danger of reduction of data coverage.

Note that before the pandemic, the GDP had a large number of deployments through the second half of 2019. These deployments, coupled with a doubling of buoy half-life since 2016, resulted in an array maintained in size through 2020. However, many of the 2019 deployments were in dense clusters that did not sustain global spatial coverage. Both float array size and spatial coverage (Figure 3.7, upper and lower, respectively) have been decreasing steadily in 2021, with notable gaps in the Indian Ocean and the South Atlantic.

3.3.2 Argo profiling floats

Argo floats are the backbone of the contemporary subsurface eGOOS, and in many areas and depths, the only observing platform. Furthermore, Argo contributes to the surface eGOOS through the near-surface portion of its sampling scheme. Argo comprises around 4,000 active floats globally, drifting for 10 days at depth, then measuring core variables of pressure/temperature/salinity from 2000 m to the surface. Deep Argo floats take measurements from as deep as 6000 m. Biogeochemical Argo (BGC Argo) floats additionally measure dissolved oxygen, nitrate, pH, chlorophyll fluorescence, and bio-optics. 'First cycles' (Figure 3.6a) are the first received profiles from a particular float, designating a successful deployment. Floats are deployed mainly from RVs, with some from SOOP merchant ships. The total number of active floats (Figure 3.8a) dropped slightly over the pandemic as float cessations outnumbered float deployments in all but the fourth quarter of 2020 and 2021 (Figure 3.8b). A lack of deployment due to pandemic restrictions and rising costs per float will start to create holes in the global coverage of Argo as older floats die and/or disperse out of particular ocean areas. April-June 2020 marked the lowest number of first cycles since the first years of the Argo program. It is important to note that deployments have been trending downward since 2015 due

to increased cost per float, and deployments are highly variable by quarter, but the 50 deployments in April-June of 2020 mark a clear low. Extensive work by the Argo community to find deployment opportunities since then has resulted in 230, 139, 237, and 145 first cycles in the third and fourth quarter of 2020 and first and second quarters of 2021. Significant effort was needed to find ships from which to deploy floats during the pandemic, especially in areas such as the South Pacific Ocean which had sparse cruise traffic. Despite these efforts, the total number of active/reporting Argo floats dropped below 4,000 in the fourth quarter of 2020 for the first time since 2015. It is hoped that the excess of deployments over float cessations in the fourth quarter of 2021 marks a return to stable float replenishment. A consideration for Argo floats is that while the number of floats has remained relatively steady through the pandemic due in part to long battery life (Figure 3.9), instrument performance can deteriorate over time. Therefore, while Argo floats can operate over many years, continual quality assessment of the data is imperative. This is an important issue for Argo salinity, as float measurements are known to be affected by sensor drifts as a result of physical changes in the conductivity cells through time. Historically, when floats approach the age of about 6 years, about 30% of them will require a salinity adjustment of about 0.01 (unitless; Wong *et al.*, 2020). On the other hand, temperature data are known to remain stable through time. Hence aging of floats is not a factor in ocean temperature monitoring.

3.3.3 Moored buoys

Moored buoys are platforms that are anchored to the seafloor at specific geographic locations. Moored buoys typically report marine meteorological readings, surface oceanographic measurements, and in some cases subsurface oceanographic measurements, often at high

temporal frequency. Most moored buoys are near-coastal, with the significant exception of the tropical moored buoy arrays, which span the tropical ocean basins. Coastal moored buoys provide data on local conditions while the tropical arrays provide information on tropical phenomena which affect global weather and climate patterns, such as El Nino.

The coastal moored buoy NRT data returns show no discernable drop during the pandemic period in 2020 - 2021 relative to the non-pandemic period in 2018 - 2019 (Figure 3.10). Coastal moored buoy NRT data have a seasonal pattern, with higher observation counts during the northern hemisphere summer. Non-NRT ECV monitoring from coastal buoys, as with underway data, relies on a smaller highly maintained network. Due to postponements of servicing cruises, NOAA's Ocean Acidification Observing Network of surface buoys suffered a reduction in data return of 13% compared to pre-pandemic values as sensors failed due to lack of maintenance.

Moored buoys require ship maintenance on site through recovery and re-deployment at regular service cycles. The pandemic has created significant challenges for maintaining open ocean moored buoys. OceanSITES is the collective for research quality deep ocean monitoring sites, most of which include instrumented moored buoy time series of ECVs. The tropical moored buoy arrays are a subset of OceanSITES buoys. Mooring losses in tropical moored buoy arrays, which were already in decline, in the past year have far exceeded any previous year's losses. In the tropical Pacific, the TAO array (Chen *et al.*, 2018) did have regularly scheduled maintenance. All moorings in RAMA (McPhaden *et al.*, 2009) in the tropical Indian Ocean have been deployed well beyond their 1-year design life. Mooring cruise operations in PIRATA (Bourlès *et al.*, 2019) in the tropical Atlantic have partially resumed, and most of PIRATA has been serviced in 2020-2021 to improve data return rates. However, travel restrictions and cruise

cancellations remain a problem for accessing and servicing moorings in RAMA. Figure 3.10 (dashed line) indicates a dramatic drop of reporting tropical moored buoys, due to extended periods (>2 years) of inability to schedule cruises in the Indian Ocean. Many of the moorings have stopped transmitting due to power loss (design life is 1 year), or have broken free of their anchored positions after wear and tear from extended periods at sea or potential vandalism incidents. However, the first pandemic period RAMA maintenance cruise in over 2 years aboard the Korean ship R/V Isabu in January 2022 has helped to mitigate the declines. Planning for additional cruises in the Indian Ocean is underway. In addition to the impacts of mooring losses, ongoing impacts related to the pandemic also include increasing problems with equipment shipping delays and the emergence of high inflation, which places additional pressures on budgets that do not grow to keep up with inflation. The long-term impacts from data losses in the Indian Ocean array is difficult to quantify since many of the data impacts are only now being realized. However, RAMA data are used extensively to provide accurate weather and monsoon forecasts over south Asia, to improve understanding and impacts of the Madden-Julian Oscillation (MJO), to provide initial conditions for operational global coupled forecasting systems, to provide verification of ocean-atmosphere flux products in the Indian Ocean, among other applications. Documented impacts to each of these applications have been observed by various forecasting centers around the world. An example of pandemic difficulties on a deep ocean mooring is provided by the Stratus Ocean Reference Station at 20° S, 85° deg W under the stratus clouds west of northern Chile. The 2021 cruise was ready to go with personnel already in Chile, then canceled the day before sailing. Quarantine costs and quadrupled cost of shipping to the pandemic added expenses to the cruise. Time between maintenance allowed for fouling of conductivity cells and consequent low-quality upper ocean salinity measurements. Similarly.

Gooseneck barnacles on sensor heads and propellers affected current velocity measurements. Battery lifetime of 12-14 months was exceeded before maintenance cruise arrival causing loss of data.

3.3.5 Animal borne ocean sensors (AnIBOS)

Instrumented animals, in particular pinnipeds, are a growing constituent of subsurface temperature observations in the upper ocean (< 1500m) and higher latitudes (75°S - 50°S & > 70°N), augmenting other observing platforms, and in some areas (e.g. Ross Sea), providing some of the only consistent measurements (McMahon *et al.* 2021). Instrument life mounted on marine animals is limited to one year (McMahon *et al.* 2021). Since 2015, the number of deployments has remained fairly consistent at approximately 103 instruments total *per annum.* Typically, the instruments are deployed during the hemispheric summers. The 2019-2020 summer deployments in the southern hemisphere were completed before the onset of the pandemic (Figure 3.11). In contrast, in the northern summer 2020 (May - August), i.e. during the height of the first wave of the pandemic, only six pinnipeds were instrumented, well short of previous deployments between 2017-2019. Plans for the 2020-2021 southern summer deployments were scaled back to 35 on Kerguelen Island and 25 in the Ross Sea. The total number of active instruments rose after the southern summer 2020-2021 deployments to 79 total reporting pinnipeds globally in the first quarter of 2021. Both northern and southern hemisphere reporting instrumented pinnipeds increased through the end of 2021, though the southern hemisphere instrumenting season was just beginning at the end of the year.

3.3.6 Uncrewed Systems (UxS)

Gliders are uncrewed buoyancy driven vehicles which are usually deployed for high density limited duration surveys of ocean variables in areas on shelves or near coasts. Glider movements can be guided remotely to some extent from shipboard or land. Glider observations extend the ocean observing system into areas not usually covered by Argo floats and are instrumental in maintaining near coastal time series. The pandemic strongly impacted glider deployment pace with no authorization of deployment at its early stage (April to June 2020). To balance that and to maintain the glider array at an acceptable level, the duration of the missions operational at the time were extended leading to a quasi-normal cumulated number of gliders days at sea during this period (Figure 3.12). Thanks to its capacity to deploy close to the shore from small boats, the deployment pace returned to normal in August 2020. The most prejudicial impact was on long term time series that now have observational gaps. Difficulties in deployment of gliders caused by the pandemic have had an effect on the continuity of the observing network. One example, in the absence of the usual research vessel deployment for the glider line off Trinidad Head, California, a charter vessel was used. This same charter vessel accidentally ran over the glider, resulting in loss of the glider and an irreplaceable gap in the time series of measurements along the line. USV are relatively new platforms, without sufficient history to assess the effects of the pandemic through data receipt. There were, however, tangible effects of the pandemic on USV deployment. Several international USV air-sea CO_2 missions in 2020 and 2021 were postponed as lab facilities were closed and travel restrictions were implemented.

3.4. Effects of the pandemic on global ECV monitoring

The goal of the eGOOS is monitoring and understanding global weather and climate by providing marine meteorological and ocean observations of specific ECVs. The effects of data loss at specific locations and regionally results in the interruption of high-quality time series and geographic coverage. On a global scale, the effects of the pandemic can be quantified, or at least defined through specific ECV product sustainment.

3.4.1 Effects on weather and ocean forecast models

NRT observations, both marine meteorological as well as SST, SSS, and subsurface temperature and salinity are essential inputs for ocean and atmosphere data assimilation and their loss has direct consequences for real-time monitoring and forecasts (e.g. Vidard et al, 2007; Fujii *et al.*, 2015; and Chen 2020). Ocean state estimate relies heavily on satellite and *in situ* observations and is used for forecast initialization, validation, and verification. The most immediate impact resulting from the reduction of NRT and RT *in situ* observations is the loss constraint they provide during the data assimilation for adjusting drift in guess analysis provided by the model. The reduction of available *in situ* observations certainly impacted the accuracy of the synoptic and seasonal predictions of the ocean and weather state, however the scope of this impact is hard to quantify. Another impact of the reduced observations is their longer-term influence on future analyses efforts with improved data assimilation systems (the so called reanalyses) that are essential for our improved understanding of ocean climate variability and predictability. Effects of the pandemic on eGOOS data flowing through the GTS, and hence on weather and climate models are reflected in changes to the geographic specific volume of marine meteorological data reported (Figure 3.13), represented most notably by a drop-in air temperature reports in the North

Atlantic in both 2020 and 2021 and additional data gaps in the South Atlantic and Indian in 2021. Given the relative coverage in the basins, the data loss in the South Atlantic and Indian Oceans may be more critical than the persistent data reduction in the North Atlantic. Ocean observing simulation experiments (Xue *et al.* 2017; Zhu *et al.* 2021) in future are needed to quantify the influence in the loss of *in situ* observations during the pandemic.

3.4.1 Effects on SST time series

SST is a major sea surface variable, influencing short and long-term weather patterns as well as an indicator of decadal cycles and longer-term climate trends. The Extended Reconstruction of Sea Surface Temperature (ERSST; Huang *et al.* 2017) calculates global SST change from the late 1800s to present. ERSST utilizes the SST observing system on a monthly basis, combining moored/drifting buoys, ship-based observations and Argo profiling floats near-surface measurements. Figure 3.14 indicates that for the combined ship+buoy+Argo float observations, we saw a slight drop (< 5%) in coverage in early 2020 which has persisted. The slight drop is a combination of drops in ship coverage starting in early 2000 and drops in buoy coverage starting in late 2020/early 2021. Argo float coverage was mostly steady with a slight (< 5%) increase during the two-year period. Overall, the observational coverage and high-quality data receipt needed for ERSST has not been affected globally by the pandemic to date.

3.4.2 Effects on Ocean heat content (subsurface temperature) time series

The ocean absorbs more than 90% of excess heat in the Earth's system, so estimation of ocean heat content (OHC) change is vital to understanding the Earth's Energy Imbalance (EEI) and sea level change (e.g. von Schuckmann *et al.* 2020). The percent coverage of the global ocean from

subsurface temperature data is directly related to uncertainty of the OHC estimate. The percent data coverage has increased rapidly since 2000 (Figure 3.15) as the Argo array reached global extent around 2006-2007 and has been fairly steady since at around 65% globally. This increase in global subsurface temperature data coverage since year 2000 has led to a decrease in uncertainty in the OHC estimates (Boyer *et al.*, 2016; Johnson *et al.*, 2020). There is a no appreciable drop in the percent data coverage in the pandemic period, fluctuations during the pandemic no larger than the fluctuations in previous years, so the observing system has sustained the receipt of quality subsurface temperature measurements in 2020-2021 for the calculation of seasonal ocean heat content time series to this point despite the pandemic. Note that the criteria for coverage SST time series and ocean heat time series are different given the nature of the calculations of the respective ECVs.

3.4.3 Effects of the pandemic on other ocean ECVs

Of the remaining ocean ECVs, only salinity approaches the volume, distribution, and timeliness of temperature observations. Salinity requires more quality assurance than temperature, including adjustments for sensor drift in the conductivity cells used on Argo floats. Salinity adjustment in Argo is done as part of the delayed-mode data processing procedure, which has been mostly unaffected by the pandemic. However, the loss of ship-based salinity measurements as a result of canceled GO-SHIP cruises during the pandemic is irretrievable. Even though there is no operational freshwater content time series, the salinity equivalent of ocean heat content, ocean salinity is the subject of long-term climate studies (e.g. Durack *et al.*, 2012). SSS are utilized in blended *in situ*-satellite products (e.g. Xie *et al.*, 2014) at a monthly time scale. Other data products provide subsurface salinity monthly mean global fields at standard ocean depths

from Argo data (e.g. Roemmich and Gilson, 2009), and from all observing system data (e.g. Good *et al.*, 2013). For surface ocean carbon, multi-platform air-sea CO_2 data contribute to the Surface Ocean CO_2 Atlas (SOCAT), which is the basis for annual observation-based estimates of ocean CO_2 uptake (Bakker *et al.* 2016) that inform the annual Global Carbon Budget (Friedlingstein *et al.* 2021). For the subsurface carbon ECV, as well as for ocean nutrients, monitoring mainly takes the form of long-term climatological means (e.g. the Global Ocean Data Assimilation Project - GLODAP; Lauvset *et al.* 2021, World Ocean Atlas - WOA; Garcia *et al.* 2018). Any data loss can be felt in a lack of representativeness of the pandemic years within the overall time period mean, as well as a delay in the accumulation of sufficient data to document global time variations. For ocean dissolved oxygen, global inventory time series are in the research stage (Ito *et al.*, 2017; Grégoire *et al.*, 2021). Operationalizing *in situ* global dissolved oxygen monitoring will be dependent on the proliferation of BGC Argo and other independent platforms with oxygen sensors and the quality assessment of this sensor data through high quality research cruise data, all of which were affected by the pandemic. Surface ocean currents derived from *in situ* drifter trajectories are also inventoried yearly (e.g. Lumpkin *et al.*, 2021).

3.5. Conclusions

During the course of 2020 and 2021, the pandemic created serious challenges for maintaining the eGOOS to the point that the observing system for ECVs reliant mainly or wholly on research cruises were not sustained. Merchant ships and independent platforms did provide for sustained monitoring of ECVs, but within limitations of deployments, battery life, and instrument reliability over time. These limitations have led to a slow deterioration in the monitoring capabilities for these ECVs, and which need to be addressed.

3.5.1 Lessons from the pandemic for the eGOOS

1. Research cruises are the backbone of the eGOOS in terms of providing high quality measurements for detecting and monitoring climate signals in ECVs, validating and calibrating satellite and NRT *in situ* measurements, deploying and maintaining independent platforms, and continual development and improvement in end-to-end ECV monitoring systems. The research fleet is not as resilient as the merchant fleet in developing strategies to meet unexpected obstacles. Partly this is due to the economic necessities of merchant ship operation. Strategies for funding and logistics should be implemented to ensure continuity in research cruise operations in the face of unexpected factors such as the pandemic, otherwise monitoring for ECVs cannot be considered sustained.
2. The eGOOS is resilient where independent platforms can be relied upon, within the battery life constraints, instrument constraints, calibration/validation against high quality ship measurements, and maintenance schedules necessary for ensuring high quality measurements. Deployment methods independent of research cruises should be pursued where possible, but with care to ensure high rates of success with the complex instrumentation, where success means not only recording and transmission of measurements, but of high-quality measurements. Battery life extension needs to be accompanied by increased sensor stability.
3. The augmentation of RV measurements with sensors on independent platforms needs to continue to be emphasized, and accelerated if possible, with specific focus on EOVs such as carbon (pH, alkalinity, dissolved inorganic carbon, and pCO_2), oxygen, and nutrients.

This is underway with the growth of BGC and Deep Argo and other programs. Research to validate sustained sensor measurements should be expanded and systematized to provide confidence in the reliability of global sustained ECV monitoring for these variables.

4. Every marine meteorological, surface ocean, and subsurface ocean *in situ* measurement available in NRT is of value to weather and ocean models. Every measurement can be reused for long-term study and hindcast reanalysis. The data flow of pertinent RV ocean measurements (temperature and salinity) to the GTS in NRT can and should be increased to encompass the entire global RV fleet. The flow of all ECVs from RVs and other platforms to the long-term databases needs to be optimized and sustained to gain full utility of the eGOOS through reuse of the data for climate study.

5. Consolidated monitoring and logistic support of the eGOOS is essential to identifying gaps and coordinating planning for system sustainment.

6. Emerging platforms such as AniBOS and Ocean Gliders, are critical to fill in data gaps in under sampled areas and along the coasts. Other innovative solutions, including new independent systems, as well as enhanced private/public partnerships, could potentially increase data volumes available to research and operational workflows.

7. Securing the supply chain for oceanographic instrumentation and analysis tools is imperative for continuous cost-effective observations.

3.6 Figures

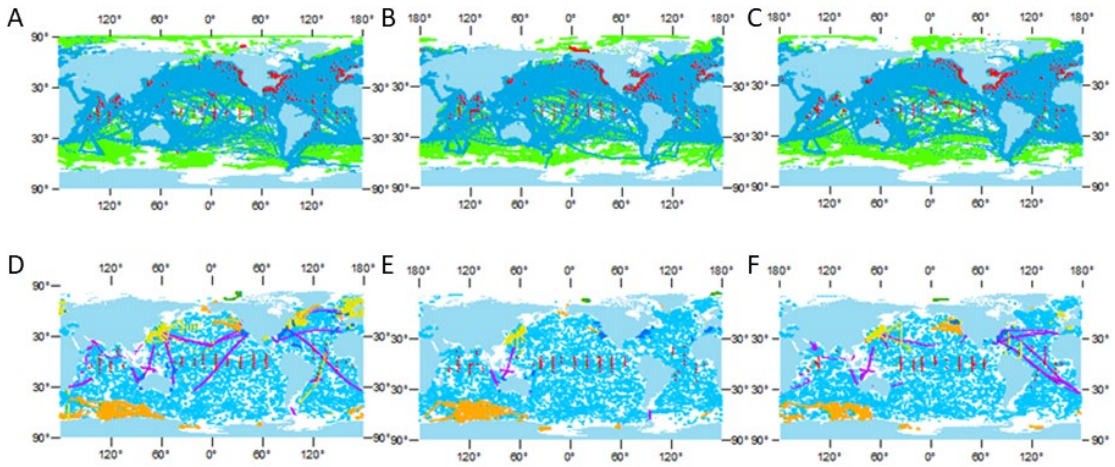

Figure 3.1. Geographic distribution of marine meteorological and ocean surface observations from ships (blue), moored buoys (red) and drifting buoys (green) for April through June a) 2019, b) 2020, and c) 2021. Subsurface observations (at any depth) from Argo floats (turquoise), Expendable Bathythermographs (purple), ship-based Conductivity-Temperature-Depth (orange), gliders (light blue), tropical moored buoys (red), pinniped mounted sensors (yellow), and ice-tethered profilers (dark green) for April through June: d) in 2019, e) in 2020, and f) in 2021. Note that surface observations from other platforms overlay drifting buoys (green) in a), b), c) while subsurface observations overlay observations from Argo floats (turquoise) in d), e), f). Drifting buoys and Argo floats are well represented, but not visible in all areas outside of marginal seas and high latitudes.

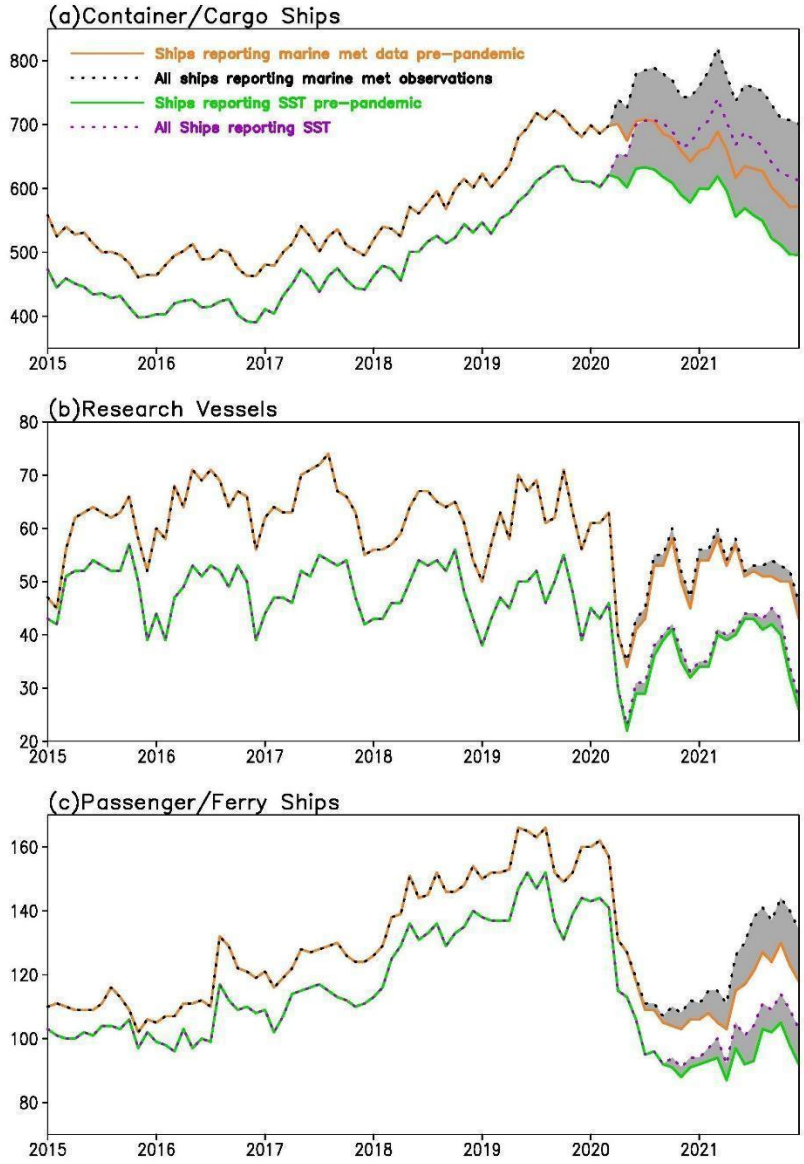

Figure 3.2. Number of ships with independent WMO call sign numbers since 2015 in the ICOADS R3.0.2 near real-time collection. Top panel (a) is for the container/cargo ships, middle panel (b) for the research vessels/ships, and bottom panel (c) for passenger/ferry ships. The Orange and Black lines are for all ships, compared to the Green and Purple lines which are for subsets of ships reporting SST measurements. The solid lines are for the number of ships that were reporting data pre-pandemic (defined as March 2020) and have continued since then, while the dashed lines are the total number of ships reporting data during the pandemic.

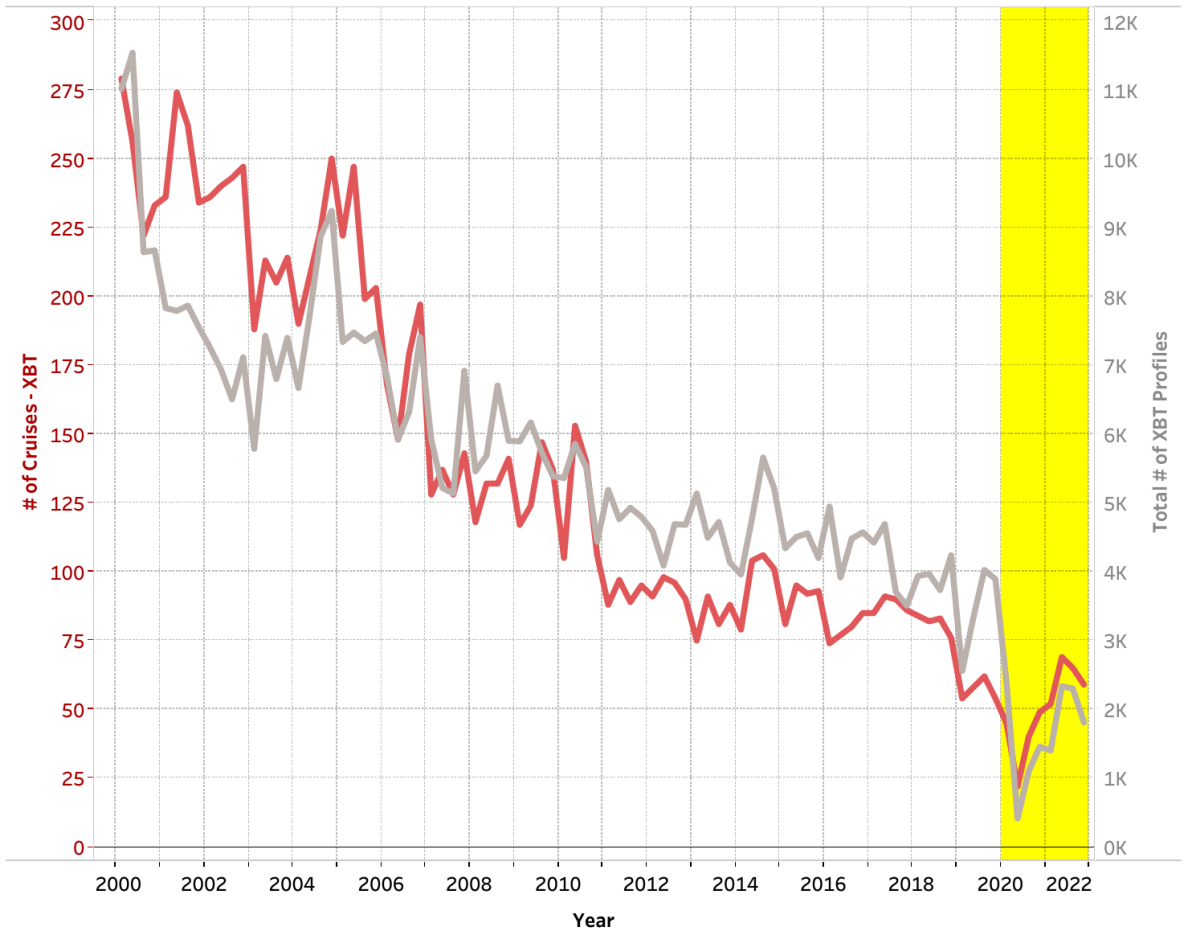

Figure 3.3. Expendable Bathythermograph (XBT) cruises 2000- 2021 (red) and total number of XBT profiles (grey) by quarter. Yellow shading for January 1, 2020 – December 31, 2021.

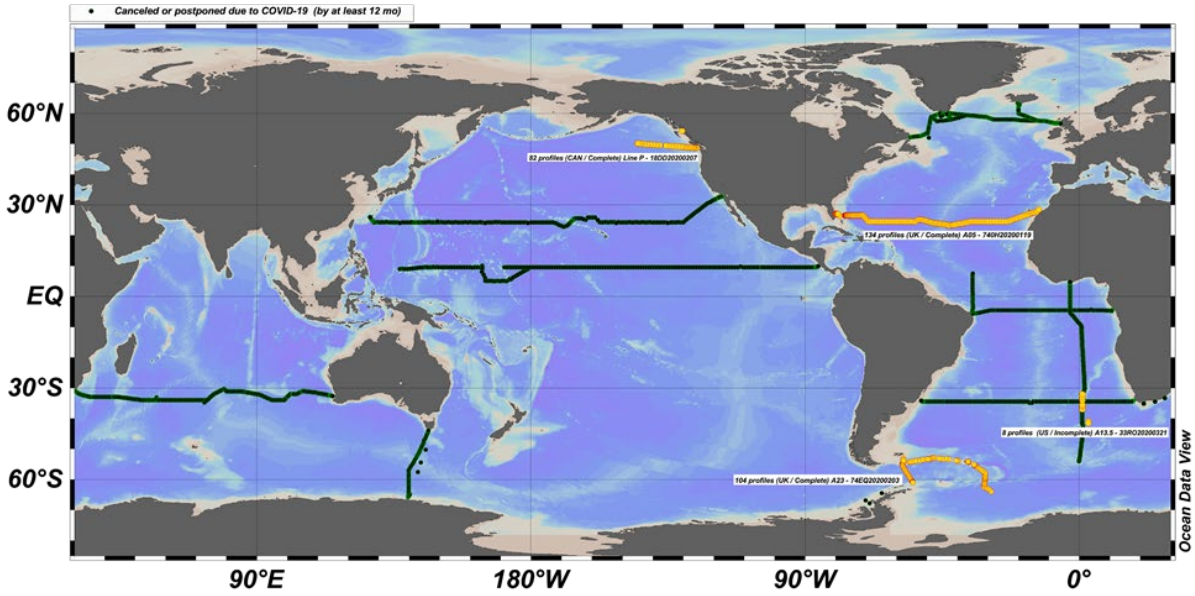

Figure 3.4. Global Ocean Ship-Based Hydrographic Investigations Program (GO-SHIP) repeat hydrography cruises planned and/or completed in 2020. Cruises in green were planned, but were subsequently ended prematurely, canceled, or delayed into the future. Orange dots show where profiles were measured in 2020 for completed and partially completed cruises

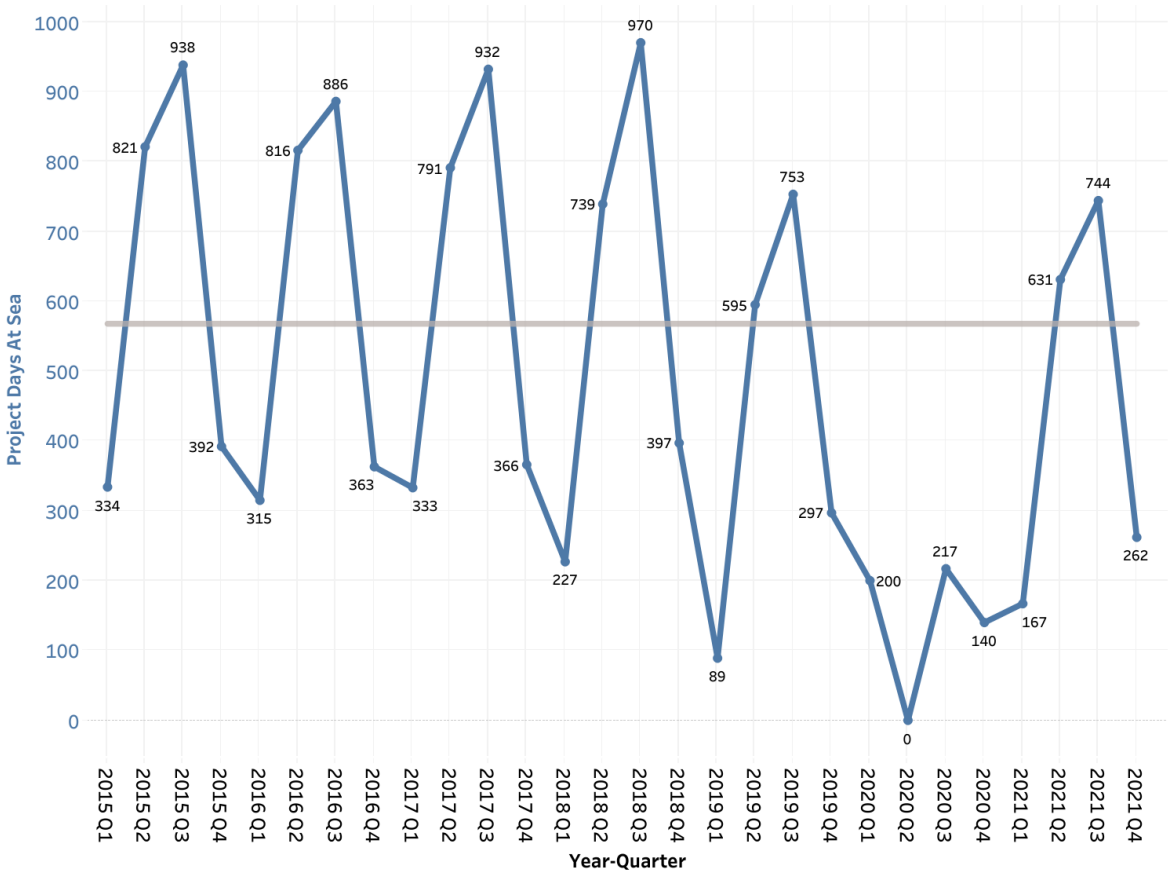

Figure 3.5. Ship days at sea for the U. S. National Oceanographic and Atmospheric Administration (NOAA) research fleet by quarter, from 2015 through the end of 2021. The blue line represents the total number of project days at sea, with the bold gray indicating the mean quarterly ship days from 2015-2019.

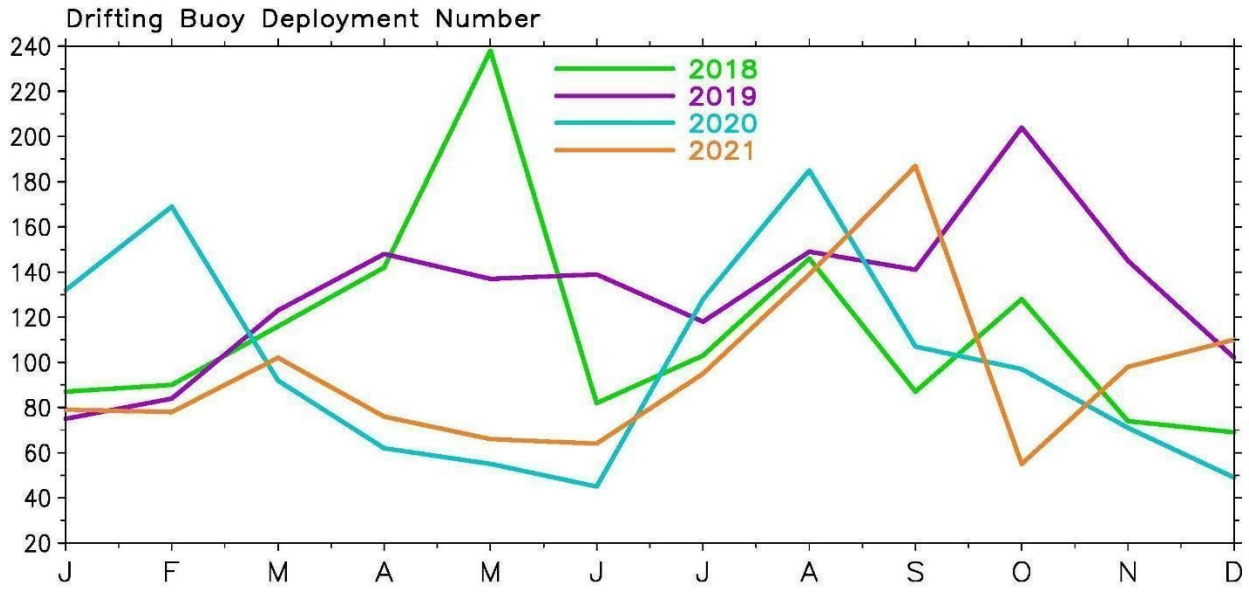

Figure 3.6. Worldwide monthly surface drifting buoy deployments for years 2018-2021 based on first instance of a buoy found in the International Comprehensive Oceanographic and Atmospheric Data Set (ICOADS R3.0.2; Liu *et al.* 2021)

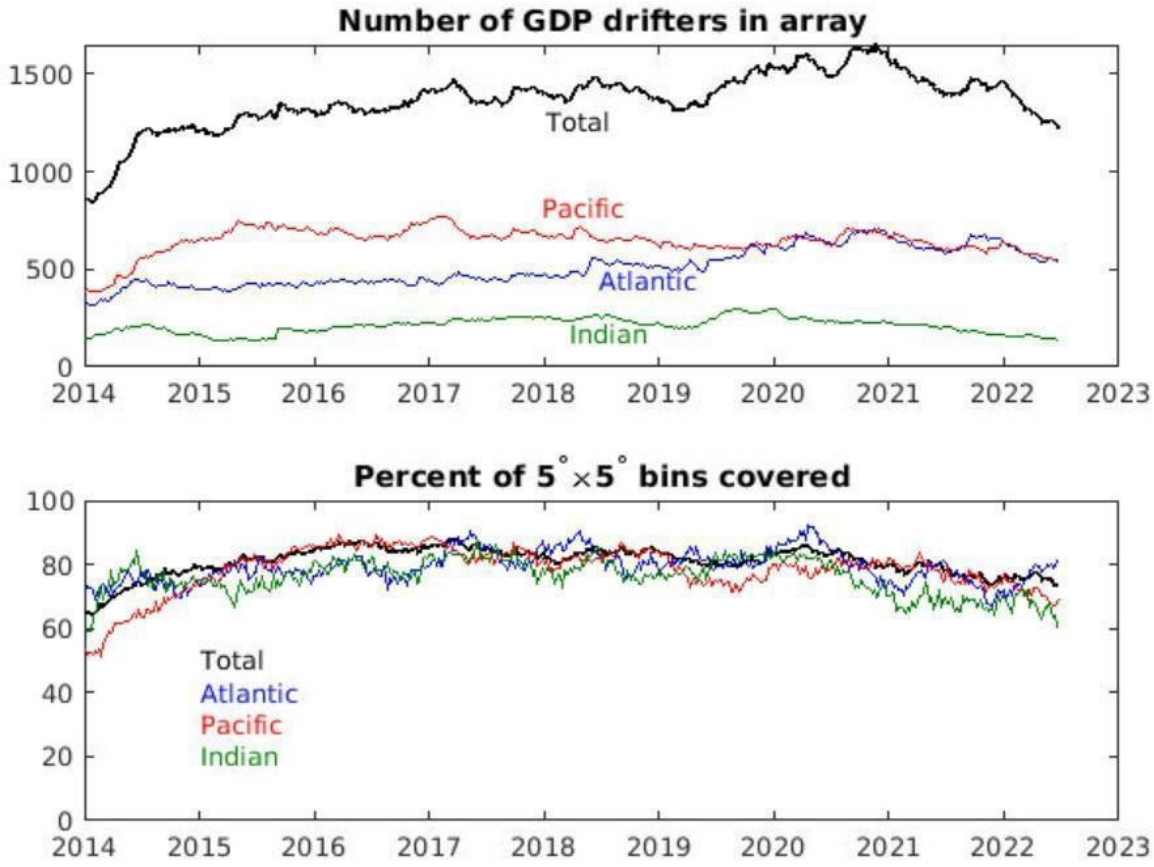

Figure 3.7. Total active number of surface drifters (top panel) and percentage of ocean spatial coverage in 5x5° lon/lat boxes (bottom panel) maintained by the Global Drifter Program (GDP; https://www.aoml.noaa.gov/phod/gdp/; Lumpkin *et al.*, 2016) based on GOOS criteria for SST and ocean surface current monitoring.

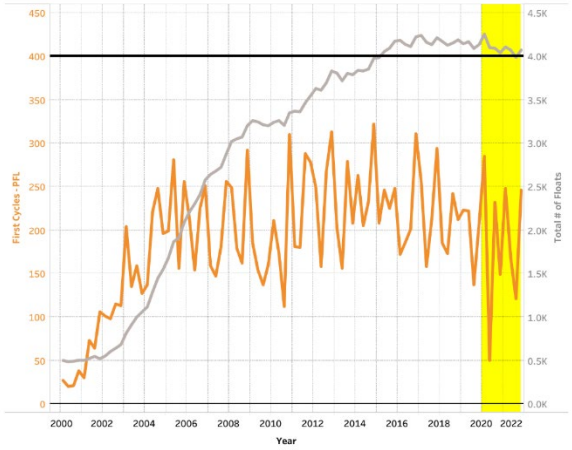

a)

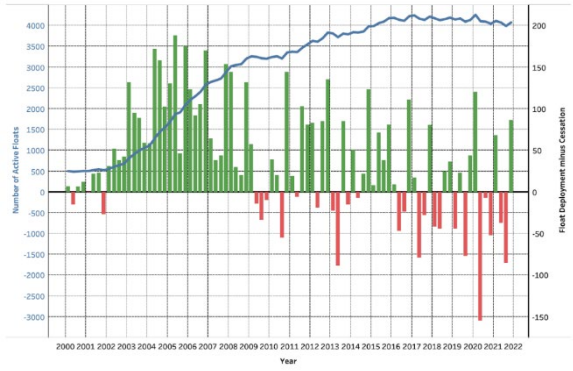

b)

Figure 3.8. a) Argo float first cycles, 2000-2021 (orange). A first cycle is the first transmitted pressure-temperature-salinity profile set, signifying a newly deployed and actively reporting float. Total reporting Argo floats 2000-2021 (gray). The time period January 1, 2020 – December 31, 2021 shaded yellow. The black line denotes the 4000 reporting floats level. b) Newly deployed minus stopped reporting floats by quarter. Green denotes quarters with more deployments than cessation, red denotes more float cessation than floats deployed.

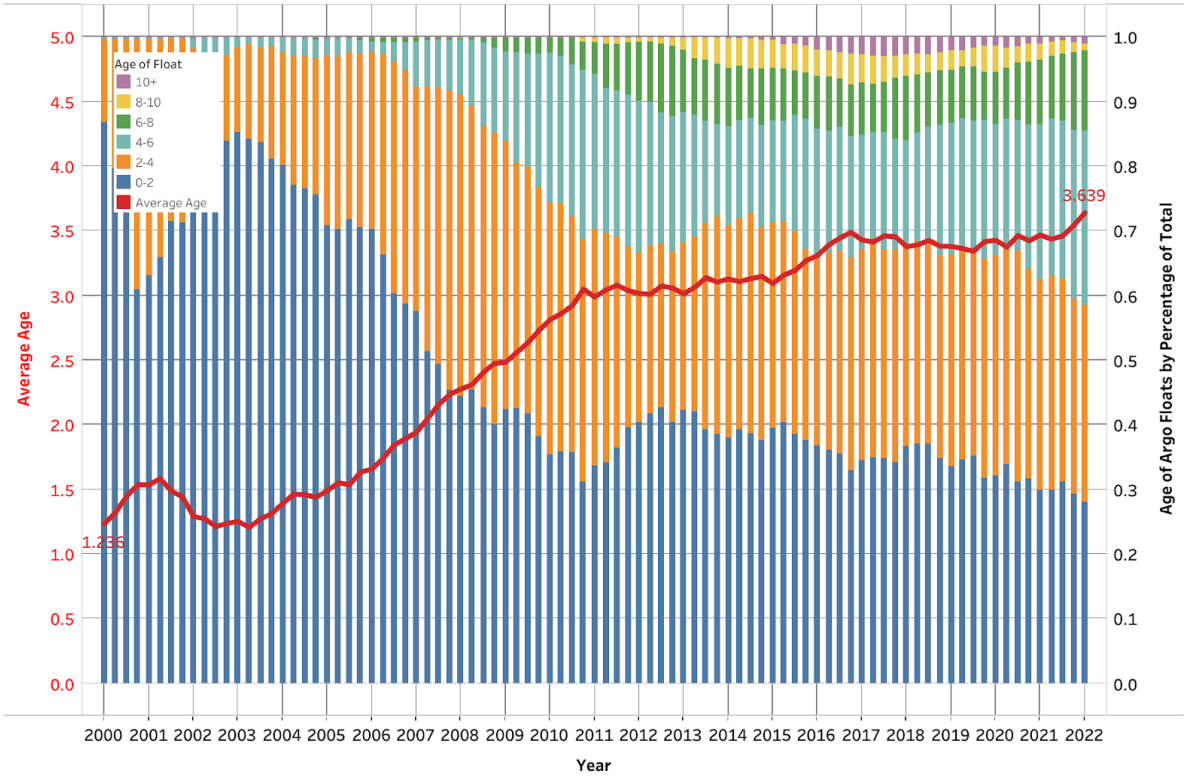

Figure 3.9. Average age of the Argo fleet (red line) and percent of floats in each age distribution (bars) 2000-2021.

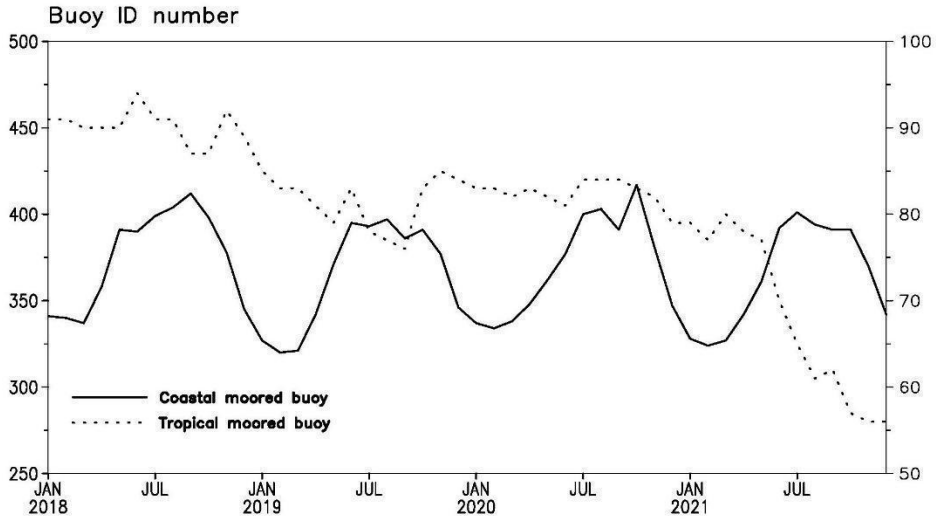

Figure 3.10. Number of moored buoys in the ICOADS R3.0.2 (Liu *et al.* 2021) near real-time collection: solid line and left y-axis are for the coastal buoys, and dashed and right y-axis are for the tropical buoys.

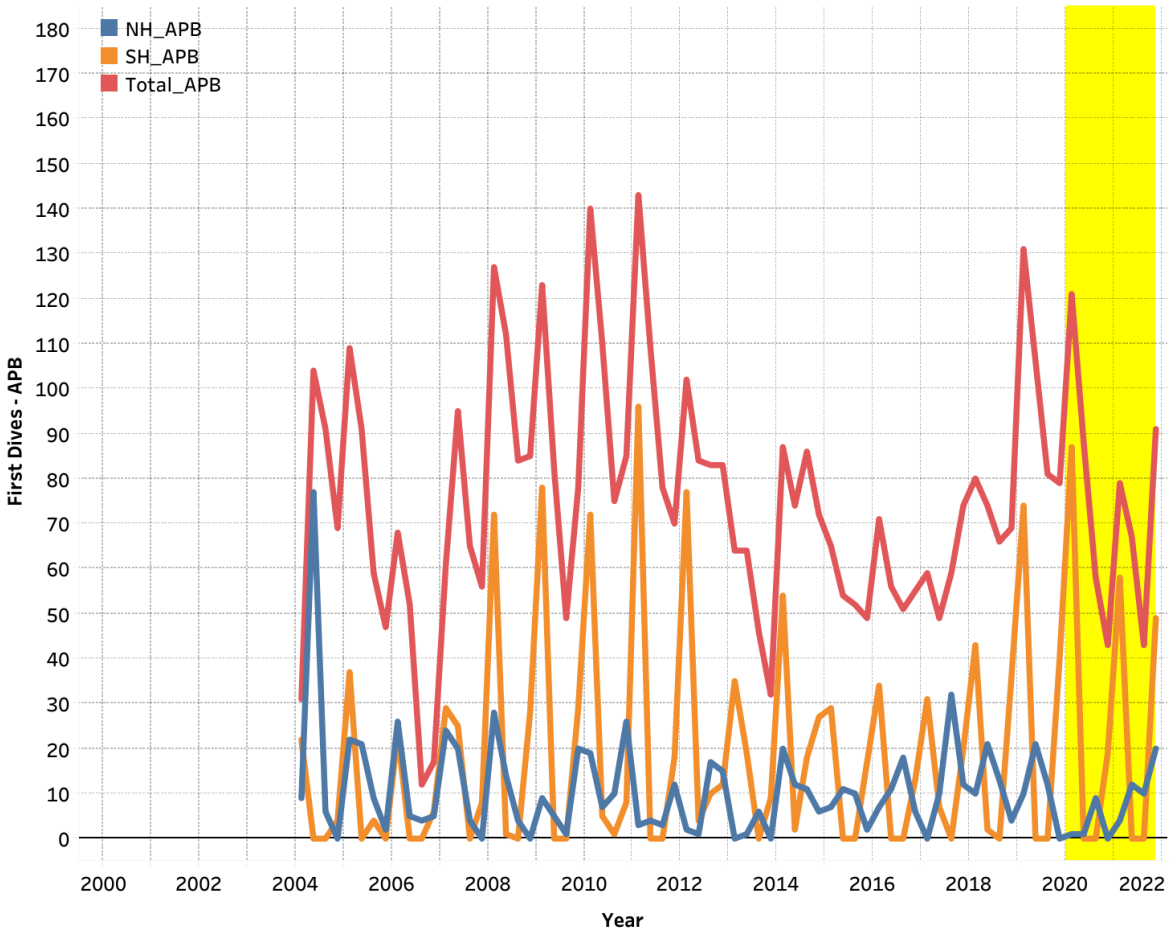

Figure 3.11. Individual instrumented pinnipeds by quarter 2004-2021 in the northern hemisphere (blue) and the southern hemisphere (orange). Total number of actively reporting instrumented pinnipeds by quarter (red). Yellow shading for January 1, 2020 – December 31, 2021.

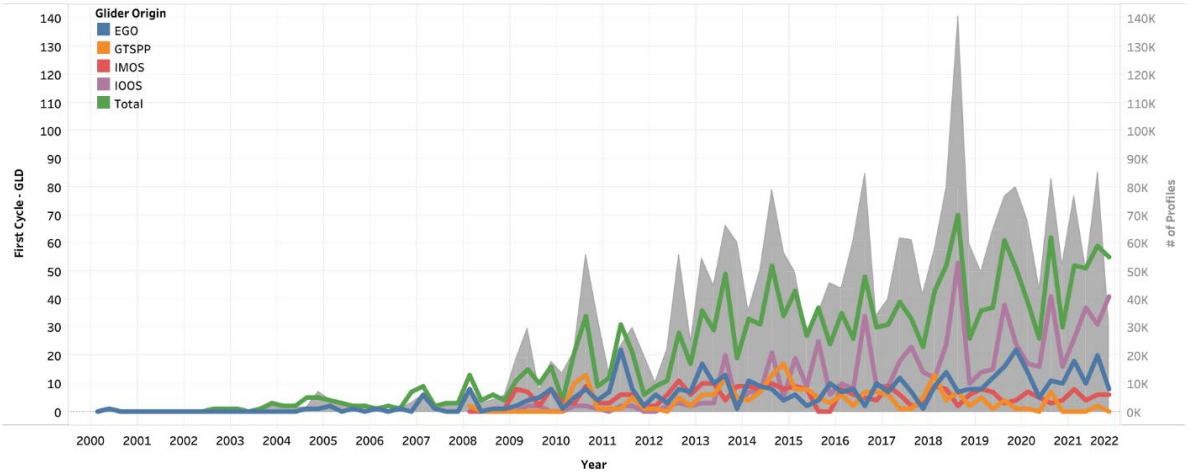

Figure 3.12. Glider missions 2000-2021 by season as reflected in the three main glider data assembly centers (Everyone's Gliding Observatories, EGO - blue; Australia's Integrated Marine Observing System, IMOS - red; NOAA Integrated Ocean Observing System Glider Data Assembly Center, IOOS, purple) and posted to the Global Telecommunications System (GTS) found in the Global Temperature and Salinity Profile Program (GTSPP, orange). Total number of glider missions in green, total glider cycles in gray shading.

a)

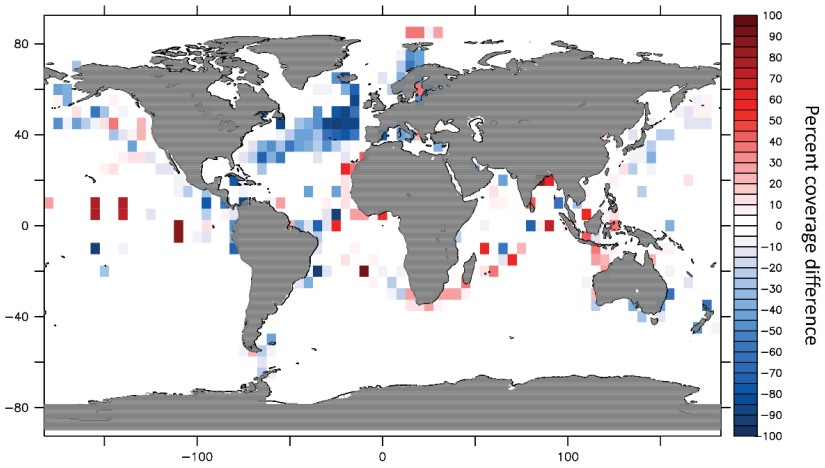

b)

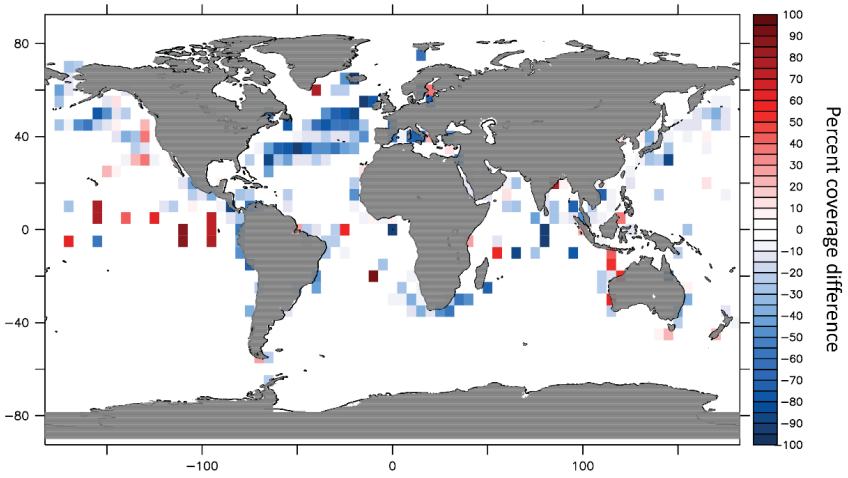

Figure 3.13. Difference in percentage of weeks, between a) April-June 2020 and April-June, 2019 where there were 25 or more weekly Air Temperature observations from the GTS in a 5x5° lon/lat grid. b) Difference between April-June 2021 and April-June 2019. Blue shading in grid boxes where there were fewer weeks with defined coverage in the later time period, red shading more weeks with defined coverage in the later time period.

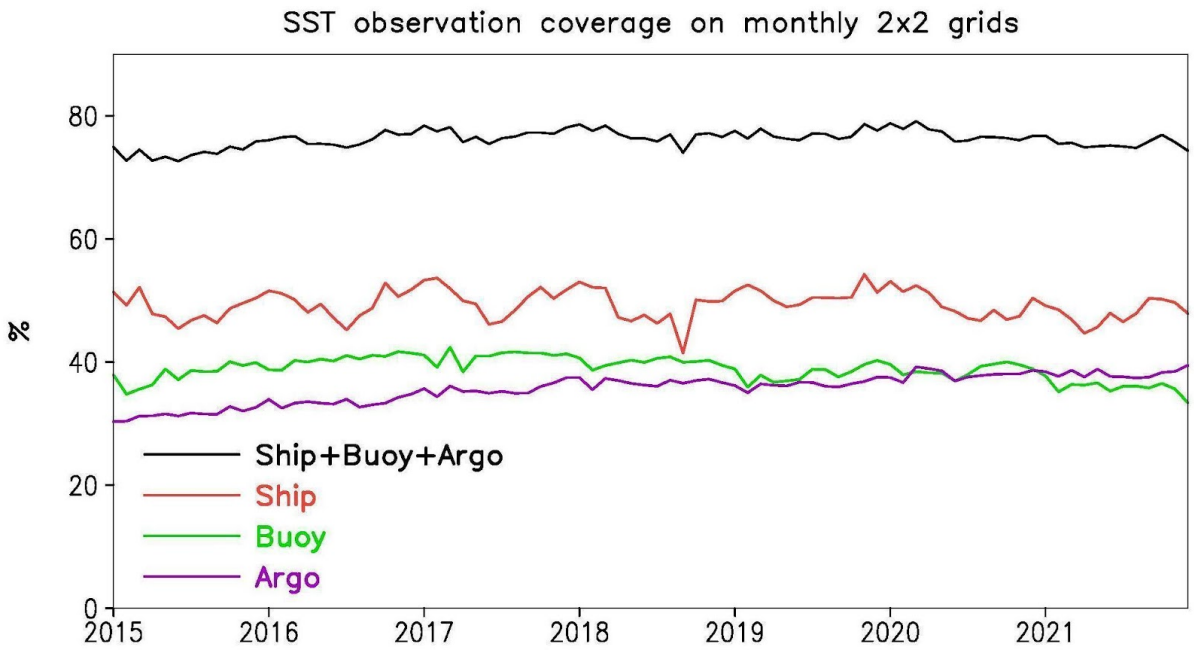

Figure 3.14. Percent global coverage of monthly sea surface temperature (SST) measurements January 2015 – December, 2021, calculated as the fraction of 2°x2° lon/lat grids with at least one SST report for the month.

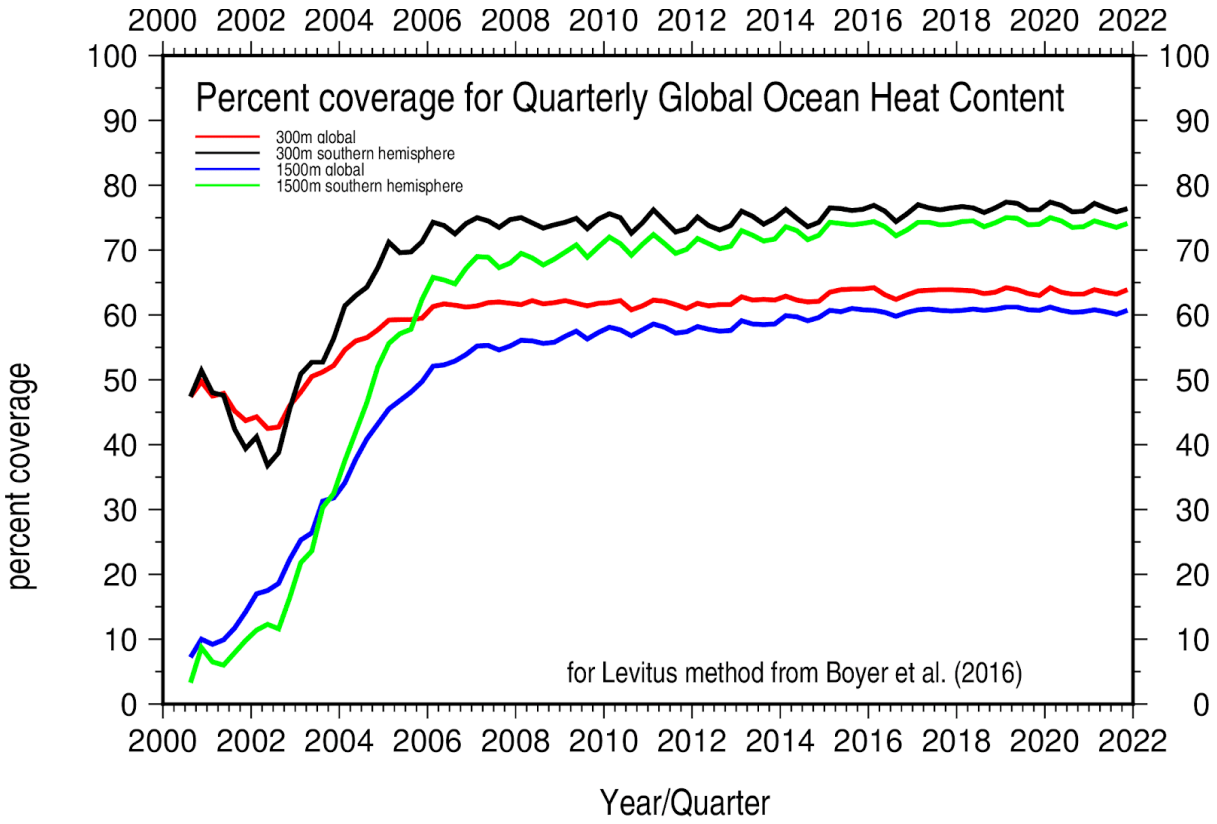

Figure 3.15. Percent coverage of subsurface temperature data at 300 m and 1500 m depth globally and for the southern hemisphere by season (3-month period) 2000-2021 for the calculation of ocean heat content calculated as fraction of 1°x1° lon/lat grid boxes with at least three temperature measurements within 400 km of the grid-box center.

Chapter 4. Sensitivity of Global Upper-Ocean Heat Content Estimates to Mapping Methods, XBT Bias Corrections, and Baseline Climatologies

This material appeared in: Boyer, T., C.M. Domingues, S.A. Good, G.C. Johnson, J.M. Lyman, M. Ishii, V. Gouretski, J.K. Willis, J. Antonov, S. Wijffels, J.A. Church, R. Cowley, and N.L. Bindoff (2016): Sensitivity of global upper-ocean heat content estimates to mapping methods, XBT bias corrections, and baseline climatologies. Journal of Climate, 29(13), 4817–4842, https://doi.org/10.1175/JCLI-D-15-0801.1.

4.1 Introduction

Ocean heat content (OHC) is an essential climate variable for understanding interannual, decadal and longer time scale changes in the climate system and Earth's energy budget. Earths energy budget is currently imbalanced (Wild *et al.* 2013 and references therein; Trenberth *et al.*, 2014), with an estimated +0.5 W m^{-2} to +1.0 Wm^{-2} net top-of-the-atmosphere energy flux over the first decade of the 21st century (Trenberth *et al.* 2014) . Oceans cover more than 70% of Earth's surface. Their extensive interface with the atmosphere, combined with their high heat capacity, low albedo, and great depth, has resulted in ocean sequestration of more than 90% of Earth's excess heat over recent years (Roemmich *et al.* 2015) and recent decades (Bindoff *et al.*, 2007, Rhein *et al.* 2013). This net buildup of excess heat in the ocean mitigates surface warming, but it increases ocean temperature, contributing to sea ice melt (Liu and Curry 2010; Polyakov *et al.* 2010), melting at the marine terminations of ice sheets (Straneo and Heimbach 2013; Rignot *et al.* 2013), changes in atmospheric and oceanic circulations (e.g., Hoerling *et al.* 2001; Toggweiler and Russell 2008), and sea level rise (Church *et al.* 2011). Since the 1970s, about one-third of the observed global mean sea level rise is explained by thermal expansion of the ocean's volume caused by increases in OHC (Church *et al.* 2013). Here we focus on changes to OHC anomaly (OHCA) because of its importance to the global energy balance of the Earth. While OHCA is expressed in joules, the rate of change of OCHA is often expressed in terms of W m^{-2} applied over the Earth's surface area (5.1×10^{14} m^2) for comparisons with and constraints on net Top of the Atmosphere (TOA) energy fluxes. OHCA can be calculated from *in situ* measurements by differencing ocean temperature profile data from a baseline climatology, multiplying this temperature anomaly by density and the specific heat of seawater, and volume integrating this

product. Several research groups routinely produce OHCA estimates from *in situ* data that are widely used for ocean and climate science, model evaluations, outreach activities, and in governmental reports. All of these estimates show that the global ocean has significantly warmed in the upper 700 m during the past decades; however, they can disagree in variability and warming rates (Rhein *et al.* 2013; Abraham *et al.* 2013), although some differences are not statistically significant. Differences arise because, in practice, there are many sources of uncertainty in OHCA estimation (Lyman *et al.* 2010, Palmer *et al.* 2010), and groups deal with them in different ways. Two relevant issues in OHCA estimation are associated with the evolving nature of the technology used to gather subsurface ocean temperature profiles (*e.g.*, mix of instrumental accuracies and biases as well as quality control procedures) and the uneven distribution of the observational coverage in time, depth and geographically (Abraham *et al.* 2013; Gould *et al.* 2013).

Before the Argo program (Roemmich *et al.* 2009) array of autonomous profiling floats, which began implementation around 2000, became near-global most ocean temperature profile data were obtained from instrumentation dropped over the side of a ship (Johnson and Wijffels 2011; Abraham *et al.* 2013). This practice limited ocean temperature profile measurements in hard-to-reach areas away from major shipping routes and during seasons of inclement weather, resulting in an uneven distribution of temperature profiles in time and space. To estimate global integrals of OHCA, algorithms must be developed to put temperature anomaly/OHCA information on a regular grid, cope with data sparse regions, and smooth out temporal and spatial variability. These algorithms will hereafter be referred to as 'mapping methods'. Prior to the middle of the 20th century, ocean temperature profile data are too sparse to calculate OHCA with any mapping method without very large uncertainties (Gouretski *et al.* 2012). From the middle of the 20th

century to present, mapping method is still a source of uncertainty in OHCA estimates from *in situ* data (Gregory *et al.* 2004; AchutaRao *et al.* 2006). Lyman *et al.* (2010) compared global OHCA estimates in the upper 700 m for 1993–2008 to quantify sources of uncertainty in OHCA calculations, including combined quality control and expendable bathythermograph (XBT) measurement bias corrections, climatological reference, observational sampling and mapping method. Their calculations were all relative to comparisons using the same representative mean (PMEL_R) mapping method from Lyman and Johnson (2008), except in the mapping method case. Uncertainty due to mapping method was quantified by matching pairs of OHCA estimates that had the same XBT corrections between those originally published by individual research groups and those mapped by using the PMEL_R routine, although original estimates included differences other than just mapping method (e.g., baseline climatology and non-XBT data). Lyman *et al.* (2010) concluded that the largest source of uncertainty was found to be the combination of quality control and XBT bias corrections. Observational sampling uncertainties include horizontal and vertical variations in sampling (Lyman and Johnson, 2008), changes in vertical sampling resolution (spacing between adjacent measurements, Cheng and Zhu, 2014a), and changes in the ocean observing system (Cheng and Zhu, 2014b).

Here we investigate the sensitivity of global OHCA estimates in the upper 700 m for 1970–2008 and 1993–2008 to mapping methods, XBT bias corrections, and baseline climatologies. Our sensitivity experiments extend the earlier work of Lyman *et al.* (2010) by directly quantifying uncertainty attributable to mapping method and separately quantifying uncertainty attributable to different baseline climatologies. Our analyses also cover a longer period, 1970– 2008, including years prior to 1993, when data were sparser and hence global estimates more susceptible to larger mapping uncertainties. However, we do not address the influence of quality control of *in situ*

temperature in detail. Monthly baseline climatological means are used in all instances to remove the seasonal cycle and minimize the impact on OHCA calculations. Not all extant mapping methods are examined here (e.g., Cheng and Zhu 2014b; Cheng *et al.* 2015a). Observational sampling changes and their effects on uncertainty are not addressed directly here, though they create differences arising from mapping methods and baseline climatologies. Below we briefly describe the mapping methods routinely used by the seven research groups involved in this study, their baseline climatologies, and provide an overview of the available set of XBT bias adjustments. Section 2 provides details on the sensitivity experiments performed in this study. Results are found in Section 3 and conclusions in Section 4.

4.1.1 Details of mapping methods

The mapping methods used in each of the estimates of OHCA analyzed here are described below:

4.1.1a Levitus (LEV) mapping

Levitus *et al.* (2000) compute OHCA for the upper 300 m and for the upper 3000 m for the years 1948–1998 using five-year (pentadal) running means as the compositing time period and monthly climatologies calculated from all available data from the World Ocean Atlas 2001 (WOA01; Stephens *et al.* 2002; years 1772–1998) as the long-term mean. This work shows an increase in OHCA over the years under study and provides an estimate of OHC changes for the second half of the 20th century. The procedure outlined in Levitus *et al.* (2000) has been modified since then, deepening the shallower depth layer from 300 m to 700 m and shortening the compositing time period to one year (Levitus *et al.* 2005). Two subsequent updates on this work were published (Levitus *et al.* 2009; 2012) which use a baseline monthly climatology calculated using data only for the years 1955–2006. Pentadal, yearly, and seasonal OHCA are calculated based on the

method outlined in these works and posted every three months at http://www.nodc.noaa.gov/OC5/3M_HEAT_CONTENT/. Currently, this time series covers the years 1955–2015. The method used by Levitus *et al.* (hereafter LEV) is an objective analysis technique developed by Cressman (1959) for meteorological data, modified by Barnes (1964). The technique calculates a correction factor at each grid point based on the weighted difference between a first-guess value and a mean value for each grid point within a radius of influence. The first-guess field is zero (°C for temperature anomalies, joules for OHCA, etc.). The mean value is the difference between an *in situ* value and the baseline monthly climatology averaged over all such differences within a one-degree latitude by longitude grid box. The grid point is the center of the one-degree box. Weights are calculated based on distance from the grid point within the radius of influence (Barnes, 1964). The correction factor is applied to the first-guess field at each grid point, a 5-point smoother (Schuman, 1957) applied, and the procedure is repeated twice more, with progressively smaller radii of influence preserve smaller scale signal when possible. The three radii of influence are 880 km, 660 km, and 440 km, approximately 8, 6, and 4 degrees of latitude and longitude at the Equator. Full details, including a complete description of the weight function, can be found in Locarnini *et al.* (2010).

4.1.1b Ishii (ISH) mapping

Ishii *et al.* (2006) calculates global OHCA for the upper 700 m using subsurface temperatures computed with an analysis based on a variational minimization scheme (Derber and Rosati 1989) with spatio-temporal covariance of background error. Mixed-layer temperatures are constrained by sea-surface temperature (SST; Ishii *et al.* 2005). The analysis scheme is detailed in Ishii *et al.* (2003). The Tikhonov term in Ishii *et al.* (2003) is replaced by background error decorrelation as a function of both horizontal and vertical distances for later OHCA calculations (Ishii *et al.* 2006;

Ishii and Kimoto 2009). Spatial decorrelation scales vary with depth. The surface horizontal decorrelation scale is given as a cosine function of latitude, with 900 km at the equator and a minimum of 300 km. At the surface the vertical decorrelation scale is 10 m and temporal decorrelation scale is 15 days. Monthly differences from a baseline climatological monthly mean were calculated in the analysis scheme, binning all data within 120 days of the 15th day of each month.

4.1.1c Willis (WIL) mapping

Willis *et al.* (2004) calculates OHCA for the years 1993–2003 for the upper 750 m of the global ocean using altimeter data to compensate for sparse *in situ* temperature profile data. As outlined in Willis *et al.* (2003, hereafter WIL) a two-term covariance with large (920 km) and small (100 km) scales is used to map the *in situ* data to all grid points. The covariance function is chosen based on global wave number – frequency spectrum for altimetric sea-surface height (Zang and Wunsch 2001). The seasonal cycle is removed by subtracting out baseline climatological means. Altimeter fields of sea-surface height (AVISO, Ducet *et al.* 2000) are then used to modify the objectively mapped *in situ* values using the following :

$$<\text{INSIT}>\text{difference estimate} = <\text{INSIT} - (\alpha\text{AH})> + <\alpha\text{AH}> \qquad (4.1)$$

Where INSIT is the *in situ* field, AH is the altimeter sea-surface height field and α is a time-averaged regression coefficient for AH onto INSIT. The brackets (<>) denote objective mapping as described above. So, equation (4.1) results in an objective mapping of a quantity (INSIT) using altimetric sea-surface height, represented in terms of INSIT as a first-guess. In the case of OHCA, INSIT is derived from a mean difference between observed and baseline mean monthly temperature.

4.1.1d Pacific Marine Environmental Laboratory (PMEL) mapping

PMEL mapping methods are derived from the objective mapping methods of Willis *et al.* (2004, WIL described above). As with all other methods, seasonal cycle is removed by subtracting out baseline climatological monthly means. Instead of using sea surface height anomalies from satellite altimeter data to compensate for sparse *in situ* ocean temperature profile data as in WIL, the PMEL method calculates a representative mean, which effectively assumes that unsampled regions have the same anomalies as the mean anomaly of the sampled regions (Lyman and Johnson 2008). This method is used to compensate for areas where the distance between measurements is large compared with mapping correlation length scales or the amount of data are insufficient to overcome the noise-to-signal ratios (Lyman and Johnson, 2008). The initial global estimate in the PMEL method is the mean of the maps, (hereafter PMEL_M, called SI in Lyman and Johnson 2008). In the mean of the maps, the objective map relaxes back toward the initial guess of zero anomalies in data-sparse regions. The second step in the mapping is the calculation of the global representative mean (hereafter PMEL_R), wherein data sparse areas are effectively given a value equal to the mean value for all well- represented areas (Lyman and Johnson, 2008). While the PMEL_M product should be viewed as an intermediate step to the final global integral of PMEL_R, both are retained here so that PMEL_M can be compared against other objectively mapped products.

4.1.1e Met Office Hadley Centre EN dataset (EN) mapping

The Met Office Hadley Centre produces monthly objectively analyzed temperature fields using a modified version of the method outlined in quality control procedures for the Enhanced Ocean Data Assimilation and Climate Prediction (ENACT) and ENSEMBLES projects (Ingelby and

Huddleston 2007). The mapping method is a modified successive correction scheme which approximates Optimal Interpolation (Lorenc *et al.* 1991; Bell *et al.* 2000). The background for the analysis for each month is the combination of climatology and a damped persistence of anomalies from the previous month's analysis:

$$B_{i+1} = C_{i+1} + \alpha(A_i - C_i) \quad (4.2)$$

Where C_i is the climatological mean for month i, A_i is the analyzed value for the given month/year, α is a factor, here set to 0.9 (based on experimental best fit), and B_{i+1} is the background for the following month. This creates a first-guess field that has damped persistence from the previous month/year, relaxing to climatology where there are no data. The combination of the background and the observations is governed by estimates of observation error variance and background error covariance. The covariance is parameterized using two second-order auto-regressive (SOAR) functions with horizontal scales of 300 km and 400 km. The former is extended near the Equator to 1500 km. The analysis scheme used in this study corresponds to that used to produce the 'EN3 version 2a' dataset (http://www.metoffice.gov.uk/hadobs/en3).

4.1.1f Domingues (DOM) mapping

The CSIRO-ACECRC-IMAS research group produces global OHCA estimates for the upper 700 m of the ocean by summing two depth-integrated layers, 0–300 m and 300–700 m (Domingues *et al.* 2008; Church *et al.* 2011). *In situ* temperature observations from Argo floats, bottles, CTDs and XBT-corrected data (Wijffels *et al.* 2008) are first converted into thermosteric sea level. Anomalies are obtained using a historical climatology that includes annual, semi-annual, and linear trend terms (Alory *et al.* 2007; Wijffels *et al.* 2008). Thermosteric sea level anomaly profiles are depth-integrated for the layers mentioned above. If more than one profile exists in the

same 1° x 1° grid box, within 65°N-65°S, their median is used. These one-degree estimates are then projected onto the first 30 EOFs, derived from the satellite record altimeter (since 1993), to reconstruct spatially complete fields, at monthly timescales, from 1950s onwards. The reconstruction method is based on a reduced-space optimal interpolation (Kaplan *et al.* 2000), which formalism provides estimates of errors on the basis of the *in situ* data distribution and uncertainties (instrumental and geophysical errors) as well as ocean eddy variability based on satellite altimeter data. Finally, thermosteric sea level anomaly fields are converted into OHCA using coefficients obtained from a spatially variable linear regression between OHCA and thermosteric sea level anomalies on a 10° x 10° grid, for each of the two depth layers (similarly to Willis *et al.* 2004). To reduce unwanted noise, monthly estimates are yearly-averaged and then a 3-year running mean is applied. The version history of these reconstructed global OHCA and thermosteric sea level anomalies, including the latest available estimates are found at: http://www.cmar.csiro.au/sealevel/thermal_expansion_ocean_heat_timeseries.html.

4.1.1g Gouretski (GOU) mapping

Gouretski *et al.* (2012, hereafter GOU) calculate OHCA from median temperature anomalies for a depth layer over 5° gridboxes. The depth layers are 0–20 and 0–400-m. Temperature profiles are first interpolated to 1-m increments. The 0–400-m vertical temperature average is obtained using correlations between the mean temperature of the entire layer to mean temperatures in shallower levels. The correlations are calculated based on high-resolution CTD temperature profiles. The mean layer temperature anomaly is then differenced from a baseline monthly mean. Baseline monthly mean layer temperatures are calculated on a 0.25° grid from temperature profiles measured during 2001–2010. The baseline mean is calculated using a weighting function

$$W=(R^2-r^2)/(R^2+r^2), \qquad (4.3)$$

where R is the radius of influence, set to 111 km, and r is the distance from observation to each gridpoint. The global average layer temperature anomaly is then the sum of all 5° median layer temperature anomalies divided by the number of 5° gridboxes containing data. This is converted to OHCA over the entire ocean surface area, thus assuming a mean global layer anomaly for all 5° ocean gridboxes without data. This assumption is similar to that used in PMEL_R and Palmer *et al.* (2007).

4.1.2 XBT bias adjustments

Temperature profiles collected by XBTs make up a large part of the available subsurface temperature data from 1970 to 2003. Without these data, calculations of OHCA for *in situ* profiles would be very difficult for these decades. Even now, when the Argo program is the dominant observing system, XBTs make up on the order of 10% of available subsurface temperature profiles each year. The depths of temperature measurements from XBTs are estimated from elapsed time since launch using a fall rate equation. It was known early on that there were systematic errors in the XBT data (Flierl and Robinson 1977). Hanawa *et al.* (1995) introduced a correction for the most commonly used XBTs (Sippican and TSK T4, T6, and T7 models) based on a time-invariant fall-rate equation to mitigate the biases. However, Gouretski and Koltermann (2007) showed that XBT biases vary with year, and thus corrections need to be time-dependent. Since then, a number of XBT corrections have been proposed for depth (Wijffels *et al.* 2008, hereafter W08 for their Table 4.1 corrections; Ishii and Kimoto 2009, hereafter I09 when referring to XBT corrections; Good 2011, hereafter G11), for temperature (Levitus *et al.* 2009, hereafter L09 when referring to XBT corrections), and for both depth and temperature (Gouretski and Reseghetti 2010, hereafter GR10; Hamon *et al.* 2012; Gouretski 2012, hereafter

GO12; Cowley *et al.* 2013, hereafter C13 when referring to the Thermal Gradient XBT correction). Of the different calculations of OHCA, LEV uses L09, ISH, PMEL_M and PMEL_R use I09, WIL uses Wijffels *et al.* (2008) (their Table 4.2), DOM uses W08, GOU and EN use GR10. The XBT bias, when modeled as a fall-rate correction only, tends to report water parcels as being deeper than their true depths. Since water temperature generally decreases with depth, the deeper displacement increases the reported temperature at the deeper depth, thereby increasing the OHCA relative to an unbiased measurement. Splitting the XBT types into shallow (< 550 m) and deep (> 550 m) as per W08, the depth-bias is approximately 10 m at 400 m depth for the shallow probes, and 10 m at 700 m depth for the deeper probes averaged over all years, but with significant year-to-year variations. Viewing the XBT bias as pure (but depth-dependent) temperature offset (L09), results in a temperature correction that is on the order of +0.1°C averaged over the 0–700-m depth range. C13 estimate a mean temperature bias of +0.05°C with a widely varying depth bias by probe and year, but generally smaller than the depth-only corrections of W08. All XBT bias correction methods are time (year-to-year) varying in depth and/or temperature correction. Differences among methods have implications for OHCA calculations. Cheng *et al.* (2015b) report on recommendations by the XBT community that XBT corrections account for five factors (depth bias, pure temperature bias, temperature induced depth bias, temperature induced temperature bias, and depth offset). Only one correction scheme (Cheng *et al.*, 2014) directly accounts for all five of these factors explicitly. Work is still in progress to quantify which XBT bias correction method works best. For experimental simplicity and clarity of results, rather than using all extant XBT correction methods, XBT correction methods were selected from the categories of depth correction, temperature correction, and depth plus temperature correction. The importance of initial velocity variations of the XBT probe due

to drop height has recently been documented using a numerical method (Abraham *et al.*, 2012) and empirically from water tank experiments (Bringas and Goni, 2015). C13 (and Cheng *et al.* 2014) account for this effect in the depth offset corrections. As previously indicated, Lyman *et al.* (2010) show that the differences due to XBT corrections and quality control combined are the largest source of uncertainty in OHCA calculations. In the present work, we quantify uncertainties owing to XBT corrections, but without the complicating influence of quality control. We make a comparison of OHCA using the different mapping methods and the same XBT corrections. We also compare OHCA using each mapping method with different XBT corrections to see how each mapping method is affected by the XBT correction used. Since there is no consensus yet on the best XBT correction scheme to implement , the W08 XBT corrections, as the longest in-use XBT correction for OHCA (Domingues *et al.* 2008) will be used for comparison of mapping methods with different baseline climatologies.

4.1.3 Baseline climatologies

Also, not part of the actual mapping method, but of vital importance to the OHCA calculation, is the baseline mean subtracted from observations to compute anomalies. Ishii and Kimoto (2009) find (see their Table 5) a 10% difference in the linear trend of OHCA (0.14 ZJ yr^{-1}; 1 ZJ is 1×10^{21} J) from 1951–2005 when using the World Ocean Atlas 2005 (Locarnini *et al.* 2006, hereafter WOA05) in place of the WOA01. The difference between WOA05 and WOA01 is in the input data, the World Ocean Database 2005 (Boyer *et al.* 2006, hereafter WOD05) and the World Ocean Database 2001 (Conkright *et al.* 2002, hereafter WOD01), respectively. WOD05 contains data from 7 additional years (1999–2005), additional historical data, and additional quality control. However, WOD05 and WOD01 are used as input data for temperature anomalies as well in the respective cases, so some of the difference in OHCA found by Ishii and Kimoto (2009)

may be due to these data differences. Lyman *et al.* (2010) compare OHCA using baseline climatologies calculated using data from year periods 1993–2003 and from 2005–2008 for their comparison and find negligible differences in OHCA curves due to baseline climatology after adjustment for the warmer ocean in the 2005–2008 period. Lyman and Johnson (2014) show a striking difference in OHCA for the PMEL_M mapping method when using a baseline climatology for 2005–2010 from Argo data compared to the same climatology adjusted to reflect estimates of mean ocean temperature differences in 1955 relative to 2005–2010. The difference in baseline does not affect their final product, the PMEL_R method (Lyman and Johnson 2014). The mapping methods described above all use baseline monthly mean temperature climatologies over different time periods. LEV currently uses monthly WOA09 as a baseline (Levitus *et al.* 2009). WOA09 monthly climatologies are the means of five decadal (or near- decadal) climatologies (1955–64, 1965–74, 1975–84, 1985–94, 1995–2006), thus producing a mean climatology 1955–2006 that is not skewed toward any one decade. The most recent PMEL maps (Johnson *et al.* 2015a) use a monthly baseline climatology 2004–2013 derived from Argo data only. OHCA are then adjusted to reflect differences from the period 1993–2013. The most current ISH (Ishii and Kimoto 2009) uses a baseline climatology encompassing years 1961–2000. DOM uses a climatology that has the long-term linear trend of temperature change removed (Alory *et al.* 2007). EN uses a time-varying baseline mean that incorporates persistence of temperature change from previous years, as described above. All of the above use climatological monthly mean temperatures at discrete depths on a one-degree grid. GOU uses climatological monthly mean vertically averaged temperature on a ¼-degree grid. Similar to Ishii and Kimoto (2009) and Lyman *et al.* (2010), OHCA in this study is calculated relative to

different baseline climatologies. These calculations are used to assess the impact of baseline climatology on each of the mapping methods.

4.2. Methods

To perform the intercomparison experiments for this study, a uniform set of input data is generated. To prepare the data for mapping, the method outlined in Domingues *et al.* (2008, supplementary material) is followed. For 1970–2004 the EN 3 version 2a database (EN3v2a; Ingleby and Huddleston 2007) of *in situ* temperature profiles is used for all bottle, CTD, and XBT data. For 2000–2008, the real-time and delayed mode temperature profiles from Argo profiling floats as in Barker *et al.* (2011) are used. Only temperature profile data from the above mentioned instrument classes are used. Data from moored buoys, drifting buoys, towed CTDs, and MBTs are not used following the data choice of Domingues *et al.* (2008). Inclusion/exclusion of specific ocean profile data types will have an effect on OHCA uncertainty. It should be noted that the Argo array still had geographic gaps in its target coverage until 2006/7 and was not designed initially to cover continental shelves, marginal seas, or areas where ice is present (Roemmich *et al.* 2015). Of the years in this study with only Argo data (2005–2008), year 2005 should not be considered to have full Argo coverage. After removal of gross outliers using a simple check (Domingues *et al.* 2008), quality flags set in the EN3v2a quality control procedures (Ingleby and Huddleston 2007) are used almost exclusively for bottle, CTD, and XBT data. If a profile had a measurement with a quality flag other than good, the entire profile was excluded from use. Additionally, profiles are not used if they have coarse vertical resolution (as per Willis *et al.* 2004), or if they terminate at depths shallower than 100 m. For each temperature profile OHCA is calculated relative to a baseline climatology for 0–300 m and for 300–700 m. The 0 700-m OHCA is the sum of the OHCA for each of the two layers. Splitting of the ocean into two

layers follows Domingues *et al.* (2008) and allows for the inclusion of profile data which do not reach to the full 700-m study depth. Vertical sampling depth contributes to OHCA uncertainties. Each of the mapping methods is applied to this same input OHCA data set to calculate a one-degree latitude/longitude bin gridded field of OHCA between 65°S and 65°N for each year 1970–2008(five-degree gridded bins in GOU method, years 1993–2008 only for WIL method) . The years are chosen to start with the advent of the XBT, which provided increased global data coverage for 0–300 m for 1970 onward compared to previous years (Church *et al.* 2011; Gleckler *et al.* 2012; Abraham *et al.* 2013; Lyman and Johnson 2014). Since the only difference between the gridded fields produced is the mapping method, the effect of different mapping methods on OHCA calculations can be readily examined. Furthermore, by using the same input dataset as described above, with different sets of XBT corrections and base climatologies, an examination of the relative effect of these factors on the different mapping methods can be evaluated. The different test cases using the same input data (EN3v2a + Barker Argo) are as follows, using as naming convention CY_T_XXX for each case. The CY_T portion of the name refers to the baseline climatology used, whereas the XXX portion refers to the XBT bias correction (see Table 4.1 for a complete listing).

Uncertainty is represented by the yearly standard deviation among grouped cases. There are seven mapping methods (eight for 1993–2008), six XBT correction schemes, and three baseline climatologies representing the different cases studies here, so the standard deviation is based on relatively few separate cases, especially the for baseline means. Furthermore, as discussed in Lyman *et al.* (2010), the different cases are not completely independent, since they use the same input data set. To better quantify confidence in the standard deviation as uncertainty, Effective Degrees of Freedom (EDOF) are given for each case. The value of the EDOF is always smaller

than the simple degrees of freedom for standard deviation since it accounts for the interdependence of the data sets (Lyman *et al.*, 2010, based on Bretherton *et al.*, 1999).

4.2.1. Baseline climatologies

Three monthly mean temperature climatologies – two historical (C1_H and C2_H) and one modern (C3_M) – were used to calculate OHCA (without seasonal variability) for each temperature profile from the input dataset versions for the sensitivity tests (Table 4.1). The historical climatologies (C1_H and C2_H) were originally mapped by Alory *et al.* (2007) and are based on historical observations from the EN3v1d database (Ingleby and Huddleston 2007) – the previous version to EN3v2a – merged with recent Argo data (Barker *et al.* 2011). Cheng and Zhu (2015) show that historical climatologies can have inconsistencies in the mean year for different regions of the ocean based on sampling patterns (e.g., good coverage most years in the Northern Hemisphere, good coverage in the Southern Hemisphere only during the Argo era). If mean year is different for different regions, OHCA calculations will be inconsistent among the regions. As part of the Alory *et al.* (2007) mapping technique, a long-term linear trend was removed at each grid point to reduce the impact this sampling biases from the observing system, ameliorating the inconsistent mean year problem. At the same time, inclusion of Argo data helped to reduce aliasing of seasonal signals into historical changes, particularly in high-latitude areas of the southern hemisphere (not shown), which are historically poorly sampled in winter. C1_H contains temperature data from bottles, CTDs and Argo floats, whereas C2_H also includes bias-corrected XBT from Wijffels *et al.* (2008, their Table 1). By including XBT data, C2_H has a greater number of profiles, and thus a better sampling coverage than C1_H. On the other hand, C2_H is burdened with uncertainties due to XBT bias corrections. The modern monthly mean temperature climatology (C3_M), originally mapped by Locarnini *et al.* (2013), is dominated by

Argo data for 2005-2012 but also includes data from bias-corrected XBTs (Levitus *et al.* 2009), moored buoys, drifting buoys, gliders, and undulating CTDs from the WOA13 (Locarnini *et al.* 2013). Although its 8-year period is relatively short, C3_M presents a more temporally uniform temperature field, which is not biased to different epochs depending on location, as for many historical climatologies, C3_M also represents a warmer ocean than both C1_H and C2_H. (C3_M global OHC is 157 ZJ higher than C1_H, 141 ZJ higher than C2_H). The latter two are representative of longer baseline periods with cooler means.

4.2.2. XBT bias corrections

The XBT corrections examined are as follows: XXX=None, W08, L09, I09, G11, GO12, C13. Each case is described above in section 1.2. There are more available XBT corrections, but those used here represent a cross-section of approaches – temperature corrections only (L09), depth corrections only (W08, I09, G11), and depth and temperature corrections (GO12, C13). 'None' is the case where no XBT correction (other than Hanawa *et al.* (1995) where necessary) is applied. Since it is clear that there are XBT biases which necessitate correction (Gouretski and Koltermann 2007), results from the None case are presented for perspective but are not included in any calculations of uncertainties.

4.3. Results

The global OHCA time series created as part of the sensitivity experiments (Table 4.1) are organized into three groups to assess the spread introduced:

(i) by mapping methods for each XBT correction (Section 3.1);

(ii) by XBT corrections for each mapping method (Section 3.2); and

(iii) by baseline climatologies for each mapping method (Section 3.3).

In the figures, the same historical climatology (C1_H) underpins the results shown for (i) and (ii) and the same XBT correction (W08) for (iii).

4.3.1 Effect of mapping methods

The globally integrated OHCA estimates using eight different mapping methods using six different XBT corrections and the no XBT correction case, relative to the C1_H climatology (Figures 4.1a-f) exhibit apparent differences for all years over the 1970–2008 period. Since we use the same climatology for all estimates, no shifting to a common mean is required for purposes of comparison here. The uncertainty of OHCA due to XBT corrections is discussed below. Those features that are common to Figures 4.1a-e (but not necessarily the no XBT correction case) are evaluated as differences attributable to mapping method. In the Argo data only years (2005–2008) ISH mapping produces the lowest globally integrated OHCA, WIL, DOM, PMEL_R, and GOU produce the highest OHCA values, while LEV, PMEL_M and EN are similarly clustered in the middle (Figure 4.1). Some mapping method/XBT correction combinations have peak OHCA in 2004 with a minimum in 2007 before increasing in 2008. 2004 was the last year for this experiment in which XBT data were used, pointing to possible OHCA calculation uncertainty due to choice of input ocean profile data. For earlier years, with more XBT data, ISH, PMEL_M, and EN are usually very similar, within about 20 ZJ of each other. LEV, DOM, PMEL_R, and GOU generally track along with the other three OHCA mappings, but with some larger year-to-year spikes (e.g., the increase of 79 ZJ from 1976 to 1977 followed by a decrease of 32 ZJ in 1978 in the LEV W08 case), most often of higher OHCA than ISH, PMEL_M, and EN. DOM yearly estimates contain large spikes, which are usually reduced with a 3-year running mean average (e.g., Domingues *et al.* 2008; Church *et al.* 2011). This

smoothing, however, is not applied here the better to allow intercomparisons. These spikes are not entirely physical, but due to the specific mapping method. The range of OHCA estimates from the eight mapping methods is given in terms of standard deviations (Figure 4.2). Calculated EDOF associated with the standard deviations of mapping methods are approximately 4 for years 1970–2008, and 3 for years 1993–2008 (Table 4.2). The differences among standard deviations for each XBT correction case are discussed below, focusing on mapping method differences. For the six XBT corrections the standard deviation for the different mapping methods is 16.5 ZJ over the 39-year period, with local minimum of 10.0 ZJ in 1976 and 1985 and local maximum above 30.0 ZJ in 1997 and 2001. Mean standard deviations among estimates using different mapping methods over 1970–2008 for different XBT corrections range from 14.0 ZJ for W08 to 17.9 ZJ for C13. Over 1993–2008, the range of OHCA mapping method standard deviations for different XBT corrections is larger (12.5 ZJ for W08 to 20.0 ZJ for L09), and the average is 17.1. The average standard deviations, 16.5 for 1970–2008, and 17.1 for 1993–2008, are used as the overall estimates of the uncertainty due to mapping method. This uncertainty is a measure of the spread of OHCA values among the mapping methods within a year. It is not exactly comparable to the 9.0 ZJ standard error of the mean estimated by Lyman *et al.* (2010) for the 1993–2008 time period. In Lyman *et al.* (2010) uncertainties were given as standard errors, but we present them here as standard deviations to facilitate comparisons among the different mapping methods, which produce time-series with different decorrelation time scales. The discrepancies among OHCA estimates from different mapping methods diminish and converge toward the end of the time series (Figure 4.1), when global coverage improves during the Argo period, as discussed below. The standard deviations of the OHCA values from the mid to late 2000s are below the average over the entire period analyzed (Figure 4.2), but similar to values found in early 1990s.

Even with the increased global coverage of the Argo array, there are still differences due to mapping method, both for areas still without data coverage and for areas with sufficient data coverage.

Insight into the differences in OHCA estimates from the various mapping methods can be gained by exploring the yearly variations of fractional coverage for ocean temperature data for each mapping method (Figure 4.3). Fractional coverage, the fraction of total ocean area with sufficient information to estimate OHCA (Lyman and Johnson 2008), is specific to each mapping method. Alternatively, this quantity can be thought of as what fraction of a globally uniform signal is recovered by each mapping routine given the spatial and temporal data distribution. In general, fractional coverage is relatively high during the 1990s when the World Ocean Circulation Experiment (WOCE) collected substantial numbers of ocean temperature profiles around the world, and even higher during the last few years of the record, when the global Argo array of profiling CTD floats builds to its initial target strength. The GOU mapping generally has the smallest fractional coverage because it requires data within a 5º grid box to assume coverage is sufficient, but after the final step its fractional coverage becomes one in every year. PMEL_M and ISH methods are similar, probably because they both use objective mapping methods that incorporate similar correlation length scales, and additionally give less weight to anomalies in regions where there are few data points. The EN method, while using spatial decorrelation length-scales similar to the other methods, adds temporal persistence beyond a year to their monthly estimates as described above, so that even one year after a data point is collected, it still has a 28% effect on the anomaly estimate at that location in the absence of new data. Hence, the EN fractional coverage is somewhat higher than those of PMEL_M and ISH. The LEV maps use the longest spatial correlation length-scales of all, and also do not take signal-to-noise ratios into

account in their smoothing, and thus result in large yearly fractional coverages, lower only than WIL and PMEL_R. Since the PMEL_R estimates assume that the mean anomalies of sampled regions apply to unsampled regions, similar to the final GOU estimates, they also effectively have fractional coverage of 1 for every year after that step has been taken. The DOM curve does not show fractional coverage as defined above, but percent of one-degree ocean boxes with data, as their method does not use a spatial mapping radius. DOM compensates for this relative data paucity with a well-developed related field of sea level height on which to regress the temperature data for OHCA estimates. The relatively low percent coverage may also lead to some of the spikes seen in the DOM estimates. The spikes are not apparent in three-year means of OHCA which is how results of the DOM mapping method are generally presented. The different mapping methods yield different results regionally as well as in the global integral. The geographic distribution of OHCA for the year with highest percent coverage in this study (2008) varies by method (Figure 4.4). Coverage is nearly global due to the Argo data and extends at least to the 700m depth, the limit for this study, in almost all areas of the ocean (Figure 4.4a). La Niña conditions present in 2008 are represented by cooler tropical and subtropical Eastern Pacific waters in all mappings except EN (Figure 4d). Warming along the Indian Ocean Antarctic zone, warming over most of the Atlantic Ocean, and cooling in the central Indian Ocean are all represented to some degree in each mapping method. The DOM (Figure 4.4b) and ISH (Figure 4.4f) OHCA fields for 2008 are smoother than the LEV, PMEL_M (Figure 4.4e), and WIL (Figure 4.4h) OHCA fields, which exhibit more small-scale features. The differences can be explained for each case. The EOF mapping using sea-surface height patterns in DOM can only resolve the larger scale features (Kaplan *et al.* 1998; 2000). The LEV mapping does not give less weight to sparse data (a lone data point within a radius of influence will fully describe the OHCA

at a point in the absence of additional data points, whereas other mapping methods will weigh the singular data point at a value less than one, diminishing its influence), the PMEL_M and WIL mapping includes a small spatial correlation length scale, and the WIL mapping makes use of detailed fields of altimetric sea-surface height, all of which tend to preserve smaller scale features. Whether some of these smaller scale features are noise introduced by the point measurements of the *in situ* temperature profiles, factors influencing sea-surface height other than OHCA, or if they may legitimately represent the influences of eddies and other small-scale ocean features will not be investigated here. The different mapping methods are filtering noise and smoothing at different length scales and this accounts for some of the differences in OHCA from different mapping methods.

The fractional global coverage for 1980 ranges from 45% (GOU) to 81% (LEV), and in general is much lower than the coverage for 2008 (Figure 4.3, Figure 4.5a). Areas with data, such as the North Pacific, do not have coverage below 300 m (Figure 4.5a). The DOM mapped OHCA for 1980 (Figure 4.5b) is positive or close to 0.0 ZJ over most of the global ocean, with the exception of the far western Pacific, east of the Philippines, along the track of the Southern Pacific Convergence Zone (roughly) and west of Australia. The DOM mapping also shows a coherent warm region in the Central East and North East Pacific. Other mappings exhibit localized cooling in the Northwest Atlantic and in the eastern Pacific. All mappings show warming > 10 x 10^{18} J in the central Indian Ocean, but this warming is particularly strong in LEV (Figure 5c) and GOU (Figure 4.5g), possibly due influence on these mapping methods of the isolated data in the area (Figure 4.5a). Despite the higher coverage in the Northern Hemisphere for 1980 compared to the Southern Hemisphere (Figure 4.5a) the 18 ZJ difference in OHCA for the Northern Hemisphere between DOM and LEV are not that much smaller than the 24.5 ZJ difference for the

Southern Hemisphere. In all maps, the Indian Ocean is mainly positive, with higher OHCA for LEV and GOU (Figure 4.5c and g). Strong positive OHCA in all three basins of the Southern Ocean are only seen in DOM (Figure 4.5b). Each mapping method has slightly different land/ocean definitions but only the DOM method excludes marginal seas and ice-covered areas. In addition, compared to the LEV mask, there are also some differences along coastlines. (Figures 4.4b and 4.5b, dark shading). Despite that, the effect of the different land/ocean definitions for DOM and LEV is not large with respect to integrated global OHCA in comparison to mapping method differences (Figure 4.2, green curve).

Quality control of the *in situ* profile data is also important and can cause differences in OHCA using different mapping methods or keeping the mapping method constant. The 2008 OHCA field using LEV mapping with the World Ocean Database (WOD) quality control flags and World Ocean Atlas 2009 baseline climatology (Figure 4.4i) is different from the field produced by LEV with the Barker Argo data quality control (Figure 4.4c), due to the sensitivity of the LEV mapping method to data quality control. While these fields are very similar on the large (basin) scale, there are some differences. For instance, the cool OHCA in the eastern Pacific is larger in the LEV method with WOD quality control (Figure 4.4i) than in the LEV method with Barker Argo quality control (Figure 4.4c). The 1980 OCHA field mapped with the LEV method using WOD quality control flags (Figure 4.5h) has fewer small-scale features that using EN3v2a quality control (Figure 4.5c), although there are some anomalous features in Figure 5h not in Figure 5c (vis. northern North Atlantic). None of the anomalous features are found using the DOM mapping (Figure 4.5b), or as pronounced in the other mappings, which use large spatial scale bins or give less weight to spatially isolated profiles. Quality control of *in situ* temperature profile data is not explored further here as a source of difference in OHCA.

4.3.1 Effects of XBT corrections

Here we explore the effect of each XBT correction on the global integral of OHCA by mapping method (Figure 4.6) relative to the C1_H baseline climatology. Yearly values for different XBT corrections can vary widely using the same mapping method. The W08 XBT correction is a clear outlier from 1999–2001 in most panels (e.g., panels a, c, d, e, g and h). Part of this deviation is explained by the use of different dataset versions. At least for DOM, the OHCA increase over 2000–2004 when using the EN3v1d data (Domingues *et al.* 2008) is about 50% smaller than observed in Figure 4.6a (based on EN3v2a data). For the LEV estimate, however, these differences are smaller (not shown). An investigation of the differences between EN3v1d and EN3v2a would be needed to understand these changes.

EDOF for XBT correction for each mapping method are approximately 4 for years 1970–2008 and 3 for 1993–2008, less than the number of mapping methods investigated (7 for 1970–2008, for 1993–2008, Table 4.1). Some mapping methods exhibit larger standard deviations for estimates using different XBT corrections in a given year, showing more sensitivity to the XBT correction used (Figure 4.7). The DOM mapping method is the most sensitive to XBT correction method used, while ISH and PMEL_M are the least sensitive, based on the mean standard deviation (Figure 4.7). Again, we use the standard deviation of different XBT corrections for a given mapping method as a measure of the variations inherent in estimates due to XBT correction used for each mapping method (Figure 4.7). The mean standard deviations for different XBT corrections applied to each mapping method are calculated excluding the years 2005–2008, for which only Argo data were used. The mean standard deviation for XBT corrections for the ensemble of mapping methods is 12.1 ZJ for the period 1970–2004 and 14.9 ZJ for the period 1993–2004. Excluding years 1999–2001 due to the outliers in W08, these values are 11.6 ZJ for

1970–2004 and 12.2 JZ for 1993–2004. These values excluding years 1999–2001 will be used in comparing XBT correction uncertainty. XBT correction is a larger factor than mapping method for DOM for both time periods, though nearly equal for 1993– 2008. This result could arise because of the DOM mapping method focuses on large-scale patterns, possibly making it more susceptible to changes in sampling in data sparse areas and also because of variations in XBT corrections in these areas. For all other mapping methods, XBT correction engenders a smaller mean uncertainty than do uncertainties due to mapping method. XBT correction uncertainty was calculated using the C1_H baseline climatology. This uncertainty was also calculated for C2_H and C3_M baselines for the DOM and LEV mapping methods (not shown). There was very little difference in XBT correction uncertainty between the C1_H and C2_H cases for DOM and LEV. However, the C3_M case produced smaller yearly standard deviations for some years (not shown), namely those years with outliers, such as 1999–2001 (discussed above for the W08 correction) and also years such as 1990–1991 with one or more XBT correction outliers. Use of the C3_M baseline climatology ameliorated the effects of XBT correction outliers while giving nearly identical standard deviation for years with smaller differences between corrections. The mean standard deviation values for different XBT corrections using the C3_M baseline climatology for DOM mapping method are 15.9 ZJ for 1970–2004 (compared with 16.7 ZJ, excluding years 1999–2001) and 17.1 ZH for 1993–2004 (compared with 18.9 ZJ, again excluding years 1999–2001). For LEV, mean standard deviations are 10.2 ZJ for 1970–2004 (11.1 ZJ using C1_H) and 8.8 ZJ for 1993–2004 (10.4 ZJ using C1_H). Why the C3_M baseline lessens the effects of outlier XBT corrections is a question for further study.

4.3.2 Effects of Baseline Climatologies

The final variable in the calculation of OHCA that we examine with respect to the different mapping methods is baseline climatology. For all mapping methods, a baseline monthly mean of temperature or sea level is subtracted from *in situ* temperature observations to calculate an anomaly value that is then used to map OHCA. All OHCA calculations to this point use the C1_H climatological baseline mean. C1_H uses a baseline temperature climatology calculated from all bottle, CTD, and Argo profiling floats for all available years. The climatological monthly means are constructed with a model that includes a linear trend with time, to reduce temporal biases in the climatology owing to long-term temperature changes (Alory *et al.* 2007). For comparison, a similarly calculated baseline, C2_H is used. C2_H uses a baseline temperature climatology calculated in the same way as Alory *et al.* (2007) except with the addition of XBT data corrected using W08 estimates of fall-rate corrections. C2_H has the benefit of greatly increased spatial and temporal data coverage with the disadvantage of the uncertainty introduced by the XBT bias and choice of correction. Cheng and Zhu (2015) recommend using an Argo era climatology rather than a longer, historical time period. This recommendation arises because of the full geographical and temporal sampling during the Argo era compared with the non-geographically uniform time period (e.g. Southern Hemisphere with a different mean year of all observations relative to the Northern Hemisphere) found in historical data climatologies. The C1_H and C2_H climatologies calculate a trend factor for each ocean grid to make the mean year geographically uniform, mitigating this issue (Alory *et al.*, 2007). To address differences due to the use of temporally limited data coverage representing the Argo period, baseline mean C3_M uses the World Ocean Atlas 2013 (WOA13) climatology from the 2005–2012 time period (Locarnini *et al.* 2013). All instrument types are used, including XBTs corrected using the L09 method, but the time period is dominated by Argo measurements. OHCA in the 2005–2012 time

period is warmer than over the rest of the 1970–2008 time period under consideration and can have an effect on the results from some mapping methods (Lyman and Johnson 2014). The global integral of OHC for CM_3 is 157 ZJ warmer than CH_1, while that for CH_2 is only 16 ZJ warmer than CH_1.

For simplicity, only the W08 XBT correction case is examined. Results using other XBT correction cases were nearly identical (in yearly standard deviation, means within 0.1 ZJ) for the DOM and LEV methods for each of the XBT correction cases, but could possibly be different for other mapping methods (not calculated).. We choose to adjust results from the three climatological cases for comparison. Since 2008 has the widest and most homogenous spatial and temporal coverage (and does not include XBT data) we adjust OHCA estimates for C2_H and C3_M by subtracting out the difference in OHCA between these cases and the C1_H case for year 2008. The 2008 differences from C1_H for C2_H are < 18 ZJ, but those for C3_M are larger, being 167 ZJ for DOM, 103 ZJ for LEV, 118 ZJ for ISH, 154 ZJ for PMEL_M, 167 ZJ for PMEL_R, 154 ZJ for EN, 152 ZJ for GOU, and 149 ZJ for WIL.

After these 2008 offsets are applied, the mapping methods are still affected to differing degrees by the change in baseline climatology (Figures 4.8a-g). For all mapping methods except GOU, the difference between OHCA using C1_H and C2_H is small, < 5 ZJ for most years, never exceeding 16 ZJ. For GOU in the 1990s and early 2000s, the difference in OHCA between C1_H and C2_H cases is > 25 ZJ for most years. It is not clear why this is occurs only with the GOU mapping method. Differences between OHCA using the C1_H and C3_M baseline climatologies are more pronounced for all mapping methods than between C1_H and C2_H cases. For DOM, LEV, and PMEL_R mapping methods, the C3_M OHCA yearly values are generally lower than the C1_H values, consistent with Cheng and Zhu (2015) more so for the DOM mapping method

than the other two. For the PMEL_M, ISH, and EN mapping methods, the C3_M OHCA yearly values are higher than for the C1_H OHCA values and the difference is larger for years earlier in the time series. The effect of baseline mean on the PMEL_M and ISH, methods, variants on zero infill, with the warmer baseline (2005–2012 in C3_M) result in smaller linear trends than the cooler historical climatologies (C1_H, C2_H), similar to the results of the experiment documented in Lyman and Johnson (2014).

The EDOF for baseline climatology comparison for each mapping method (Table 4.2) is very low, approximately 1. With that result in mind we turn to standard deviations of the estimates using different climatologies for the same mapping method (Figure 4.9). WIL and LEV show a low sensitivity to baseline climatology, with LEV having mean standard deviations of 3.5 ZJ and 2.7 ZJ for 1970–2008 and 1993–2008 respectively (Table 4.3), and WIL having a 3.1 ZJ mean standard deviation for 1993–2008. PMEL_R and ISH, have mean standard deviations due to changes in baseline climatology of 6.6 ZJ and 8.6 ZJ respectively for 1970–2008, higher than LEV, but lower than for the other mapping methods. The results for ISH are similar to the results reported in Ishii and Kimoto (2009). DOM, EN, GOU, and PMEL_M all have mean standard deviations due to baseline climatology > 10.0 ZJ for 1970–2008. The standard deviation of the GOU method has the largest differences between C1_H and C2_H cases in the 1993–2008 period.

Standard deviations are constructed here only from the three baseline cases for each mapping method for each year, a very small sample size (approximately 1 EDOF, Table 4.2), and are subject to our choice to force agreement at 2008, which impacts both magnitudes and temporal structures of the standard deviations. Subject to these caveats, the effects of different baseline mean in all mapping methods are smaller than the difference between the mapping methods

themselves. However, relative importance of difference due to XBT correction and to baseline climatology is more year-dependent, with XBT correction uncertainty larger in later years (1990s, 2000s) and baseline climatology uncertainty larger in earlier years (1970s, 1980s) for some mapping methods with zero infill variants (PMEL_M, ISH) as well as EN. So, the choice of the baseline climatology is of importance in estimating the uncertainty in OHCA with a widely varying dependence on the mapping method used. The choice of a latter year (Argo period) climatology (recommended in Cheng and Zhu 2015), may be appropriate for some mapping methods, but will cause larger uncertainties for methods with variants on zero infill if applied to data sparse years. For other mapping methods, such as LEV and WIL, the uncertainties due to baseline climatology are small in comparison to other uncertainties. A further study, resolving the caveats listed above, would help to clarify the results given here.

4.3.3 Linear Trend

Finally, we consider linear trend estimates for OHCA in the global ocean (Table 4.4 and Figure 4.10) for each mapping method and each case (XBT correction and baseline climatology) examined here. Here standard errors are given for linear trend uncertainties. Degrees of freedom are estimated for each time-series by dividing the time-series length by its decorrelation time-scale and then subtracting two. The decorrelation time scale for each time series is estimated as twice the maximum value of the lagged autocorrelation of the residual computed by subtracting the linear trend from the time series (von Storch and Zwiers 1999). For 1970–2008 (Table 4.4a, Figure 4.10a), the DOM linear trend is highest in five of the eight test cases including each baseline climatology, while PMEL_R linear trend is highest in four (both have the same value for W08 C1_H case). The GOU, DOM, and PMEL_R mapping methods form a distinct group with average linear trend over all cases of > +4.0 ZJ yr^{-1}. These results make sense for PMEL_R and

GOU, since they both explicitly infill data-sparse regions with the average of well-sampled regions when constructing a global mean. PMEL_M, ISH, and EN all reach their lowest value using C3_M baseline, the warmest climatology. This result makes sense as well, since these mapping methods will tend to underestimate trends using warm climatologies when earlier, colder years are data-sparse (Lyman and Johnson, 2014). ISH consistently exhibits the lowest trend value for all XBT correction cases, excepting C3_M. ISH, along with LEV, PMEL_M, and EN form a group of mapping method whose average linear trend over all eight cases is < +3.5 ZJ yr^{-1} . Finally, all cases for all mapping methods exhibit a warming trend within the standard error over the period 1970–2008, even the PMEL_M results using C3_M baseline case (Figure 4.10) which has the lowest linear trend of all cases at 1.3 ± 0.74 ZJ yr^{-1} . The reasons for that low result have been carefully explained, along with the reason PMEL_R is preferable for global integrals of OHCA (Lyman and Johnson 2014).

For the period 1993–2008 (Table 4.4b, Figure 4.10b) WIL has the highest linear trend for all cases using C1_H baseline, except the GO12 XBT correction case, where PMEL_R is higher. WIL also has the highest linear trend for the C2_H case, while GOU has the highest linear trend for the C3_M case. The highest linear trend in the study is the PMEL_R C1_M case with the GO12 XBT correction (9.4 ± 2.4 ZJ yr^{-1}). For 1993–2008, PMEL_M, EN, and GOU all have average linear trends between +6.0 and +6.2 ZJ yr^{-1}, while DOM, LEV, and ISH all have average linear trends <= +5.1 ZJ. PMEL_R and WIL have the highest trend, both at +7.2 ZJ yr^{-1} for 1993–2008. DOM

average linear trend for 1993–2008 over all cases is lowest of all mapping methods, at +3.6 ±1.5 ZJ yr^{-1}, while the DOM method produces the second highest average linear trend over 1970–2008 (with PMEL_R highest) with ISH lowest for 1970–2008. While the standard error of the

mean for cases over 1993–2008 are higher than the same cases over 1970–2008, warming trends are all positive within the standard error, except the W08, L09, and C13 (C1_H) cases for the DOM method (3.3±3.4 ZJ yr^{-1}, 2.3±2.9 ZJ yr^{-1}, and 1.5 ± 1.6 ZJ yr^{-1} respectively). For some perspective, the recent estimate of OHCA linear trend 1970–2005 of 5.6 ± 0.15 ZJ yr^{-1} from Cheng *et al.* (2015b) is higher than any of the present results, though within uncertainty of all DOM, PMEL_R, and GOU cases and all but one historical baseline climatology PMEL_M case. This is due to a combination of all factors tested here (mapping method, XBT correction, baseline mean) as well as input data set/quality control. There are also three fewer years in Cheng *et al.* (2015b), but their 1970–2014 linear trend (5.5 ± 0.15 ZJ) is nearly identical to their 1970–2005 trend.

Of the five estimates of 1993–2014 OHCA linear trend from Johnson *et al.* (2015a), all are within uncertainty of the most similar case from the present work for 1993-2008, with four higher (their PMEL/JPL/JIMAR compared with PMEL_R, their NODC compared with LEV, their CSIRO/ACE CRC/IMAS-UTAS compared with DOM, their Met Office Hadley Centre compared with EN) and one lower linear trends (their MRI/JMA compared with ISH). Differences are due in part to the different time period covered, but also due to factors such as baseline climatology and data set/quality control used.

4.4 Conclusions

By holding input data constant, we isolate the sensitivity of global OHCA estimates in the upper 700 m of the ocean over a 39-year period, 1970–2008, to mapping method, XBT bias correction, and baseline climatology.

Annual differences of roughly 17.1 ZJ in OHCA estimates can be attributed to differences in mapping methods used by seven groups (eight methods) actively performing such calculations (Table 4.3). These differences in calculations are not simply due to infilling of data gaps, but also to smoothing or filtering of fields geographically where data are present. The smoothing or filtering inherent in each mapping method is performed over different length scales. Quality flags for the input data will also affect calculated OHCA differently based on the length scale and amount of smoothing of each mapping method.

The choice of XBT bias correction has an effect on differences in calculated OHCA, as previously reported by Lyman *et al.* (2010). However, in the present study, we find that mapping method is generally the largest source of uncertainty (in six of seven calculations for 1970–2008 and five of eight calculations for 1993–2008, as shown in Table 4.3). Only for the DOM mapping method does the choice of XBT correction has a larger impact on OHCA estimates over both periods than does the overall choice of mapping method. For other mapping methods, the choice of XBT correction has a smaller impact for 1970–2008 (between 8.0 and 12.6 ZJ, Table 4.3) than the choice of mapping method (16.5 ZJ). The relative uncertainty of mapping method and XBT correction for 1993–2008 is somewhat more mapping method dependent with DOM, PMEL_R, and GOU having higher uncertainties for XBT correction than mapping method uncertainty.

The XBT community is approaching, but has not yet reached, a consensus on the annually varying corrections of both depth (probe fall-rate) and temperature to minimize the uncertainty of temperature measurements associated with XBT corrections (Cheng *et al.* 2015a). Once a consensus is reached, this particular uncertainty should be further reduced (but not eliminated) as a source of uncertainty in historical and future OHCA calculations.

The choice of baseline climatological monthly mean also has an effect on OHCA calculations that is different for the different mapping methods. As Lyman and Johnson (2014) describe, for some mapping methods, this may be due to the relation between the infilling method and the warm time period over which the 2005–2012 climatology was calculated. The warmer climatology will engender larger cool anomalies in earlier years (compared to a historical mean climatology), the effects of which are damped in the integral by infilling zero anomaly in data sparse regions. Taking into account the small 2008 offset compared to total heat content offset between C1_H and C3_M climatologies (103 ZJ vs. 157 ZJ), the LEV mapping method is not very sensitive to the baseline climatology used, despite using a variation on relaxation to climatology as infill method. For LEV, this insensitivity may be due to the more liberal definition used for the area over which the mapping method can incorporate data for each grid box (Figure 4.3). Choosing a proper baseline climatology can be method dependent, as the PMEL_M method should not be (and is not) employed with a climatology consisting of recent data only, as per the reasons outlined in Lyman and Johnson (2014). For the DOM method, further investigation would reveal which baseline climatology produces the most realistic results, possibly on a regional level. Mean linear trends for each mapping method from all cases listed in Table 4.1 (except None) range from +3.0 ZJ yr^{-1} (ISH) to +4.4 ZJ yr^{-1} (PMEL_R) for the 1970–2008 period and +3.6 ZJ yr^{-1} (DOM) to +7.2 ZJ yr^{-1} (WIL and PMEL_R) for 1993–2008 . Expressing these values in terms of W m^{-2}, the unit in which Earth's heat budget is usually discussed, the trends are 0.08 to 0.31 W m^{-2} for 1970–2008 and 0.09 to 0.58 W m^2 for 1993–2008, using the global surface area of 5.144 x 10^{14} m^2. These linear trends are small compared to the yearly uncertainties calculated here. However, all (XBT corrected) upper OHCA estimates regardless of baseline climatology or mapping method show a distinctive increase over the 1970–2008 period and, except for the

DOM method, a higher warming rate over the 1993–2008 period. Regardless of mapping method, OHCA calculations do reveal an increase in ocean heat content on both the multi-decadal and decadal time scales.

We find that the uncertainty in calculation of OHCA from irregular spatial and temporal data distribution is larger than inter-annual variability in OHCA, but long-term trends are still statistically robust, in agreement with Lyman *et al.* (2010), even when extending the time series back to 1970 and including years with relatively sparse data distribution. The mapping method is shown here to be a source of uncertainty on the order of 17 ZJ. XBT corrections and baseline climatological mean add uncertainties dependent on the mapping method used, but at least the uncertainty due to the XBT correction should be reduced if a consensus can be reached on the optimum corrections. Furthermore, care is indicated in choosing the best baseline climatology, perhaps on a method dependent basis.

The present work carries forward understanding of the uncertainties affecting *in situ* estimates of OHCA, but there is still much work to do. Future work will include

- Refinement in understanding the role of the baseline climatology in OHCA uncertainty, with a fuller exploration of the relative effects of the more uniform spatial and seasonal coverage vs. shorter time span inherent in Argo float era climatologies . For instance, a 10-year Argo period climatology constructed from subsampled model data is unbiased when compared to the spatially complete model data for the same period, but a shorter-term Argo-era climatology results in larger errors than a longer-term climatology in some regions (Good 2016).
- Exploring the benefits and deficiencies in filtering OHCA signals at different spatial scales as well as on differences due to non-seasonal signals (e.g., El Niño).

- Testing whether different grid sizes for averaging *in situ* data affect OHCA calculations (same mapping method, varying grid size).
- Quantifying the uncertainty introduced by data set choices and quality control choices. Quantifying XBT correction schemes effectiveness compared with a CTD reference data.
- Better understanding the effects of vertical sampling, both spacing between adjacent measurements and the absence or presence of data in different depth ranges.

Augmenting the current historic temperature profile database especially for data sparse regions.

In summary, though the present work helps to quantify the uncertainties in OHCA estimation from *in situ* oceanographic profile data, there is still much work to be done to refine the process and interpret the results.

4.5 Tables

A	1970–2008	1993–2008	B	1970–2008	1993–2008	C	1970–2008	1993–2008
W08	4.3	3.4	DOM	3.6	3.0	DOM	1.3	1.6
L09	3.6	3.6	LEV	3.6	3.1	LEV	1.4	1.3
I09	3.7	3.7	PMEL_M	4.2	2.9	PMEL_M	1.1	1.4
C13	3.9	3.7	PMEL_R	4.2	2.9	PMEL_R	1.8	1.8
GO12	3.9	3.5	ISH	3.6	2.9	ISH	1.2	1.6
G11	4.3	3.8	EN	3.9	3.1	EN	1.2	1.4
			GOU	3.9	2.9	GOU	1.9	1.3
			WIL		2.9	WIL		1.4

Table 4.1. Summary of the sensitivity experiments performed in this study, in terms of variations in XBT data, climatological baselines and mapping methods.

XBT cases		Mapping Methods							
		DOM	**EN**	**LEV**	**GOU**	**ISH**	**PMEL_M**	**PMEL_R**	**WIL**
No XBT correction		H		H	H	H	H	H	H
W08	Depth	H 2 M	H 2 M	H 2 M	H 2 M	H 2 M	H 2 M	H 2 M	H 2 M
IO9		H	H	H	H	H	H	H	H
L09	Temperature	H	H	H	H	H	H	H	H
GO12	Depth + Temperature	H	H	H	H	H	H	H	H
C13		H	H	H	H	H	H	H	H
G11	Depth (Bathym. approach)	H	H	H	H	H	H	H	H

Legends

XBT corrections:

W08: Wijjfels *et al.* (2008, their table 1)
IO9: Ishii and Kimoto (2009)
L09: Levitus *et al.* (2009)
GO12: Gouretski (2012)
C13: Cowley *et al.* (2013, their CH method)
G11: Good, 2011

Climatological baseline cases:

(H) C1_H: Historical period, only bottles, CTDs and Argo data
(2) C2_H: Historical period, as above but including XBT data corrected by W08.
(M) C3_M: Modern period (2005-2012), Argo and concurrent non-Argo data from the WOA13

Mapping methods:

DOM: Domingues *et al.* (2008), Church *et al.* (2011)
EN: Met Office Hadley Centre ENACT/ENSEMBLES, Ingleby and Huddleston (2007)
LEV: Levitus *et al.* (2000; 2005; 2009; 2012)
GOU: Gouretski *et al.* (2012)
ISH: Ishii *et al.* (2003; 2006), Ishii and Kimoto (2009)
PMEL_M (mean of the maps): Lyman and Johnson (2008; 2014)
PMEL_R (representative mean): Lyman and Johnson (2008; 2014)
WIL: Willis *et al.* (2004)

Table 1: Summary of the sensitivity 1087 experiments performed in this study, in terms of variations in XBT data, climatological baselines and mapping methods.

A	1970–2008	1993–2008	**B**	1970–2008	1993–2008	**C**	1970–2008	1993–2008
W08	4.3	3.4	DOM	3.6	3.0	DOM	1.3	1.6
L09	3.6	3.6	LEV	3.6	3.1	LEV	1.4	1.3
I09	3.7	3.7	PMEL_M	4.2	2.9	PMEL_M	1.1	1.4
C13	3.9	3.7	PMEL_R	4.2	2.9	PMEL_R	1.8	1.8
GO12	3.9	3.5	ISH	3.6	2.9	ISH	1.2	1.6
G11	4.3	3.8	EN	3.9	3.1	EN	1.2	1.4
			GOU	3.9	2.9	GOU	1.9	1.3
			WIL		2.9	WIL		1.4

Table 4.2 Effective Degrees of Freedom (EDOF) Calculated for a) mapping method cases comparison, b) XBT correction cases, c) baseline mean cases. EDOF calculated after Lyman *et al.* (2010).

	Mapping Method	XBT bias correction	Baseline Climatology
DOM	16.5 (17.1) ZJ	16.7 (18.9) ZJ	11.8 (7.1) ZJ
LEV	16.5 (17.1) ZJ	11.1 (10.4) ZJ	3.5 (2.7) ZJ
PMEL_M	16.5 (17.1) ZJ	7.4 (11.5) ZJ	14.5 (4.7) ZJ
PMEL_R	16.5 (17.1) ZJ	12.1 (15.3) ZJ	6.6 (4.9) ZJ
ISH	16.5 (17.1) ZJ	9.5 (10.5) ZJ	8.6 (3.9) ZJ
EN	16.5 (17.1) ZJ	12.8 (15.1) ZJ	11.8 (5.6) ZJ
GOU	16.5 (17.1) ZJ	11.3 (15.2) ZJ	11.5 (9.8) ZJ
WIL*	*(17.1) ZJ	* (12.8) ZJ	* (3.1) ZJ
Average	16.5 (17.1)	11.6 (12.2)	9.8 (5.2)

Table 4.3. Time-mean standard deviations of global OHCA associated with variations in XBT bias corrections and baseline climatologies for different mapping methods for 1970–2008 and 1993–2008 (in parentheses). * WIL method can only be calculated from 1993–2008. XBT bias correction standard deviation only through 2004, since XBT were not used in this experiment beyond that year. XBT bias correction standard deviations also exclude years 1999-2001 due to obvious outliers in the W08 method for those years.

Table 4.4a.

	DOM	LEV	PMEL_M	PMEL_R	ISH	EN	GOU	MEAN
W08	3.9±0.65,9.7	3.1±0.48,12.7	3.2±0.61,7.1	3.9±0.65,10.8	2.9±0.47,7.5	3.4±0.60,7.7	3.7±0.70,11.8	3.4±0.4
L09	5.0±0.81,6.8	3.7±0.44,14.2	3.9±0.67,4.4	4.9±0.75,7.9	3.5±0.55,4.8	4.2±0.78,5.0	4.8±0.78,10.7	4.3±0.6
C13	3.7±0.66,8.7	3.0±0.44,13.6	3.5±0.67,4.9	4.2±0.77,8.0	2.9±0.50,5.1	3.4±0.70,5.7	4.0±0.79,10.1	3.5±0.5
I09	4.1±0.42,17.0	3.1±0.35,17.0	3.7±0.44,7.6	4.6±0.48,14.2	3.1±0.31,8.97	3.6±0.48,8.0	4.4±0.59,14.7	3.8±0.6
G11	4.1±1.0,5.3	3.3±0.69,7.4	3.5±0.73,5.1	4.4±0.85,7.1	3.1±0.83,3.3	3.6±1.1,3.8	4.1±1.0,7.9	3.7±0.4
GO12	4.8±0.75,7.0	3.7±0.44,13.4	3.4±0.91,3.7	4.3±1.11,5.2	3.4±0.79,3.3	3.7±1.1,3.5	4.1±0.87,9.1	3.9±0.5
None	3.9±1.4,5.5	2.9±0.78,7.3	4.4±0.67,6.2	5.3±0.95,7.4	3.1±0.66,5.2	3.5±1.0,4.9	5.1±1.1,7.9	4.0±0.9
C2_H	3.9±0.65,9.7	3.1±0.49,12.7	2.9±0.69,6.6	3.7±0.78,9.0	2.7±0.53,6.7	3.2±0.66,7.2	3.7±0.70,11.8	3.3±0.4
C3_M	4.7±0.70,9.8	3.4±0.61,10.2	1.3±0.74,5.8	4.0±0.82,9.1	2.0±0.51,7.2	2.3±0.58,7.9	3.6±1.1,9.0	3.0±1.1
MEAN	4.2 ± 0.4	3.3±0.3	3.3±0.8	4.4±0.5	3.0±0.4	3.4±0.5	4.2±0.5	

Table 4.4b.

	DOM	LEV	PMEL_M	PMEL_R	ISH	EN	GOU	WIL	MEAN
W08	3.3±3.4,2.3	4.0±2.5,3.0	6.2±3.0,1.8	7.0±2.7,2.4	5.1±2.4,1.9	5.8±3.2,2.2	6.0±2.7,2.5	7.1±2.7,1.7	5.6±1.3
L09	2.3±2.9,2.5	3.9±1.5,5.2	5.9±1.1,5.3	6.7±2.8,3.0	4.8±1.2,3.5	5.6±1.7,4.6	5.3±2.9,3.3	7.0±1.5,3.2	5.2±1.4
C13	1.5±1.6,3.6	3.2±1.3,5.5	5.1±1.2,4.9	5.7±2.3,3.8	4.2±0.88,3.8	4.7±1.6,4.5	4.5±0.23,3.6	6.1±1.3,3.0	4.4±1.4
I09	2.0±1.3,4.5	3.3±1.4,5.0	5.5±1.0,5.4	6.1±2.3,3.0	4.4±1.0,3.59	5.0±1.4,4.6	5.0±1.8,4.4	6.3±1.3,2.9	4.7±1.4
G11	3.7±0.95,14	4.2±1.5,5.0	6.3±1.3,5.1	7.1±1.7,5.3	5.4±1.1,4.2	6.2±1.7,4.8	6.2±1.8,0.78	7.5±1.3,3.6	5.8±1.2
GO12	6.0±2.0,2.8	5.7±1.5,4.8	8.0±1.3,4.7	9.4±2.4,3.7	6.7±1.2,3.1	8.7±1.7,4.2	8.4±2.3,3.7	9.0±1.6,2.7	7.7±1.3
None	-2.8±5.4,1.6	0.7±2.2,4.0	2.5±2.0,3.2	2.2±5.0,1.8	1.8±2.4,2.0	1.8±2.2,3.6	0.53±4.7,2.0	3.4±3.0,2.1	1.3±1.8
C2_H	4.2±3.7,2.1	4.0±2.6,3.0	6.6±3.1,1.8	7.7±3.1,14	5.6±2.4,1.9	6.4±3.2,2.2	6.0±2.7,2.5	7.4±3.1,1.6	6.0±1.3
C3_M	5.6±4.0,2.0	4.8±3.1,2.6	6.0±1.9,2.5	7.9±3.6,2.0	4.9±1.8,2.3	5.5±2.2,2.9	8.2±3.9,1.9	7.2±2.8,1.7	6.3±1.2
MEAN	3.6±1.5	4.1±0.8	6.2±0.8	7.2±1.1	5.1±0.7	6.0±1.2	6.2±1.3	7.2±0.8	

Table 4.4. Linear trends of OHCA (ZJ yr^{-1}) for a) 1970–2008 and b) 1993–2008 by mapping and test case with standard errors and degrees of freedom (after the comma). Degrees of freedom are estimated as described in the text. The W08 case is equivalent to the C1_H case. The None case is not included in the MEAN value in the final row. The uncertainty of the MEAN in the last row (column) is the standard deviation of the included cases.

4.6 Figures

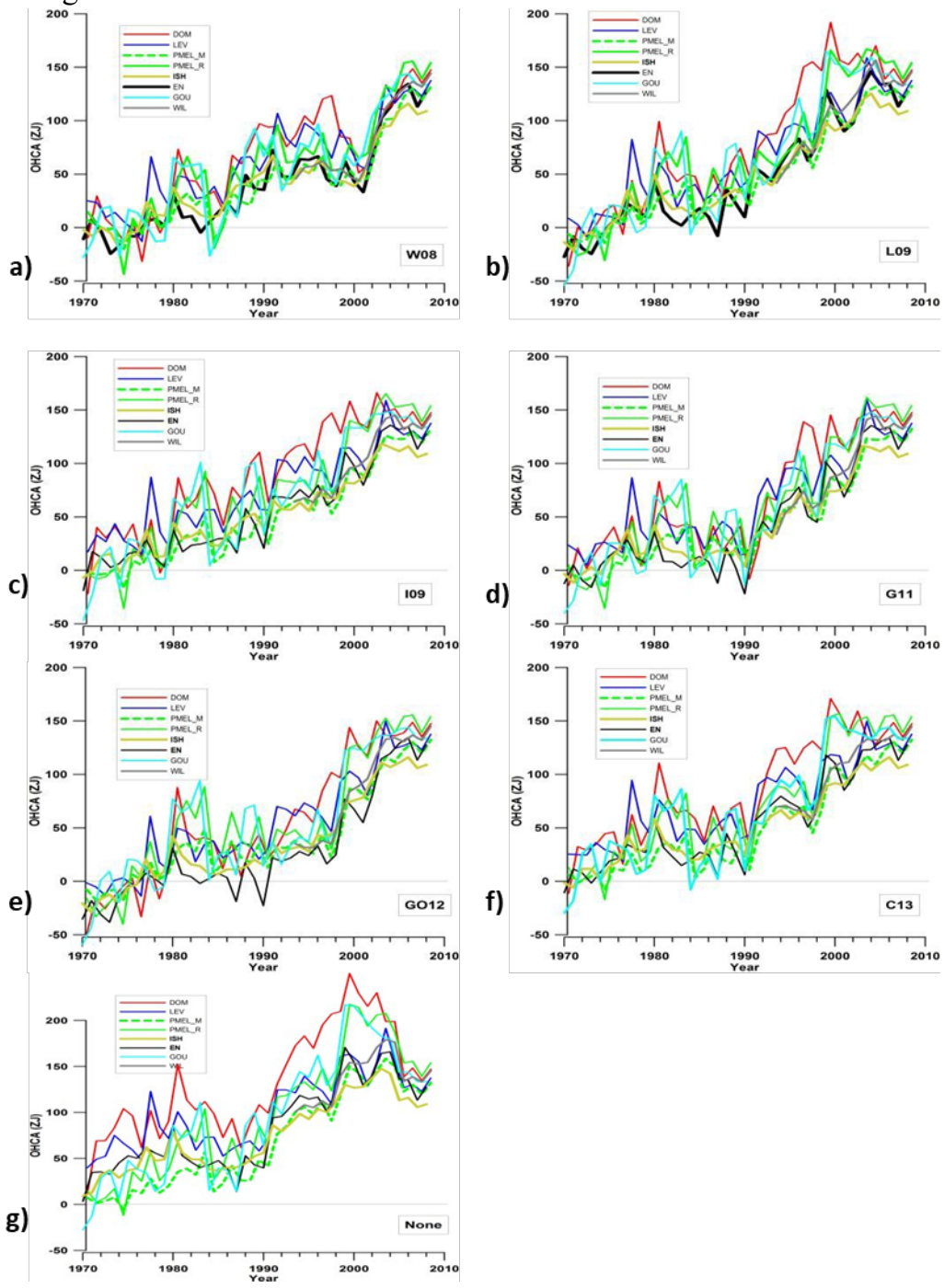

Figure 4.1. Annual globally integrated OHCA (ZJ) time series for 1970–2008 computed using different mapping methods (see legends) using C1_H baseline climatology, and XBTs corrected with a) W08, b) L09, c) I09, d) G11, e) GO12, f) C13, g) None

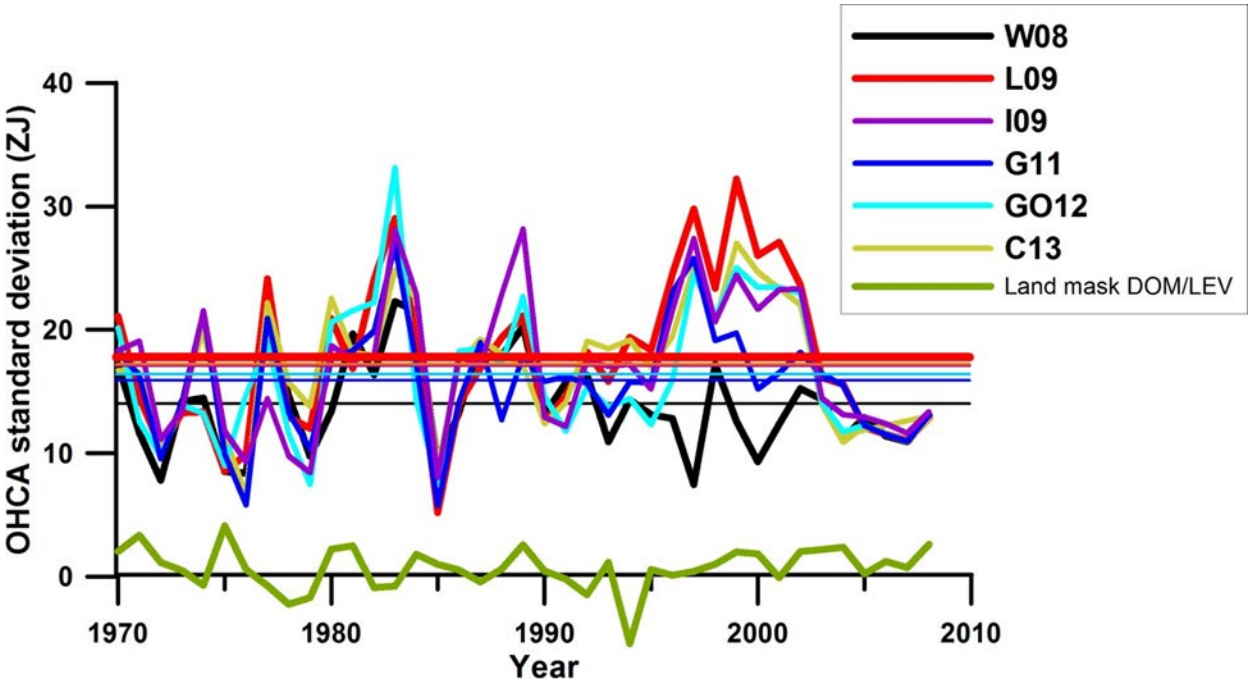

Figure 4.2. Standard deviations of global OHCA (ZJ) for 1970–2008 from ensemble means of the eight different mapping methods for each of the six XBT bias corrections (see legend) referenced to the C1_H baseline climatology. Horizontal lines represent means over standard deviations over the full time period. The green line denotes the OHCA difference between DOM and LEV results where land/ocean grids are represented in one or the other method, but not both (ocean definition differences).

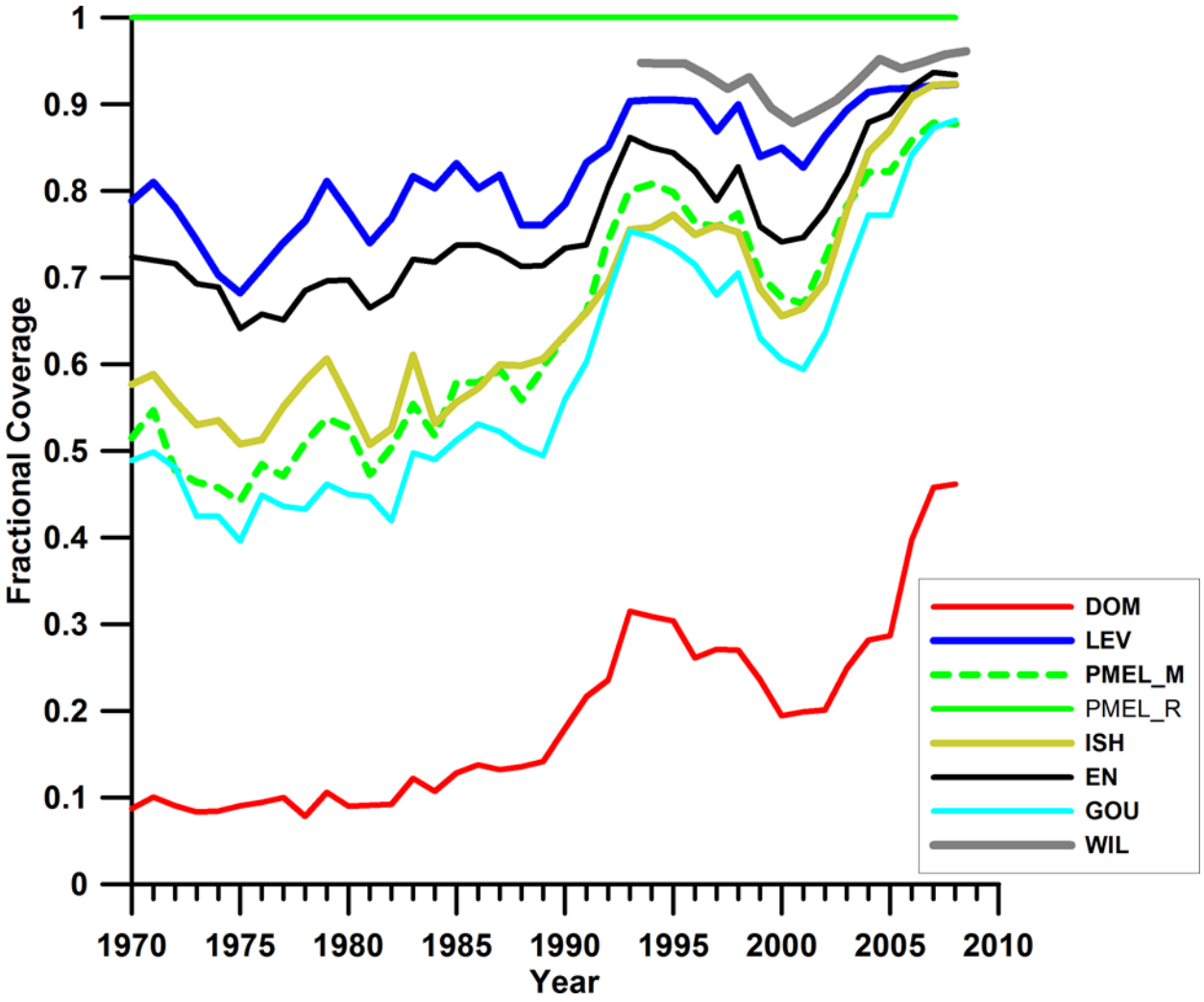

Figure 4.3. Fraction of the global ocean considered sampled for temperature data in each year for each mapping method (see legend). The PMEL_R and GOU method after its final infilling step are unity for every year (green solid line). DOM curve (red) is not fractional coverage but indicates where data were available for one-degree grid boxes without including additional spatial radius.

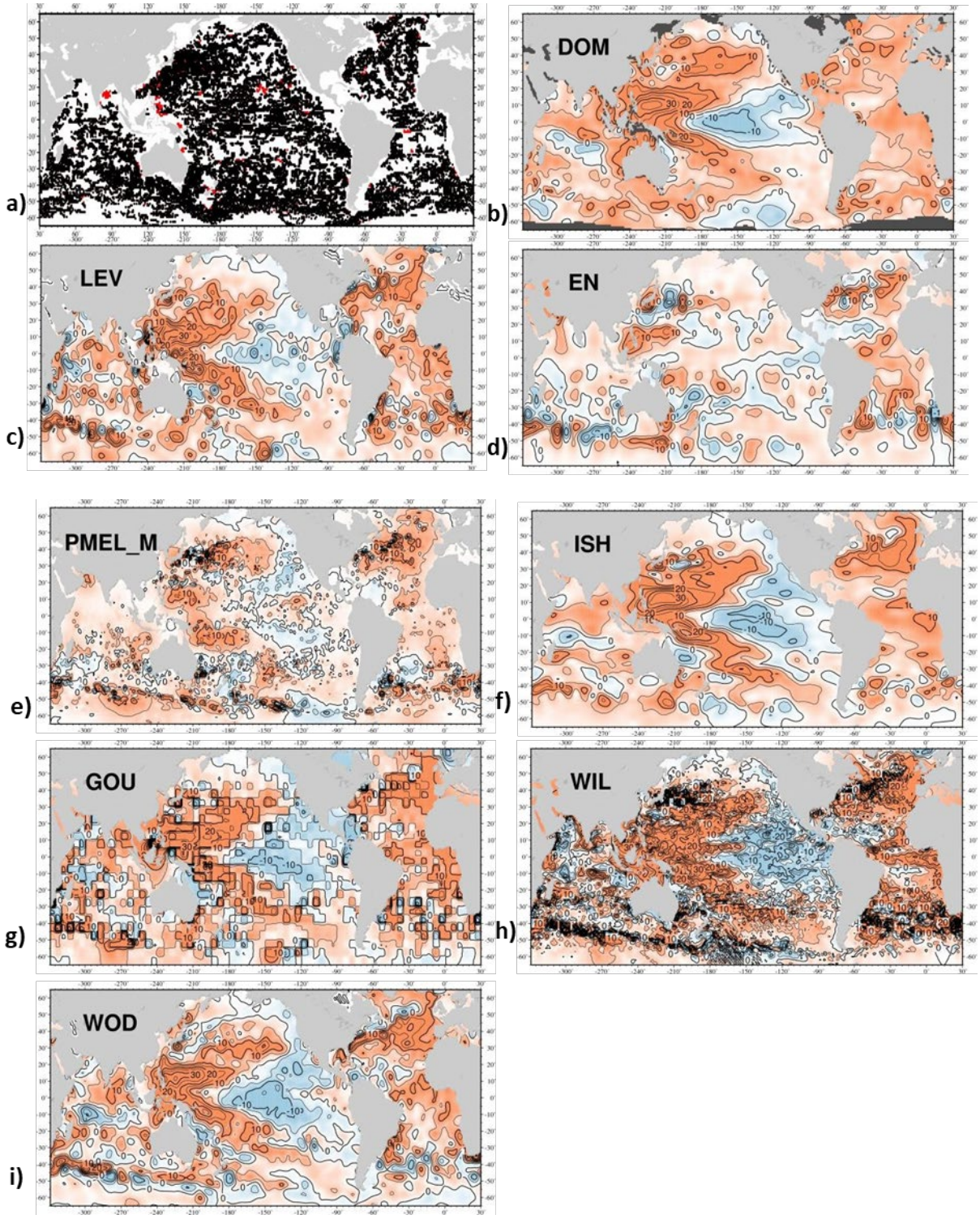
a)
b)
DOM
c)
LEV
d)
EN
e)
PMEL_M
f)
ISH
g)
GOU
h)
WIL
i)
WOD

Figure 4.4. Geographic distribution for 2008 of ocean profiles (red is 0-300m data only, blackis 0-300m and 300-700m data) and OHCA for b) DOM mapping, c) LEV mapping (using EN3v2 and Barker quality controlled data), d) EN mapping, e) PMEL_M mapping, f) ISH mapping, g) GOU mapping, h) WIL mapping, and i) LEV mapping using WOD quality controlled data For b through i, contour interval of 5 x 1018 J, red is positive OHCA, blue negative. Dark grey shading in b) are areas without calculated OHCA.

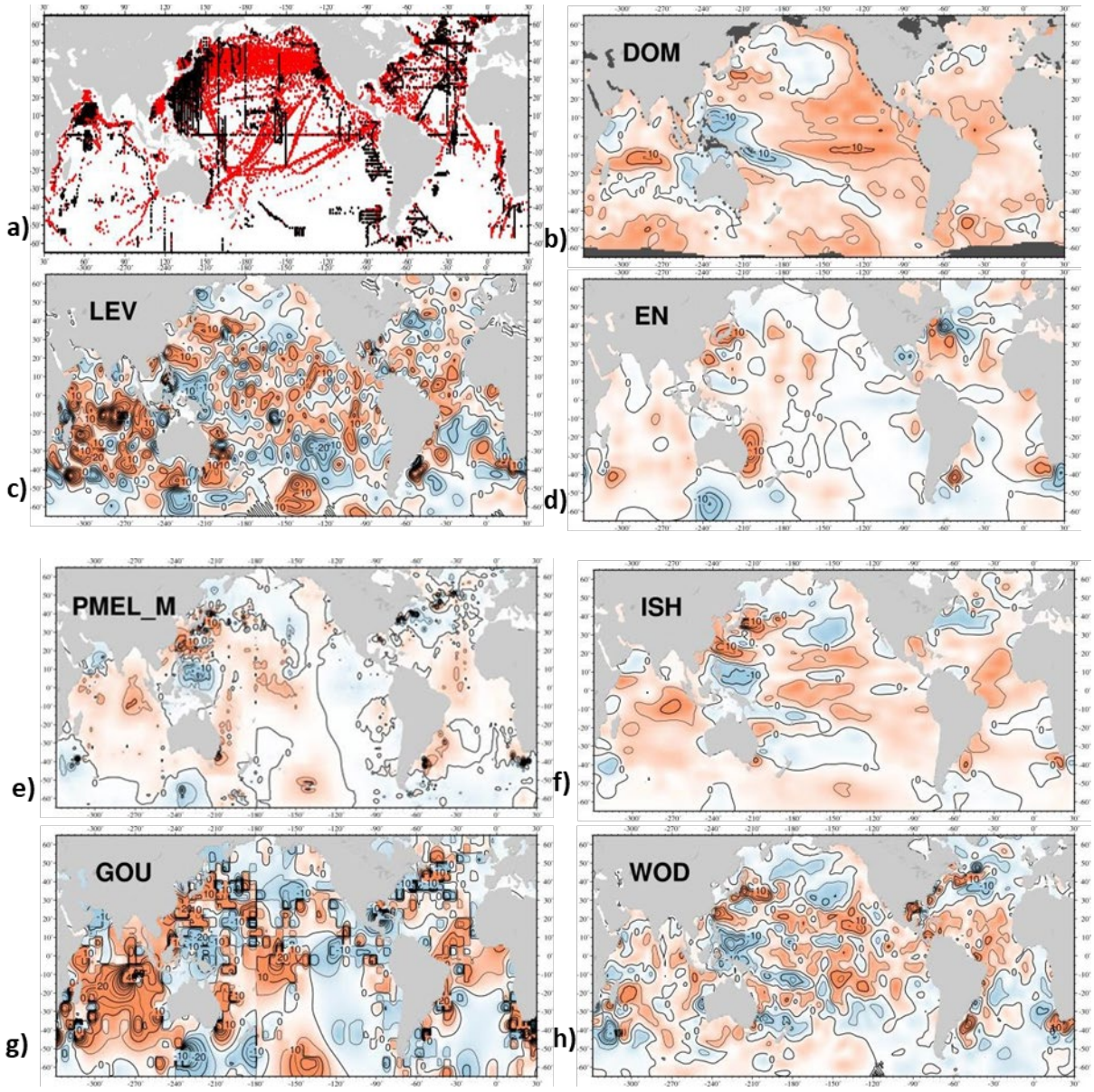

Figure 4.5. Geographic distribution for 1980 of a) ocean profiles (red is 0-300m data only, black is 0-300m and 300-700m data) and OHCA for b) DOM mapping, c) LEV mapping, d) EN mapping, e) PMEL_M mapping, f) ISH mapping, g) GOU mapping, and h) LEV mapping using WOD quality controlled data. For b through h, contour interval of 5 x 1018 J, red is positive OHCA, blue negative. Dark grey shading in b) are areas without calculated OHCA.

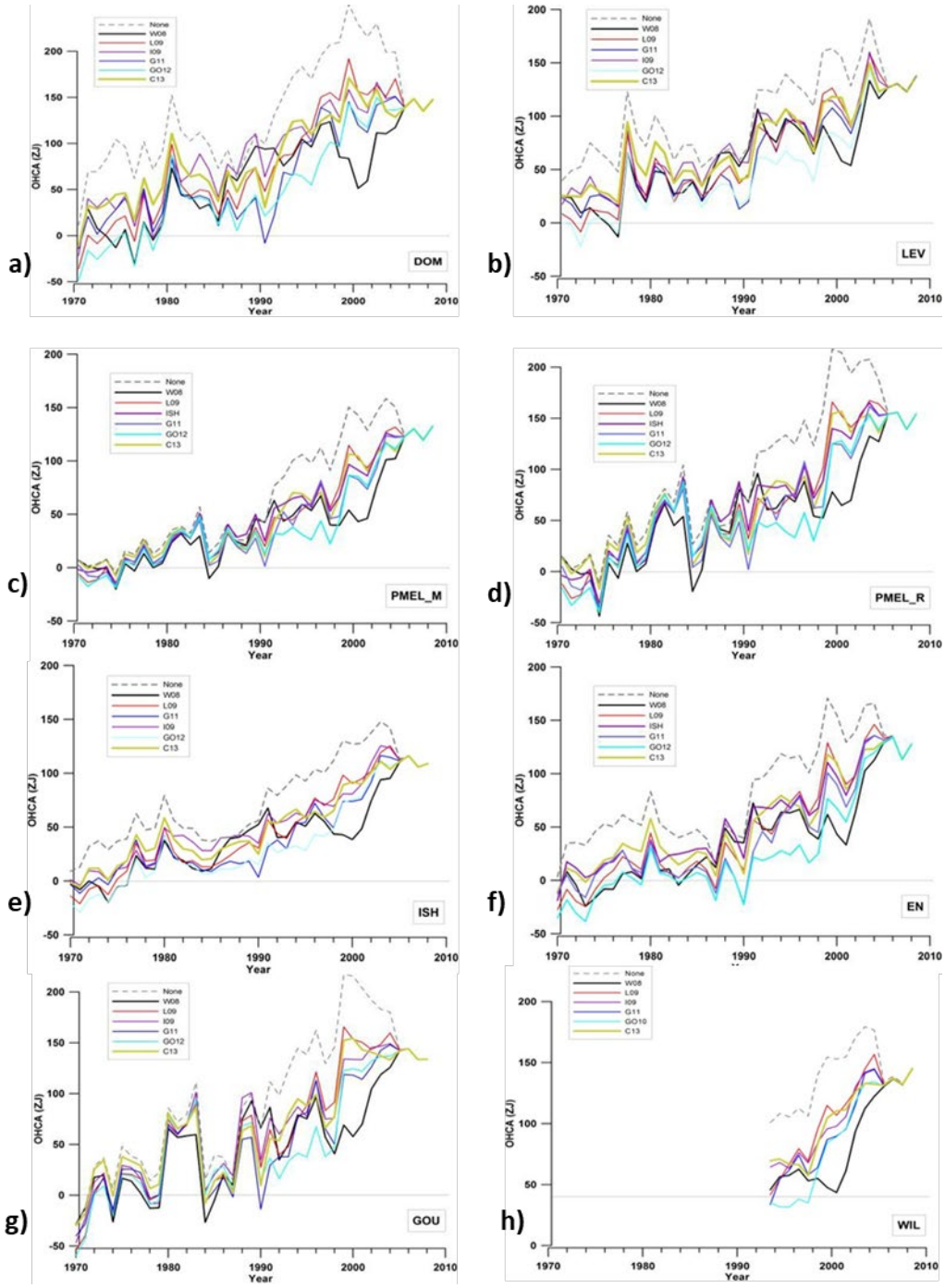

Figure 4.6. Annual globally integrated OHCA (JZ) time series for 1970–2008 for a) DOM mapping, b) LEV mapping, c) PMEL_M mapping, d) PMEL_R mapping, e) ISH mapping, f) EN mapping, g) GOU mapping, and h) WIL mapping for 1993–2008, relative to the C1_H baseline climatology using different XBT corrections: W08, L09, G11, I09, GO12, C13, and None**.**

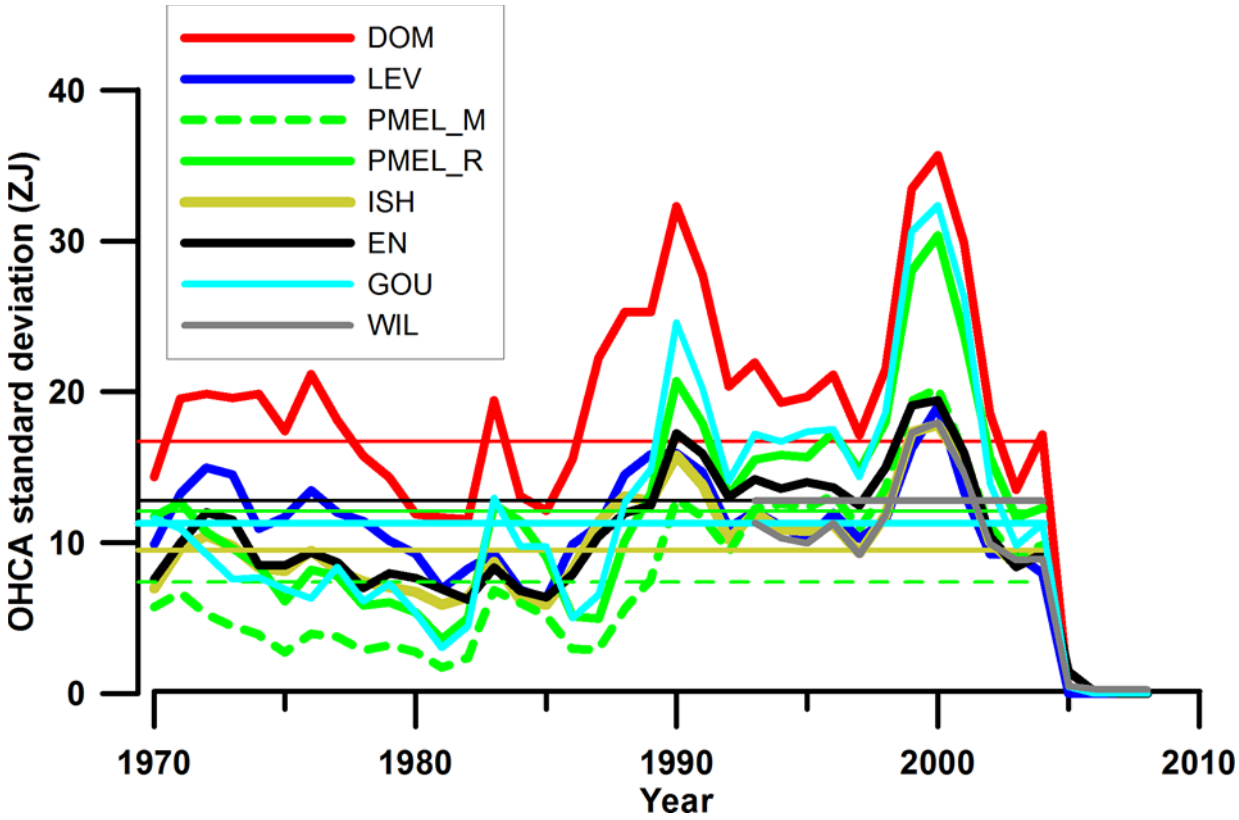

Figure 4.7. Standard deviations for the yearly ensemble means of global OHCA (ZJ) for 1970–2008 using different XBT corrections for each mapping method (see legend) from 1970–2008 referenced to the C1_H baseline climatology. Horizontal lines represent mean standard deviations over full time series.

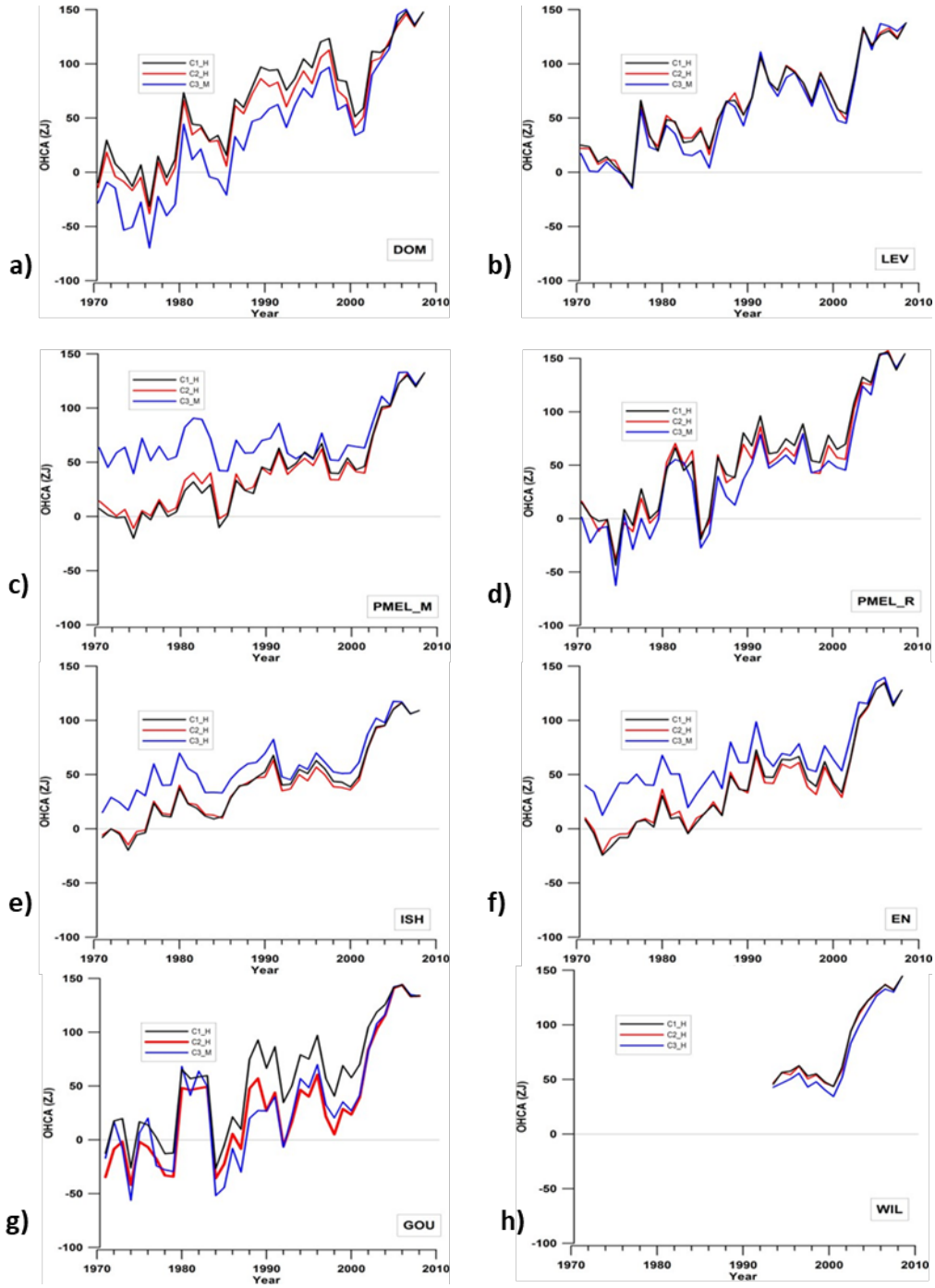

Figure 4.8. Annual globally integrated OHCA (ZJ) time series for 1970–2008, using the W08 XBT correction relative to three climatological mean baselines (see legends) for a) DOM mapping, b) LEV mapping, c) PMEL_M, d) PMEL_R, e) ISH mapping, f) EN mapping, g) GOU mapping, and h) WIL mapping for 1993–2008. Individual curves have been shifted to overlie in 2008, the year with the best coverage (Fig. 3).

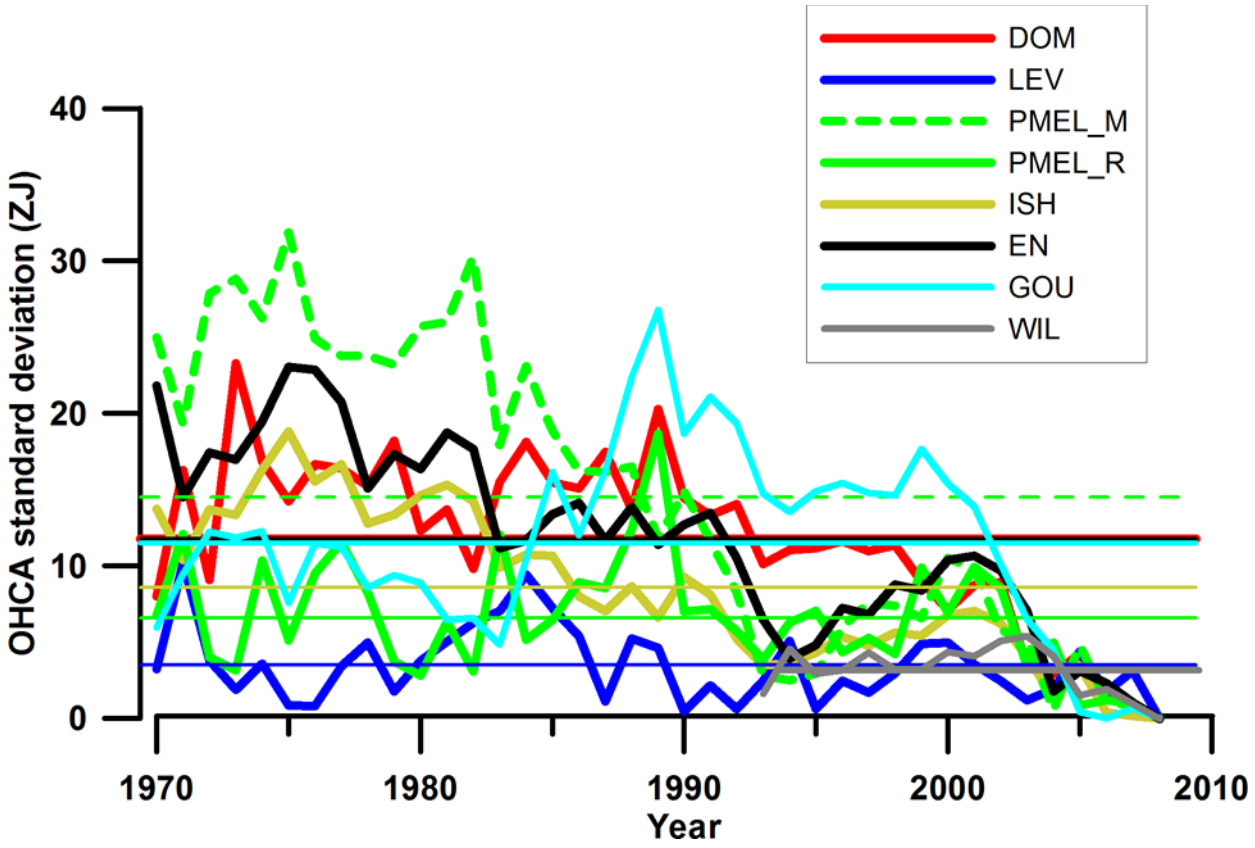

Figure 4.9. Standard deviations of for the yearly ensemble means of global OHCA (ZJ) for 1970– 2008 based on three different baseline climatologies for each mapping method (see legend). Horizontal lines represent mean standard deviations over full time period

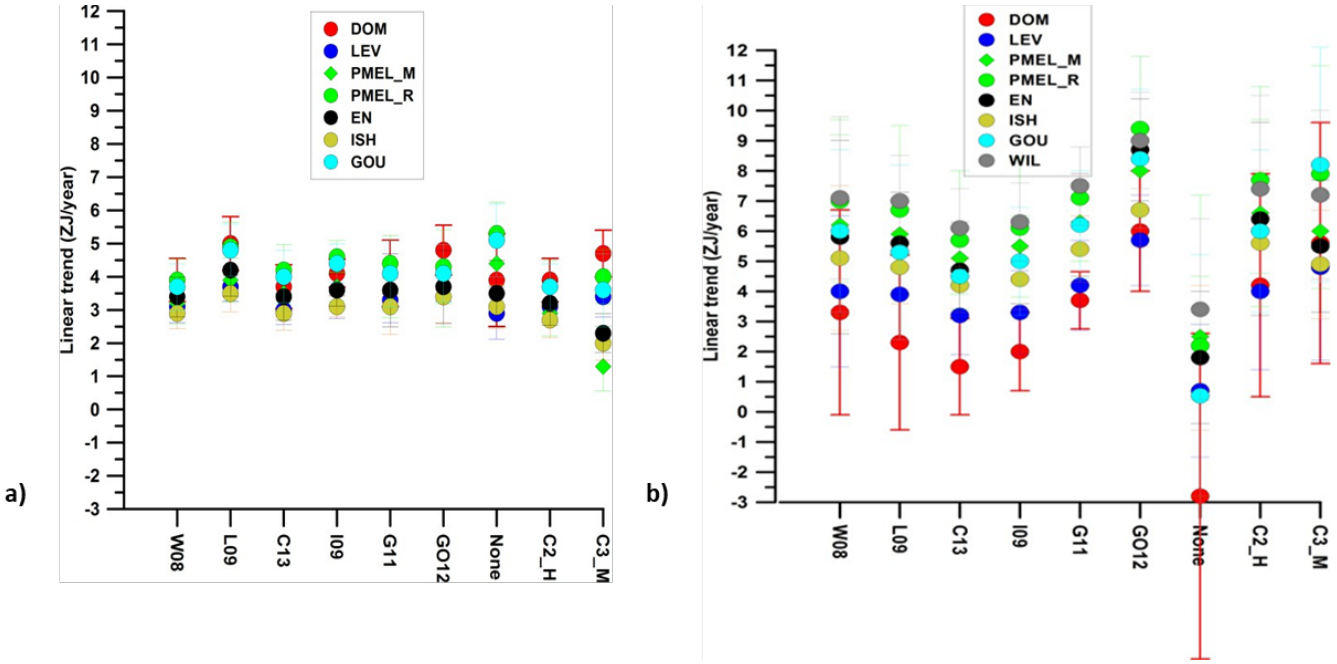

Figure 4.10. Linear trends (filled circles) of annual globally integrated OHCA (ZJ yr-1) with standard errors of the mean (error bars) for a) 1970–2008 and b) 1993–2008 by mapping method (see legends) and for all test cases (see horizontal axis labels). C2_H and C3_M cases used W08 XBT bias corrections. W08, L09, C13, I09, G11, GO12, and None cases used C1_H baseline climatology

Chapter 5 Conclusions and future work

5.0 Conclusions and future work

Examination of OHCA as a benchmark climate indicator rather than GMST through the mechanisms which led to the global warming hiatus, exploration of the resilience of the observing system for $OHCA_O$ calculation with certainty, and comparison of differences between members of an ensemble of $OHCA_O$ time series due to different factors lead to a blueprint for future work to improve calculations of $OHCA_N$ and a full accounting of uncertainty through examination of aspects of the calculation method and improvement of the data flow and quality assurance of the historic ocean temperature profile data.

5.1 OHCA and GMST

The global warming hiatus (1998-2012) saw decadal increase in GMST of 0.05°C$decade^{-1}$, compared to the long-term (1951-2012) decadal mean increase of 0.15°C$decade^{-1}$. In contrast, OHU_N during the years 1998-2012 saw a 0-2000 m decadal mean increase of 86 ZJ, compared to average decadal increase 1971-2023 of 69 ZJ over 0-2000 m. (Note the different time period of OHU_N decadal mean increase calculation from GMST decadal mean increase. If the same period were used for OHU_N as for GMST, the decadal mean increase in OHU_N is 45 ZJ, but the 1955-1970 period is data sparse at deeper depths, underestimating OHU for that period.) Uncertainties are not shown, they are on the order of 10 ZJ annually 0-2000 m based on the standard error of the analysis (see Appendix A), on the same order as annual OHU, but less than 10% of the decadal signal. Near-surfaced, in the upper 150 m, there was less OHU_N accumulated in the hiatus period than the long-term decadal mean, but at deeper depths, more OHU_N accumulated during the hiatus period than the long-term decadal mean (Figure 5.1). Increase in North Atlantic subduction during the hiatus period, as detailed in Chen and Tung (2014), is a

mechanism by which OHU increases at deeper depths. Another mechanism discussed in terms of the hiatus which leads to OHU variability is the PDO. The hiatus period was a period of negative and occasionally neutral phase of the PDO characterized by near-zero (+0.03 ZJ 0-2000) annual OHU_N in the north Pacific (20°N-60°N; Figure 5.2). The earlier negative phase of the PDO (represented here in the years 1960-1976) exhibited a negative mean annual OHU less than -0.5 ZJ, while the positive phase PDO 1977-1997 immediately preceding the hiatus period had mean annual OHU_N greater than +0.5 ZJ 0-2000 m. The positive phase of the PDO following the hiatus period had a mean annual OHU greater than +2.7 ZJ 0-2000 m, with +2.4 ZJ accumulating in the top 300 m. North Pacific OHU_N for 2022-2023, a negative phase of the PDO are not shown as the current phase consists of only two years. Over those two years, in the north Pacific, OHU_N is positive in the upper 100 m, but total accumulation to 2000 m is negative, more negative than the PDO phase represented by years 1960-1976. So OHU in the north Pacific has a specific pattern of accumulation in for phase of the PDO, but the negative/neutral phase of the PDO in the hiatus period regionally decreases OHU in the north Pacific. Again, uncertainty is not shown in the figures. For the region, 0-2000 m, the uncertainty based on the standard error of the analysis is mainly between 0.5 and 1.5 ZJ annually, but reaching as high as 4 ZJ in the earliest years. So, on an annual basis, the signal in the north Pacific, at least for years before the Argo era, is of the same order as the uncertainty. Looking more closely at the geographic distribution of OHU_N for the upper 700 m during different phases of the PDO (Figure 5.3), the north Pacific exhibits a pattern of north and east north Pacific negative OHU_N and positive OHU_N in the west and south during negative phases of the PDO (Figure 5.3a,c) and the converse during positive PDO phase (Figures 5.3b,d). So, the transport of heat from the western Pacific to the Indian Ocean during the hiatus (Lee *et al.*, 2015; Nieves *et al.*, 2015; Liu *et al.*,

2016) is another mechanism by which OHU was different during the hiatus than in the preceding and following positive phases of the PDO. There is also significant OHU_N increase along much of the north of the ACC in both the hiatus period and the following positive phase of the PDO (Figures 5c,d). To really isolate the short-term flow of heat between the atmosphere and ocean to understand the fluctuations of OHU during the hiatus period and their effects on long-term heat storage vs. short-term storage in the atmosphere, OHU at regional scale and on a monthly time span is necessary, through the careful use of *in situ* data, either mapped to a complete grid, or as input to reanalyses models. At the annual time scale, OHU is a better indicator of EEI than GMST as shown through the rate of increase during the hiatus period of OHU, but not GMTS.

Mean SST was higher in 2023 than in any previous year, with the anomaly from long-term mean more than four standard deviations from the long-term mean anomaly in 2023 (Huang *et al.* 2024). However, OHU_N was 9 ±5 ZJ in 2023 (Cheng *et al.*, 2024), roughly equal to the 9±9 ZJ increase in 2022 (Cheng *et al.*, 2023), with smaller uncertainty. In 2022, the third year in a row with a La Niña, there was essentially no OHU_N accumulation in the upper 100 m, increasing to 9 ZJ cumulative for the upper 300 m, with little additional accumulated OHU_N below that depth to 2000 m. In 2023, accumulated OHU_N in the upper 100 m reached 26 ZJ, with most of that excess uptake compensated by 300 m depth, and to a level equal, within uncertainty to 2022 OHU_N by 2000 m depth (Figure 5.4). Geographic distribution of OHU_N (Figure 5.5) shows the main area of accumulation in the upper 700 m along the central and eastern equatorial Pacific and along the eastern Pacific coast in both directions north and south of the Equator. Note the contour interval in Figure 5.5 is an order of magnitude larger than the contour interval in Figures 5.3. Alison *et al.* (2020) show that OHU signal in the upper 0-100 m is negatively correlated with the signal 100-250 m, a signal strongly influenced by the tropical Pacific, with the clearer

signal of OHU found by integrating to deeper depths. This is evident in the comparison of OHU_N in 2022 and 2023. The cumulative OHU_N by depth shown in Figures 5.1 through 5.5 are all annual OHU_N. While La Niña conditions spanned the entire year in 2022, El Niño onset in 2023 did not occur until the middle of the year, so an annual mean OHU_N does not resolve conditions in one ENSO phase nor the other, nor, critically, conditions in the transition from one phase to the other. Similarly, annual OHU_N does not fully represent that period of transition of the PDO which may be affected by short time span changes in atmospheric forcing. von Schuckmann *et al.* (2023) show annual atmospheric heat content time series which exhibits spikes in strong El Niño years such as 1998 and 2010 of as much as 2 ZJ, a significant proportion of yearly EEI. It may be that in El Niño years, the atmosphere is retaining large proportions of EEI on the scale of months. Investigation of OHU_O at sub-yearly scales is important future work which can only be carried out with a full accounting of uncertainty with the smaller available set of observations on shorter time scales. Hansen *et al.* (2023) argue that thresholds of 1.5℃ GMST will be passed in the 2020s, and 2.0℃ by 2050, more rapidly than estimates from the IPCC AR6, due, in part, to ultrafast feedbacks not accounted for by current calculations of ECS. Hansen *et al.* (2023) also notes that the difference between observed SST and predicted SST based on ECS of1.0℃ and ECS of1.5℃ is due to the effects of aerosols which are decreasing in the atmosphere, also noting that underestimates of ocean mixing in many models is compensated by increasing the aerosol forcing parameter. Finally, Hansen *et al.* (2023) note that satellite monitoring of EEI and ocean *in situ* monitoring are essential for understanding climate change. As with the global warming hiatus, the difficulty in using GMST as the benchmark indicator for changes due to greenhouse gas emissions is evident in Hansen *et al.* (2023), pointing to OHU as the potential benchmark indicator, if uncertainty can be better quantified and, ideally, lowered.

The ensemble of OHCA calculations (*in situ*, satellite, model) show a spread in both OHU and acceleration of OHU between 0.40 ± 0.12 to 0.96 ± 0.08 Wm^{-2}, and -0.03 ± 0.13 to 1.11 ± 0.6 Wm^{-2} dec^{-1} respectively as shown in Hakuba *et al.* (2024).

5.2 Mapping method improvements

Examination of the uncertainty between OHCA ensemble members shows sources of uncertainty which need to be addressed as well as a general need to examine all aspects of the objective analysis process specifically for $OHCA_N$, as follows:

5.2.1 Baseline mean

In principal, there should be no difference in $OHCA_N$ calculated from different baseline long-term mean climatologies excepting an offset due to any difference in the observation years used to calculate the climatological mean. A climatological mean encompassing more recent years would be expected to be warmer than a climatological mean encompassing earlier years. OHCA based on more recent year baseline would be lower in absolute values, but with the year-to-year variations equal to OHCA using an earlier year baseline. However, given the highly heterogeneous observation pattern for ocean profiles, the baseline climatology will reflect the highly heterogeneous observation patterns of ocean profiles in data sparse areas and times, even when steps such as decadal averaging are taken to homogenize the baseline climatology. Experimentation is underway on the use of a baseline climatology for the 1991-2020 period. This period encompasses the WOCE project in the 1990s and the Argo program from 2001 onwards, a period in which the upper 2000 m of the ocean is covered in as seasonally homogeneous and geographically complete manner as is available in a 30-year period. A 30-year period is the period considered a climate normal, of sufficient length to represent a mean climate state (WMO, 2017). Figure 5.6 compares $OHCA_N$ (which uses WOA09 as a baseline climatology) with $OHCA_N$ using WOA23 decadal mean climatology (1955-2020) and $OHCA_N$ using WOA23 1991-2020 climate normal, Figure 5.6a with the initial time series, Figure 5.6b,

the time series all referenced to the 1991-2020 period. Accounting for the offset, the time series are quite similar, nearly identical after 2001. Moving back in the time series, $OHCA_N$ diverges from the $OHCA_N$ calculated with WOA23 baselines. Some of this can be attributed to the different vertical resolutions and updated quality control of the observations in the WOA23 baseline cases. The two cases using the WOA23 baselines do not diverge greatly further back in time, though there is a small offset, even after being referenced to the same time period. Exploration is ongoing into the optimal baseline climatology for $OHCA_N$.

5.2.2 Depth resolution

The number of depth levels in the WOA has increased from the WOA09 baseline for $OHCA_N$ to the latest version, WOA23 from 26 levels between the surface and 2000 m., to 57 levels. In the top 100 m., the resolution is 5 m for WOA23 (variable for WOA09). This is to allow for better resolution of vertical features in the water column. Helber *et al.* (2012) shows that mixed-layer depth calculated from lower resolution observations is generally deeper than from high-resolution (3 m. or less) observations. It is worth exploring whether higher vertical resolution can better quantify $OHCA_N$ as well, potentially limiting the penetration from the surface to depth by diminishing the volume around each standard depth level which is represented by the standard depth level. First experiments, as shown in Figure 5.2, do not show differences in the time period with the most prevalence of high-resolution observations (2001-2020), which would presumably allow for better vertical standard depth resolution of OHCA. More work is necessary to quantify any changes due specifically to vertical resolution. Increased vertical resolution, even if it does not significantly affect the global integral of $OHCA_N$ can be useful in better quantifying specific vertical layers, aiding better quantification of cumulative OHU_N by depth, such as in Figure 5.1. Extending $OHCA_N$ below 2000 m is another means to improve the

calculation and provide more utility for OHU comparison with EEI. Even if OHU to depths deeper than 2000 m is less than 5% of total annual OHU (Purkey and Johnson, 2010, updated in Meyssignac *et al.*, 2019), regionally identifying areas of deep changes in energy uptake and quantifying interannual and long-term changes in these areas is important for understanding changes in the oceans capacity to store energy at deeper depths. Deep temperature observations have historically been limited mainly to repeat hydrographic cruises on a decadal time scale. The Deep Argo program is in the process of deploying floats which can reliably observe the ocean surface to bottom. However, Deep Argo deployments across the global ocean have been slowed by funding and logistics concerns. Deployment of Deep Argo floats specifically to areas in and near deep transport of heat is critical to fully monitor $OHCA_O$ in the global ocean.

5.2.3 Ocean volume

Hakuba *et al.* (2024) show that different published calculations of OHCA use different ocean volumes. Some do not include high latitudes (between 60°N and 60°S) due to sparsity of data and expected small contribution to global OHCA. Others do not include ocean areas less than 300 m. depth due to high short-term variability and often lack of data. As shown here, difference in ocean volume used can account for up to 4% difference in $OHCA_O$. For $OHCA_N$ the defined coastline/ocean bottom is based on a superseded version of the ETOPO bathymetry. For comparison of OHCA from different sources, the difference in ocean volume should be accounted for. For $OHCA_N$, the use of the most up to date version of ETOPO is future work, along with an accounting of the difference the change in bathymetry makes in $OHCA_N$.

5.2.4 First-guess field

A difference between described mapping methods is the means by which data sparse analyzed ΔT values are calculated (or assigned). For $OHCA_N$, a first-guess field of 0.0°C is used, leading to a relaxation to no change in areas with no data at all within the largest radius of influence (8°in latitude/longitude at the equator). A first-guess field closer to the actual final $OHCA_N$ filed should lead to yearly values of $OHCA_N$ further from the baseline mean, leading to more certainty in interannual variability and long-term trend of $OHCA_N$. The difficulty is in understanding the interannual patterns of warming and cooling in the different areas of the ocean and the correlation length scales of OHCA. Correlation length scales of ocean circulation patterns are not necessarily the same as for surface heat flux which has a strong latitudinal insolation component. A solution used in Cheng and Zhu (2016) is a large initial radius of influence of > 20° latitude/longitude at the equator. This is well beyond correlation length scales for OHCA, at least meridionally in most areas. Rather the first iteration of the objective analysis, even if the first-guess field were 0.0°C, will have few, if any, grid boxes with no observations within the radius of influence. The results of this iteration are a first-guess field for the next iteration, in effect hewing closer to the original method of Barnes (1964). A first-guess field based on *in situ* data in some proximity to a grid box is expected to be a better first-guess value than 0.0°C. An uncertainty can be calculated based on the distance of the observed means within the large radius of influence relative to the correlation length scale. This is work in progress.

Comparison of different methods for calculating yearly $OHCA_O$ from heterogeneous observed mean distributions is a partial quantification of the uncertainty of the calculation. It is also informative in suggesting areas of improvement for individual mapping methods, in this case $OHCA_N$. Improvement in the method which need to be explored as means to diminish the uncertainty in $OHCA_N$ include investigating the use of a more homogeneous baseline

climatology, in mean time for observational means and across seasons; higher vertical resolution; an improved bathymetry for better accounting of ocean volume; and a more realistic first-guess field than 0.0°Ceverywhere. If these improvements can lead to lower uncertainty for $OHCA_N$, they can also lower uncertainty for an ensemble of OHCA calculations from *in situ* ocean profiles.

5.3 Establishing uniform data set for OHCA calculation

The WOD is an international project of the International Oceanographic Data Exchange (IODE) which has grown out of the need for reproducibility of the WOA climatological mean fields and the time varying climate indicators calculated with the WOA climatologies as a baseline, first and foremost $OHCA_N$. WOD is updated quarterly with recent temperature observations for calculation of $OHCA_O$. WOD is also updated with previously unavailable historic data sets, and updates, improvements, corrections to existing observations in the WOD. An example is current work by Kizu and Reseghetti through the International Quality Controlled Database (IQuOD) project to meticulously check XBT profiles in the WOD against original cruise reports to identify those which are actually AXBT dropped from aircraft rather than ship-based XBTs. AXBT have a very different drop-rate and correction than ship-based XBTs (Boyd, 1987; Boyd and Linzell, 1993). AXBTs have been particularly prevalent in Gulf of Mexico both for general surveys and hurricane condition observations. Regional OHCA in the Gulf of Mexico is a factor in sea level rise along the coast of the Gulf of Mexico, and has indeed been increasing at a higher rate that the global ocean (Wang *et al.*, 2023). The WOD, the base dataset for Wang *et al.* (2023) analysis of OHCA, is constantly changing, in this case in a way that can affect the historical OHCA in the Gulf of Mexico which will affect the trend calculations for $OHCA_N$. There are other historical ocean profile data sets which have been assembled as input data to $OHCA_O$

(among other uses). The EN4 data set (Good *et al.*, 2013) contains a data set of temperature and salinity profiles used for calculation of monthly gridded temperature means and $OHCA_O$ at the U. K. Met Office. EN4 is updated periodically from the WOD, but not as frequently as updates are made to historical data in the WOD. The Coriolis Ocean Dataset for ReAnalysis (CORA; Szekely *et al.*, 2019) is a data set which incorporates both EN4 and WOD temperature profiles to be used for assimilation into ocean RAs at the Copernicus Marine Environmental Monitoring Service (CMEMS) including the in-situ analysis system (ISAS) OHCA (Gaillard *et al.*, 2016). CORA is not updated from the WOD as frequently as the WOD historical data are improved. It is also the case that EN4 and CORA have other sources of historic data which are not in the WOD. Using different input historical data sets is a source of uncertainty in historic $OHCA_O$ that can be eliminated if a globally managed data set, the WOD were used as a community best copy for ocean casts, and data sets constructed for specific institutions or projects were regularly updated from the WOD, or used the WOD directly. It is similarly recognized that the Argo data set is continually updating not only with new observations, but with quality-controlled versions of existing observations. The pace of update and improvement to existing observations is faster than the pace of update of the WOD from Argo and Argo recommends using the data directly from the Argo Global Data Assembly Center rather than a composite data set such as WOD.

The WOD only contains information that is available with the individual data sets in the NCEI archive or in associated cruise reports or other published sources. The information necessary to correctly utilize the observations is not always available. For instance, more than half of XBT temperature profiles do not contain information on the probe type as there was not thought to be differences in the performance of the different probes. It is now well known that bias corrections are probe type dependent. Even if the information is not available, there are some markers of the

data which are available which can be used to make an informed decision on which probe type was used. For instance, if an XBT was dropped from a Japanese ship, it is very likely it was manufactured by TSK. Based on the depth of the temperature profile, the type of TSK can be inferred. In this way, the IQuOD project has constructed 'intelligent metadata' to designate the probe type for every XBT cast which does not otherwise have this information in the WOD (Palmer *et al.* 2018). If this information is used when preparing observed temperature profiles for observed means for $OHCA_O$ calculation, a source of uncertainty, lack of metadata, is diminished.

5.4 Establishing best practices in quality control of observations

Even when using a best copy of historical ocean casts, decisions on which profiles, which individual observations, to use in calculating the observed means, method of interpolation to standard depths, the standard depths chosen, all lead to differences in $OHCA_O$ calculated. Some of the published work detailing different quality assurance steps from temperature observations to observational mean are Boyer and Levitus, 1994 (NCEI), Szekely *et al.*, 2019 (CORA), Good *et al.* 2013 (EN4) and Tan *et al.* (2023); IAP. Different choices based on quality tests to go from temperature observations to observed means becomes another source of uncertainty. As part of the IQuOD project, a survey of automated quality assurance tests across different groups who were preparing temperature profile data for observed means for $OHCA_O$ calculation was executed, comparing the results from different combinations of tests against expert (visual) quality-controlled data sets – one a subset of AniBOS data, the other a subset of Argo profiling float data (Good *et al.* 2023). Realizing that utilizing the maximum amount of data possible is

one priority, minimizing the amount of anomalous data is another, Good *et al.* (2023) suggests three sets of tests, one to minimize anomalous data marked as good for $OHCA_O$ calculation, one to minimize suitable data marked as anomalous, and a compromise between the two. Even with three choices, the formalization of an internationally agreed upon set of quality assurance for temperature observations for $OHCA_O$ calculation would be a step toward reducing uncertainty due to choices of which observations to utilize for $OHCA_O$ calculation. This is a work in progress.

5.4.1 Distinguishing between anomalous surface flux and anomalous internal heat transport

The final mean/standard deviation filter in the calculation of the observed means, both for the baseline climatological mean and $OHCA_N$ calculations, is, in essence, a purpose specific quality assurance step to ensure anomalous observations are not incorporated into the observed means where the objective analysis will tend to exaggerate the magnitude and geographic extent of the anomalous observations. Observations, especially by Argo in areas and seasons without a great deal of historic observations, are recording features which are far from the long-term mean simply because the features have not been observed before. As noted before, in a point source observing system, an eddy representing large lateral heat movement without a corresponding measurement of the heat loss in the area from where the eddy was spawned will be represented in $OHCA_N$, even though it does not represent surface flux. At the same time, a greater number of Argo temperature profiles are flagged using the mean/standard deviation filter in more recent years, not due to mesoscale features, but due to the large recent warming in some areas which is beyond 3-5 standard deviations from the long-term mean. Kuusela and Stein (2018) describe a statistical mapping method with methodology for dealing with observations at the tails of the

Gaussian distribution for temperature which are cross-validated with covariance matrices. This method has been utilized to calculate $OHCA_O$ in the Argo era (Kuusela and Giglio, 2022), it is not certain the performance of the method in earlier data sparse eras. Figure 5.7 shows $OHCA_N$ from 2005-2022 using only Argo program quality flagging and $OHCA_N$ using the mean/standard deviation filter. The difference is consistently around 10% (larger in the earliest years), with the Argo flagging only $OHCA_N$ always higher. A means to preserve data which are simply warmer than the long-term mean/standard deviation while identifying observations which are in anomalous features can allow for differentiation anomalous dynamic features representing lateral heat movement and warming due to surface flux. Tan *et al.* (2023) utilizes a median filter instead of a mean filter with an increase in resultant $OHCA_O$. Reagan *et al.* (in prep) is examining identifying areas (time, depth, geographically) in which temperature observations are Gaussian, rather than the single depth layer 5° grid boxes over which the filter is applied now. A method for detecting mesoscale eddies (Roman-Stork *et al.*, 2023) using altimeter and other satellite measurements is also being test.

5.4.2 Weighing observations based on measurement uncertainty

Accounting for the different uncertainties for different temperature instruments (reversing thermometer, single depth thermistor, CTD, etc.) on different platforms (ship, Argo float, glider, buoy, etc.) can factor in to the calculation of the observed mean for $OHCA_N$ calculations. In the calculation of an observed mean for a grid box, individual observations can be weighted based on the uncertainty of each observations. For instance, if there are 3 CTD observations, 2 XBT observations, and 1 MBT observations all on the same standard depth in the same grid box, the 3 CTDs can be weighted more heavily than the 2 XBT, which are weighted more heavily than the 1 MBT. Assigned uncertainties to each observation also allows for use in calculation of the

overall uncertainty of $OHCA_N$ in a more complete accounting that simply using the standard error of the objective analysis. To facilitate these uses, Cowley *et al.* (2021) assigned an uncertainty to each observation in each temperature profile based on the manufacturer's specifications for accuracy of the pressure (depth) and temperature of the particular instrument on the given platform. This is a first step, as the uncertainties ideally will also reflect the level of calibration/processing applied to the observations, the measurement method (e.g. signal digitization and calibration of XBTs as per Roemmich and Cornuelle (1987), and any other factors which can affect the uncertainty. The Argo program assigns its own uncertainty value to each observation from Argo floats based on manufacture specifications and level of quality inspection.

5.4.3 Accounting for point source representation error

Another factor in an uncertainty calculation for point source ocean observations is the representation error (Elipot *et al.*, 2022). How well can an observation at a single point in time and space represent a designated geographic area (1°grid box in $OHCA_N$) over a given time frame (one year in $OHCA_N$ calculation). The IQuOD project is exploring the use of standard deviation of temperature observations over 1° grid boxes as a measure of representation error as a contribution to the overall uncertainty of $OHCA_O$ calculations. The difficulty in the quantification of representation error is that it is dependent on the time and space which are to be represented by the point source observations. Sparse data coverage also limits the utility of a representation error as it is difficult to assess if the observations in a given area represent all possible states of the area. For the first time in the WOA series, the WOA23 includes objectively analyzed fields of standard deviation from the mean of temperature in 1° grid boxes. These fields will be used to explore quantification of the representation error as part of the

uncertainty quantification for $OHCA_N$. Given that the objectively analyzed mean fields of standard deviation are still based on a limited set of observations, the use of models to also quantify standard deviation and representative uncertainty is being explored.

The quantification of uncertainty due to sparse data distribution is another aspect of assembling a complete uncertainty for $OHCA_O$ calculations. Kuusela and Stein (2018) for instance, calculate robust uncertainty statistics, but under the assumption that data distribution can be treated as the same in each year. This may be a viable statistical assumption using only Argo data in the Argo era, but is not a viable assumption in earlier years. Lyman and Johnson (2008) subsampled Archiving, Validation, and Interpretation of Satellite Oceanographic (AVISO) sea surface height data at distributions of *in situ* temperature observations for each year, using the difference between objectively analyzed fields and actual AVISO fields as a measure of uncertainty due to data distribution for a single mapping method. The MapEval4OceanHeat project is utilizing ocean model data in a similar fashion across a number of mapping methods to calculate uncertainty based on data distribution for the different mapping methods. It is particularly critical in areas of high baroclinicity where eddy generation is common and a major mechanism of energy transport, not only laterally but to deeper depths, not only to quantify representation error, but to increase observations in order to observe both the mesoscale eddies and the region of high baroclinity from which the eddies were formed. This is of particular importance along boundary currents and areas of high baroclinicity, with the ACC as a primary example, an area in which Argo floats do not spend much time due to quick transport. A means to rapidly replenish floats in the ACC or utilize other observation platforms, such as gliders, is necessary to adequately sample this highly active heat transport area.

5.4.4 Continued investigation of instrument bias correction

Finally, while the C14 XBT correction has been found to be the most reliable of all available corrections (Cheng *et al.* 2016), it is important to continually compare with other methods and refine as needed. Figure 5.8 shows the current yearly $OHCA_N$ method with WOA09 baseline and L09 XBT bias corrections in comparison with three iterations of $OHCA_N$ calculated from WOA18 baseline, yearly with L09 XBT bias corrections, five-year running mean OHCA with L09 corrections and five-year running mean $OHCA_N$ with C14 corrections. The WOA18 baseline for the OHCA using L09 corrections is a variant of the WOA18 published baseline which was calculated itself using L09 corrections, whereas the published WOA18 uses the C14 corrections. In the 1990s the two $OHCA_N$ time series calculated using the C14 corrections are nearly flat with a steep increase in 2001 whereas the time series using the L09 correction have a near-linear (with inter-annual variations) increase through the 1990s with no jump in the early 2000s. The reason for the difference is that the C14 corrections used the pre-Argo profiling floats from the WOCE period in matchups with XBT data in the calculation of the XBT bias. The matchup and the resultant overcorrection of the XBTs in the 1990s actually points to a possible pressure observation problem in the pre-Argo floats. So, not only should the XBT corrections be calculated without using the pre-Argo profiling floats, but the pre-Argo floats should not be used in calculations of $OHCA_N$. In addition to XBT corrections, more work needs to be done for the current $OHCA_N$ calculation to investigate the use of the Gouretski and Cheng (2020) MBT bias corrections so that the best available corrections are used. Similarly, the use of the corrections for reversing thermometer (bottle cast) data as defined by Gouretski *et al.*(2022) needs to be investigated.

5.4.5 Need for continued monitoring of ocean observing system and for robust uncertainties

The observing system for ocean temperatures, with the Argo profiling floats in near-full geographic coverage of the ice-free ocean outside of shallow seas and shelf regions since at least 2007, provides seasonally consistent yearly $OHCA_O$ with good agreement between different methods. Even through the pandemic with the disruption in merchant, passenger, and research ship cruise, the autonomous Argo profiling floats maintained a high percent coverage of the global ocean. But this global coverage is tenuous, relying on extended battery life for Argo floats and dedicated logistics from a coalition of countries, institutes, and ship operators. Further, quality observations for comparison is dependent on research grade CTDs from research ships. Research ships are also the primary means of deploying Argo floats to keep the network of floats comprehensive globally especially in areas not often replenished. It is of high importance to maintain the Argo array for $OHCA_N$ calculations to monitor EEI. The continuous quality monitoring or Argo needs to continue to ensure the certainty of $OHCA_O$ calculations. This quality monitoring is greatly facilitated by observations from research ships, but also from other ocean subsurface temperature observing systems. Further, a complete accounting of uncertainty factors is necessary to understand how effective a measure of EEI is $OHCA_O$, including measurement uncertainties, representation error, and uncertainties due to data distribution. This is current and future cross-community work in conjunction with the IQuOD project and the MapEval4OceanHeat project.

5.5 The need to maintain operational $OHCA_N$ calculation system

It is also important for understanding the time evolution of $OHCA_N$ (OHU_N) and EEI to continually improve the WOD as a database of record for ocean profile data, to make sure that local databases for $OHCA_O$ calculation are in sync with the database of record, and to work to a utilization of the most effective set of quality control checks and anomaly filters. A note of caution, $OHCA_O$ time series are highly used across ocean and climate communities. Research into improvements in mapping methods and data handling are occurring simultaneously with the use of the results. Implementation of improvements to either need to be vetted and clearly explained in the peer-reviewed literature. The published methods need to be implemented in a robust data flow and calculation sequence. Table 5.1 shows the results from yearly papers (Cheng *et al.*, 2019, 2020, 2021, 2022a, 2023, 2024) list of 5 highest years in the Institute of Atmospheric Physics (IAP) $OHCA_O$ and $OHCA_N$ time series. Some of the differences from paper to paper for the same year are due to data added to the WOD and additional quality control by the Argo program, but most of the change is due to improvements in mapping method or quality assessment, or inconsistencies in the data flow from WOD.

5.6 Concluding remarks

OHCA is of primary importance for understanding time variations of EEI. It may not be the factor that directly affects all human population, as does surface temperature, represented by GMST, but the storage of energy in the ocean, and the year to year variations in storage are a controlling factor in the accumulation of heat in the atmosphere which is reflected in GMST. Small changes of OHCA relative to the yearly global integral can have large effect on temporary and long-term storage of heat in the atmosphere. It is also important to understand how short-term variations in atmospheric circulation and heat storage affect OHU and the advection of heat energy in the ocean to deeper depths where long-term storage on the order of decades to

centuries occurs. This requires monitoring of OHU on regional scales and on sub-annual time scales. This is difficult using point source *in situ* data with incomplete coverage. The current observing system, with Argo profiling floats at the forefront has dramatically increased ocean coverage in the upper 2000 m and has proved resilient, even through highly disruptive events such as the COVID-19 pandemic. The current observing system can still bear improvement to sustain OHU monitoring on a monthly time scale and to improve coverage in specific regions of the ocean. Better coordination between elements of the observing system, such as gliders on continental shelves, near-shore and in enclosed seas, ice-tethered profilers, in the Arctic, and research and ship of opportunity programs for areas in and near high velocity ocean currents, where Argo floats have short residence times can ensure more complete coverage. Continued implementation of Deep Argo and decadal hydrographic cruises will allow for better quantification of OHU below 2000 m. Even if OHU below 2000 m is less than 5% of total OHU, where the deep uptake is occurring is critical for understanding the changing atmospheric circulation and ocean state effects on overall heat storage in the ocean. While the current subsurface ocean observing system has succeeded in increasing coverage for and lowering uncertainty in OHU_O monitoring, there is only a fixed set of observations available for extending OHU_O time series back in time to sufficient length to study multi-decadal evolution of OHU. Steps can be taken to lower the uncertainty of OHU_O calculations from historical data by careful international coordination of the historical data set, utilizing global knowledge of the observations to organize a best-copy of subsurface ocean temperature observations with correct metadata, highest available resolution, best practice bias corrections, and uncertainty quantification at the measurement level, as is being implemented by the World Ocean Database and the International Quality Controlled Oceanographic Database (IQuOD). Even with a best-

copy historical data set and an optimized current monitoring system for OHU, there is still a need for optimizing methods for estimating a complete, regularly gridded OHCAO from sparse data (historically) and from point source data which cannot fully capture lateral advection through mesoscale features. RAs have the ability to calculate full fields of OHCA from irregular *in situ* data through equations of physical motion, but the largest source of uncertainty for RA is the input is situ data. $OHCA_O$ also provides validation for RA models, as well as full coverage satellite-based estimates of OHU and EEI. So, improving individual $OHCA_O$ calculations to lower the uncertainty in an ensemble mean $OHCA_O$ is important for understanding trends, interannual variations and acceleration in OHCA across the last 65 to 70 years. Improving $OHCA_N$ and better quantifying uncertainty from all aspects of the calculation, from point source measurement to full gridded ocean field estimation, in particular is important as an independent OHCA time series dependent only on *in situ* ocean profiles to ensure it is a reliable baseline for *in situ*-based methods which incorporate SST, altimeter, and/or model data, as well as for RAs, predictive models, and satellite-only methods for calculating OHCA and EEI. Improving and utilizing all means of calculating OHCA will allow for high confidence in OHU as a primary monitoring tool for EEI and for understanding the mechanisms of interaction between the components of the Earth's energy system and their effects of short and long-term storage of energy in the system.

5.7 Tables

Year	IAP24	IAP23	IAP22	IAP21	IAP20	IAP19
2023	286					
2022	271	245				
2021	254	234	235			
2020	237	221	221	234		
2019	228	214	214	214	228	
2018			195	195	203	197
2017		202	202	202	193	188
2016					180	175
2015				186	185	180
2014						162
Year	**NCEI24**	**NCEI23**	**NCEI22**	**NCEI21**	**NCEI20**	
2023	247					
2022	238	238				
2021	229	229	227			
2020	211	211	211	211		
2019	210	210	210	210	217	
2018			196	196	196	
2017		189	189	189	189	
2016					164	
2015				180	180	

Table 5.1. Values of Ocean heat content anomaly ($OHCA_O$) in zetajoules (ZJ) calculated by the Institute of Atmospheric Physics (IAP) and the National Centers for Environmental Information (NCEI) from Cheng *et al.* (2019. 2020, 2021. 2022a, 2023, 2024) five highest OHCA anomaly years.

5.8 Figures

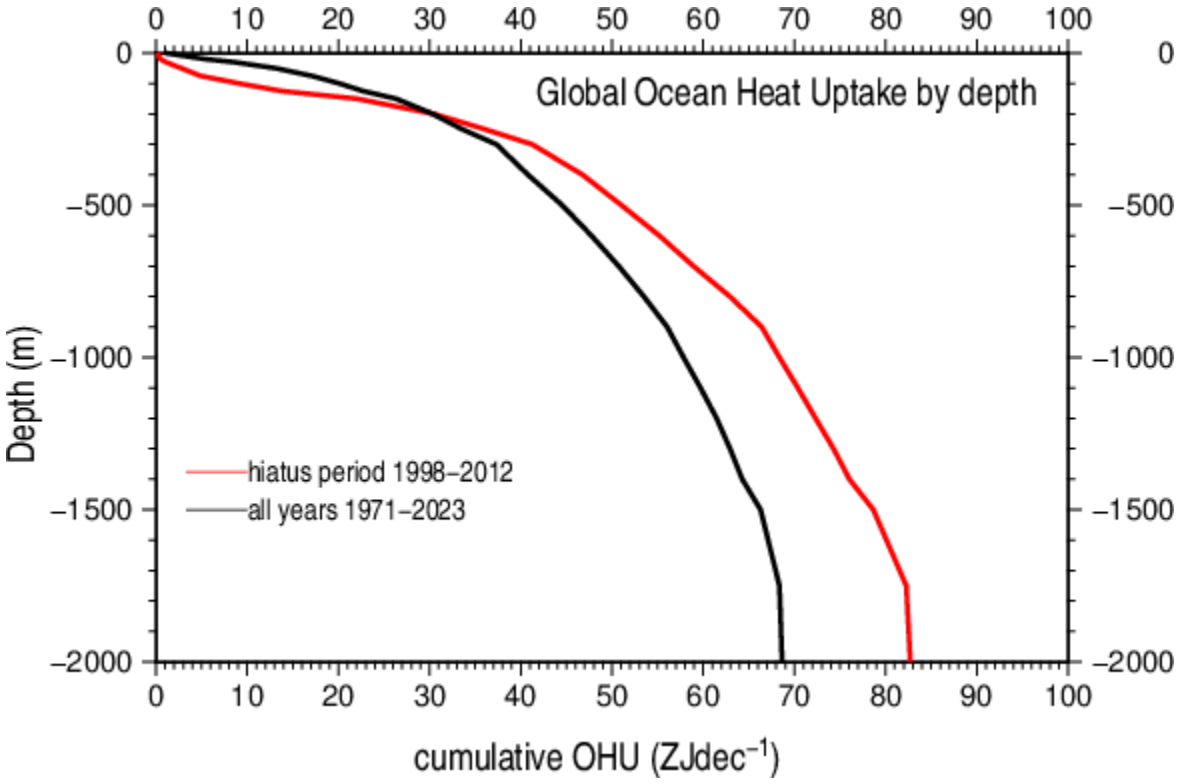

Figure 5.1. Mean decadal cumulative Ocean Heat Uptake (OHU_N) in zetajoules per decade ($ZJdec^{-1}$) from the surface to the given depth for years 1971-2023 (black) and during 1998-2012, the global warming hiatus period (red).

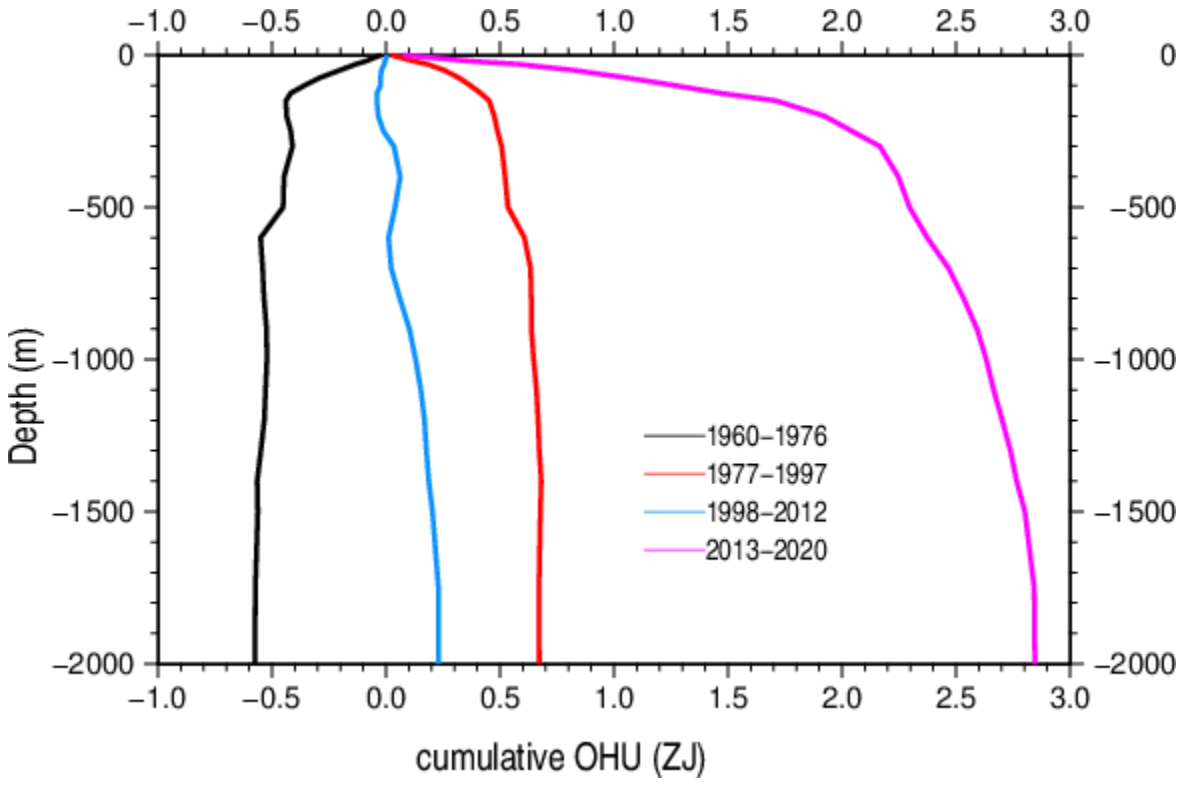

Figure 5.2. Annual cumulative ocean heat uptake (OHU_N) from the surface to given depth in the north Pacific Ocean (20°N - 60°N) during different phases of the Pacific Decadal Oscillation. Positive phases 1977 – 1997 (red) and 2013 – 2020 (purple). Negative phases 1960 – 1976 (black) and 1998 – 2012 (blue).

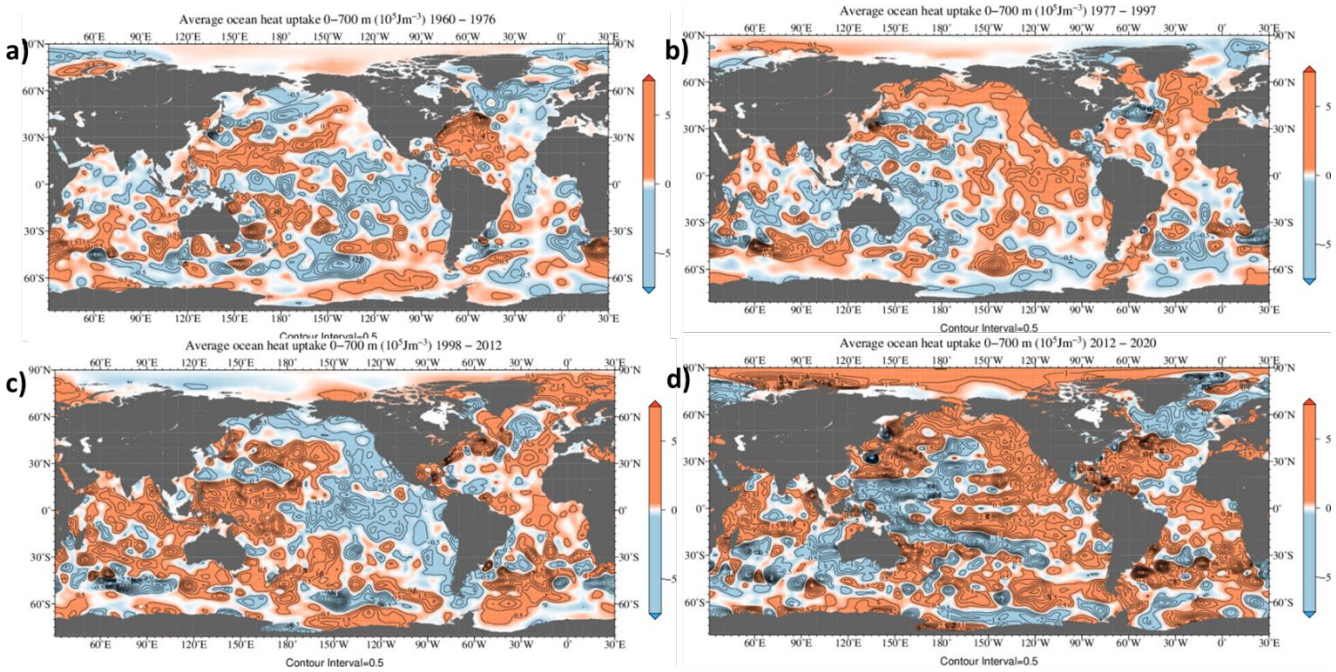

Figure 5.3. Geographic distribution of mean Ocean Heat Uptake (OHU_N) 0-700 m during different phases of the Pacific Decadal Oscillation: a) 1960-1976, negative phase, b) 1977-1997, positive phase, c) 1998-2012 (negative phase), d) 2013-2020 (positive phase). Contour interval is 0.5 x 10^5Jm^{-3}. Red shading in areas of positive OHU_N, blue shading in areas of negative OHU_N,, white areas (no shading) increase or decrease of OHU_N less than 0.5 x 10^5Jm^{-3} .

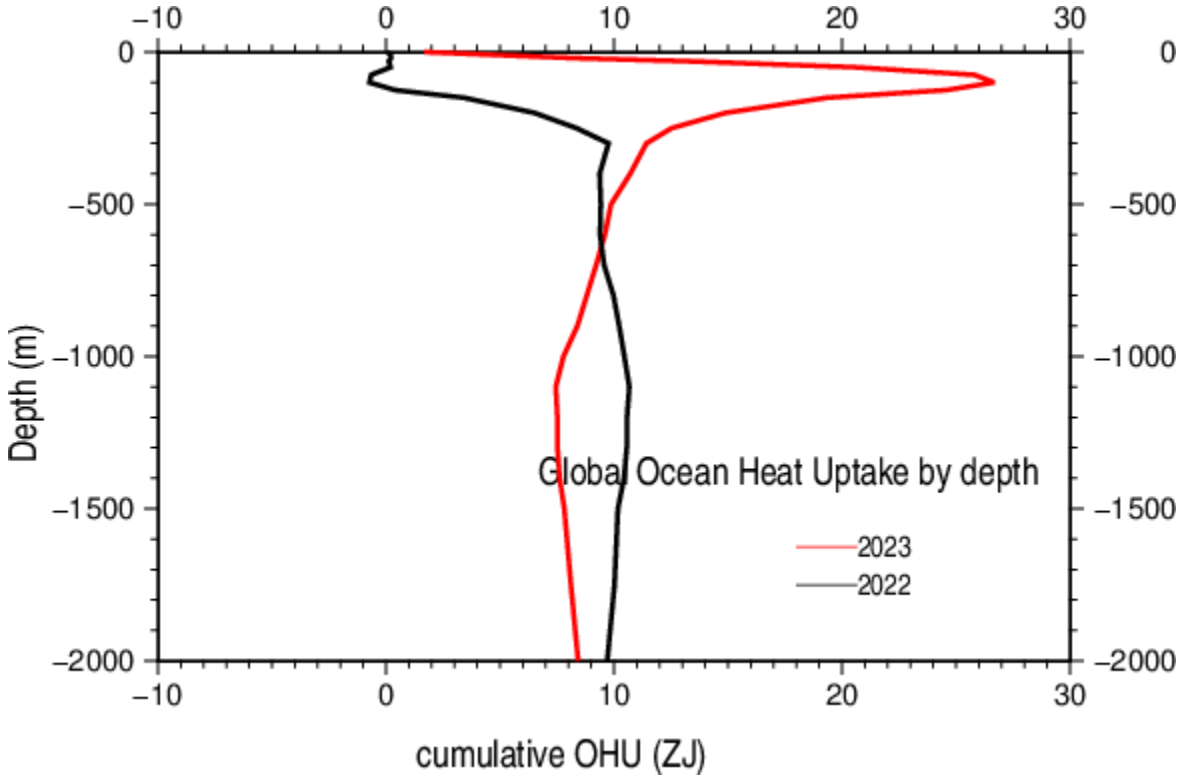

Figure 5.4. Annual cumulative Ocean Heat Uptake (OHU_N) from surface to given depth for 2022 (black) and 2023 (red).

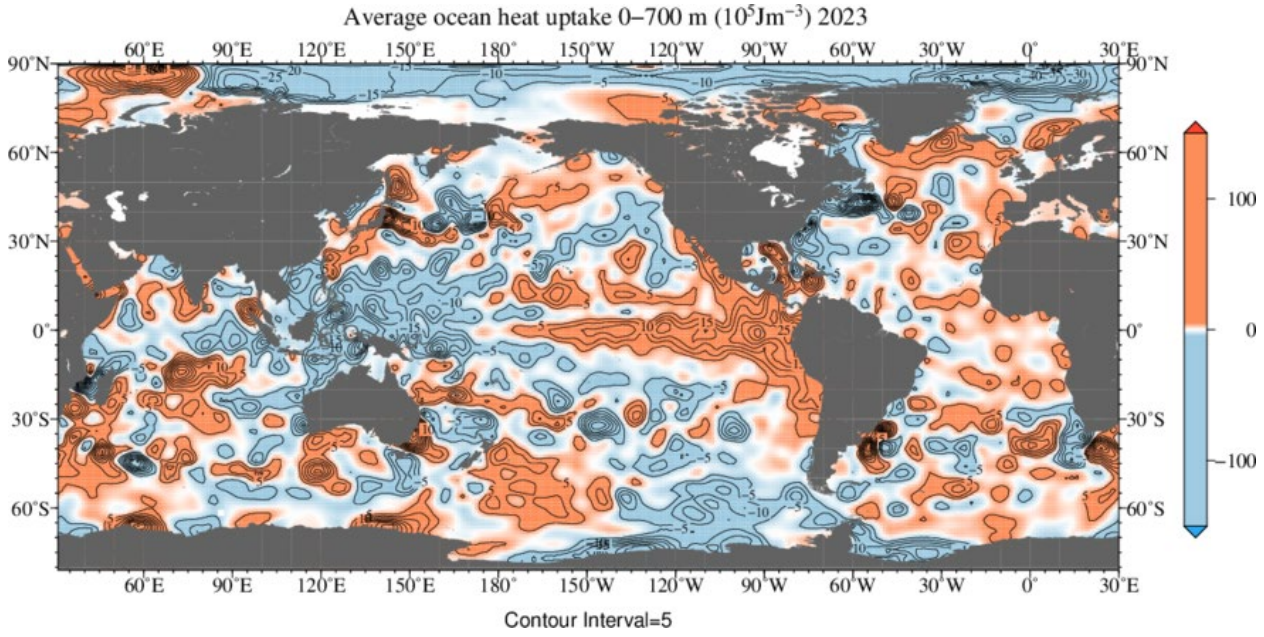

Figure 5.5. Geographic distribution of Ocean Heat Uptake (OHU_N) 0-700 m for 2023. Contour interval is 5 x $10^5 Jm^{-3}$. Red shading in areas of positive OHU_N, blue shading in areas of negative OHU_N,, white areas (no shading) increase or decrease of OHU_N less than 5 x $10^5 Jm^{-3}$.

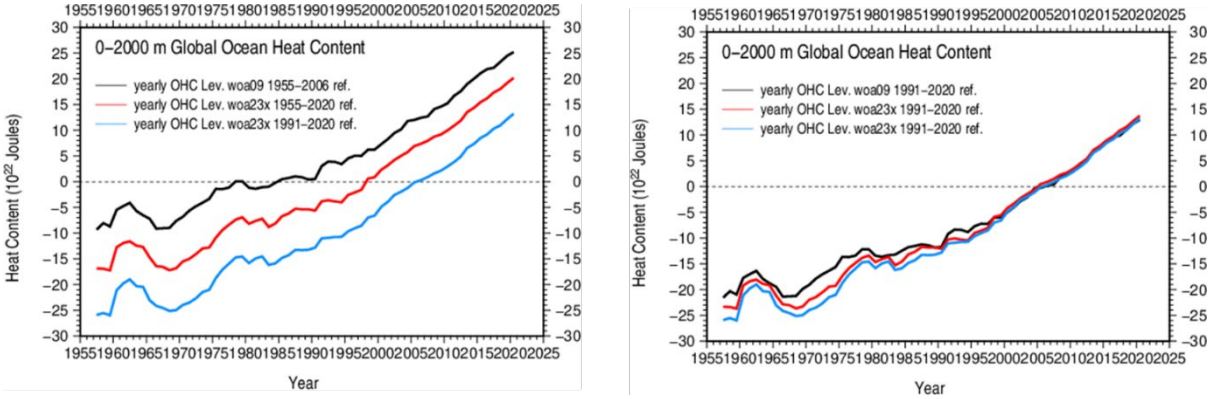

Figure 5.6. (a) $OHCA_N$(black) OHCA with Levitus *et al.* (2012) method, but with WOA23 1955-2020 baseline climatology (red), and with WOA23 1991-2020 baseline climate normal (black) (b) same as in (a) but referenced to 1991-2020 by subtracting out mean yearly OHCA 1991-2020 from each of the other time series.

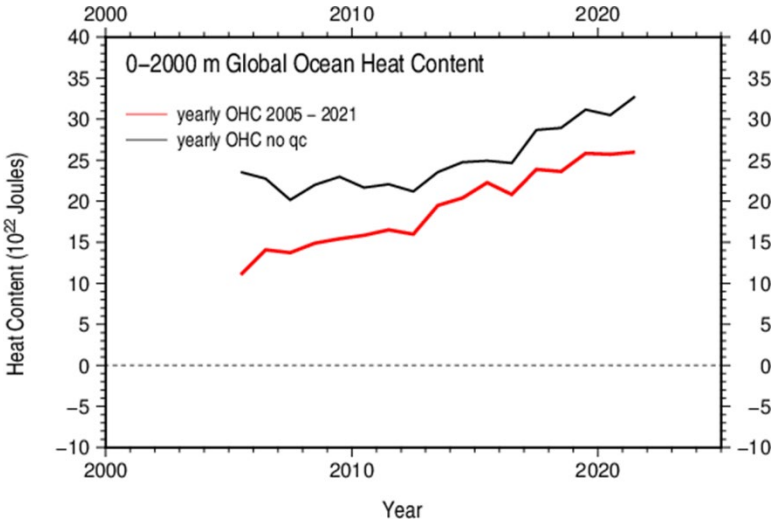

Figure 5.7. $OHCA_N$ (red) and $OHCA_N$ but with no additional quality control beyond flagging (values 3 and 4) provided by the Argo program (black).

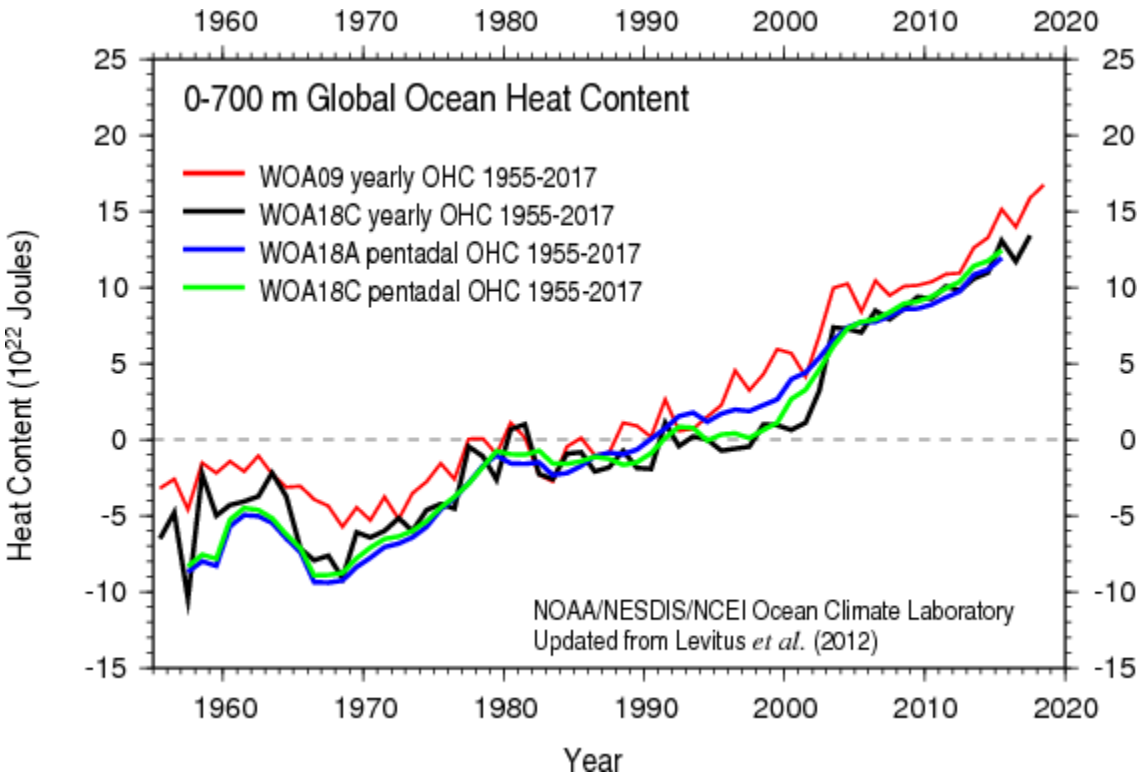

Figure 5.8. $OHCA_N$ calculations 1955-2017 yearly with WOA09 baseline, L09 XBT bias corrections (red), WOA18 baseline and C14 XBT bias corrections (black); $OHCA_N$ calculations five-year running means (pentadal) WOA18 baseline L09 XBT bias corrections (blue) and WOA18 baseline with C14 XBT bias corrections.

Appendix A Description of $OHCA_N$ method

A.1 Preparation of WOD for $OHCA_N$ calculation

All of the observational *in situ* temperature profile data are archived and preserved in the form received at NCEI. They are also uploaded to the WOD with any quality flagging performed by the data provider, as well as any provided information which is needed to describe the observations and the quality of the data. Data are split into separate data sets with similar characteristics (Table 1.1). A set of quality tests are performed on the observed profiles in the data sets (Boyer and Levitus, 1994), including minimum and maximum ranges by depth, and unrealistic gradients and inversions in the vertical. The profiles, which have been measured and recorded at different resolutions, different depths, are interpolated to a set of standard depths for analysis using all available data. Given the nature of the vertical gradients in the ocean and the large amount of profiles with low vertical resolution data (> 5 m separation between observations) a method of interpolation is needed to as accurately as possible preserve vertical structure. Reiniger and Ross (1968) describe an interpolation schema which starts with a reference curve from linear interpolations between four points around a standard level. Two three point Lagrangian interpolations (two above, one below and one above, two below) are fit to the reference curve preserves vertical gradients, at least when the observations are within proximity to the standard level. In cases where observations are outside of a set distance from a standard level, a single Lagrangian interpolation may be all that is possible, and in some cases only a two point linear interpolation. If observations are spaced too far apart, a standard depth level value will not be calculated. It is important not to use too far spaced observations so as not to create too large an uncertainty in the value on a standard level. The inner limits (limits for the closest deeper and shallower observations to a standard depth level) are 50 m for standard depths

at or less than 200 m, 100 m for standard depths at or less than 800 m, 200 m for standard depths at or less than 1,750 m, and 1,000 m for all deeper depths. The outer limits (limits for second closest deeper and shallower observations to a standard depth are 200 m for standard depths at or less than 400 m, 400 m for standard depths at or less than 1,200 m, and 1,000 m for all deeper standard depths. Allowances are made for XBT data which were recorded at inflection points only, meaning values in the profile were preserved only at depths where the temperature changed from the previously recorded observation by at least 0.2°C. The Reiniger and Ross (1968) method was recommended for use by the Joint Panel on Oceanographic Tables and Standards (JPOTS, 1991). Barker and McDougall (2020) describe another vertical interpolation scheme using Piecewise Cubic Hermite Interpolating Polynomials (PCHIPS). Li *et al.* (2022) show that PCHIPS results in 12% improvement in values of $OHCA_O$ compared to a linear interpolation method, and similar results to Reiniger and Ross (1968) but with some cases of improved results. The interpolation schema used to prepare WOD data for $OHCA_N$ is Reiniger and Ross (1968). The interpolation to standard levels, which is done separately for temperature and salinity profiles from the same cast, can result in density inversions when calculated locally (after Lynn and Reid, 1968; see equation A.7 below) between standard depth levels. If one such inversion is calculated, the two temperature observations at standard depth levels are flagged and not used further. Small instantaneous inversions are found in the ocean, but it is unlikely to find two such inversions in one vertical profile. If two or more local density inversions are found, the entire profile is excluded from further use.

A.2 Calculation of observed means

All observations interpolated to standard depths which pass all quality checks are used to calculate observed means for each 1°grid box with at least one observation. A grid box is

defined as a 1°latitude x 1°longitude area bound by whole number latitude and longitudes with whole number edges to the north and east. So, an example grid box will contain observations at geographic positions > 1.0° N latitude and ≤ 2.0° N latitude; > 1.0° E longitude and ≤ 2.0° E longitude. Observations with a latitude of exactly 1.0°N or exactly 1.0°E longitude would be in different grid boxes. This exacting a definition may seem trivial, but especially with historical data, with cruises following meridians or latitudes, pre-Global Positioning, positions were often recorded as exactly on the latitude or longitude – and observational means could be quite different grid box to grid box if the grid box were defined with whole number edges to the south and west (or using the whole number positioned observations in both adjacent grid boxes).

The observed mean (T_o) for baseline climatology calculation is the average of all N temperature values (T) on a given standard depth for each grid box (i,j)

$$T_O(i,j) = \frac{\Sigma_{n=1}^{N\langle i,j\rangle} T(n)}{N(i,j)}. \qquad \text{(A.1)}$$

For $OHCA_N$ calculations the observed mean is the temperature anomaly (ΔT)

$$\Delta To(i,j) = \frac{\sum_{n=1}^{N(i,j)} T(n) - T_A\left(i,j,M(n)\right)}{N(i,j)} \qquad \text{(A.2)}$$

where N is the number of observations on (or interpolated to) the given standard depth for grid box (i,j), i with indices 1-360 corresponding to longitudes starting at > 0°, ≤ 1°E longitude, j with indices 1-180, corresponding to latitudes starting at 90°S, ≤ 89°S (noting that 90°N is included when j is equal to180). T_A is the baseline mean temperature at grid box (i,j) for month M in which observation (n) was taken. This is repeated for each standard depth level between the surface and the standard depth immediately above the ocean bottom (or to the maximum depth of

analysis) for each grid box (i,j) which is designated ocean. The observed means form a regular grid of values from the heterogeneous point observations (Figure A.1**).** The calculation of the observed mean also acts as a final filter for observations in anomalous features such as warm or cold core eddies or shifts away from mean positions of a boundary current. For baseline climatology, the features are nor representative of a climatological long-term mean. For ΔT, the anomalous features may not represent surface flux of heat, but rather a lateral redistribution of heat for which a data sparse observing system may not be able to resolve spatial extent of the anomalous feature and may not observe the heat loss from the area from which the anomalous feature advected, where ΔT is not actually anomalous. Observed means and standard deviations over 5° latitude/longitude grid boxes are calculated from the same set of observations as the 1°latitude longitude grid boxes. The 1° observed means are then recalculated, this time using the 5°grid box means and standard deviations as a filter. If an observation is more than M times the standard deviation from the mean of the 5° grid box within which the observation was taken, it is not used to calculate the mean of the 1° grid box. M is3 for all open ocean 5° grid boxes below 50 m depth and at least two standard depth above the ocean bottom. M is 4 for 5° grid boxes which are adjacent to 5° grid boxes which include 1°grid boxes designated land and at standard depth levels one standard depth above the ocean bottom for any 1° grid box in the 5° grid box. M is equal to 5 for any 5° grid box with 1° grid boxes designated land at and above 50 m depth. While the 5° standard deviation check does succeed in filtering out anomalous features, it is a check which assumes a Gaussian distribution of observations. However, there are 5° boxes for which the distribution of observations is not Gaussian. As long as there are sufficient observations for each local maximum in the distribution, the standard deviation envelope will be wide enough to encompass multiple local maxima. If the distribution of observations is skewed

toward one of the local maxima, the 5° standard deviation check can have the effect of selectively filtering out an entire subset of observations. Figure A.2 gives an example of this (for salinity observed mean) in an area in which a 5° grid box encompasses both sides of the North Atlantic Drift, but with many more observations on the northwest, fresher side of the current. The result is selectively filtering high salinity observations. The solution in this case was to utilize the statistics in an adjacent 5° grid box which had similar observations, but more evenly distributed between high and low salinity values. The observed mean is calculated three times, the second and third with 5° statistical filters with successively smaller standard deviation envelopes.

There is one more factor in the observed mean due to the relatively high-resolution observation patterns of some observing system. Data from GLD, UOR, PFL, ice-tethered profilers (in DRB), and APB. Multiple profiles in a small geographic area from one of these observing systems over a short time span each have as much weight as, for example, one CTD profile from a research cruise making station every 100 km in a 1°grid box observed mean. To give equal weight to each observation event, observations at each standard level from the potential high-resolution (in space and time) observation systems are pre-averaged over a monthly time interval in each 1° grid box. So, one pre-averaged monthly mean observation will have the same weight in the observed mean for a given 1° grid box as an observation from a single CTD, XBT, bottle (OSD), or MBT.

A.3 Mapping method

In order to integrate $OHCA_O$ over the entire global ocean from sparse heterogeneous geographic coverage a technique to use existing information to calculate a regular latitude/longitude-based grid of values, homogeneous across each time period in the $OHCA_O$ time series is necessary – referred to as the mapping method. The mapping method use for $OHCA_N$ is the same method used to calculate the long-term climatological mean fields of temperature at standard depths which are used as a baseline for calculating yearly ΔT for $OHCA_N$. The description of the mapping method will focus on the baseline climatological mean field calculation first then on the ΔT fields used for $OHCA_N$. The method is an adaptation of Barnes (1964), developed for atmospheric variables, to oceanographic variables, first described in Levitus (1982). Barnes schema is a "convergent weighted-averaging interpolation scheme which can be used to obtain any desired amount of detail in the analysis of a set of randomly spaced data" (Barnes, 1964). The Barnes scheme is based on the assumption that a two-dimensional field of an atmospheric (per Levitus, oceanographic) variable can be represented by the sum of an infinite series of waves – a Fourier integral. A radius of influence around an analysis point – the center of a 1°latitude by 1°longitude grid box, encompasses an area representing a particular wavelength associated with characteristics of the system. The smallest of three radii of influence for Levitus (1982) and subsequent iterations of long-term synoptic (climatological) mean fields calculated by the Ocean Climate Laboratory at NCEI (World Ocean Atlas – WOA98, Antonov *et al.* 1998a,b,c; WOA01, Stephens *et al.*, 2002l WOA05, Locarnini *et al.*, 2006; WOA09, Locarnini *et al.*, 2010; WOA13, Locarnini *et al.*, 2013; WOA18, Locarnini *et al.*, 2018, and WOA23, Locarnini *et al.*, 2024) is 446 km, 4 degrees of longitude (or latitude) at the equator. It is also approximately two times the Rossby radius of deformation at the equator allowing for the exclusion of mesoscale eddy signal while retaining larger scale feature. Note that WOA94

(Levitus and Boyer, 1994) used a single radius of influence of 555m (after Barnes, 1973) which was insufficient to resolve features in data sparse regions (Barnes, 1994). Barnes (1964) itself is based on earlier work which explored techniques to move away from manual drawing of contours of atmospheric variables based on data from weather stations. The technique as developed in Bergthorssen and Döös (1955) and Cressman (1959) was termed objective analysis to differentiate from the subjective analysis inherent in hand drawing contours. The equation developed by Barnes based on the earlier work as detailed in Locarnini *et al.* (2024) – indeed in any of the WOA series is

$$C_{i,j} = \frac{\sum_{z=1}^{n} W_z Q_z}{\sum_{z=1}^{n} W_z} \qquad \text{(A.3)}$$

in which: (i,j) - coordinates of a grid box in the east-west and north-south directions respectively; $C_{i,j}$ - the correction factor at grid box coordinates (i,j); n is the number of observed means that fall within the area around the analysis point i,j defined by the influence radius; Qs is the difference between the observed mean and the first-guess at the Sth point in the influence area;

$$W_s = e^{-\frac{Er^2}{R^2}} \text{ (for } r \leq R\text{)}, \; W_s = 0 \text{ (for } r > R\text{)} \qquad \text{(A.4)}$$

where r is the distance of the observed mean from the point i,j, R is the radius of influence, and E is equal to 4.

The derivation of the weight function W_s will not be dealt with here, it can be found in detail in Locarnini *et al.* (2024). The salient point of the weight function is a dependence on the distance of the individual observed means from the analysis point (grid box center). (Figure A.3a). The further the observed mean from the grid box being analyzed, the lower the weight, with the

observed mean at the point of analysis having the largest weight (if indeed there is an observed mean at the point of analysis). However, since the correction factor $C_{i,j}$ is a summation of all observed means minus first-guess fields within the radius of influence, if the only observed means are at the outer edge of the radius of influence, since all weights sum to 1, the correction factor for a particular point of analysis can be set completely by outer values. Of course, if there are no observed means within a radius of influence, there can be no correction whatsoever and the first-guess is also the analysis value (Figure A.3b). Figure A.3b also shows a difficulty in oceanographic analysis, which is that the analysis field is discontinuous at the land boundary. Since there is no influence of any observed mean outside the radius of influence, there is an error factor since the assumption of the Fourier integral is an integration to infinity. The Barnes derivation of the integration from the radius of influence to infinity quantifies this error and incorporates it into the final weight function.

Analyzed value $G_{i,j}$ is then the sum of the first-guess and the correction factor at each grid box which has an observed mean within the radius of influence of the analysis point (equation A.5).

$$G_{i,j} = F_{i,j} + C_{i,j} \qquad \text{(A.5)}$$

A key point of the Barnes scheme is the analysis of the correction factor (summed observed mean minus first-guess) rather than the values of the variable (ocean temperature in this case). This allows for radii of influence to extend across boundary currents and other dynamic features, utilizing observations which are responding to surface flux and other factors in the same manner while exhibiting different temperature structure. The use of the correction factor also preserves gradients in the mean geographically distributed structure. Still, the treatment of each grid box separately, even when the set of observed means is similar to neighboring grid boxes, results in

small geographic scale noise which is not characteristic of long-term means. A median filter (Tukey, 1974; Rabiner *et al.*, 1975) is applied after the objective analysis, followed by a 5-point smoothing function (Shuman, 1957).

A.3.1 Choice of radius of influence, number of analysis iterations

Barnes (1973) details a one iteration objective analysis schema using an additional constant in the weighting function in part to preserve short wavelength signal (also to reduce computational overhead). Achtemeir (1987) takes a careful look at one, two, and three iterations of the objective analysis, finding that three iterations with the same weighting function does slightly degrade the longer wavelengths but gives a better fit to wavelengths shorter than eight times the minimum wavelength. For data sparse cases, successively reducing the radius of influence to reduce the influence of distant observations is advisable. In the case of baseline climatology and observed mean ΔT for $OHCA_N$, radii of influence for three successive iterations of the objective analysis are (1) 892 km, (2) 669 km, and (3) 446 km, or approximately 8, 6, and 4 longitudinal grids at the equator (latitudinal grids everywhere). As per Levitus (1982) a gridded field has the limitation that it takes seven or eight Δx to describe a Fourier component, where Δx is the distance between adjacent grid points. So, the ideal interpolation procedure would remove all wavelengths shorter than $8\Delta x$ completely. At the Equator, Δx is 111 km, and $8\Delta x$ is equivalent to the largest radius of influence. The smallest radius of influence is approximately 2 times the Rossby radius of deformation at the equator. Moving away from the equator, the radii of influence covers more grid boxes, as Δx (east-west direction) grows smaller. Calculating the response function D from the given smallest radius of influence R using the equation of Barnes (equation A.6; as noted in Locarnini *et al.*, 2024):

$$D = e^{-\left(\frac{\alpha R}{4}\right)^2} = e^{-\left(\frac{\pi R}{2\lambda}\right)^2} \quad \text{(A.6)}$$

in which α is $2\pi/\lambda$, and λ is the wavelength of a particular Fourier component. The results for Levitus (1982) and each edition of the WOA (including 1/4°resolution) are shown in Figure A.4 (from Locarnini *et al.*, 2024).

A.3.2 First-guess field determination

As noted by Cressman (1959) "In order to obtain the greatest amount of accuracy with the least amount of computation, it is essential that the first guess be as accurate an approximation to the final field as possible." For WOA long-term climatologies of temperature at a standard depth, the baseline for $OHCA_N$, the first-guess field for the annual (all months) time period is a zonal average of 1° observed means regardless of year of observation. The first-guess for each season (Winter is January to March, Spring is April to June, Summer is July to September, Fall is October to December) is the objectively analyzed annual mean, and the first-guess for each month is the respective objectively analyzed seasonal mean. Then all months are averaged together to create a new first-guess field for a new objective analysis on the annual time scale above 1500 m depth and the seasons are averaged together to create a new first-guess field for the annual objective analysis from 1500 m to 5500 m depth. The annual objective analysis is the first-guess for a new seasonal objectively analyzed field, which in turn is the new first-guess for each respective month.

The initial first-guess for the annual time span, zonal averages, is the furthest from Cressman's admonishment of greatest amount of accuracy with least amount of computation dependent on good approximation in the first-guess field. Computation time is not as important an issue as in Cressman's time, but it is still a consideration. Accuracy in the objective analyzed field is also a

consideration, where accuracy here is representation of the long-term means of an oceanographic variable at a given standard depth. If every 1° grid box for every standard depth had at least one observation at least one point in time from which to construct a complete first-guess field, this would be an optimal starting point for the objective analysis. However, even in the Argo era, there are still some 1° grid boxes in the global ocean which have never had a single temperature profile. 2% of grid boxes at 10 m do not have a single historic measurement, increasing to 8% at 800 m (deeper than T7 XBT deepest depth), and 31% at 2000 m (Argo floats make observations from 2000 db, which is less than 2000 m). A zonal average is a means to ensure that each 1° grid box has a value at least commensurate with latitudinal specific processes such as insolation. A problem with the zonal average, is that characteristics of small areas of the ocean may be so different from the mean along a latitude that the difference from the observations of the first-guess field leads to a large correction and an unrealistic analyzed value. An example is the Sulu Sea, surrounded by the Philippine Islands, which at deeper depths has temperatures 4-6°C warmer than the surrounding Indian and Pacific Oceans. To account for this eventuality, a set of distinct basins have been defined, starting with the largest (Pacific, Indian, Atlantic) and including smaller areas such as the Sulu Sea, for which zonal averages are calculated separately. This leads to some instances when there are no observations along a latitude in a particular basin for calculation of a first-guess field. In these cases, a basin-wide value is used for the first-guess field. In the case that there are no observations in the basin, the closest zonal value from a basin with observations is used. At any rate, the zonal average is the first-guess only for the first iteration of the objective analysis on the all-year annual time span. There are three iterations of the objective analysis on the all-year annual time-span, with the results of each successive

iteration used as the first-guess for the next iteration. In turn, the all-year annual field is the first-guess for subsequent fields.

For $OHCA_N$, the first-guess field for the annual temperature anomalies (difference between observations at standard depths and baseline climatology) is 0.0°C everywhere. In a warming ocean this would seem to violate Cressman's statement about constructing the first-guess field as close to the final field as possible based on a priori information (usually the observations themselves). A first-guess field of 0.0°C essentially sets regions with no data to a condition of no change over time. In the Argo era with homogeneous data distribution in the open ocean this is not an issue. However, for earlier, less uniform, sparser observation distribution years, a first-guess of no change will underestimate the difference of yearly $OHCA_N$ from the baseline mean (an overestimate of $OHCA_N$ in earlier years, an underestimate in later years dependent on the time span of the baseline mean) as pointed out by Lyman and Johnson (2008, 2023). The difficulty with a non-zero first-guess field is that, while the global ocean is increasing in thermal energy, not all regions are warming uniformly – in fact some regions are cooling relative to baseline mean for some years, even recent years (Cheng et al, 2024) and the patterns of warming or cooling areas are variable year to year. It has been shown that significant warming trends are now more prevalent across the global ocean than cooling trends (Johnson and Lyman, 2020), but La Niña years and El Niño years still bring shifting patterns including areas of cooling relative to baseline mean. For this reason, a first-guess field (or gap-fill field) such as used in Lyman and Johnson (2008, 2014) using the mean anomaly of all grid boxes with observed means may overestimate $OHCA_O$ in data sparse regions. Similarly, the concept of persistence (using the damped preceding time span anomaly field as the background for optimal interpolation of the

next) as in the EN4 method (Ingleby and Huddleston, 2007, Good *et al.*, 2013) can represent patterns of warm and cool regions which are no longer extant, even on a month to month time span. Willis *et al.* (2003, 2004) use a covariance function based on sea level change measured from altimeter which is well correlated with $OHCA_O$. However, sea level change is a combination of factors, only one of which is thermosteric expansion, the factor which is a consequence of OHCA. Cheng and Zhu (2016) essentially use the results of a first analysis iteration with a radius of influence of 21° in longitude at the equator (and all latitude) as a first-guess field. A potential problem with this approach is that it assumes unrealistic correlation length scales, according to Lyman and Johnson (2023). In other words, a first-guess field for temperature anomalies for $OHCA_O$ calculation which is as close to the actual field as possible is a difficult problem, at least for years for which observations are sparse in some regions. The choice of 0.0°C is known to be an underestimate for most years but a known underestimate is at least that, known, and is not dependent on any source of data other than in-situ observations, preserving independence of the calculation method for $OHCA_O$.

A.3.3 Averaging objectively analyzed fields

Historically, there is uneven distribution of observations across seasons and across years. Ship-based observations, due to ocean and weather conditions, are predominant in the hemispheric summer and scarcest in the hemispheric winter. The advent of autonomous platforms for subsurface temperature observations around year 2000 has allowed for an even distribution of temporal observations across seasons, at least in the open ocean outside of continental shelves, enclosed seas, and ice-free areas. However, an all-year annual climatological mean field can still have seasonal bias in many areas. So, as a final step, all 12 monthly analyzed fields are averaged together at and above 1500 m, 4 seasonal fields 1500 m to 5500 m depth to create the final all-

year long-term climatological mean annual field. The respective 3 months are averaged together to 1500 m depth for the final all-year long-term climatological seasonal fields. Below 1500 m the seasonal objective analysis is used as the final climatological mean field, as is the case for all levels for each month. The depth of 1500m is used as it is below the effects of seasonal changes due to surface flux over most of the ocean. The expectation for depths deeper than 1500 m is that objectively analyzed values will not change from season to season due to any seasonal cycle, rather the differences will be in observation quality and calibration, so the averaging is to ameliorate any bias which may be introduced by particular (pre-Argo) cruises and projects. Critical for a baseline climatological mean to calculate $OHCA_O$, the different historic coverage of temperature profiles leads to a different median age (year of the observations) for the northern hemisphere, which has had relatively steady coverage over the years, and the southern hemisphere, which has only in the Argo era experienced consistent coverage, in an all-year climatological mean, as noted in Domingues *et al.* (2008). If different areas of the ocean have different median age within the same baseline climatology, the $OHCA_O$ calculated from the baseline will not be a consistent measure of global change from a specific time period. To produce a more uniform median age, decadal climatological mean fields are produced and averaged together as a baseline climatology for $OHCA_N$. In this way the long-term climatological mean, in addition to having a set time period as opposed to an all-year climatological mean, will have equal representation from each time period – one value per each 1° grid box per decade. In practice, there are areas of the ocean, such as the southeast southern hemisphere Pacific, with high data sparsity in earlier decades to a degree that analyzed values essentially default to the first-guess field in the decadal mean, so a decadal bias is not completely removed. The all-year climatological mean fields are used as a first-guess for an initial objective

analysis of decadal climatological mean fields – for WOA09, decades (and quasi-decade for the last) 1955-1964, 1965-1974, 1975-84, 1985-1994, 1995-2006, for WOA23, decades 1955-64, 1965-1974, 1985-1994, 1995-2004, 2005-2014, 2015-2022. The reason for mentioning WOA09 and WOA23 is that WOA09 is the baseline climatology currently used for $OHCA_N$, WOA23 is used herein in experimentation on updated methods for $OHCA_N$ as a new baseline climatology. The WOA09 long-term 1955-2006 temperature climatological mean is an average of the five decadal objectively analyzed fields – where averaging is done at each grid box at each standard depth. The WOA23 field used experimentally is a climate normal from 1991-2020, the average of three decades 1991-2000, 2001-2010, 2011-2020 where the first-guess is an objectively analyzed climatological mean over 1991-2020 regardless of year in that period whose first-guess is the all-year objectively analyzed climatological mean for the respective time span (annual, seasonal, monthly). A climate normal is defined as per WMO (2017) and is used to provide more direct comparison of OHCA results with other climate variables also using a climatological normal baseline period. 1991-2020 is also a period where temporal coverage is relatively even, in the 1990s due to WOCE (Chapman, 1998, Gouretski, 2018; Lehman, 2021), and due to the Argo profiling float program in the 2000s and 2010s. At some point,10-15 years in the future, the even temporal distribution of Argo and the overall ocean observing system may allow for a uniform median age across the entire global ocean without decadal averaging.

A.3.4 Nonlinearity of the equation of state effects on temperature climatological mean

Lozier *et al.* (1994) detect and describe an unrealistic feature in density computed from the climatological mean fields of temperature and salinity of Levitus (1982). The feature was not found in computation of density from profiles of temperature and salinity observed in the same

area. Density is a non-linear computation dependent on pressure, temperature, and salinity. Objectively analyzed climatological fields of temperature and salinity do not have the same input set of observations. A significant portion of observations (e.g. 2.4 million MBT casts and 2.4 million XBT casts out of 18.5 million total casts in WOD) are temperature only profiles. For another subset of observations (e.g. APB) temperature observations are used for the calculation of temperature climatological mean fields but salinity observations are not used due to the perceived quality assurance difficulties of a salinity sensor attached to a living animal. Further, the objective analysis of the observed means is executed on temperature separate from salinity, the correction factors are of different magnitude relative to the full values of temperature and salinity and with respects to density. In stark terms, climatological mean fields of temperature and salinity represent slightly different oceans based on input data and objective analysis method. The optimal method for producing a climatological mean field of density is to calculate density from concurrent observations of temperature and salinity, calculate observed means from these observational based densities, then objectively analyzed the observed means of density (see Locarnini *et al.*, 2018). Even so, the difference between density calculated from observations and density calculated from climatological means of temperature and salinity is small over most of the global ocean. A method to preserve the density relationship when calculating temperature and salinity climatological mean fields on depth or pressure surfaces is to first calculate depths of isopycnal surfaces from concurrent temperature and salinity observations, then interpolate temperature and salinity from observations onto the isopycnal surfaces, map full fields of temperature and salinity onto the isopycnal surfaces, then interpolate the mapped fields from isopycnal to isobaric (constant depth) surfaces. Gouretski (2018) shows that the results from isopycnal mapping interpolated to constant depth and constant depth mapping is small for

temperature (and salinity), even including differences in input observation and quality assessment of observations. In order to bring the constant depth climatological means of temperature and salinity into more consistency with density in the $OHCA_N$ baseline climatology is a technique of minimal adjustments to temperature and/or salinity to achieve local stability E is greater than or equal to 0 in each 1°grid box is applied. The method is an adaptation of Jackett and McDougall (1995) as described by Boyer *et al.* (2005). E is the Hesselberg–Sverdrup criteria described by Lynn and Reid (1968) and Neumann and Pierson (1966), defined as

$$E = \lim_{\delta z \to 0} \frac{1}{\rho_0} \frac{\delta \rho}{\delta z} \qquad \text{(A.7)}$$

in which z is the depth, ρ is *in situ* density, $\rho 0$ is 1020 kg m^{-3}, and $\delta\rho$ is the individual density difference defined by adiabatic vertical displacement of a deeper water parcel to the depth of a shallower water parcel. The adjustments are, as designed, small in the vertical temperature and salinity profiles of the climatological mean fields. Many of the adjustments are near-surface, in areas of high salinity variability, such as river outflow and ice formation/melt regions and are made to salinity. However, there are changes to temperature as well.

A final note on mapping method for baseline climatology and $OHCA_N$ calculation, while the method will be updated and adapted based on the experiments detailed herein, the basic tenets of the method as outlined by Levitus (1982), based on the earlier work of Barnes (1964) are still retained. This is despite advances in other purely *in situ* based methods – notably what is known as optimal interpolation (OI), detailed for oceanographic data in the work of Gandin (1963) and Bretherton *et al.* (1976). OI is a definite advance in objective analysis technique, using secondary statistics – in the case of Bretherton *et al.* (1976) an inversion of a covariance matrix of the observed means (or observations themselves), and producing robust error statistics. The

difficulty with OI for baseline temperature climatology, but more so for yearly OHCA calculation, is determining covariance matrices in data sparse regions from the observations themselves. As noted by Gandin, there are two limiting cases for analysis of oceanographic data. In the first, high density data distribution, results are expected to be similar for different analysis techniques. In the second with low data density, techniques which employ secondary statistics are of questionable value.

A.3.5 Choice of standard depth levels

Temperature anomalies used for $OHCA_N$ calculation are objectively analyzed on 26 standard depths between the surface and 2000 m. Baseline temperature climatological mean fields are calculated on the same 26 depths as well as 7 deeper levels down to 5500 m. The 33 total standard depths are modifications (Levitus, 1982) from the standard depths recommended in Sverdrup *et al.* (1942) based on suggestions of the International Association for the Physical Sciences of the Ocean (IAPSO). At the time, all temperature profiles were measured using thermometers attached to a series of water sample bottles. Attempting to make measurements at standard levels or interpolating from observed levels to standard depth levels allowed for utilization of observations from different cruises to gather information which could be compiled and used to gain a more synoptic picture of the subsurface ocean. Even as sensor measurements allowed for higher vertical frequency in measurements, limitations of recording and exchanging data often limited temperature profile information to standard depth levels. Only since the mid-1980s have high resolution temperature profiles become more prevalent. Later versions of the World Ocean Atlas (WOA13, WOA18, and WOA23) take advantage of the prevalence of more high vertical resolution observations to increase the number of standard depths from the surface

to 2000m from 26 to 57, and to 5500 m from 33 to 102. The full set of standard depths, with the depths used for OHC calculations highlighted are shown in Table 1.2.

A.3.6 Definition of land/ocean bottom

Hakuba *et al.* (2024) demonstrate that the some of the differences between OHCA calculated by different methods are due to difference of the area over which OHCA is integrated. Many of the satellite-based methods are limited to 60°S to 60°N due to limitations of satellite coverage. But there are also differences in the number of grid boxes which are defined as land vs. ocean, or in grid boxes which are, or are not included, in integration due to differing definitions of the depth of individual grid boxes. WOA09 and $OHCA_N$ calculations use the same 1° land mask/bathymetry which is derived from the ETOPO2 two-minute bathymetry (NGDC, 2001 – accessed 12/02/2006). There have been updates of the ETOPO2 since 2006, but for reasons of consistency, the derived 1° land mask/bathymetry used for WOA09 and $OHCA_N$ has not reflected these updates. The derivation of the 1°land mask/bathymetry is not directly from ETOPO2, but rather from a 1/4°grid box land mask/bathymetry which is derived from ETOPO2. This preserves continuity in the definition of land/bathymetry between 1/4°climatological mean field and 1°climatological mean field spatial definitions, allowing for use of 1° climatological mean fields as first-guess for objective analysis of 1/4°fields (not used in $OHCA_N$). For the translation from ETOPO2 two-minute averaged bathymetry to 1/4° land mask/bathymetry, if 5/9ths or more of the two-minute averaged bathymetry values in a 1/4°grid box are designated land (zero or positive elevation) the corresponding 1/4° grid box is designated land. Two-minute grid boxes do not exactly fit into 1/4° grid boxes, so not every 1/4° grid box has the same number of two-minute values. For two-minute grid boxes with negative elevation, the closest deeper standard depth is assigned. If 5/9ths or more of all two-minute grid boxes within a

1/4°grid box are assigned the same standard depth, the 1/4° grid box is assigned this value. If not, if 1/3 or more of all two-minute grid boxes have the deepest standard depth of all two-minute grid boxes within the 1/4° grid box, the deepest standard depth is assigned to the 1/4°grid box. Otherwise a simple average of all standard depth levels is used to assign closest standard depth for the 1/4°grid box. This same procedure is used to derive the 1° land mask/bathymetry from 1/4° version, except there must be $9/16^{th}$ of all 1/4° standard depths defined as land or a given standard depth to define the corresponding 1° grid box as land or the given standard depth and $5/16^{th}$ of all 1/4° grid boxes with the same maximum depth to assign the corresponding 1° grid box the given standard depth. Known land areas with elevations below zero (e.g. Death Valley, the Australian Great Basin, African Rift Valley) are set to land. Bodies of water such as the Caspian Sea and Aral Sea are not designated land, and there are observations in both Seas.

A.3.7 Evolution of $OHCA_N$ method, current implementation

The $OHCA_N$ method developed over the last thirty years, starting with Antonov (1993) calculating ΔT for a 25-year period (1957-1987) in the North Atlantic and North Pacific using ocean temperature observations from the World Data Center-B for Oceanography (Obninsk), which built on earlier work on the changing thermal structure of the North Atlantic. Levitus (1989a; 1989b) had also done work on temperature change in the North Atlantic between the 1950s and 1970s. Additional temperature observations at the World Data Center-A for Oceanography (Silver Spring) collocated with the United States National Oceanographic Data Center (NODC, now NCEI), the ocean temperature observation data set used by Levitus (1982), almost 1.5 million oceanographic casts plus an additional 1 million casts, together comprising the NODC temperature data set (released on compact disc in 1991) which became the basis for

the WOD provided the opportunity for temporal and geographic expansion of study of changing ocean temperatures, resulting in Levitus *et al.* (1994a; 1994b), and Levitus and Antonov (1995). Continued addition of historical oceanographic casts to the archive and to WOD, partly through the Global Oceanographic Data Archaeology and Rescue (GODAR) project, led to sufficient available observations for Levitus *et al.* (2000) to provided global $OHCA_N$ time series yearly in the upper 300 m, pentadal (five-year) to 3000 m depth from the mid-1950s to the mid-1990s. The estimate for $OHCA_N$ 1955-1998 was 200 ZJ. Additional available historical observations from earlier years in the record revised $OHCA_N$ 1955-1998 0-3000 m downward to 140 ZJ (Levitus et al, 2005). Levitus *et al.* (2009) corrected for the XBT bias as revealed by Gouretski and Koltermann (2007). Only OHU_N rate for 0-700m 1969-2003 is given (3.2 ZJ/yr), compared to Domingues *et al.* (2008; 4.1 ZJ/yr) and Ishii and Kimoto (2009; 2.4 ZJ/yr) both of which corrected XBT data with different methods. L09 does note that results were similar to Levitus *et al.* (2005) in magnitude of trend. Finally, Levitus *et al.* (2012) extended the $OHCA_N$ time series through 2010, into the Argo era, for 0-2000 m, calculating $OHCA_N$ from 1955-2010 of 240 ZJ ±19 ZJ - for the first time including an uncertainty calculation. Since 2012, $OHCA_N$ yearly time series starting at 1955 for 0-2000 m has been updated each year (https://www.ncei.noaa.gov/access/global-ocean-heat-content/) following the method as outlined in Levitus *et al.* (2012).

A.3.8 $OHCA_N$ uncertainty

The uncertainty defined in the supplementary information of Levitus *et al.* (2012) is the standard error of the analysis following Taylor (1997). Expanding $C_{i,j}$ from Equation (A.3)

$$C_{i,j} = \frac{w_1 Q}{W} + \frac{w_2 Q_2}{W} + \cdots + \frac{w_n Q_n}{W} \quad \text{(A.8)}$$

where W is the summation of all N weights in grid box i,j.

Then,

$$c_n = \frac{w_n Q_n}{W} \quad \text{(A.9)}$$

for each grid box in the radius of influence and

$$\sigma_A = \sqrt{\left(\frac{\partial A}{\partial Q_1}\sigma_{c_1}\right)^2 + \cdots + \left(\frac{\partial A}{\partial Q_n}\sigma_{c_n}\right)^2 + 2\sum_{n=1}^{N-1}\sum_{m=n+1}^{N}\left(\frac{\partial A}{\partial Qn}\right)\left(\frac{\partial A}{\partial Qm}\right)\sigma_{c_{nm}}} \quad \text{(A.10)}$$

where σ_{cn} is the standard deviation of the anomaly values in the nth grid box within the radius of influence surrounding the point of analysis $A_{i,j}$ and $\sigma_{cn,m}$ is the cross covariance between the nth and mth grid boxes containing observed means within the radius of influence. Solving equation (A.9) for Q and substituting in to equation (A.10) gives σ_A, the standard deviation of the analysis in terms of the weights and standard deviation/covariances of the corrections. The problem is that there are not sufficient data within the radius of influence of each point of analysis for robust covariances or even in some cases standard deviations. So, a one pass objective analysis with a 0.8 gamma factor in the correction approximates the three-iteration analysis (as per Barnes, 1973) and σ_o, the standard deviation of the one pass correction factor for each grid box with data is calculated. In place of covariance, $\sigma_n\sigma_m$ is used, as per the Schwartz inequality, the absolute value of $\sigma_{n,m}$ is $\leq \sigma_n\sigma_m$. Assuming that $\sigma_n = \sigma_o$, the final equation (A.11) for the standard error of the analysis is

$$\sigma_A = \frac{\sigma_0}{W} \sum_{n=1}^{N} \; w_n^2 + 2 \sum_{n=1}^{N-1} \; \sum_{m=n+1}^{N} \; w_n w_m \quad \text{(A.11)}$$

A.4 Tables

Name	Description
OSD	Ocean Station Data, Low-resolution CTD/XCTD, Plankton data
CTD	High-resolution Conductivity-Temperature-Depth / XCTD data
MBT	Mechanical / Digital / Micro Bathythermograph data
XBT	Expendable Bathythermograph data
APB	Animal Observing system data
MRB	Moored buoy data
PFL	Profiling float data (mainly Argo)
DRB	Drifting buoy data (mainly ice drifters)
UOR	Undulating Oceanographic Recorder data
GLD	Glider data

Table 1.1. Data set names and data types in the WOD.

0	**5**	**10**	**15**	**20**	**25**	**30**	**35**	**40**	**45**	**50**	**55**
60	**65**	**70**	**75**	**80**	**85**	**90**	**95**	**100**	**125**	**150**	**175**
200	**225**	**250**	**275**	**300**	**325**	**350**	**375**	**400**	**425**	**450**	**475**
500	**550**	**600**	**650**	**700**	**750**	**800**	**850**	**900**	**950**	**1000**	**1050**
1100	**1150**	**1200**	**1250**	**1300**	**1350**	**1400**	**1450**	**1500**	**1550**	**1600**	**1650**
1700	**1750**	**1800**	**1850**	**1900**	**1950**	**2000**	**2100**	**2200**	**2300**	**2400**	**2500**
2600	**2700**	**2800**	**2900**	**3000**	**3100**	**3200**	**3300**	**3400**	**3500**	**3600**	**3700**
3800	**3900**	**4000**	**4100**	**4200**	**4300**	**4400**	**4500**	**4600**	**4700**	**4800**	**4900**
5000	**5100**	**5200**	**5300**	**5400**	**5500**						

Table 1.2. Standard depths in meters for WOA23 climatological mean fields. Shaded depths are standard depths for WOA09 baseline mean and $OHCA_N$

A.5 Figures

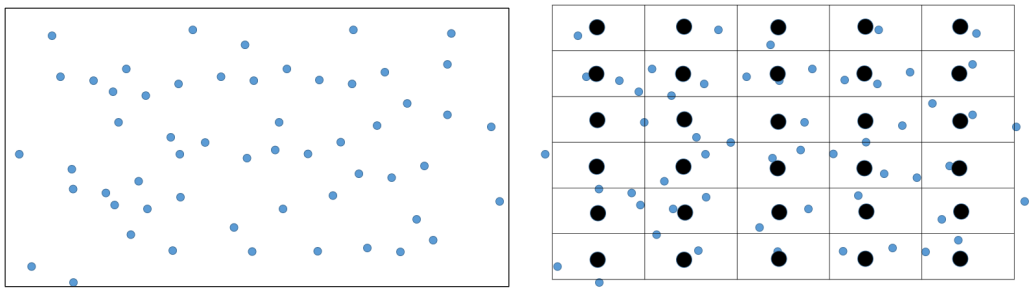

Figure A.1. a) point observations in a 5°longitude X 6° latitude area b) observed means (black dots) on a regular grid calculated from the point observations, each representing the entire grid box, with position at the center of the grid box.

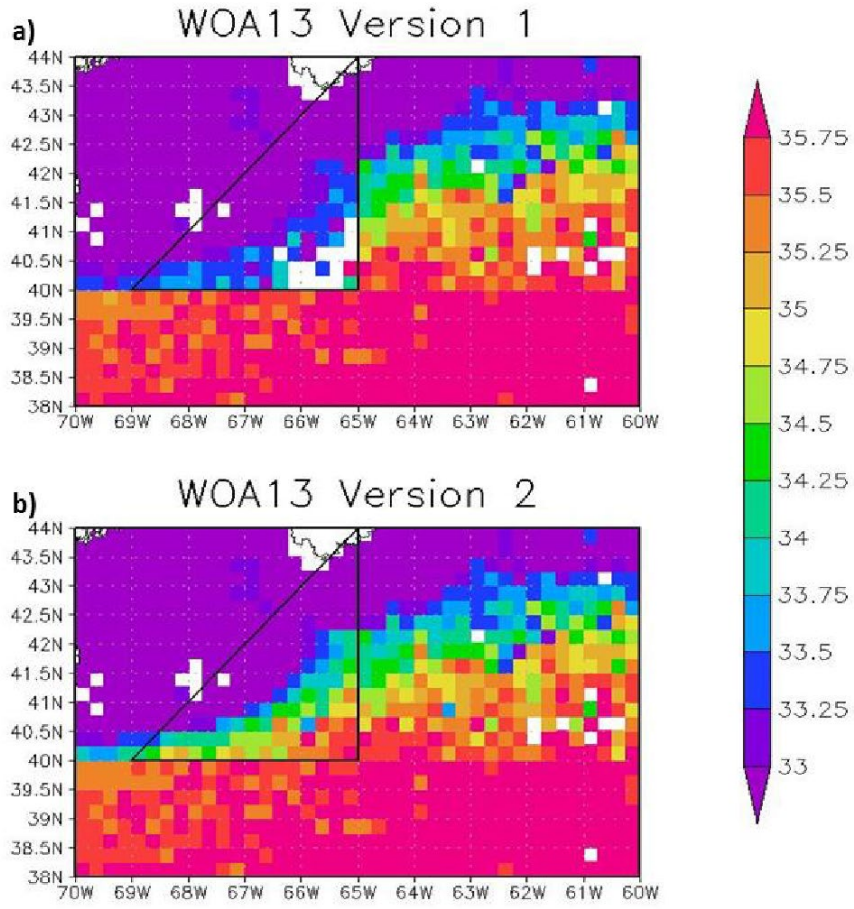

Figure A.2. 1955-2012 1°observed mean salinity (annual) at 55 m depth for a) WOA13v1 and b) WOA13v2. Black triangle delineates area which uses five-degree statistics from adjacent five-degree box (directly to the east). (Reproduced from Boyer *et al.* unpublished document: https://www.ncei.noaa.gov/sites/default/files/2020-04/woa13v2_changes.pdf)

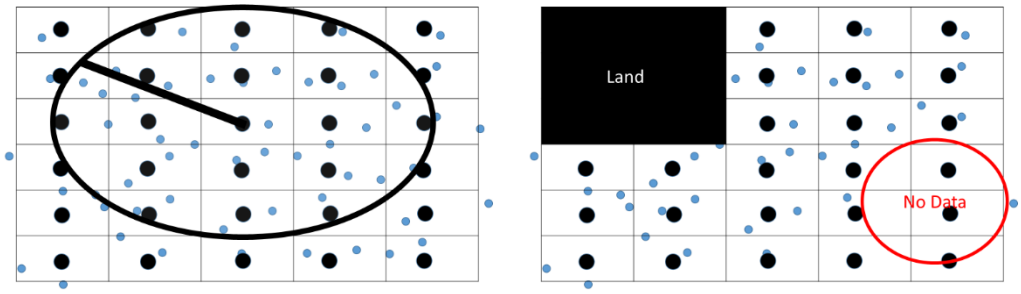

Figure A.3. a) Center point is analyzed with weighted mean of all grid boxes with observed means whose center points fall within the radius of influence. b) difficulties of analysis on an ocean grid interrupted by land with data sparse or data void regions.

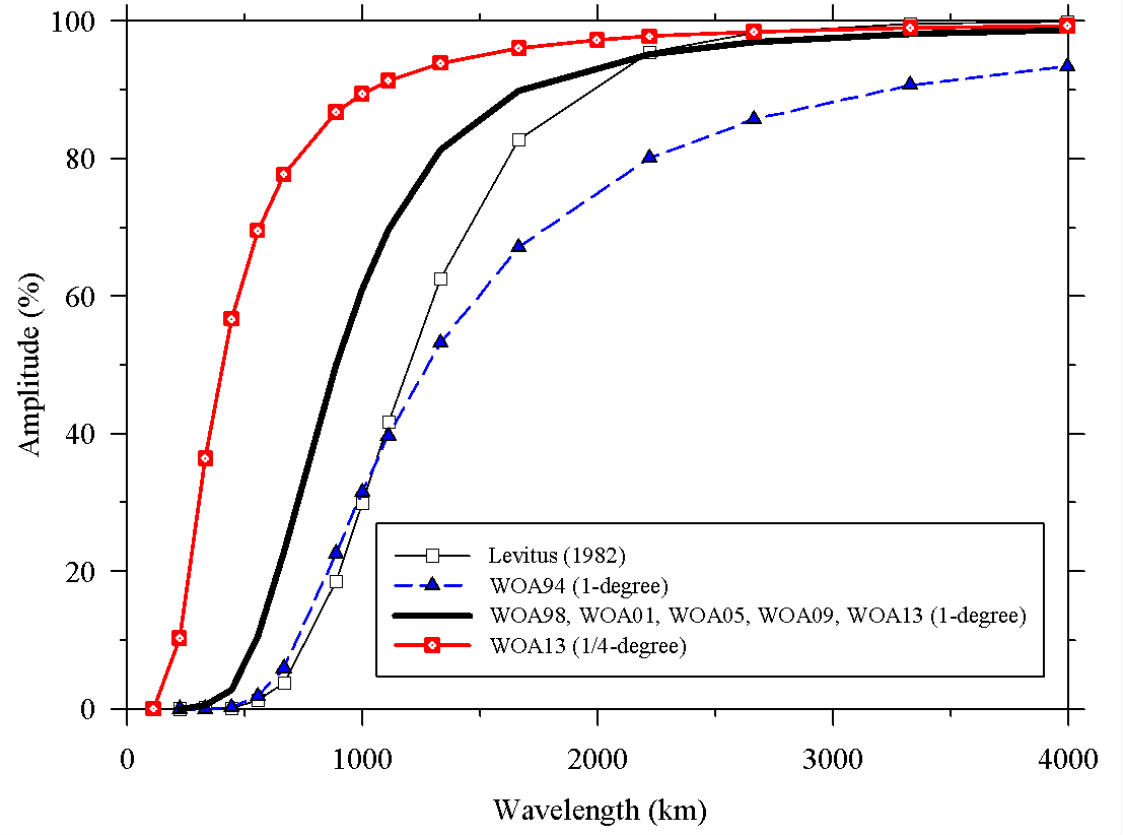

Figure A.4. Response function of the WOA18, WOA13, WOA09, WOA05, WOA01, WOA98, WOA94, and Levitus (1982) objective analysis schemes.

References

Abraham, J. P., J. Gorman, F. Reseghetti, E. M. Sparrow, and W.J. Mincowycz (2012). Drag Coefficients for Rotating Expendable Bathythermographs and the Impact of Launch Parameters on Depth Predictions, Numerical Heat Transf. A – Appl., 62, 25-43. https://doi.org/10.1080/10407782.2012.672898

Abraham, J. P., M. Baringer, N. L. Bindoff, T. Boyer, L. J. Cheng, J. A. Church, J. L. Conroy, C. M. Domingues, J. T. Fasullo, J. Gilson, G. Goni, S. A. Good, J. M. Gorman, V. Gouretski, M. Ishii, G. C. Johnson, S. Kizu, J. M. Lyman, A. M. Macdonald, W. J. Minkowycz, S. E. Moffitt, M. D. Palmer, A. R. Piola, F. Reseghetti, K. Schuckmann, K. E. Trenberth, I. Velicogna, J. K. Willis (2013). A review of global ocean temperature observations: Implications for ocean heat content estimates and climate change, Rev. Geophys., 51, 450–483. https://doi.org/10.1002/rog.20022

Achtemeier, G. L. (1987). On the Concept of Varying Influence Radii for a Successive Corrections Objective Analysis. Mon. Wea. Rev., 115, 1760–1772, https://doi.org/10.1175/1520-0493(1987)115<1760:OTCOVI>2.0.CO;2

AchutaRao, K. M., B. D. Santer, P. J. Gleckler, K. E. Taylor, D. W. Pierce, T. P. Barnett, and T. M. L. Wigley (2006). Variability of ocean heat uptake: Reconciling observations and models, J. Geophys. Res.,111, C05019. https://doi.org/10.1029/2005JC003136

Allison, L. C., M. D. Palmer, R. P. Allen, L. Hermanson, C. Liu, and D. M. Smith (2020). Observations of planetary heating since the 1980s from multiple independent datasets, Environ. Res. Commun. 2 101001. https://doi.org/10.1088/2515-7620/abbb39

Alory, G., Wijffels, S. and Meyers, G. M., 2007: Observed temperature trends in the Indian Ocean over 1960-1999 and associated mechanisms. Geophys. Res. Lett., 34, L02606. https://doi.org/10.1029/2006GL028044

Antonov, J. I. (1993). Linear Trends of Temperature at Intermediate and Deep Layers of the North Atlantic and the North Pacific Oceans: 1957–1981. J. Climate, 6, 1928–1942, https://doi.org/10.1175/1520-0442(1993)006<1928:LTOTAI>2.0.CO;2.

Antonov, J.I., S. Levitus, T.P. Boyer, M.E. Conkright, T.D. O'Brien, and C. Stephens (1998a) World Ocean Atlas 1998. Vol. 1: Temperature of the Atlantic Ocean. NOAA Atlas NESDIS 27, U.S. Government Printing Office, Washington, D.C., 166 pp.

Antonov, J.I., S. Levitus, T.P. Boyer, M.E. Conkright, T.D. O'Brien, and C. Stephens (1998b). World Ocean Atlas 1998. Vol. 2: Temperature of the Pacific Ocean. NOAA Atlas NESDIS 28, U.S. Government Printing Office, Washington, D.C., 166 pp.

Antonov, J.I., S. Levitus, T.P. Boyer, M.E. Conkright, T.D. O'Brien, C. Stephens, and B. Trotsenko (1998c). World Ocean Atlas 1998. Vol. 3: Temperature of the Indian Ocean. NOAA Atlas NESDIS 29, U.S. Government Printing Office, Washington, D.C., 166 pp.

Antonov, J. I., S. Levitus, and T. P. Boyer (2002), Steric sea level variations during 1957–1994: Importance of salinity, J. Geophys. Res. Oceans, 107(C12), 8013. https://doi.org/10.1029/2001JC000964

Antonov, J. I., S. Levitus, and T. P. Boyer (2004). Climatological annual cycle of ocean heat content, Geophys. Res. Lett., 31, L04304. https://doi.org/10.1029/2003GL018851

Argo Science Team (1998). On the design and implementation of Argo: An initial plan for a global array of profiling floats, in International CLIVAR Project Office Report 21, GODAE Report 5. GODAE International Project Office, Melbourne Australia.

Armour, K., J. Marshall, J. Scott, A. Donohoe and E. R. Newsom (2016) Southern Ocean warming delayed by circumpolar upwelling and equatorward transport. Nature Geosci 9, 549–554. https://doi.org/10.1038/ngeo2731

Bakker, D. C. E., B. Pfeil, C. S. Landa, N. Metzl, K. M. O'Brien, A. Olsen, K. Smith, C. Cosca, S. Harasawa, S. D. Jones, S.-I. Nakaoka, N. Yukihiro, U. Schuster, T. Steinhoff, C. Sweeney, T. Takahashi, B. Tilbrook, C. Wada, R. Wanninkhof, S. R. Alin, C. F. Balestrini, L. Barbero, N. R. Bates, A. A. Bianchi, F. Bonou, J. Boutin, Y. Bozec, E. F. Burger, W.-J. Cai, R. D. Castle, L. Chen, M. Chierici, K. Currie, W. Evans, C. Featherstone, R. A. Feely, A. Fransson, C. Goyet, N. Greenwood, L. Gregor, S. Hankin, N. J. Hardman-Mountford, J. Harlay, J. Hauck, M. Hoppema, M. P. Humphreys, C. W. Hunt, B. Huss, J. S. P. Ibánhez, T. Johannessen, R. Keeling, V. Kitidis, A. Körtzinger, A. Kozyr, E. Krasakopoulou, A. Kuwata, P. Landschützer, S. K. Lauvset, N. Lefèvre, C. L. Monaco, A. Manke, J. T. Mathis, L. Merlivat, F. J. Millero, P. M. S. Monteiro, D. R. Munro, A. Murata, T. Newberger, A. M. Omar, T. Ono, K. Paterson, D. Pearce, Denis P., L. L. Robbins, S. Saito, J. Salisbury, R. Schlitzer, B. Schneider, R. Schweitzer, R. Sieger, I. Skjelvan, K. F. Sullivan, S. C. Sutherland, A. J. Sutton, K. Tadokoro, M. Telszewski, M. Tuma, S. M. A. C. van Heuven, D. Vandemark, B. Ward, A. J. Watson, and S. Xu (2016). A multi-decade record of high-quality fCO2 data in version 3 of the Surface Ocean CO2 Atlas (SOCAT). Earth Syst. Sci. Data, 8(2), 383-413. http://www.earth-syst-sci-data.net/8/383/2016/

Balmaseda, M. A., K. E. Trenberth, and E. Källén (2013). Distinctive climate signals in reanalysis of global ocean heat content, Geophys. Res. Lett., 40(9), 1754-1759. https://doi.org/10.1002/grl.50382.

Barker, P. M., J. R. Dunn, C. M. Domingues, and S. E. Wijffels, 2011: Pressure Sensor Drifts in Argo and Their Impacts. J. Atmos. Oceanic Technol., 28, 1036–1049. http://dx.doi.org/10.1175/2011JTECHO831.1

Barnes, S. L. (1964). A Technique for Maximizing Details in Numerical Weather Map Analysis. J. Appl. Meteor. Climatol., **3**, 396–409, https://doi.org/10.1175/1520-0450(1964)003<0396:ATFMDI>2.0.CO;2

Barnes, S. L. (1973). Mesoscale objective map analysis using weighted time series observations. NOAA Technical Memorandum ERL NSSL-62, 60 pp.

Barnes, S. L. (1994). Applications of the Barnes Objective Analysis Scheme. Part III: Tuning for Minimum Error. J. Atmos. Oceanic Technol., 11, 1459–1479. https://doi.org/10.1175/1520-0426(1994)011<1459:AOTBOA>2.0.CO;2

Barnoud, A., Pfeffer, J., Cazenave, A., Fraudeau, R., Rousseau, V., and Ablain, M. (2023). Revisiting the global mean ocean mass budget over 2005–2020, Ocean Sci., 19, 321–334. https://doi.org/10.5194/os-19-321-2023

Bell, M. J., Forbes, R. M., and Hines, A. (2000). Assessment of the FOAM global data assimilation system for real-time operational ocean forecasting. J. Mar. Syst., 25, 1-22. https://doi.org/10.1016/S0924-7963(00)00005-1

Beltrami, H. (2001a). Surface heat flux histories from geothermal data: Inference from inversion, Geophys. Res. Lett., 28, 655–658. https://doi.org/10.1029/2000GL012238

Beltrami, H. (2001b). Surface heat flux histories from inversion of geothermal data: Energy balance at the Earth's surface, J. Geophys. Res., 106(B10), 21979–21993. https://doi.org/10.1029/2000JB000065

Beltrami, H., J. Smerdon, H. Pollack, and S. Huang (2002). Continental heat gain in the global climate system, Geophys. Res. Lett., 29(8). https://doi.org/10.1029/2001GL014310

Bentamy, J.F. Piollé, A. Grouazel, R. Danielson, S. Gulev, F. Paul, H. Azelmat, P.P. Mathieu, K. von Schuckmann, S. Sathyendranath, H. Evers-King, I. Esau, J.A. Johannessen, C.A. Clayson, R.T. Pinker, S.A. Grodsky, M. Bourassa, S.R. Smith, K. Haines, M. Valdivieso, C.J. Merchant, B. Chapron, A. Anderson, R. Hollmann, S.A. Josey (2017). Review and assessment of latent and sensible heat flux accuracy over the global oceans, Remote Sensing of Environment, 201, 196-218. https://doi.org/10.1016/j.rse.2017.08.016

Bergthorssen P., and Döös, P. (1955). Numerical Weather Map Analysis, Tellus, 7 (3), pp. 329-340.

Bindoff, N.L., J. Willebrand, V. Artale, A, Cazenave, J. Gregory, S. Gulev, K. Hanawa, C. Le Quere, S. Levitus, Y. Nojiri, C.K. Shum, L.D. Talley and A. Unnikrishnan (2007) Observations: Oceanic Climate Change and Sea Level. In: Climate Change 2007: The Physical Science Basis. Contribution of Working Group I to the Fourth Assessment Report of the Intergovernmental Panel on Climate Change [Solomon, S., D. Qin, M. Manning, Z. Chen, M. Marquis, K.B. Averyt, M. Tignor and H.L. Miller (eds.)]. Cambridge University Press, Cambridge, United Kingdom and New York, NY, USA.

Boehme, L., P. Lovell, M. Biuw, F. Roquet, J. Nicholson, S.E. Thorpe, M.P. Meredith, and M. Fedak (2009). Technical Note: Animal-borne CTD-satellite relay data loggers for real-time oceanographic data collection. Ocean Science Discussions 6:1,261–1,287. https://doi.org/10.5194/osd-6-1261-2009

Bohren, C. F., and B. A. Albrecht (1998). Atmospheric Thermodynamics. Oxford University Press, 402 pp.

Bojinski, S., Verstraete, M., Peterson, T. C., Richter, C., Simmons, A., & Zemp, M. (2014). The Concept of Essential Climate Variables in Support of Climate Research, Applications, and Policy, Bulletin of the American Meteorological Society, 95(9), 1431-1443. https://doi.org/10.1175/BAMS-D-13-00047.1

Boyd, J.D. (1987). Improved depth and temperature conversion equations for Sippican AXBTs. J. Atmos. Oceanic Technol., 4, 545-551. https://doi.org/10.1175/15200426(1987)004%3C0545:IDATCE%3E2.0.CO;2

Boyd, J.D. and R.S. Linzell (1993). Evaluation of the Sparton tight-tolerance AXBT. J. Atmo. Oceanic Technol., 10, 892-899. https://doi.org/10.1175/1520-0426(1993)010%3C0892:EOTSTT%3E2.0.CO;2

Boyer T. P. and Levitus, S (1994). Quality control and processing of historical oceanographic temperature, salinity, and oxygen data, NOAA technical report NESDIS, 81, 72 pp.

Boyer, T., Levitus, S., Garcia, H., Locarnini, R.A., Stephens, C. and Antonov, J. (2005). Objective analyses of annual, seasonal, and monthly temperature and salinity for the World Ocean on a 0.25° grid. Int. J. Climatol., 25: 931-945. https://doi.org/10.1002/joc.1173

Boyer, T.P., J.I. Antonov, H.E. Garcia, D.R. Johnson, R.A. Locarnini, A.V. Mishonov, M.T. Pitcher, O.K. Baranova, I.V. Smolyar (2006). World Ocean Database 2005. S. Levitus, Ed., NOAA Atlas NESDIS 60, U.S. Gov. Printing Office, Wash., D.C., 190 pp., DVDs.

Boyer, J. I. Antonov , O. K. Baranova, H. E. Garcia, D. R. Johnson, R. A. Locarnini, A. V. Mishonov, T. D. O'Brien, D. Seidov, I. V. Smolyar, M. M. Zweng (2009). World Ocean Database 2009. S. Levitus, Ed., NOAA Atlas NESDIS 66, U.S. Gov. Printing Office, Wash., D.C., 216 pp., DVDs.

Boyer, T.P., J.I. Antonov, O.K. Baranova, C. Coleman, H.E. Garcia, A. Grodsky, D.R. Johnson, R.A. Locarnini, A.V. Mishonov, T.D. O'Brien, C.R. Paver, J.R. Reagan, D. Seidov, I.V. Smolyar, M.M. Zweng, 2013, World Ocean Database (2013). Sydney Levitus, Ed.; Alexey Mishonov, Technical Ed.; NOAA Atlas NESDIS 72, 209 pp.

Boyer, T.P., O.K. Baranova, C. Coleman, H.E. Garcia, A. Grodsky, R.A. Locarnini, A.V. Mishonov, C.R. Paver, J.R. Reagan, D. Seidov, I.V. Smolyar, K. Weathers, M.M. Zweng (2018). World Ocean Database 2018. A.V. Mishonov, Technical Ed., NOAA Atlas NESDIS 87.

Bourlès, B., M. Araujo, M. J. McPhaden, P. Brandt, G. R. Foltz, R. Lumpkin, H. Giordani, F. Hernandez, N. Lefèvre, P. Nobre, E. Campos, R. Saravanan, J. Trotte-Duhà, M. Dengler, J. Hahn, R. Hummels, J. F. Lübbecke, M. Rouault, L. Cotrim, A. Sutton, M. Jochum, R. C. Perez. (2019). PIRATA: A sustained observing system for tropical Atlantic climate research and forecasting. Earth and Space Science, 6, 577–616. https://doi.org/10.1029/2018EA000428

Bretherton, F. P., R. E. Davis, and C. Fandry (1976). A technique for objective analysis and design of oceanographic experiments applied to mode-73. Deep-Sea Res. Oceanogr. Abstr., 23 (7), 559–582. https://doi.org/10.1016/0011-7471(76)90001-2

Bretherton, C. S., M, Widmann, V. P. Dymnkikov, J. M. Wallace, and I. Blade (1999) The effective number of spatial degrees of freedom of a time varying field. J. Climate, 12, 1990-2009. https://doi.org/10.1175/1520-0442(1999)012%3C1990:TENOSD%3E2.0.CO;2

Bringas, F., and G. Goni (2015) Early Dynamics of Deep Blue XBT Probes. J. Atmos. Oceanic Technol., 32, 2253–2263. https://doi.org/10.1175/JTECH-D-15-0048.1

Brown, N. L. (1974). A precision CTD microprofiler, Engineering in the Ocean Environment, Ocean ’74, IEEE International Conference, 270–278

Cael, B. B. (2022). Ocean heat uptake efficiency increase since 1970. Geophysical Research Letters, 49, e2022GL100215. https://doi.org/10.1029/2022GL100215

Carton, J. A., B. S. Giese, and S. A. Grodsky (2005). Sea level rise and the warming of the oceans in the Simple Ocean Data Assimilation (SODA) ocean reanalysis, J. Geophys. Res., 110, C09006. doi:10.1029/2004JC002817

Chambers, D. P., J. Wahr, M. E. Tamisiea, and R. S. Nerem (2010). Ocean mass from GRACE and glacial isostatic adjustment J. Geophys. Res. (Solid Earth) 115 B11415. https://doi.org/10.1029/2010JB007530

Chapman, P. (1998). The WOCE Data Resource. Bull. Amer. Meteor. Soc., 79, 1037–1042. https://doi.org/10.1175/1520-0477(1998)079<1037:TWDR>2.0.CO;2

Chen, D., N. Smith, and W. Kessler (2018). The evolving ENSO observing system. Natl. Sci. Rev., 5, 805–807. https://doi.org/10.1093/nsr/nwy137

Chen, X., and K.-K. Tung (2014). Varying planetary heat sink led to global-warming slowdown and acceleration, Science, 345(6199), 897-903. https://doi.org/10.1126/science.1254937

Chen, Y. (2020). COVID-19 Pandemic Imperils Weather Forecast, Geophys. Res. Lett., 15 July 2020. https://doi.org/10.1029/2020GL088613

Cheng, L. and J. Zhu (2014a). Uncertainties of the Ocean Heat Content Estimation Induced by Insufficient Vertical Resolution of Historical Ocean Subsurface Observations. J. Atmos. Oceanic Technol., 31, 1383–1396. doi: http://dx.doi.org/10.1175/JTECH-D-13-00220.1

Cheng, L., and J. Zhu (2014b), Artifacts in variations of ocean heat content induced by the observation system changes, Geophys. Res. Lett., 41, 7276–7283, https://doi.org/10.1002/2014GL061881

Cheng L., J. Zhu, R. Cowley, T. Boyer, and S. Wijffels, 2014: Time, Probe Type, and Temperature Variable Bias Corrections to Historical Expendable Bathythermograph Observations. J. Atmos. Oceanic Technol., 31, 1793–1825. http://dx.doi.org/10.1175/JTECH-D-13-00197.1

Cheng, L., and J. Zhu (2015) Influences of the choice of climatology on ocean heat content estimation. J. Atmos. Ocean Tech., 32, 388-394. https://doi.org/10.1175/JTECH-D-14-00169.1

Cheng, L., J. Abraham, G. Goni, T. Boyer, S. Wijffels, R. Cowley, V. Gouretski, F. Reseghetti, S. Kizu, S. Dong, F. Bringas, M. Goes, L. Houpert, J. Sprintall, J. Zhu (2015a) Fourth XBT Science Workshop progress report: making consensus and establishing best practices to reduce XBT biases, Bull. Am. Meteorol. Soc. http://dx.doi.org/10.1175/BAMS-D-15-00031.1

Cheng, L., F. Zheng, and J. Zhu (2015b). Distinctive ocean interior changes during the recent warming slowdown, Sci. Rep., 5, 14346. https://doi.org/10.1038/srep14346

Cheng, L., J. Zhu and J. Abraham (2015) Global Upper Ocean Heat Content Estimation: Recent Progress and the Remaining Challenges, Atmospheric and Oceanic Science Letters, 8:6, 333-338. http://dx.doi.org/10.3878/AOSL20150031

Cheng, L., J. Abraham, G. Goni, T. Boyer, S. Wijffels, R. Cowley, V. Gouretski, F. Reseghetti, S. Kizu, S. Dong, F. Bringas, M. Goes, L. Houpert, J. Sprintall, and J. Zhu (2016). XBT Science: Assessment of Instrumental Biases and Errors. Bull. Amer. Meteor. Soc., 97, 924–933. https://doi.org/10.1175/BAMS-D-15-00031.1

Cheng, L., and J. Zhu (2016). Benefits of CMIP5 Multimodel Ensemble in Reconstructing Historical Ocean Subsurface Temperature Variations. J. Climate, 29, 5393–5416. https://doi.org/10.1175/JCLI-D-15-0730.1

Cheng, L., J. Zhu, J. Abraham, K. E. Trenberth, J. T. Fasullo, B. Zhang, F. Yu, L. Wan, X. Chen and X. Song (2019). Continues Record Global Ocean Warming. Adv. Atmos. Sci. 36, 249–252. https://doi.org/10.1007/s00376-019-8276-x

Cheng, L., J. Abraham, J. Zhu, K. E. Trenberth, J. Fasullo, T. Boyer, R. Locarnini, B. Zhang, F. Yu, L. Wan, X. Chen, X. Song, Y. Liu and M. E. Mann (2020). Record-Setting Ocean Warmth Continued in 2019. Adv. Atmos. Sci. 37, 137–142. https://doi.org/10.1007/s00376-020-9283-7

Cheng, L., J. Abraham, K. E. Trenberth, J. Fasullo, T. Boyer, R. Locarnini, B. Zhang, F. Yu, L. Wan, X. Chen, X. Song, Y. Liu, M. E. Mann, F. Reseghetti, S. Simoncelli, V. Gouretski, G. Chen, A. Mishonov, J. Reagan and J. Zhu (2021). Upper Ocean Temperatures Hit Record High in 2020. Adv. Atmos. Sci. 38, 523–530. https://doi.org/10.1007/s00376-021-0447-x

Cheng, L., J. Abraham, K. E. Trenberth, J. Fasullo, T. Boyer, M. E. Mann, J. Zhu, F. Wang, R. Locarnini, Y. Li, B. Zhang, Z. Tan, F. Yu, L. Wan, X. Chen, X. Song, Y. Liu, F. Reseghetti, S. Simoncelli, V. Gouretski, G. Chen, A. Mishonov and J. Reagan (2022a). Another Record: Ocean Warming Continues through 2021 despite La Niña Conditions. Adv. Atmos. Sci. 39, 373–385. https://doi.org/10.1007/s00376-022-1461-3

Cheng, L., G. Foster, Z. Hausfather, K. E. Trenberth, and J. Abraham (2022b). Improved Quantification of the Rate of Ocean Warming. J. Climate, 35, 4827–4840, https://doi.org/10.1175/JCLI-D-21-0895.1

Cheng, L., K. von Schuckmann, J. P. Abraham, K. E. Trenberth, M. E. Mann, L. Zanna, M. H. England, J. D. Zika, J. T. Fasullo, Y. Yu, Y. Pan, J. Zhu, E. R. Newsom, B. Bronselaer, and X. Lin (2022c). Past and future ocean warming. Nat Rev Earth Environ 3, 776–794. https://doi.org/10.1038/s43017-022-00345-1

Cheng, L., J. Abraham, K. E. Trenberth, J. Fasullo, T. Boyer, M. E. Mann, J. Zhu, F. Wang, R. Locarnini, Y. Li, B. Zhang, F. Yu, L. Wan, X. Chen, L. Feng, X. Song, Y. Liu, F. Reseghetti, S. Simoncelli, V. Gouretski, G. Chen, A.Mishonov, J. Reagan and G. Li (2023). Another Year of Record Heat for the Oceans. Adv. Atmos. Sci. 40, 963–974. https://doi.org/10.1007/s00376-023-2385-2

Cheng, L., J. Abraham, K. E. Trenberth, T. Boyer, M. E. Mann, J. Zhu, F. Wang, F. Yu, R. Locarnini, J. Fasullo, F. Zheng, Y. Li, B. Zhang, L. Wan, X. Chen, D. Wang, L. Feng, X. Song, Y. Liu, F. Reseghetti, S. Simoncelli, V. Gouretski, G. Chen, A. Mishonov, J. Reagan, K. von Schuckmann, Y. Pan, Z. Tan, Y. Zhu, W. Wei, G. Li, Q. Ren, L. Cao and Y. Lu (2024). New Record Ocean Temperatures and Related Climate Indicators in 2023. Adv. Atmos. Sci. https://doi.org/10.1007/s00376-024-3378-5

Church, J. A., N. J. White, L. F. Konikow, C. M. Domingues, J. G. Cogley, E. Rignot, J. M. Gregory, M. R. van den Broeke, A. J. Monaghan, and I. Velicogna (2011). Revisiting the Earth's sea-level and energy budgets from 1961 to 2008, Geophys. Res. Lett., 38, L18601, https://doi.org/10.1029/2011GL048794

Church, J.A., P.U. Clark, A. Cazenave, J.M. Gregory, S. Jevrejeva, A. Levermann, M.A. Merrifield, G.A. Milne, R.S. Nerem, P.D. Nunn, A.J. Payne, W.T. Pfeffer, D. Stammer and A.S. Unnikrishnan (2013). Sea Level Change. In: Climate Change 2013: The Physical Science Basis. Contribution of Working Group I to the Fifth Assessment Report of the Intergovernmental Panel on Climate Change [Stocker, T.F., D. Qin, G.-K. Plattner, M. Tignor, S.K. Allen, J. Boschung, A. Nauels, Y. Xia, V. Bex and P.M. Midgley (eds.)]. Cambridge University Press, Cambridge, United Kingdom and New York, NY, USA.

Clem, K. R. and M. N. Raphael, Eds. (2023). Antarctica and the Southern Ocean [in “State of the Climate in 2022“]. Bull. Amer. Meteor. Soc., 104 (9), S322–S365. https://doi.org/10.1175/BAMS-D-23-0077.1.

Cook J. and G. Forster (1821). The Three Voyages of Captain Cook Round the World, Vol. III (of VII) Being the First of the Second Voyage. London, England, Printed by A. & R. Spottiswoode, New-Street-Square.

Conkright, M. E., S. Levitus, T. O.’Brien, T.P. Boyer, C. Stephens, D. Johnson, O. Baranova, J. Antonov, R. Gelfeld, J. Rochester, C. Forgy (1999) World Ocean Database Documentation and Quality Control, National Oceanographic Data Center Internal Documentation 14. 118 pp.

Conkright, M. E., J. I. Antonov, O. Baranova, T. P. Boyer, H. E. Garcia, R. Gelfeld, D. Johnson, R. A. Locarnini, P. P. Murphy, T. D. O'Brien, I. Smolyar, C. Stephens (2002). World Ocean Database 2001, Volume 1: Introduction. S. Levitus, Ed., NOAA Atlas NESDIS 42, U.S. Government Printing Office, Wash., D.C., 167 pp., CD-ROMs.

Costello, M. J., A. Cheung, N. De Hauwere (2010). Topography statistics for the surface and seabed area, volume, depth and slope, of the world's seas, oceans and countries. Environ. Sci. Technol., 44, pp. 8821-8828. https://doi.org/10.1021/es1012752

Cowley, R., S. Wijffels, L. Cheng, T. Boyer, and S. Kizu (2013). Biases in Expendable Bathythermograph Data: A New View Based on Historical Side-by-Side Comparisons. J. Atmos. Oceanic Technol., 30, 1195–1225, https://doi.org/10.1175/JTECH-D-12-00127.1

Cowley, R., R. E. Killick, T. Boyer, V. Gouretski, F. Reseghetti, S. Kizu, M. D. Palmer, L. Cheng, A. Storto, M. Le Menn, S. Simoncelli, A. M. Macdonald, C. M. Domingues (2021). International Quality-Controlled Ocean Database (IQuOD) V0.1: The temperature uncertainty specification. Front. Mar. Sci., 11. https://doi.org/10.3389/fmars.2021.689695

Cowtan, K., and R. G. Way (2014). Coverage bias in the HadCRUT4 temperature series and its impact on recent temperature trends, Q. J. R. Meteorolog. Soc. , 140(683), 1935-1944. https://doi.org/10.1002/qj.2297

Cressman, G. P. (1959). An Operational Objective Analysis System. Mon. Wea. Rev., **87**, 367–374. https://doi.org/10.1175/1520-0493(1959)087<0367:AOOAS>2.0.CO;2

Cuesta-Valero, F. J., H. Beltrami, S. Gruber, A. García-García, and J. F. González-Rouco (2022). A new bootstrap technique to quantify uncertainty in estimates of ground surface temperature and ground heat flux histories from geothermal data, Geosci. Model Dev., 15, 7913–7932. https://doi.org/10.5194/gmd-15-7913-2022, 2022.

Cuesta-Valero, F. J., H. Beltrami, A. García-García, G. Krinner, M. Langer, A. H. MacDougall, J. Nitzbon, J. Peng, K. von Schuckmann, S. I. Seneviratne, W. Thiery, I. Vanderkelen, and T. Wu (2023). Continental heat storage: Contributions from ground, inland waters, and permafrost thawing, Earth Syst. Dynam. Discuss. https://doi.org/10.5194/esd-2022-32

Davis, R. E., D. C. Webb, L. A. Reiger, and J. Dufour (1992). The Autonomous Lagrangian Circulation Explorer (ALACE), J. Atmos. Oceanic Technol., 18, 982–993. https://doi.org/10.1175/1520-0426(1992)009%3C0264:TALCE%3E2.0.CO;2.

Davis, R. E., J. T. Sherman, and J. Dufour (2001). Profiling ALACEs and other advances in autonomous profiling floats: An Argo perspective, J. Atmos. Oceanic Technol., 22, 292–301. https://doi.org/10.1175/1520-0426(2001)018%3C0982:PAAOAI%3E2.0.CO;2.

Davis, R. E., C. C. Eriksen, and C. P. Jones (2002). Autonomous Buoyancy-Driven Underwater Gliders, Chapter 3, Technology and Applications of Autonomous Underwater Vehicles, Edited by Gwyn Griffiths, CRC press, 22 pp. https://doi.org/10.1201/9780203522301

de Boisséson, E., M. A. Balmaseda, and M. Mayer (2018). Ocean heat content variability in an ensemble of twentieth century ocean reanalyses. Clim Dyn 50, 3783–3798. https://doi.org/10.1007/s00382-017-3845-0

Derber, J., A. Rosati, 1989: A Global Oceanic Data Assimilation System. J. Phys. Oceanogr., 19 1333–1347. http://dx.doi.org/10.1175/1520-0485(1989)019<1333:AGODAS>2.0.CO;2

Domingues, C., J. Church, N. White, P. J. Gleckler, S. E. Wijffels, P. M. Barker, and J. R. Dunn (2008). Improved estimates of upper-ocean warming and multi-decadal sea-level rise. Nature, 453, 1090–1093. https://doi.org/10.1038/nature07080

Ducet, N., P. Y. Le Traon, and G. Reverdin (2000). Global high-resolution mapping of ocean circulation from TOPEX/Poseidon and ERS-1 and -2, J. Geophys. Res., 105(C8), 19477–19498. https://doi.org/10.1029/2000JC900063

Durack P J, S. E. Wijffels and R. J. Matear (2012). Ocean salinities reveal strong global water cycle intensification during 1950–2000 Science 336 455–8

Durack, P., P. Gleckler, F. Landerer, and K. E. Taylor, (2014). Quantifying underestimates of long-term upper-ocean warming. Nature Clim Change, 4, 999–1005. https://doi.org/10.1038/nclimate2389. https://doi.org/10.1126/science.1212222

Dushaw, B. D. (2018). Ocean acoustic tomography in the North Atlantic. J. Atmos. Oceanic Technol. 36, 183–202. https://doi.org/10.1175/JTECH-D-18-0082.1

Elipot, S., K. Drushka, A. Subramanian, and M. Patterson (2022). Overcoming the challenges of ocean data uncertainty, Eos, 103. https://doi.org/10.1029/2022EO220021

Eriksen, C.C., T.J. Osse, R.D. Light, T. Wen, T.W. Lehman, P.L. Sabin, J.W. Ballard, and A.M. Chiodi (2001). Seaglider: A long-range autonomous underwater vehicle for oceanographic research, IEEE J. Oceanic Eng., 26(4), 424-436. https://doi.org/10.1109/48.972073

England, M. H., S. McGregor, P. Spence, G. A. Meehl, A. Timmermann, W. Cai, A. S. Gupta, M. J. McPhaden, A. Purich, and A. Santoso (2014). Recent intensification of wind-driven circulation in the Pacific and the ongoing warming hiatus, Nature Clim. Change, 4(3), 222-227. https://doi.org/10.1038/nclimate2106

Flierl, G., and A. Robinson (1977). XBT measurements of thermal gradients in the MODE eddy, J. Phys. Oceanogr., 7, 300–302.

Forster, P. M. F., and J. M. Gregory (2006). The Climate Sensitivity and Its Components Diagnosed from Earth Radiation Budget Data. J. Climate, 19, 39–52. https://doi.org/10.1175/JCLI3611.1

Forster, P. M. (2016). Inference of Climate Sensitivity from Analysis of Earth's Energy Budget, Annual Review of Earth and Planetary Science, 44, 85-106. https://doi.org/10.1146/annurev-earth-060614-105156

Forster, P., T. Storelvmo, K. Armour, W. Collins, J.-L. Dufresne, D. Frame, D.J. Lunt, T. Mauritsen, M.D. Palmer, M. Watanabe, M. Wild, and H. Zhang (2021). The Earth's Energy Budget, Climate Feedbacks, and Climate Sensitivity. In Climate Change 2021: The Physical Science Basis. Contribution of Working Group I to the Sixth Assessment Report of the Intergovernmental Panel on Climate Change [Masson-Delmotte, V., P. Zhai, A. Pirani, S.L. Connors, C. Péan, S. Berger, N. Caud, Y. Chen, L. Goldfarb, M.I. Gomis, M. Huang, K. Leitzell, E. Lonnoy, J.B.R. Matthews, T.K. Maycock, T. Waterfield, O. Yelekçi, R. Yu, and B. Zhou

(eds.)]. Cambridge University Press, Cambridge, United Kingdom and New York, NY, USA, pp. 923–1054. https://doi.org/10.1017/9781009157896.009

Freeman, E., S.D. Woodruff, S.J. Worley, S.J. Lubker, E.C. Kent, W.E. Angel, D.I . Berry, P. Brohan, R. Eastman, L. Gates, W. Gloeden, Z. Ji, J. Lawrimore, N.A. Rayner, G. Rosenhagen, and S.R. Smith. (2017) ICOADS Release 3.0: A major update to the historical marine climate record. Int. J. Climatol. (CLIMAR-IV Special Issue), 37, 2211-2237. https://doi.org/10.1002/joc.4775

Friedlingstein, P., M. W. Jones, M. O'Sullivan, R. M. Andrew, D. C. E. Bakker, J. Hauck, C. Le Quéré, G. P. Peters, W. Peters, J. Pongratz, S. Sitch, J. G. Canadell, P. Ciais, R. B. Jackson, S. R. Alin, P. Anthoni, N. R. Bates, M. Becker, N. Bellouin, L. Bopp, T. T. T. Chau, F. Chevallier, L. P. Chini, M. Cronin, K. I. Currie, B. Decharme, L. M. Djeutchouang, X. Dou, W. Evans, R. A. Feely, L. Feng, T. Gasser, D. Gilfillan, T. Gkritzalis, G. Grassi, L. Gregor, N. Gruber, Ö. Gürses, I. Harris, R. A. Houghton, G. C. Hurtt, Y. Iida, T. Ilyina, I. T. Luijkx, A. Jain, S. D. Jones, E. Kato, D. Kennedy, K. K. Goldewijk, J. Knauer, J. I. Korsbakken, A. Körtzinger, P. Landschützer, S. K. Lauvset, N. Lefèvre, S. Lienert, J. Liu, G. Marland, P. C. McGuire, J. R. Melton, D. R. Munro, J. E. M. S. Nabel, S.-I. Nakaoka, Y. Niwa, T. Ono, D. Pierrot, B. Poulter, G. Rehder, L. Resplandy, E. Robertson, C. Rödenbeck, T. M. Rosan, J. Schwinger, C. Schwingshackl, R. Séférian, A. J. Sutton, C. Sweeney, T. Tanhua, P. P. Tans, H. Tian, B. Tilbrook, F. Tubiello, G. R. van der Werf, N. Vuichard, C. Wada, R. Wanninkhof, A. J. Watson, D. Willis, A. J. Wiltshire, W. Yuan, C. Yue, X. Yue, S. Zaehle, and J. Zeng (2022). Global Carbon Budget 2021, Earth Syst. Sci. Data, 14, 1917–2005. https://doi.org/10.5194/essd-14-1917-2022, 2022

Fujii, Y., J. Cummings, Y. Xue, A. Schiller, T. Lee, M. A. Balmaseda, E. Remy, S. Masuda, G. Brassington, O. Alves, B. Cornuelle, M. Martin, P. Oke, G. Smith and X. Yang/ (2015) Evaluation of the Tropical Pacific Observing System from the ocean data assimilation perspective, Q. J. R. Meteorol. Soc. 141: 2481–2496. https://doi.org/10.1002/qj.2579

Fyfe, J. C., N. P. Gillett, and F. W. Zwiers (2013). Overestimated global warming over the past 20 years, Nature Clim. Change, 3(9), 767-769. https://doi.org/10.1038/nclimate1972.

Fyfe, J. C., G. A. Meehl, M. H. England, M. E. Mann, B. D. Santer, G. M. Flato, E. Hawkins, N. P. Gillett, S.-P. Xie, Y. Kosaka, and N. C. Swart (2016). Making sense of the early-2000s warming slowdown, Nature Clim. Change, 6(3), 224-228. https://doi.org/10.1038/nclimate2938.

Gaillard, F., T. Reynaud, V. Thierry, N. Kolodziejczyk, and K. von Schuckmann (2016). *In situ*–Based Reanalysis of the Global Ocean Temperature and Salinity with ISAS: Variability of the Heat Content and Steric Height. J. Climate, 29, 1305–1323, https://doi.org/10.1175/JCLI-D-15-0028.1

Gandin, L. S. (1963). Objective Analysis of Meteorological fields. Gidromet Izdat, Leningrad (translation by Israel program for Scientific Translations), Jerusalem, 1966, 242 pp.

Gao, L., S. R. Rintoul, and W. Yu (2018). Recent wind-driven change in Subantarctic Mode Water and its impact on ocean heat storage. Nature Clim Change 8, 58–63. https://doi.org/10.1038/s41558-017-0022-8

Gilgen, H., M. Wild, and A. Ohmura (1998) Means and Trends of Shortwave Irradiance at the Surface Estimated from Global Energy Balance Archive Data. J. Climate, 11, 2042–2061. https://doi.org/10.1175/1520-0442(1998)011<2042:MATOSI>2.0.CO;2

Gleckler, P. J., Santer, B. D., Domingues, C. M., Pierce, D. W., Barnett, T. P., Church, J. A., … Caldwell, P. M. (2012). Human-induced global ocean warming on multidecadal timescales. Nature Clim. Change, 2, 524–529. http://dx.doi.org/10.1038/nclimate1553

Good, S. A., Martin, M. J., and Rayner, N. A. (2013). EN4: Quality controlled ocean temperature and salinity profiles and monthly objective analyses with uncertainty estimates, J. Geophys. Res. Oceans, 118, 6704– 6716. https://doi.org/10.1002/2013JC009067

Good, S. A. (2016). The impact of observational sampling on time series of global 0-700 m ocean average temperature: a case study, Int. J. Climatol. https://doi.org/10.1002/joc.4654

Goni, G., D. Roemmich, R. Molinari, G. Meyers, C. Sun, T. Boyer, M. Baringer, V. Gouretski, P. DiNezio, F. Reseghetti, G. Vissa, S. Swart, R. Keeley, S. Garzoli(1), T. Rossby, C. Maes, G. Reverdin (2010). "The Ship of Opportunity Program" in Proceedings of OceanObs'09: Sustained Ocean Observations and Information for Society (Vol. 2), Venice, Italy, 21-25 September 2009, Hall, J., Harrison, D.E. & Stammer, D., Eds., ESA Publication WPP-306, https://doi.org/10.5270/OceanObs09.cwp.35

Goni G. J., J. Sprintall, F. Bringas, L. Cheng, M. Cirano, S. Dong, R. Domingues, M. Goes, H. Lopez, R. Morrow, U. Rivero, T. Rossby, R. E. Todd, J. Trinanes, N. Zilberman, M. Baringer, T. Boyer, R. Cowley, C. M. Domingues, K. Hutchinson, M. Kramp, M. M. Mata, F. Reseghetti, C. Sun, TVS U. Bhaskar, and D. Volkov (2019). More Than 50 Years of Successful Continuous Temperature Section Measurements by the Global Expendable Bathythermograph Network, Its Integrability, Societal Benefits, and Future, Frontiers in Marine Science, 24. https://doi.org/10.3389/fmars.2019.00452

Good, S. A. (2011) Depth Biases in XBT Data Diagnosed Using Bathymetry Data. J. Atmos. Oceanic Technol., 28, 287–300. https://doi.org/10.1175/2010JTECHO773.1

Good, S. A., M. J. Martin, and N. A. Rayner (2013). EN4: Quality controlled ocean temperature and salinity profiles and monthly objective analyses with uncertainty estimates, J. Geophys. Res. Oceans, 118, 6704–6716. https://doi.org/10.1002/2013JC009067

Good S., B. Mills, T. Boyer, F. Bringas, G. Castelão, R. Cowley, G. Goni, V. Gouretski, C. M. Domingues (2023). Benchmarking of automatic quality control checks for ocean temperature profiles and recommendations for optimal sets, Frontiers in Marine Science, 9. https://www.frontiersin.org/articles/10.3389/fmars.2022.1075510

Gould, J., B. Sloyan, M. Visbeck (2013). *In situ* Ocean Observations: A Brief History, Present Status, and Future Directions Ocean Circulation and Climate, Vol. 103. http://dx.doi.org/10.1016/B978-0-12-391851-2.00003-9

Gouretski, V., and K. P. Koltermann (2007) How much is the ocean really warming? Geophys. Res. Lett., 34, L01610. https://doi.org/10.1029/2006GL027834

Gouretski, V. and F. Reseghetti (2010) On depth and temperature biases in bathythermograph data: Development of a new correction scheme based on analysis of a global ocean database. Deep-Sea Research I, Vol. 57(6), pp. 812-834. https://doi.org/10.1016/j.dsr.2010.03.011

Gouretski, V. (2012) Using GEBCO digital bathymetry to infer depth biases in the XBT data, Deep Sea Research-I, 62, 40-52. https://doi.org/10.1016/j.dsr.2011.12.012

Gouretski, V., J. Kennedy, T. Boyer, and A. Köhl (2012) Consistent near-surface ocean warming since 1900 in two largely independent observing networks, Geophys. Res. Lett., 39, L19606, doi:10.1029/2012GL052975

Gouretski, V. (2018) World Ocean Circulation Experiment – Argo Global Hydrographic Climatology, Ocean Sci., 14, 1127–1146. https://doi.org/10.5194/os-14-1127-2018

Gouretski, V., and L. Cheng, 2020: Correction for Systematic Errors in the Global Dataset of Temperature Profiles from Mechanical Bathythermographs. J. Atmos. Oceanic Technol., 37, 841–855, https://doi.org/10.1175/JTECH-D-19-0205.1

Gouretski, V., L. Cheng, and T. Boyer (2022): On the Consistency of the Bottle and CTD Profile Data. J. Atmos. Oceanic Technol., 39, 1869–1887, https://doi.org/10.1175/JTECH-D-22-0004.1.

Green, A. W. (1984). Bulk dynamics of the expendable bathythermograph (XBT), Deep Sea Res Oceanogr Res Paper, 31, 415–426. https://doi.org/10.1016/0198-0149(84)90093-1

Grégoire, M., Garçon, V., Garcia, H., Breitburg, D., Isensee, K., Oschlies, A., *et al.* (2021): A Global Ocean Oxygen Database and Atlas for Assessing and Predicting Deoxygenation and Ocean Health in the Open and Coastal Ocean. Front. Mar. Sci. 8, 724913. https://doi.org/10.3389/fmars.2021.724913

Gregory, J. M., R. J. Stouffer, S. C. B. Raper, P. A. Stott, and N. A. Rayner (2002). An Observationally Based Estimate of the Climate Sensitivity. J. Climate, 15, 3117–3121. https://doi.org/10.1175/1520-0442(2002)015<3117:AOBEOT>2.0.CO;2

Gregory, J. M., H. T. Banks, P. A. Stott, J. A. Lowe, and M. D. Palmer (2004). Simulated and observed decadal variability in ocean heat content, Geophys. Res. Lett., 31, L15312. https://doi.org/10.1029/2004GL020258.

Gregory, J.M., S. M. Griffies, C. W. Hughes, J. A. Lowe, J. Church, I. Fukimori, N. Gomez, R. E. Kopp, F. Landerer, G. Le Cozannet, R. M. Ponte, D. Stammer, M. E. Tamisiea and R. S. W. van de Wal (2019). Concepts and Terminology for Sea Level: Mean, Variability and Change, Both Local and Global. Surv Geophys 40, 1251–1289. https://doi.org/10.1007/s10712-019-09525-z

Hakuba, M. Z., S. Fourest, T. Boyer, B. Meyssignac, James A. Carton, Gaël Forget, L. Cheng, D. Giglio, G. C. Johnson, S. Kato, R. Killick, N. Kolodziejczyk, M. Kuusela, F. Landerer, W. Llovel, R. Locarnini, N. Loeb, J. M. Lyman, A. Mishonov, P. Pilewskie, J. Reagan, A. Storto, T. Sukianto, K. von Schuckmann (2024). Trends and Variability in Earth's Energy Imbalance and Ocean Heat Uptake since 2005, Surveys in Geophysics, accepted.

Hamon, B. V. (1955). A temperature-salinity-depth recorder, Journal du Conseil International pur l'Exploration de la Mer, 21, 72–73.

Hamon, B. V., and N. L. Brown (1958). A temperature-chlorinity-depth recorder for use at sea, J. Sci. Instrum., 35, 452.

Hamon, M., G. Reverdin, and P. Le Traon (2012). Empirical Correction of XBT Data. J. Atmos. Oceanic Technol., 29, 960–973. https://doi.org/10.1175/JTECH-D-11-00129.1

Hanawa, K., P. Rual, R. Bailey, A. Sy, and M. Szabados (1995) A new depth time equation for Sippican or TSK T-7, T-6 and T-4 expendable bathythermographs (XBT), Deep Sea Res., Part I, 42, 1423–1451, https://doi.org/10.1016/0967-0637(95)97154-Z.

Hansen, J. E., M. Sato. L. Simons, L. S. Nazarenko, I. Sangha, P. Kharecha, J. C. Zachos, K. von Schuckmann, N. G. Loeb, M. B. Osman, Q. Jin, G. Tselioudis, E. Jeong, A. Lacis, R. Ruedy, G. Russell, J. Cao, and J. Li (2023). Global warming in the pipeline, Oxford Open Climate Change, 3 (1). kgad008. https://doi.org/10.1093/oxfclm/kgad008

Hartmann, D. L., A. M. G. Klein Tank, M. Rusticucci, L. V. Alexander, S. Brönnimann, Y. Charabi, F. J. Dentener, E. J. Dlugokencky, D. R. Easterling, A. Kaplan, B. J. Soden, P. W. Thorne, M. Wild, and P. M. Zhai (2013). Observations: Atmosphere and Surface, in Climate Change 2013: The Physical Science Basis. Contribution of Working Group I to the Fifth Assessment Report of the Intergovernmental Panel on Climate Change, edited by T. F. Stocker, D. Qin, G.-K. Plattner, M. Tignor, S. K. Allen, J. Boschung, A. Nauels, Y. Xia, V. Bex and P. M. Midgley, pp. 159–254, Cambridge University Press, Cambridge, United Kingdom and New York, NY, USA. https://doi.org/10.1017/CBO9781107415324.008

Helber, R. W., A. B. Kara, J. G. Richman, M. R. Carnes, C. N. Barron, H. E. Hurlburt, and T. Boyer (2012). Temperature versus salinity gradients below the ocean mixed layer, J. Geophys. Res., 117, C05006. https://doi.org/10.1029/2011JC007382

Heinmiller, R. H., C. C. Ebbesmeyer, B. A. Taft, T. B. Olson, and O. P. Nikitin (1983). Systematic errors in expendable bathythermograph (XBT) profiles, Deep Sea Res., 30, 1185–1197. https://doi.org/10.1016/0198-0149(83)90096-1

Hellend-Hansen, B., and F. Nansen (1909). The Norwegian Sea: Its physical oceanography based upon the Norwegian Researchers 1900–1904, Reports on Norwegian Fishery and Marine Investigations, 11, 390.

Hoerling, M. P., J. Hurrell, and T. Xu (2001). Tropical origins for North Atlantic climate change. Science, 292, 90-92. http://www.jstor.org/stable/3082892

Hood, M., M. Fukasawa, N. Gruber, G. C. Johnson, A. Koertzinger, C. Sabine, B. Sloyan, K. Stansfield, and T. Tanhua (2009). Ship-based repeat hydrography: a strategy for a sustained global program, in OceanObs'09: Sustained ocean observations and information for society (Vol. 2), Venice, Italy, 21-25 September, edited by J. Hall, D. E. Harrison and D. Stammer, ESA Publication WPP-306. https://doi.org/10.5270/OceanObs09.cwp.44

Howe, B., J. Miksis-Olds, E. Rehm, H. Sagen, P. F. Worcester, and G. Haralabus (2019). The roles of underwater acoustics in observing the global ocean. Front. Mar. Sci., 6. https://doi.org/10.3389/fmars.2019.00426

Huang, B., C. Liu, V. F. Banzon, H.-M. Zhang, T. R. Karl, J. H. Lawrimore, and R. S. Vose (2016). Assessing the impact of satellite-based observations in sea surface temperature trends, Geophys. Res. Lett. , 43(7), 3431-3437. https://doi.org/10.1002/2016GL068757

Huang, B., P. W. Thorne, V. F. Banzon, T. Boyer, G. Chepurin, J. H. Lawrimore, M. J. Menne, T. M. Smith, R. S. Vose, H. Zhang (2017). NOAA Extended Reconstructed Sea Surface Temperature (ERSST), Version 5. NOAA National Centers for Environmental Information. https://doi.org/10.7289/V5T72FNM

Huguenin, M.F., R. M. Holmes, and M. H. England (2022). Drivers and distribution of global ocean heat uptake over the last half century. Nat Commun 13, 4921. https://doi.org/10.1038/s41467-022-32540-5

Huffman, G. J., R. F. Adler, A. Behrangi, D. T. Bolvin, E. J. Nelkin, G. Gu, and M. R. Ehsani (2023) The New Version 3.2 Global Precipitation Climatology Project (GPCP) Monthly and Daily Precipitation Products. J. Climate, 36, 7635–7655, https://doi.org/10.1175/JCLI-D-23-0123.1

Ito, T., Minobe, S., Long, M. C., and Deutsch, C. (2017). Upper ocean O_2 trends: 1958–2015, Geophys. Res. Lett., 44, 4214– 4223. https://doi.org/10.1002/2017GL073613

Intergovernmental Oceanographic Commission (IOC), Scientific Committee on Oceanographic Research (SCOR), and International Association for the Physical Sciences of the Oceans (IAPSO) (2010). The International Thermodynamic Equation of Seawater – 2010: Calculation and Use of Thermodynamic Properties. Intergovernmental Oceanographic Commission, Manuals and Guides No. 56. Paris: UNESCO, 196.

Intergovernmental Panel on Climate Change (IPCC) (2013). Climate Change 2013: The Physical Science Basis. Contribution of Working Group I to the Fifth Assessment Report of the Intergovernmental Panel on Climate Change, 1535 pp., Cambridge University Press, Cambridge, United Kingdom and New York, NY, USA. https://doi.org/10.1017/CBO9781107415324

International Association for the Properties of Water and Steam (IAPWS) (2008). Berlin, Release on the IAPWS Formulation 2008 for the Thermodynamic Properties of Seawater, Berlin, Germany.

Ingleby, B., and M. Huddleston (2007). Quality control of ocean temperature and salinity profiles—Historical and real-time data, J. Mar. Syst., 65, 158–175. https://doi.org/10.1016/j.jmarsys.2005.11.019

Irrgang, C., J. Saynisch, and M. Thomas (2019). Estimating global ocean heat content from tidal magnetic satellite observations. Sci Rep 9, 7893. https://doi.org/10.1038/s41598-019-44397-8

Ishii, M., M. Kimoto and M. Kachi (2003) Historical ocean subsurface temperature analysis with error estimates, Mon. Wea. Rev., 131, 51–73. https://doi.org/10.1175/1520-0493(2003)131%3C0051:HOSTAW%3E2.0.CO;2

Ishii, M., Shouji, A., Sugimoto, S. and Matsumoto, T. (2005). Objective analyses of sea-surface temperature and marine meteorological variables for the 20th century using ICOADS and the Kobe Collection. Int. J. Climatol., 25: 865–879. https://doi.org/10.1002/joc.1169

Ishii, M., M. Kimoto, K. Sakamoto, and S.I. Iwasaki (2006) Steric sea level changes estimated from historical ocean subsurface temperature and salinity analysis, J. Oceanogr. , 62, 155-170. https://doi.org/10.1007/s10872-006-0041-y

Ishii, M., and M. Kimoto (2009). Reevaluation of historical ocean heat content variations with time-varying XBT and MBT depth bias corrections, J. Oceanogr., 65, 287–299. https://doi.org/10.1007/s10872-009-0027-7

Ishii, M., Y. Fukuda, H. Hirahara, S. Yasui, T. Suzuki, and K. Sato (2017). Accuracy of Global Upper Ocean Heat Content Estimation Expected from Present Observational Data Sets. SOLA, Vol. 13, 163 – 167. https://doi.org/10.2151/sola.2017-030

Jackett, D. R., and T. J. Mcdougall, (1995). Minimal Adjustment of Hydrographic Profiles to Achieve Static Stability. J. Atmos. Oceanic Technol., 12, 381–389. https://doi.org/10.1175/1520-0426(1995)012<0381:MAOHPT>2.0.CO;2

Ji, F., Z. Wu, J. Huang, and E. P. Chassignet (2014). Evolution of land surface air temperature trend, Nature Clim. Change, 4(6), 462-466. https://doi.org/10.1038/nclimate2223

Johnson, G. C., and S. E. Wijffels (2011). Ocean density change contributions to sea level rise. Oceanogr., 24, 112–121. https://doi.org/10.5670/oceanog.2011.31.

Johnson, G.C., J.M. Lyman, J. Antonov, N. Bindoff, T. Boyer, C.M. Domingues, S.A. Good, M. Ishii, and J.K. Willis (2015a). Ocean heat content. In State of the Climate in 2014, Global Oceans. Bull. Am. Meteorol. Soc., 96(7), S64–S66, S68.

Johnson, G. C., J. M. Lyman, and S. G. Purkey (2015b). Informing Deep Argo Array Design Using Argo and Full-Depth Hydrographic Section Data, J. Atmos. Oceanic Technol. , 32(11), 2187-2198. https://doi.org/10.1175/JTECH-D-15-0139.1.

Johnson, G. C., J. M. Lyman, and N. G. Loeb (2016). Improving estimates of Earth's energy imbalance. Nature Climate Change, 6(7), 639–640. https://doi.org/10.1038/nclimate3043

Johnson, G.C., and J. M. Lyman (2020). Warming trends increasingly dominate global ocean. Nat. Clim. Chang. 10, 757–761. https://doi.org/10.1038/s41558-020-0822-0

Johnson, G.C., F. W. Landerer, N. G. Loeb, J. M. Lyman, M. Mayer, A. L. S. Swann & J. Zhang (2023). Closure of Earth's Global Seasonal Cycle of Energy Storage. Surv Geophys. https://doi.org/10.1007/s10712-023-09797-6

JPOTS (Joint Panel on Oceanographic Tables and Standards) Editorial Panel (1991). Processing of Oceanographic Station Data. UNESCO, Paris, 138 pp.

Kaplan, A., M. A. Cane, Y. Kushnir, A. C. Clement, M. B. Blumenthal, and B. Rajagopalan, (1998). Analyses of global sea surface temperature 1856–1991, J. Geophys. Res., 103(C9), 18567– 18589. https://doi.org/10.1029/97JC01736

Kaplan, A., Y. Kushnir, M. A. Cane (2000). Reduced space optimal interpolation of historical marine sea level pressure: 1854–1992. J. Climate, 13, 2987–3002. https://doi.org/10.1175/1520-0442(2000)013%3C2987:RSOIOH%3E2.0.CO;2

Karl, T. R., A. Arguez, B. Huang, J. H. Lawrimore, J. R. McMahon, M. J. Menne, T. C. Peterson, R. S. Vose, and H.-M. Zhang (2015). Possible artifacts of data biases in the recent global surface warming hiatus, Science, 348(6242), 1469-1472. https://doi.org/10.1126/science.aaa5632

Kato, S., F. G. Rose, D. A. Rutan, T. J. Thorsen, N. G. Loeb, D. R. Doelling, X. Huang, W. L. Smith, W. Su, and S.-H. Ham (2018). Surface Irradiances of Edition 4.0 Clouds and the Earth's Radiant Energy System (CERES) Energy Balanced and Filled (EBAF) Data Product. J. Climate, 31, 4501–4527, https://doi.org/10.1175/JCLI-D-17-0523.1.

Kikuchi, T., J. Inoue, and D. Langevin (2007). Argo-type profiling float observations under the Arctic multiyear ice. Deep-Sea Research Part I 54:1,675–1,686. https://doi.org/10.1016/j.dsr.2007.05.011

Kizu, S., and K. Hanawa (2002a). Recorder-dependent temperature error of expendable bathythermograph, J. Oceanogr., 58, 469–476. https://doi.org/10.1023/A:1021261214950.

Kizu, S., and K. Hanawa (2002b). Start-up transient of XBT measurement, Deep Sea Res. Part I, 49, 935–940. https://doi.org/10.1016/S0967-0637(02)00003-1.

Kizu, S., S. I. Ito, and T. Watanabe (2005). Inter-manufacturer difference and temperature dependency of the fall-rate of T-5 expendable bathythermograph, J. Oceanogr., 61, 905–912. https://doi.org/10.1007/s10872-006-0008-z.

Kizu, S., C. Sukigara, and K. Hanawa (2011). Comparison of the fall rate and structure of recent T-7 XBT manufactured by Sippican and TSK, Ocean Sci., 7,231–244. https://doi.org/10.5194/os-7-231-2011

Klemas, V., and X.-H. Yan (2014). Subsurface and deeper ocean remote sensing from satellites: An overview and new results, Prog. Oceanogr. , 122(0), 1-9. https://doi.org/10.1016/j.pocean.2013.11.010

Kopp, G. (2014). An assessment of the solar irradiance record for climate studies, J. Space Weather Space Clim., 4, A14. https://doi.org/10.1051/swsc/2014012

Kopp G. (2021) Science Highlights and Final Updates from 17 Years of Total Solar Irradiance Measurements from the SOlar Radiation and Climate Experiment/Total Irradiance Monitor (SORCE/TIM). Sol Phys, 296(9):133. https://doi.org/10.1007/s11207-021-01853-x

Kren, A. C., P. Pilewskie, and O. Coddington (2017). Where does Earth's atmosphere get its energy? J. Space Weather Space Clim., 7, A10. https://doi.org/10.1051/swsc/2017007

Krishfield, R., J. Toole, A. Proshutinsky, and M.-L. Timmermans (2008). Automated Ice-Tethered Profilers for seawater observations under pack ice in all seasons. Journal of Atmospheric and Oceanic Technology, 25:2,0912,095. https://doi.org/10.1175/2008JTECHO587.1

Kosaka, Y., and S. P. Xie (2013). Recent global-warming hiatus tied to equatorial Pacific surface cooling, Nature, 501(7467), 403-407. https://doi.org/10.1038/nature12534

Kuhlbrodt, T., A. Voldoire, M. D. Palmer, O. Geoffroy, and R. E. Killick (2023). Historical Ocean Heat Uptake in Two Pairs of CMIP6 Models: Global and Regional Perspectives. J. Climate, 36. 2183–2203, https://doi.org/10.1175/JCLI-D-22-0468.1.

Kumar, A., and C. Wen (2016). An Oceanic Heat Content–Based Definition for the Pacific Decadal Oscillation. Mon. Wea. Rev., 144, 3977–3984. https://doi.org/10.1175/MWR-D-16-0080.1

Kuusela, M., and M. L. Stein (2018). Locally stationary spatio-temporal interpolation of Argo profiling float data, Proc. R. Soc. A, 474(2220), 20180400. https://doi.org/10.1098/rspa.2018.0400

Kuusela, M. and D. Giglio (2022). Global Ocean Heat Content Anomalies based on Argo data (1.0.0) [Data set]. Zenodo. https://doi.org/10.5281/zenodo.6131625

Ladstädter, F., A. K. Steiner, and H. Gleisner (2023) Resolving the 21st century temperature trends of the upper troposphere–lower stratosphere with satellite observations, Sci. Rep., 13, 1306. https://doi.org/10.1038/s41598-023-28222-x

L'Ecuyer, T. S., H. K. Beaudoing, M. Rodell, W. Olson, B. Lin, S. Kato, C. A. Clayson, E. Wood, J. Sheffield, R. Adler, G. Huffman, M. Bosilovich, G. Gu, F. Robertson, P. R. Houser, D. Chambers, J. S. Famiglietti, E. Fetzer, W. T. Liu, X. Gao, C. A. Schlosser, E. Clark, D. P. Lettenmaier, and K. Hilburn (2015) The Observed State of the Energy Budget in the Early Twenty-First Century. J. Climate, 28, 8319–8346. https://doi.org/10.1175/JCLI-D-14-00556.1

Lee, S.-K., W. Park, M. O. Baringer, A. L. Gordon, B. Huber, and Y. Liu (2015). Pacific origin of the abrupt increase in Indian Ocean heat content during the warming hiatus, Nature Geosci., 8(6), 445-449. https://doi.org/10.1038/ngeo2438.

Lehman, J. (2021). Sea Change: The World Ocean Circulation Experiment and the Productive Limits of Ocean Variability. Science, Technology, & Human Values, 46(4), 839-862. https://doi.org/10.1177/0162243920949932

Levitus, S. (1982). Climatological Atlas of the World Ocean, NOAA Professional Paper 13, U.S. Gov. Printing Office, Rockville, M.D., 190 pp.

Levitus, S. (1989a). Interpentadal variability of temperature and salinity at intermediate depths of the north Atlantic Ocean, 1970–1974 versus 1955–1959, J. Geophys. Res., 94(C5), 6091–6131. https://doi.org/10.1029/JC094iC05p06091

Levitus, S. (1989b). Interpentadal variability of temperature and salinity in the deep North Atlantic, 1970–1974 versus 1955–1959, J. Geophys. Res., 94(C11), 16125–16131. https://doi.org/10.1029/JC094iC11p16125

Levitus, S. and T. P. Boyer (1994). World Ocean Atlas 1994. Vol. 4: Temperature. NOAA Atlas NESDIS 4, U.S. Government Printing Office, Wash., D.C., 117 pp.

Levitus, S., J. Antonov, and T. P. Boyer (1994a). Interannual Variability of Temperature at 125 m Depth in the North Atlantic Ocean, Science 266, 96–99. https://doi.org/10.1126/science.266.5182.96

Levitus, S., T. P. Boyer, and J. Antonov (1994b). World Ocean Atlas 1994, Volume 5: Interannual Variability of Upper Ocean Thermal Structure. NOAA NESDIS Atlas series, 176 pp.

Levitus, S. and J. Antonov (1995). Observational evidence of interannual to decadal-scale variability of the subsurface temperature-salinity structure of the world ocean. Climatic Change 31, 495–514. https://doi.org/10.1007/BF01095159

Levitus, S., J. Antonov, T. P. Boyer, and C. Stephens (2000). Warming of the world ocean, Science, 287, 2225–2229. https://doi.org/10.1126/science.287.5461.2225

Levitus, S., J. Antonov, and T. Boyer (2005). Warming of the world ocean, 1955–2003, Geophys. Res. Lett., 32, L02604. https://doi.org/10.1029/2004GL021592

Levitus, S., J. I. Antonov, T. P. Boyer, R. A. Locarnini, H. E. Garcia, and A. V. Mishonov (2009). Global ocean heat content 1955–2008 in light of recently revealed instrumentation problems, Geophys. Res. Lett., 36, L07608. https://doi.org/10.1029/2008GL037155

Levitus, S., J. I. Antonov, T. P. Boyer, O. K. Baranova, H. E. Garcia, R. A. Locarnini, A. V. Mishonov, J. R. Reagan, D. Seidov, E. S. Yarosh, and M. M. Zweng (2012). World ocean heat content and thermosteric sea level change (0–2000 m), 1955–2010, Geophys. Res. Lett., 39, L10603. https://doi.org/10.1029/2012GL051106

Levitus, S., J. I. Antonov, O. K. Baranova, T. P. Boyer, C. L. Coleman, H. E. Garcia, A. I. Grodsky, D. R. Johnson, R. A. Locarnini, A. V. Mishonov, J. R. Reagan, C. L. Sazama, D. Seidov, I. Smolyar, E. S. Yarosh, M. M. Zweng (2013) The World Ocean Database, Data Science Journal, 2, WDS229-WDS234. https://doi.org/10.2481/dsj.WDS-041

Lewandowsky, S., J. S. Risbey, and N. Oreskes (2015a), On the definition and identifiability of the alleged “hiatus” in global warming, Sci. Rep. , 5, 16784, doi:10.1038/srep16784.

Lewandowsky, S., J. S. Risbey, and N. Oreskes (2015b), The “pause” in global warming: turning a routine fluctuation into a problem for science, Bull. Am. Meteorol. Soc. https://doi.org/10.1175/BAMS-D-14-00106.1

Li, Y., J. A. Church, T. J. McDougall, and P. M. Barker (2022). Sensitivity of observationally based estimates of ocean heat content and thermal expansion to vertical interpolation schemes. Geophysical Research Letters, 49, e2022GL101079. https://doi.org/10.1029/2022GL101079

Li, Z.-L., H. Wu, S.-B. Duan, W. Zhao, H. Ren, X. Liu, P. Leng, R. Tang, X. Ye, J. Zhu, Y. Sun, M. Si, M. Liu, J. Li, X. Zhang, G. Shang, B.-H. Tang, G. Yan, C. Zhou (2023). Satellite remote sensing of global land surface temperature: Definition, methods, products, and applications. Reviews of Geophysics, 61, e2022RG000777. https://doi.org/10.1029/2022RG000777

Liao, E., W. F. Lu, X.-H. Yan, Y. W. Jiang, and A. Kidwell (2015) The coastal ocean response to the global warming acceleration and hiatus, Sci. Rep. https://doi.org/10.1038/srep16630

Lindstrom, E., Gunn, J., Fischer, A., McCurdy, A., & Glover, L. K. et al (2012). Task Team for the Integrated Framework for Sustained Ocean Observing A Framework for Ocean Observing Paris France, UNESCO, 25pp. (IOC Information Document 1284, Rev. 2). https://doi.org/10.5270/OceanObs09-FOO

Liu, C., E. Freeman, E. C. Kent, D. I. Berry, S. J. Worley, S. R. Smith, B. Huang, H. Zhang, T. Cram, Z. Ji, M. Ouellet, F. Gaboury, I. Oliva, A. Andersson, W. E. Angel, A. R. Sallis, A. Adeyeye (2022). Blending BUFR and TAC Marine *in situ* Data for ICOADS Near-Real-Time Release 3.0.2. https://doi.org/10.1175/JTECH-D-21-0182.1

Liu, J., & Curry, J. A. (2010) Accelerated warming of the southern ocean and its impacts on the hydrological cycle and sea ice. Proceedings of the National Academy of Sciences, USA, 107, 14987-14992. http://dx.doi.org/10.1073/pnas.1003336107

Liu, W., S.-P. Xie, and J. Lu (2016). Tracking ocean heat uptake during the surface warming hiatus, Nature Commun., 7. https://doi.org/10.1038/ncomms10926

Llovel, W., J. K. Willis, F. W. Landerer, and I. Fukumori (2014). Deep-ocean contribution to sea level and energy budget not detectable over the past decade, Nature Clim. Change, 4(11), 1031-1035. https://doi.org/10.1038/nclimate2387

Locarnini, R. A., A. V. Mishonov, J. I. Antonov, T. P. Boyer, and H. E. Garcia (2006). World Ocean Atlas 2005. Vol. 1: Temperature. S. Levitus, Ed., NOAA Atlas NESDIS 61, U.S. Government Printing Office, Washington, D.C. 182 pp.

Locarnini, R. A., A. V. Mishonov, J. I. Antonov, T. P. Boyer, and H. E. Garcia (2010). World Ocean Atlas 2009. Vol. 1: Temperature. S. Levitus, Ed. NOAA Atlas NESDIS 68, U.S. Government Printing Office, Washington, D.C., 184 pp.

Locarnini, R. A., A. V. Mishonov, J. I. Antonov, T. P. Boyer, H. E. Garcia, O. K. Baranova, M. M. Zweng, C. R. Paver, J. R. Reagan, D. R. Johnson, M. Hamilton, and D. Seidov (2013). World Ocean Atlas 2013, Vol. 1: Temperature. S. Levitus, Ed. A. Mishonov, Tech. Ed. NOAA Atlas NESDIS 73, 40 pp.

Locarnini, R. A., A. V. Mishonov, O. K. Baranova, T. P. Boyer, M. M. Zweng, H. E. Garcia, J. R. Reagan, D. Seidov, K. Weathers, C. R. Paver, and I. Smolyar (2018). World Ocean Atlas 2018, Volume 1: Temperature. A. Mishonov Technical Ed.; NOAA Atlas NESDIS 81, 52pp

Locarnini, R. A., A. V. Mishonov, O. K. Baranova, J. R. Reagan, T. P. Boyer, D. Seidov, Z. Wang, H. E. Garcia, C. Bouchard, S. L. Cross, C. R. Paver, and D. Dukhovskoy (2024). World Ocean Atlas 2023, Volume 1: Temperature. A. Mishonov Technical Editor, NOAA Atlas NESDIS 89.

Loeb, N. G., B. A. Wielicki, D. R. Doelling, G. L. Smith, D. F. Keyes, S. Kato, N. Manalo-Smith, and T. Wong (2009). Toward Optimal Closure of the Earth's Top-of-Atmosphere Radiation Budget. Journal of Climate, 22(3), 748-766. https://doi.org/10.1175/2008JCLI2637.1

Loeb, N., J. M. Lyman, G. C. Johnson, R. P. Allan, D. R. Doelling, T. Wong, B. J. Soden and G. L. Stephens (2012) Observed changes in top-of-the-atmosphere radiation and upper-ocean heating consistent within uncertainty. Nature Geosci 5, 110–113. https://doi.org/10.1038/ngeo1375

Loeb, N. G., D.R. Doelling, H. Wang, W. Su, C. Nguyen, J. G. Corbett, L. Liang, C. Mitrescu, F. G. Rose, and S. Kato (2018a). Clouds and the Earth's Radiant Energy System (CERES) Energy Balanced and Filled (EBAF) Top-of-Atmosphere (TOA) Edition-4.0 Data Product. Journal of Climate, 31(2), 895-918. https://doi.org/10.1175/JCLI-D-17-0208.1

Loeb, N. G., T. J. Thorsen, J. R. Norris, H. Wang, and W. Su (2018b). Changes in earth's energy budget during and after the "pause" in global warming: an observational perspective. Climate 6:62. doi: 10.3390/cli6030062

Lorenc, A. C., Bell, R. S., MacPherson, B. (1991) The Meteorological Office analysis correction data assimilation scheme. Q. J. R. Meteor. Soc., 117, 59-89. https://doi.org/10.1002/qj.49711749704

Lozier, M. S., M. S. McCartney, and W. B. Owens (1994). Anomalous Anomalies in Averaged Hydrographic Data. J. Phys. Oceanogr., 24, 2624–2638, https://doi.org/10.1175/1520-0485(1994)024<2624:AAIAHD>2.0.CO;2.

Lumpkin, R., L. Centurioni and R. C. Perez (2016) Fulfilling Observing System Implementation Requirements with the Global Drifter Array. J. Atmos. Oceanic Technology. 33, 685—695. http://dx.doi.org/10.1175/JTECH-D-15-0255.1

Lumpkin, R., R. Domingues, and G. Goni (2021) Surface currents [in "State of the Climate in 2020"]. Bull. Amer. Meteor. Soc., 102 (8), S172–S175, https://doi.org/10.1175/ BAMS-D-21-0083.1

Lyman, J. M., J. K. Willis, and G. C. Johnson (2006). Recent cooling of the upper ocean, Geophys. Res. Lett., 33, L18604. https://doi.org/10.1029/2006GL027033

Lyman, J. M., and G. C. Johnson (2008). Estimating Annual Global Upper-Ocean Heat Content Anomalies despite Irregular *In situ* Ocean Sampling. J. Climate, 21, 5629–5641. https://doi.org/10.1175/2008JCLI2259.1

Lyman, J. M., S. A. Good, V. V. Gouretski, M. Ishii, G. C. Johnson, M. D. Palmer, D. A. Smith, and J. K. Willis. (2010) Robust warming of the global upper ocean. Nature, 465, 334-337, https://doi.org/10.1038/nature09043

Lyman, J. M., and G. C. Johnson (2014). Estimating Global Ocean Heat Content Changes in the Upper 1800 m since 1950 and the Influence of Climatology Choice. J. Climate, **27**, 1945–1957, https://doi.org/10.1175/JCLI-D-12-00752.1.

Lyman, J. M., and G. C. Johnson (2023). Global High-Resolution Random Forest Regression Maps of Ocean Heat Content Anomalies Using *In situ* and Satellite Data. J. Atmos. Oceanic Technol., 40, 575–586. https://doi.org/10.1175/JTECH-D-22-0058.1.

Lynn R. J. and J. L. Reid (1968). Characteristics and circulation of deep and abyssal waters. Deep-Sea Research **15**: 577–598. https://doi.org/10.1016/0011-7471(68)90064-8

Lyu, K., X. Zhang, and J. A. Church (2021). Projected ocean warming constrained by the ocean observational record. Nat. Clim. Chang., 11, 834–839. https://doi.org/10.1038/s41558-021-01151-1

Mantua, N. J., S. R. Hare, Y. Zhang, J. M. Wallace, and R. C. Francis (1997) A Pacific Interdecadal Climate Oscillation with Impacts on Salmon Production. Bull. Amer. Meteor. Soc., 78, 1069–1080. https://doi.org/10.1175/1520-0477(1997)078<1069:APICOW>2.0.CO;2

Marshall, J., and T. Radko (2003). Residual-Mean Solutions for the Antarctic Circumpolar Current and Its Associated Overturning Circulation. J. Phys. Oceanogr., 33, 2341–2354. https://doi.org/10.1175/1520-0485(2003)033<2341:RSFTAC>2.0.CO;2

Mayer, M., J. T. Fasullo, K. E. Trenberth, and L. Haimberger (2016). ENSO-driven energy budget perturbations in observations and CMIP models, Clim. Dyn. , 1-21. https://doi.org/10.1007/s00382-016-3057-z

Mayer, M., L. Haimberger, J. M. Edwards, and P. Hyder (2017) Toward Consistent Diagnostics of the Coupled Atmosphere and Ocean Energy Budgets. J. Climate, 30, 9225–9246. https://doi.org/10.1175/JCLI-D-17-0137.1

McDougall, T. J. (2003). Potential Enthalpy: A Conservative Oceanic Variable for Evaluating Heat Content and Heat Fluxes. J. Phys. Oceanogr., 33, 945–963, https://doi.org/10.1175/1520-0485(2003)033<0945:PEACOV>2.0.CO;2

McDougall, T. J., P. M. Barker, R. M. Holmes, R. Pawlowicz, S. M. Griffies, and P. J. Durack (2021). The interpretation of temperature and salinity variables in numerical ocean model output

and the calculation of heat fluxes and heat content, Geosci. Model Dev., 14, 6445–6466. https://doi.org/10.5194/gmd-14-6445-2021

McGregor, S., A. Timmermann, M. F. Stuecker, M. H. England, M. Merrifield, F.-F. Jin, and Y. Chikamoto (2014). Recent Walker circulation strengthening and Pacific cooling amplified by Atlantic warming, Nature Clim. Change, 4(10), 888-892. https://doi.org/10.1038/nclimate2330

McMahon C. R., F. Roquet, S. Baudel, M. Belbeoch, S. Bestley, C. Blight, L. Boehme, F. Carse, D. P. Costa, M. A. Fedak, C. Guinet, R. Harcourt, E. Heslop, M. A. Hindell, X. Hoenner, K. Holland, M. Holland, F. R. A. Jaine, T. Jeanniard du Dot, I. Jonsen, T. R. Keates, K. M. Kovacs, S. Labrousse, P. Lovell, C. Lydersen, D. March, M. Mazloff, M. K. McKinzie, M. M. C. Muelbert, K. O'Brien, L. Phillips, E. Portela, J. Pye, S. Rintoul, K. Sato, A. M. M. Sequeira., S. E. Simmons, V. M. Tsontos, V. Turpin, E. van Wijk, D. Vo, M. Wege, F. G. Whoriskey, K. Wilson, and B. Woodward (2021). Animal Borne Ocean Sensors – AniBOS – An Essential Component of the Global Ocean Observing System, Frontiers in Marine Science 8. https://doi.org/10.3389/fmars.2021.751840

McPhaden, M. J., G. Meyers, K. Ando, Y. Masumoto, V. S. N. Murty, M. Ravichandran, F. Syamsudin, J. Vialard, L. Yu, and W. Yu (2009). RAMA: The Research Moored Array for African–Asian–Australian Monsoon Analysis and Prediction*. Bull. Amer. Meteor. Soc., **90**, 459–480, https://doi.org/10.1175/2008BAMS2608.1

Meehl, G. A., J. M. Arblaster, J. T. Fasullo, A. Hu, and K. E. Trenberth (2011). Model-based evidence of deep-ocean heat uptake during surface-temperature hiatus periods, Nature Clim. Change, 1(7), 360-364. https://doi.org/10.1038/nclimate1229

Meehl, G. A., A. Hu, J. M. Arblaster, J. Fasullo, and K. E. Trenberth (2013) Externally forced and internally generated decadal climate variability associated with the interdecadal pacific oscillation, J. Climate 26(18), 7298-7310, doi:10.1175/JCLI-D-12-00548.1

Meehl, G. A., H. Teng, and J. M. Arblaster (2014), Climate model simulations of the observed early-2000s hiatus of global warming, Nature Clim. Change, 4(10), 898-902. https://doi.org/10.1038/nclimate2357

Mesick, S., Wang, Z., Mishonov, A., Boyer, T., & Zhang, H. M. (2020, October). Incorporating discrete Unmanned Maritime System data collections into NCEI synthesized data products. In Global Oceans 2020: Singapore–US Gulf Coast (pp. 1-8). IEEE

Meyssignac, B., T. Boyer, Z. Zhao, M. Z. Hakuba, F. W. Landerer, D. Stammer, A. Köhl, S. Kato, T. L'Ecuyer, M. Ablain, J. P. Abraham, A. Blazquez, A. Cazenave, J. A. Church, R. Cowley, L. Cheng, C. Domingues, D. Giglio, V. Gouretski, M. Ishii, G. C. Johnson, R. E. Killick, D. Legler, W. Llovel, **J**. Lyman, M. D. Palmer, S. Piotrowicz, S. Purkey, D. Roemmich, R. Roca, A. Savita, K. von Schuckmann, S. Speich, G. Stephens, G. G. Wang, S. E. Wijffels and N. Zilberman (2019). Measuring Global Ocean Heat Content to estimate the Earth Energy Imbalance, Frontiers in Marine Science, 20 (6). https://doi.org/10.3389/fmars.2019.00432

Mill, R. H. (1900), The Pettersson-Nansen insulating water-bottle, Geogr. J., 16, 469–471.

Millero, F. J., G. Perron, and J. E. Desnoyers (1973). Heat capacity of seawater solutions from 5° to 35°C and 0.5 to 22‰ chlorinity, J. Geophys. Res., 78(21), 4499–4507. doi:10.1029/JC078i021p04499.

Millero, F.J. (2010). History of the equation of state of seawater. Oceanography 23(3):18–33, https://doi.org/10.5670/oceanog.2010.21

Minière, A., K. von Schuckmann, J. B. Sallée, and L. Vogt, (2023). Robust acceleration of Earth system heating observed over the past six decades. Sci Rep 13, 22975. https://doi.org/10.1038/s41598-023-49353-1

Mishonov, A.V., T.P. Boyer, O.K. Baranova, C.N. Bouchard, S.L. Cross, H.E. Garcia, R.A. Locarnini, C.R. Paver, J.R. Reagan, Z. Wang, D. Seidov, A.I. Grodsky, J. Beauchamp (2024). World Ocean Database 2023. C. Bouchard, Technical Ed. NOAA Atlas NESDIS 97. https://doi.org/10.25923/z885-h264

Moltmann, T., J. Turton, H-M Zhang, G. Nolan, C. Gouldman, L. Griesbauer, Z. Willis, Á. Muñiz Piniella, S. Barrell, E. Andersson, C. Gallage, E. Charpentier, M. Belbeoch, P. Poli, A. Rea, E. F. Burger, D. M. Legler, R. Lumpkin, C. Meinig, K. O'Brien, K. Saha, A. Sutton, D. Zhang and Y. Zhang (2019). A Global Ocean Observing System (GOOS), Delivered Through Enhanced Collaboration Across Regions, Communities, and New Technologies, Frontiers in Marine Science, 6. https://doi.org/10.3389/fmars.2019.00291/full

Munk, W., and P. F. Worcester (1976). "Monitoring the ocean acoustically," in Science, Technology, and the Modern Navy, Thirtieth Anniversary, 1946–1976, ed. E. I. Salkovitz (Arlington, VA: Office of Naval Research), 497–508.

Munk, W. H., P. F. Worcester, and C. Wunsch (1995). Ocean Acoustic Tomography. New York, NY: Cambridge University Press.

National Geophysical Data Center (NGDC) /NESDIS/NOAA/U.S. Department of Commerce. (2001) ETOPO2, Global 2 Arc-minute Ocean Depth and Land Elevation from the US National Geophysical Data Center (NGDC). Research Data Archive at the National Center for Atmospheric Research, Computational and Information Systems Laboratory. https://doi.org/10.5065/D6668B75. Accessed 12/02/2006.

Negretti, H., and J. Zambra (1873). On a new deep-sea thermometer, Proc Roy Soc Lond, 22,238–241. https://doi.org/10.1098/rspl.1873.0034

Neumann G., and W. J. Pierson (1966) Principles of Physical Oceanography. Prentice Hall: Englewood Cliffs, NJ

Newman, M., M. A. Alexander, T. R. Ault, K. M. Cobb, C. Deser, E. Di Lorenzo, N. J. Mantua, A. J. Miller, S. Minobe, H. Nakamura, N. Schneider, D. J. Vimont, A. S. Phillips, J. D. Scott, and C. A. Smith (2016). The Pacific Decadal Oscillation, Revisited. J. Climate, 29, 4399–4427. https://doi.org/10.1175/JCLI-D-15-0508.1

Nieves, V., J. K. Willis, and W. C. Patzert (2015). Recent hiatus caused by decadal shift in Indo-Pacific heating, Science, 349(6247), 532-535. https://doi.org/10.1126/science.aaa4521

Oh, SG., B. G. Kim, Y. K. Cho, and S-W Son (2023). Quantification of The Performance of CMIP6 Models for Dynamic Downscaling in The North Pacific and Northwest Pacific Oceans. Asia-Pac J Atmos Sci 59, 367–383. https://doi.org/10.1007/s13143-023-00320-w

Ohmura, A., E. G. Dutton, B. Forgan, C. Fröhlich, H. Gilgen, H. Hegner, A. Heimo, G. König-Langlo, B. McArthur, G. Müller, R. Philipona, R. Pinker, C. H. Whitlock, K. Dehne, and M. Wild (1998) Baseline Surface Radiation Network (BSRN/WCRP): New Precision Radiometry for Climate Research. Bull. Amer. Meteor. Soc., 79, 2115–2136. https://doi.org/10.1175/1520-0477(1998)079<2115:BSRNBW>2.0.CO;2

Palmer, M. D., K. Haines, S. F. B. Tett and T. J. Ansell., 2007: Isolating the signal of global ocean warming. Geophys. Res. Lett. , 34, L23610,. https://doi.org/10.1029/2007GL031712

Palmer, M.D., Antonov, J., Barker, P., Bindoff, N.L., Boyer, T., Carson, M., Domingues, C.M., Gille, S., Gleckler, P.J., Good, S.A., Gouretski, V., Guinehut, S., Haines, K., Harrison, D.E., Ishii, M., Johnson, G.C., Levitus, S., Lozier, M.S., Lyman, J.M., Meijers, A.J., von Schuckmann, K., Smith, D., Wijffels, S.E. and Willis, J.K. (2010) Future observations for monitoring global ocean heat content, Proceedings of OceanObs'09: Sustained Ocean Observations and Information for Society, 21-25 September 2009, Venice, pp. 1-13. https://doi.org/10.5270/OceanObs09.cwp.68.

Palmer, M. D., D. J. McNeall, and N. J. Dunstone (2011). Importance of the deep ocean for estimating decadal changes in Earth's radiation balance, Geophys. Res. Lett. , 38(13), L13707. https://doi.org/10.1029/2011GL047835

Palmer, M.D., C. D. Roberts, M. Balmaseda, O. Y.-S. Chang, G. Chepurin, N. Ferry, Y. Fujii, S. A. Good, S. Guinehut, K. Haines, F. Hernandez, A. Köhl, T. Lee, M. J. Martin, S. Masina, S. Masuda, K. A. Peterson, A. Storto, T. Toyoda, M. Valdivieso, G. Vernieres, O. Wang, and Y. Xue (2017). Ocean heat content variability and change in an ensemble of ocean reanalyses. Clim Dyn 49, 909–930. https://doi.org/10.1007/s00382-015-2801-0

Palmer, M. D., T. Boyer, R. Cowley, S. Kizu, F. Reseghetti, T. Suzuki, and A. Thresher (2018). An Algorithm for Classifying Unknown Expendable Bathythermograph (XBT) Instruments Based on Existing Metadata. J. Atmos. Oceanic Technol., 35, 429–440, https://doi.org/10.1175/JTECH-D-17-0129.1.

Pan, Y., L. Cheng, K. von Schuckmann, K. E. Trenberth, G. Li, J. Abraham, Y. Liu, V. Gouretski, Y. Yu, H. Liu, and C. Liu (2023). Annual Cycle in Upper-Ocean Heat Content and the Global Energy Budget. J. Climate, 36, 5003–5026. https://doi.org/10.1175/JCLI-D-22-0776.1.

Pawlowicz, R, T. McDougall, R. Feistel, and R. Tailleux (2012). An historical perspective on the development of the Thermodynamic Equation of Seawater– 2010, Ocean Sci., 8, 161–174. https://doi.org/doi:10.5194/os-8-161-2012

Pawlowicz, R. (2013). Key Physical Variables in the Ocean: Temperature, Salinity, and Density. Nature Education Knowledge 4(4):13

Polyakov, I.V., I. A. Timokhov, V. A. Alexeev, S. Bacon, I. A. Dmitrenko, L. Fortier, I. E. Frolov, J. Gascard, E. Hansen, V. V. Ivanov, S. Laxon, C. Mauritzen, D. Perovich, K. Shimada, H. L. Simmons, V. T. Sokolov, M. Steele, and J. Toole (2010). Arctic Ocean Warming Contributes to Reduced Polar Ice Cap, J. Phys. Oceanogr., 40, 2743-2756. https://doi.org/10.1175/2010JPO4339.1

Purkey, S. G. and G. C. Johnson (2010). Warming of global abyssal and deep southern ocean waters between the 1990s and 2000s: Contributions to global heat and sea level rise budgets. J. Clim. 23, 6336–6351. https://doi.org/10.1175/2010JCLI3682.1

Rabiner, L.R., M.R. Sambur, and C.E. Schmidt (1975). Applications of a nonlinear smoothing algorithm to speech processing, IEEE Trans. on Acoustics, Speech and Signal Processing, 23, 552-557. https://doi.org/10.1109/TASSP.1975.1162749

Raper, S. C. B., J. M. Gregory, and R. J. Stouffer (2002). The Role of Climate Sensitivity and Ocean Heat Uptake on AOGCM Transient Temperature Response. J. Climate, 15, 124–130. https://doi.org/10.1175/1520-0442(2002)015<0124:TROCSA>2.0.CO;2

Reiniger, R. F. and C. F. Ross (1968). A method of interpolation with application to oceanographic data. Deep-Sea Res., 9, 185-193. https://doi.org/10.1016/0011-7471(68)90040-5

Ren, Q., Y. Kwon, J. Yang, R. X. Huang, Y. Li, and F. Wang (2024). Substantial Warming of the Atlantic Ocean in CMIP6 Models. J. Climate, 37, 3073–309. https://doi.org/10.1175/JCLI-D-23-0418.1

Ren, X., W. Liu, A. Capotondi, D. J. Amaya and N. J. Holbrook (2023) The Pacific Decadal Oscillation modulated marine heatwaves in the Northeast Pacific during past decades. Commun Earth Environ 4, 218. https://doi.org/10.1038/s43247-023-00863-w

Resplandy, L., R. F. Keeling, Y. Eddebbar, M. K. Brooks, R. Wang, L. Bopp, M. C. Long, J. P. Dunne, W. Koeve & A. Oschlie. (2018). Quantification of ocean heat uptake from changes in atmospheric O2 and CO2 composition. Nature, 563, 105–108. https://doi.org/10.1038/s41586-018-0651-8

Resplandy, L., R. F. Keeling, Y. Eddebbar, M. Brooks, R. Wang, L. Bop, M. C. Long, J. P. Dunne, W. Koeve, and A. Oschlies (2019). Quantification of ocean heat uptake from changes in atmospheric O2 and CO2 composition. Sci Rep 9, 20244. https://doi.org/10.1038/s41598-019-56490-z

Revelard. A, J. Tintoré, J. Verron, P. Bahurel, J. A. Barth, M. Belbéoch, J. Benveniste, P. Bonnefond, E. P. Chassignet, S. Cravatte, F. Davidson, B. deYoung, M. Heupel, E. Heslop, C. Hörstmann, J. Karstensen, P.-Y. Le Traon, M. Marques, C. McLean, R. Medina, T. Paluszkiewicz, A. Pascual, J. Pearlman, G. Petihakis, N. Pinardi, S. Pouliquen, R. Rayner, I. Shepherd, J. Sprintall, T. Tanhua, P. Testor, J. Seppälä, J. Siddorn, S. Thomsen, L. Valdés, M. Visbeck, A. M. Waite, F. Werner, J. Wilkin, B. Williams (2021). Ocean Integration: the needs

and challenges of effective coordination within the ocean observing system. https://doi.org/10.3389/fmars.2021.737671

Rhein, M., S.R. Rintoul, S. Aoki, E. Campos, D. Chambers, R.A. Feely, S. Gulev, G.C. Johnson, S.A. Josey, A. Kostianoy, C. Mauritzen, D. Roemmich, L.D. Talley and F. Wang, 2013: Observations: Ocean. In: Climate Change 2013: The Physical Science Basis. Contribution of Working Group I to the Fifth Assessment Report of the Intergovernmental Panel on Climate Change [Stocker, T.F., D. Qin, G.-K. Plattner, M. Tignor, S.K. Allen, J. Boschung, A. Nauels, Y. Xia, V. Bex and P.M. Midgley (eds.)]. Cambridge University Press, Cambridge, United Kingdom and New York, NY, USA, pp. 255–316. https://doi.org/10.1017/CBO9781107415324.010

Rietbroek, R., S.-E. Brunnabend, J. Kusche, J. Schröter, and C. Dahle (2016). Revisiting the contemporary sea-level budget on global and regional scales, Proc. Natl. Acad. Sci. U.S.A. , 113(6), 1504-1509. https://doi.org/10.1073/pnas.1519132113

Rignot, E., S. Jacobs, J. Mouginot, and B. Scheuchl, 2013: Ice-shelf melting around Antarctica. Science, 341, 266–270. https://doi.org/10.1126/science.1235798

Rintoul, S.R. (2018). The global influence of localized dynamics in the Southern Ocean. Nature 558, 209–218. https://doi.org/10.1038/s41586-018-0182-3

Riser, S. C., H. J. Freeland, D. Roemmich, S. Wijffels, A. Troisi, M. Belbeoch, D. Gilbert, J. Xu, S. Pouliquen, A. Thresher, P.-Y. Le Traon, G. Maze, B. Klein, M. Ravichandran, F. Grant, P.-M. Poulain, T. Suga, B. Lim, A. Sterl, P. Sutton, K.-A. Mork, P. J. Velez-Belchi, I. Ansorge, B. King, J. Turton, M. Baringer, and S. R. Jayne (2016). Fifteen years of ocean observations with the global Argo array, Nature Clim. Change, 6(2), 145-153. https://doi.org/10.1038/nclimate2872

Roemmich D. and B. Cornuelle (1987) Digitization and calibration of the expendable bathythermograph, Deep Sea Research Part A. Oceanographic Research Papers, 34 (2), 299-307. https://doi.org/10.1016/0198-0149(87)90088-4

Roemmich, D. (2009). Argo the challenge of continuing 10 years of progress, Oceanography (Washington, D.C.), 22(3), 46-55. https://doi.org/10.5670/oceanog.2009.65

Roemmich and Gilson (2009). The 2004–2008 mean and annual cycle of temperature, salinity, and steric height in the global ocean from the Argo Program. Progress in Oceanography, 82, 81-100. https://doi.org/10.1016/j.pocean.2009.03.004

Roemmich, D., and J. Gilson (2011). The global ocean imprint of ENSO, Geophys. Res. Lett. , 38(13), L13606. https://doi.org/10.1029/2011GL047992

Roemmich, D., W. J. Gould, and J. Gilson. (2012). 135 years of global ocean warming between the Challenger expedition and the Argo Programme. Nature Clim Change 2, 425–428. https://doi.org/10.1038/nclimate1461

Roemmich, D., J. Church, J., Gilson, J., Monselesan, D., Sutton, P., and Wijffels, S. (2015). Unabated planetary warming and its ocean structure since 2006. Nature Clim. Change, 5, 240–245. https://dx.doi.org/10.1038/nclimate2513

Roemmich D., M. H. Alford, H. Claustre, K. Johnson, B. King, J. Moum, P. Oke, W. B. Owens, S. Pouliquen, S. Purkey, M. Scanderbeg, T. Suga, S. Wijffels, N. Zilberman, D. Bakker, M. Baringer, M. Belbeoch, H. C. Bittig, E. Boss, P. Calil, F. Carse, T. Carval, F. Chai, D. Ó Conchubhair, F. d'Ortenzio, G. Dall'Olmo, D. Desbruyeres, K. Fennel, I. Fer, R. Ferrari, G. Forget, H. Freeland, T. Fujiki, M. Gehlen, B. Greenan, R. Hallberg, T. Hibiya, S. Hosoda, Jayne S., M. Jochum, G. C. Johnson, K. Kang, N. Kolodziejczyk, A. Körtzinger, P.-Y. L. Traon, Y.-D. Lenn, G. Maze, K. A. Mork, T. Morris, T. Nagai, J. Nash, A. N. Garabato, A. Olsen, R. R. Pattabhi, S. Prakash, S. Riser, C. Schmechtig, C. Schmid, E. Shroyer, A. Sterl , P. Sutton, and L. Talley (2019). On the Future of Argo: A Global, Full-Depth, Multi-Disciplinary Array, Frontiers in Marine Science, 6. https://doi.org/10.3389/fmars.2019.00439

Roman-Stork, H. L., D. A. Byrne, and E. W. Leuliette (2023). MESI: A Multiparameter Eddy Significance Index. Earth and Space Science, 10, e2022EA002583. https://doi.org/10.1029/2022EA002583

Rossby, C. G., and R. B. Montgomery (1935). The layer of frictional influence in wind and ocean currents, Papers in Physical Oceanography and Meteorology of the Massachusetts Institute of Technology and Woods Hole Oceanographic Institution,3,73–75.

Rottman, G. (2005). The SORCE Mission. In G. Rottman, T. Woods, & V. George (Eds.), The solar radiation and climate experiment (SORCE), pp. 7–25. Springer New York. https://doi.org/10.1007/0-387-37625-92

Rudnick, D.L., R.E. Davis, C.C. Eriksen, D.M. Fratantoni, and M.J. Perry (2004). Underwater gliders for ocean research, Mar. Tech. Soc. J., 38(2), 73-84. https://doi.org/10.4031/002533204787522703

Rudnick, D. L. (2016), Ocean research enabled by underwater gliders, Ann. Rev. Mar. Sci., 8(1), 519-541, doi:10.1146/annurev-marine-122414-033913

Rudnick, D. L., R. E. Davis, and J. T. Sherman (2016) Spray Underwater Glider Operations. J. Atmos. Oceanic Technol., 33, 1113–1122. https://doi.org/10.1175/JTECH-D-15-0252.1

Santer, B. D., C. Bonfils, J. F. Painter, M. D. Zelinka, C. Mears, S. Solomon, G. A. Schmidt, J. C. Fyfe, J. N. S. Cole, L. Nazarenko, K. E. Taylor, and F. J. Wentz (2014). Volcanic contribution to decadal changes in tropospheric temperature, Nature Geosci., 7(3), 185-189. https://doi.org/10.1038/ngeo209

Santer, B. D., S. Po-Chedley, C. Mears, J. C. Fyfe, N. Gillett, Q. Fu, J. F. Painter, S. Solomon, A. K. Steiner, F. J. Wentz, M. D. Zelinka, and C.-Z. Zou (2021). Using Climate Model Simulations to Constrain Observations. J. Climate, 34, 6281–6301. https://doi.org/10.1175/JCLI-D-20-0768.

Seaver, G. A., and S. Kuleshov (1982). Experimental and analytical error of the expendable bathythermograph, J. Phys. Oceanogr., 12, 592–600. https://doi.org/10.1175/1520-0485(1982)012%3C0592:EAAEOT%3E2.0.CO;2

Semmler, T., Jungclaus, J., Danek, C., Goessling, H. F., Koldunov, N. V., Rackow, T., and Sidorenko, D. (2021). Ocean model formulation influences transient climate response. Journal of Geophysical Research: Oceans, 126, e2021JC017633. https://doi.org/10.1029/2021JC017633

Schmidt, G. A., A. Romanou, L. A. Roach, K. D. Mankoff, Q. Li, C. D. Rye, M. Kelley, J. C. Marshall, and J. J. M. Busecke (2023). Anomalous meltwater from ice sheets and ice shelves is a historical forcing. Geophysical Research Letters, 50, e2023GL106530. https://doi.org/10.1029/2023GL106530

Shi, J.-R., S. E. Wijffels, Y.-O. Kwon, and S.-P. Xie (2023). Interhemispheric contrasts of ocean heat content change reveals distinct fingerprints of anthropogenic climate forcings. Geophysical Research Letters, 50, e2023GL102741. https://doi.org/10.1029/2023GL102741

Shuman, F.G. (1957). Numerical methods in weather prediction: II. Smoothing and filtering. Mon. Wea. Rev., 85, 357-361.

Slater, T., I. R. Lawrence, I. N. Otosaka, A. Shepherd, N. Gourmelen, L. Jakob, P. Tepes, L. Gilbert, and P. Nienow (2021) Review article: Earth's ice imbalance, The Cryosphere, 15, 233–246. https://doi.org/10.5194/tc-15-233-2021

Sloyan, B. M., R. Wanninkhof, M. Kramp, G. C. Johnson, L. D. Talley, T. Tanhua, E. McDonagh, C. Cusack, E. O'Rourke, E. McGovern, K. Katsumata, S. Diggs, J. Hummon, M. Ishii, K. Azetsu-Scott, E. Boss, I. Ansorge, F. F. Perez, H. Mercier, M. J. M. Williams, L. Anderson, J. H. Lee, A. Murata, S. Kouketsu, E. Jeansson, M. Hoppema and E. Campos (2021) The Global Ocean Ship-Based Hydrographic Investigations Program (GO-SHIP): A Platform for Integrated Multidisciplinary Ocean Science, Frontiers in Marine Science, 6. https://doi.org/10.3389/fmars.2019.00445

Smith, S. R., G. Alory, A. Andersson, W. Asher, A. Baker, D. I. Berry, K. Drushka, D. Figurskey, E. Freeman, P. Holthus, T. Jickells, H. Kleta, E. C. Kent, N. Kolodziejczyk, M. Kramp, Z. Loh, P. Poli, U. Schuster, E. Steventon, S. Swart, O. Tarasova, L. Petit de la Villéon and N. Vinogradova-Shiffer (2019). Ship-Based Contributions to Global Ocean, Weather, and Climate Observing Systems, Frontiers in Marine Science, 6. https://doi.org/10.3389/fmars.2019.00434

Snodgrass, J. M. (1968). Instrumentation and communications, in Ocean Engineering Planning and Design Goals, edited by E. Technology and J. Brahtz, pp. 393–477, John Wiley and Sons publisher, New York, NY, USA.

Sohail, T., D. B. Irving, J. D. Zika, R. M. Holmes, and J. A. Church (2021). Fifty year trends in global ocean heat content traced to surface heat fluxes in the sub-polar ocean. Geophysical Research Letters, 48, e2020GL091439. https://doi.org/10.1029/2020GL091439

Solomon, S., J. S. Daniel, R. R. Neely, J. P. Vernier, E. G. Dutton, and L. W. Thomason (2011). The Persistently Variable "Background" Stratospheric Aerosol Layer and Global Climate Change, Science, 333(6044), 866-870. https://doi.org/10.1126/science.1206027

Spilhaus, A. F. (1938). A bathythermograph. Journal of Marine Research 1, (2). https://elischolar.library.yale.edu/journal_of_marine_research/522

Steiner, A. K., F. Ladstädter, F., W. J. Randel, A. C. Maycock, Q. Fu, C. Claud, H. Gleisner, L. Haimberger, S.-P. Ho, P. Keckhut, T. Leblanc, C. Mears, L. M. Polvani, B. D. Santer, T. Schmidt, V. Sofieva, R. Wing, and C.-Z. Zou (2020). Observed Temperature Changes in the Troposphere and Stratosphere from 1979 to 2018, J. Climate, 33, 8165–8194. https://doi.org/10.1175/JCLI-D-19-0998.1

Steinman, B. A., M. E. Mann, and S. K. Miller (2015). Atlantic and Pacific multidecadal oscillations and Northern Hemisphere temperatures, Science, 347(6225), 988-991

Stephens, C., J. I. Antonov, T. P. Boyer, M. E. Conkright, R. A. Locarnini, T. D. O'Brien, and H. E. Garcia (2002). World Ocean Atlas 2001, Volume 1: Temperature. S. Levitus, Ed., NOAA Atlas NESDIS 49, U.S. Government Printing Office, Wash., D.C., 176 pp.

Storto, A., C. Yang, and S. Masina (2016). Sensitivity of global ocean heat content from reanalyses to the atmospheric reanalysis forcing: A comparative study, Geophys. Res. Lett., 43, 5261–5270, https://doi.org/doi:10.1002/2016GL068605.

Storto, A. and C. Yang (2024). Acceleration of the ocean warming from 1961 to 2022 unveiled by large-ensemble reanalyses. Nat Commun 15, 545. https://doi.org/10.1038/s41467-024-44749-7

Straneo, F., and P. Heimbach, 2013: North Atlantic warming and the retreat of Greenland's outlet glaciers. Nature, 504, 36–43. https://doi.org/10.1038/nature12854.

Su, H., X. Wu, X.-H. Yan, and A. Kidwell (2015). Estimation of subsurface temperature anomaly in the Indian Ocean during recent global surface warming hiatus from satellite measurements: A support vector machine approach, Remote Sens. Environ., 160(0), 63-71. https://doi.org/10.1016/j.rse.2015.01.001

Sverdrup, H.U., M.W. Johnson, and R.H. Fleming (1942). The Oceans: Their physics, chemistry, and general biology. Prentice Hall, 1060 pp.
Szekely, T., J. Gourrion, S. Pouliquen, and G. Reverdin (2019). The CORA 5.2 dataset for global *in situ* temperature and salinity measurements: data description and validation, Ocean Sci., 15, 1601–1614. https://doi.org/10.5194/os-15-1601-2019.

Tan, Z., L. Cheng, V. Gouretski, B. Zhang, Y. Wang, F. Li, Z. Liu, J. Zhu (2023). A new automatic quality control system for ocean profile observations and impact on ocean warming estimate, Deep Sea Research Part I: Oceanographic Research Papers, 194, 103961. https://doi.org/10.1016/j.dsr.2022.103961

Taylor, J. R. (1997). An Introduction to Error Analysis, 2nd edition, Sausalito, CA. University Science Books, 327 pp.

Thompson, P. R., M. J. Widlansky, E. Leuliette, D. P. Chambers, W. Sweet, B. D. Hamlington, S. Jevrejeva, M. A. Merrifield, G. T. Mitchum, and R. S. Nerem (2023). Sea-level variability and change [in "State of the Climate in 2022"]. Bull. Amer. Meteor. Soc., 104 (9), S173–S176, https://doi.org/10.1175/BAMS-D-23-0076.2

Toole, J. M., R. A. Krishfield, M.-L. Timmermans, and A. Proshutinsky (2011). The ice-tethered profiler: Argo of the arctic, Oceanography, 24(3), 126-135. https://doi.org/10.5670/oceanog.2011.64

Toggweiler, J.R. and Russell, J., 2008: Ocean circulation in a warming climate, Nature, 451, 286-288. https://doi.org/10.1038/nature06590

Trenberth, K. E., J. T. Fasullo, and J. Kiehl (2009) Earth's Global Energy Budget. Bull. Amer. Meteor. Soc., 90, 311–324. https://doi.org/10.1175/2008BAMS2634.1

Trenberth, K. E., and J. T. Fasullo (2013). An apparent hiatus in global warming?, Earth's Future, 1(1), 19-32. https://doi.org/10.1002/2013ef000165

Trenberth, K. E., J. T. Fasullo, and M. A. Balmaseda (2014a) Earth's Energy Imbalance. J. Climate, 27, 3129–3144. http://dx.doi.org/10.1175/JCLI-D-13-00294.1

Trenberth, K. E., J. T. Fasullo, G. Branstator, and A. S. Phillips (2014b) Seasonal aspects of the recent pause in surface warming, Nature Clim. Change, 4(10), 911-916. https://doi.org/10.1038/nclimate2341.

Trenberth, K. E. (2015). Has there been a hiatus?, Science, 349(6249), 691-692. http://dx.doi.org/10.1126/science.aac9225

Trenberth, K. E., J. T. Fasullo, K. von Schuckmann, and L. Cheng (2016). Insights into Earth's Energy Imbalance from Multiple Sources, J. Climate 29(20), 7495-7505. https://doi.org/10.1175/JCLI-D-16-0339.1

Trossman, D. S., and R. H. Tyler. (2019). Predictability of ocean heat content from electrical conductance. Journal of Geophysical Research: Oceans, 124, 667–679. https://doi.org/10.1029/2018JC014740

Trossman, D. S., and R. H. Tyler (2022). A Prototype for Remote Monitoring of Ocean Heat Content Anomalies. J. Atmos. Oceanic Technol., 39, 667–688. https://doi.org/10.1175/JTECH-D-21-0037.1

Tukey, J.W. (1974). Nonlinear (nonsuperposable) methods for smoothing data, in Proceedings of Congress Record, EASCON, Washington, D. C., p. 673

Tung, K. K., and J. Zhou (2013) Using data to attribute episodes of warming and cooling in instrumental records, PNAS, 110, 2058-2063. https://doi.org/10.1073/pnas.1212471110

UNESCO (1981). The Practical Salinity Scale 1978 and the International Equation of State of Seawater 1980. In Tenth Report of the Joint Panel on Oceanographic Tables and Standards (JPOTS) (25 p). UNESCO Technical Papers in Marine Science No. 36.

Vidard, A., D. Anderson, M. A. Balmaseda (2007) Impact of Ocean Observation Systems on Ocean Analysis and Seasonal Forecasts, Monthly Weather Review 135(2), https://doi.org/10.1175/MWR3310.1

von Schuckmann, K., J.-B. Sallée, D. Chambers, P.-Y. Le Traon, C. Cabanes, F. Gaillard, S. Speich, and M. Hamon (2013). Monitoring ocean heat content from the current generation of global ocean observing systems. Ocean Science Discussions, 10, pp.923-949. https://doi.org/10.5194/osd-10-923-2013

von Schuckmann, K., M. D. Palmer, K. E. Trenberth, A. Cazenave, D. Chambers, N. Champollion, J. Hansen, S. A. Josey, N. Loeb, P. P. Mathieu, B. Meyssignac, and M. Wild (2016). An imperative to monitor Earth's energy imbalance, Nature Clim. Change, 6(2), 138-144. https://doi.org/10.1038/nclimate2876

von Schuckmann, K., L. Cheng, M. D. Palmer, J. Hansen, C. Tassone, V. Aich, S. Adusumilli, H. Beltrami, T. Boyer, F. J. Cuesta-Valero, D. Desbruyères, C. Domingues, A. García-García, P. Gentine, J. Gilson, M. Gorfer, L. Haimberger, M. Ishii, G. C. Johnson, R. Killick, B. A. King, G. Kirchengast, N. Kolodziejczyk, J. Lyman, B. Marzeion, M. Mayer, M. Monier, D. P. Monselesan, S. Purkey, D. Roemmich, A. Schweiger, S. I. Seneviratne, A. Shepherd, D. A. Slater, A. K. Steiner, F. Straneo, M.-L.Timmermans, and S. E. Wijffels (2020). Heat stored in the Earth system: where does the energy go? Earth Syst. Sci. Data, 12, 2013–2041. https://doi.org/10.5194/essd-12-2013-2020

von Schuckmann, K., A. Minière, F. Gues, F. J. Cuesta-Valero, G. Kirchengast, S. Adusumilli, F. Straneo, M. Ablain, R. P. Allan, P. M. Barker, H. Beltrami, A. Blazquez, T. Boyer, L. Cheng, J. Church, D. Desbruyeres, H. Dolman, C. M. Domingues, A. García-García, D. Giglio, J. E. Gilson, M. Gorfer, L. Haimberger, M. Z. Hakuba, S. Hendricks, S. Hosoda, G. C. Johnson, R. Killick, B. King, N. Kolodziejczyk, A. Korosov, G. Krinner, M. Kuusela, F. W. Landerer, M. Langer, T. Lavergne, I. Lawrence, Y. Li, J. Lyman, F. Marti, B. Marzeion, M. Mayer, A. H. MacDougall, T. McDougall, D. P. Monselesan, J. Nitzbon, I. Otosaka, J. Peng, S. Purkey, D. Roemmich, K. Sato, K. Sato, A. Savita, A. Schweiger, A. Shepherd, S. I. Seneviratne, L. Simons, D. A. Slater, T. Slater, A. K. Steiner, T. Suga, T. Szekely, W. Thiery, M.-L. Timmermans, I. Vanderkelen, S. E. Wjiffels, T. Wu, and M. Zemp. (2023). Heat stored in the Earth system 1960–2020: where does the energy go?, Earth Syst. Sci. Data, 15, 1675–1709, https://doi.org/10.5194/essd-15-1675-2023

von Storch, H., and F. W. Zwiers (1999) Statistical Analysis in Climate Research, 484 pp., Cambridge University Press.

Wang, Z., T. Boyer, J. Reagan, and P. Hogan (2023). Upper-Oceanic Warming in the Gulf of Mexico between 1950 and 2020. J. Climate, 36, 2721–2734. https://doi.org/10.1175/JCLI-D-22-0409.1

Webb, D. C., P. J. Simonetti and C. P. Jones (2001). SLOCUM: an underwater glider propelled by environmental energy, IEEE Journal of Oceanic Engineering, vol. 26, no. 4, pp. 447-452, Oct. 2001. https://doi.org/10.1109/48.972077

Wielicki, B. A., B. R. Barkstrom, E. F. Harrison, R. B. Lee, G. L. Smith, and J. E. Cooper (1996) Clouds and the Earth's Radiant Energy System (CERES): An Earth Observing System Experiment. Bull. Amer. Meteor. Soc., 77, 853–868. https://doi.org/10.1175/1520-0477(1996)077<0853:CATERE>2.0.CO;2

Wijffels, S. E., J. Willis, C. M. Domingues, P. Barker, N. J. White, A. Gronell, K. Ridgway, and J. A. Church (2008). Changing Expendable Bathythermograph Fall Rates and Their Impact on Estimates of Thermosteric Sea Level Rise. J. Climate, 21, 5657–5672, https://doi.org/10.1175/2008JCLI2290.1

Wijffels, S., D. Roemmich, D. Monselesan, J. Church, and J. Gilson (2016), Ocean temperatures chronicle the ongoing warming of Earth, Nature Clim. Change, 6(2), 116-118. https://doi.org/10.1038/nclimate2924

Wild, M., D. Folini, C. Schär, N. Loeb, E. G. Dutton, and G. König-Langlo (2013) The global energy balance from a surface perspective. Clim. Dyn., 40, 3107-3134. https://doi.org/10.1007/s00382-012-1569-8

Wild, M., D. Folini, M. Z. Hakuba, C. Schär, S. I. Seneviratne, S. Kato, D. Rutan, C. Ammann, E. F. Wood and G. König-Langlo (2015). The energy balance over land and oceans: an assessment based on direct observations and CMIP5 climate models. Clim Dyn 44, 3393–3429. https://doi.org/10.1007/s00382-014-2430-z

Willis, J. K., D. Roemmich, and B. Cornuelle (2003). Combining altimetric height with broadscale profile data to estimate steric height, heat storage, subsurface temperature, and sea-surface temperature variability, J. Geophys. Res., 108 (C9), 3292, https://doi.org/10.1029/2002JC001755

Willis, J. K., D. Roemmich, and B. Cornuelle (2004). Interannual variability in upper ocean heat content, temperature, and thermosteric expansion on global scales, J. Geophys. Res., 109, C12036, https://doi.org/10.1029/2003JC002260

Willis, J. K., J. M. Lyman, G. C. Johnson, and J. Gilson (2007). Correction to “Recent cooling of the upper ocean”, Geophys. Res. Lett., 34, L16601. https://doi.org/10.1029/2007GL030323

Willis, J. K., D. P. Chambers, and R. S. Nerem (2008). Assessing the globally averaged sea level budget on seasonal to interannual timescales, J. Geophys. Res. Oceans, 113, C06015. https://doi.org/10.1029/2007JC004517

Wong, A. P. S., S. E. Wijffels, S. C. Riser, S. Pouliquen, S. Hosoda, D. Roemmich, J. Gilson, G. C. Johnson, K. Martini, D. J. Murphy, M. Scanderbeg, TVS U. Bhaskar, J. J. H. Buck, F. Merceur, T. Carval, G. Maze, C. Cabanes, X. André, N. Poffa, I. Yashayaev, P. M. Barker, S. Guinehut, M. Belbéoch, M. Ignaszewski, M. O. Baringer, C. Schmid, J. M. Lyman, K. E. McTaggart, S. G. Purkey, N. Zilberman, M. B. Alkire, D. Swift, W. B. Owens, S. R. Jayne, C.

Hersh, P. Robbins, D. West-Mack, F. Bahr, S. Yoshida, P. J. H. Sutton, R. Cancouët, C. Coatanoan, D. Dobbler, A. G. Juan, J. Gourrion, N. Kolodziejczyk, V. Bernard, B. Bourlès, H. Claustre, F. D'Ortenzio, S. Le Reste, P.-Y. Le Traon, J.-P. Rannou, C. Saout-Grit, S. Speich, V. Thierry, N. Verbrugge, I. M. Angel-Benavides,, B. Klein, G. Notarstefano, P.-M. Poulain, P. Vélez-Belchí, T. Suga, K. Ando, N. Iwasaska, T. Kobayashi, S. Masuda, E. Oka, K. Sato, T. Nakamura, K. Sato, Y. Takatsuki, T. Yoshida, R. Cowley, J. L. Lovell, P. R. Oke, E. M. van Wijk, F. Carse, M. Donnelly, J. W. Gould, K. Gowers, B. A. King, S. G. Loch, M. Mowat, J. Turton, E. P. Rama Rao, M. Ravichandran, H. J. Freeland, I. Gaboury, D. Gilbert, B. J. W. Greenan, M. Ouellet, T. Ross, A. Tran, M. Dong, Z. Liu, J. Xu, K. Kang, H. Jo, S.-D. Kim, and H.-M. Park (2020). Argo Data 1999–2019: Two Million Temperature-Salinity Profiles and Subsurface Velocity Observations From a Global Array of Profiling Floats. Frontiers in Marine Science, 7. https://doi.org/10.3389/fmars.2020.00700

World Meteorological Organization (WMO) (2017). WMO Guidelines on the Calculation of Climate Normals, WMO- NO 1203

Wouters, B., J. A. Bonin, D. P. Chambers, REM Riva, I. Sasgen, and J. Wahr (2014). GRACE, time-varying gravity, Earth system dynamics and climate change. Reports on Progress in Physics, 77(11), 1-41. https://doi.org/10.1088/0034-4885/77/11/116801

Wu, X., X.-H. Yan, Y.-H. Jo, and W. T. Liu (2012), Estimation of subsurface temperature anomaly in the north atlantic using a self-organizing map neural network, J. Atmos. Oceanic Technol. , 29(11), 1675-1688. https://doi.org/10.1175/JTECH-D-12-00013.1

Xie, S.-P., Y. Kosaka, and Y. M. Okumura (2016), Distinct energy budgets for anthropogenic and natural changes during global warming hiatus, Nature Geosci., 9(1), 29-33. https://doi.org/10.1038/ngeo2581

Xue, Y., M. A. Balmaseda, T. Boyer, N. Ferry, S. Good, I. Ishikawa, A. Kumar, M. Rienecker, A. J. Rosati, and Y. Yin (2012) A Comparative Analysis of Upper-Ocean Heat Content Variability from an Ensemble of Operational Ocean Reanalyses. J. Climate, 25, 6905–6929, https://doi.org/10.1175/JCLI-D-11-00542.1.

Xue, Y., C. Wen, X. Yang, D. Behringer, A. Kumar, G. Vecchi, A. Rosati, and R. Gudgel (2017). Evaluation of tropical Pacific observing system using NCEP and GFDL ocean data assimilation system. Climate Dynamics, 49, 843-868. https://doi.org/10.1007/s00382-015-2743-6

Yan, X.-H., Jo, Y., Liu, W.T. and M. He, (2006), A new study of the Mediterranean outflow, air-sea interactions, and Meddies using multi-sensor data, J. Phys. Oceanogr. Vol. 36, No. 4, pages 691-710. https://doi.org/10.1175/JPO2873.1

Yang, C., Storto, A. & Masina, S. (2019). Quantifying the effects of observational constraints and uncertainty in atmospheric forcing on historical ocean reanalyses. Clim Dyn 52, 3321–3342. https://doi.org/10.1007/s00382-018-4331-z

Yoon, S.-T., K.-I. Chang, H. Na, and S. Minobe (2016). An east-west contrast of upper ocean heat content variation south of the subpolar front in the East/Japan Sea, J. Geophys. Res. Oceans, 121(8), 6418-6443. https://doi.org/10.1002/2016JC011891

Zang, X., C. Wunsch, 2001: Spectral Description of Low-Frequency Oceanic Variability. J. Phys. Oceanogr., 31, 3073–3095. http://dx.doi.org/10.1175/1520-0485(2001)031<3073:SDOLFO>2

Zhang, Y., J. M. Wallace, and D. S. Battisti (1997) ENSO-like Interdecadal Variability: 1900–93. J. Climate, 10. 1004–1020, https://doi.org/10.1175/1520-0442(1997)010<1004:ELIV>2.0.CO;2

Zhu, J., G. Vernieres, T. Sluka, S. Flampouris, Arun Kumar, A. Mehra, M. F. Cronin, D. Zhang, S. Wills, J. Wang, and W. Wang , 2021: Roles of TAO/TRITON and Argo in tropical Pacific observing system: An OSSE study for multiple time scale variability. J. Climate, 34, 6797-6817. https://doi.org/10.1175/JCLI-D-20-0951.1

Zou, C.-Z., H. Xu, X. Hao, and Q. Fu (2021). Post-millennium atmospheric temperature trends observed from satellites in stable orbits. Geophysical Research Letters, 48, e2021GL093291. https://doi.org/10.1029/2021GL093291